How Interfaces in Flow Determine Droplet Breakup and Behavior

Dissertation
zur Erlangung des Grades
des Doktors der Naturwissenschaften
der Naturwissenschaftlich-Technischen Fakultät II
- Physik und Mechatronik -
der Universität des Saarlandes

von

Dipl. Phys. Michael Hein

Saarbrücken

2015

Tag des Kolloquiums: 10.08.2015

Dekan: Univ.-Prof. Dr.-Ing. Georg Frey

Mitglieder des Prüfungsausschusses:

Vorsitzender: Univ.-Prof. Dr. rer. nat. Ludger Santen

Gutacher: Univ.-Prof. Dr. rer. nat. Ralf Seemann

Univ.-Prof. Dr. rer. nat. Helmut Seidel

Univ.-Prof. Dr. rer. nat. Steffen Hardt

Akad. Mitarbeiter: Dr.-Ing. Andreas Tschöpe

Kurzzusammenfassung

Tropfenbasierte Mikrofluidik ist eine beliebte Methode zur Miniaturisierung (bio-)chemischer Analysen und Synthesen. Allerdings mangelt es bis heute an einem vollständigen Verständnis der Tropfenbildung und der Strömung von Tropfen in Mikrokanälen, welche beide durch Grenflächenkräfte und dynamische Effekte beeinflusst werden. Tropfenbildung wurde im Rahmen dieser Arbeit am Beispiel des Zerfalls flüssiger Filamente an einer topografischen Stufe untersucht. Durch Charakterisierung der Filamentform konnte der Übergang zwischen zwei Regimen der Tropfenproduktion mittels eines einfachen geometrischen Kriteriums vorhergesagt werden. Weitere Regime wurden für breitere Filamente gefunden und beschrieben. Weiterhin wird gezeigt, dass die sich die Strömung in länglichen Tropfen in rechteckigen Mikrokanälen mit zunehmender Tropfengeschwindigkeit strukturell ändert, was durch die zunehmende Deformation der Tropfen verursacht wird. Folglich lässt sich die geschwindigkeitsabhängige Akkumulation von Partikeln in länglichen Tropfen durch das Zusammenspiel von innerer Strömung und Sedimentation erklären. Die Anwendbarkeit dieses Effekts für "On-Chip" Partikel- und Zellanreicherung wird aufgezeigt. Zusätzlich wird ein Verfahren eingeführt, mit dem sich der Einfluss defokusierter Tracerpartikel auf Strömungsmessungen mittels μPIV bestimmen lässt. Dies erleichtert sowohl die Versuchsplanung als auch die Interpretation von Messungen in dreidimensionalen Strömungen.

Abstract

Droplet based microfluidics today is a popular tool for miniaturized (bio-)chemical analysis and synthesis. Despite large scientific efforts, a profound understanding of droplet formation and of the dynamics of droplets in microchannels is still wanted, both determined by interfacial forces and dynamic effects. Droplet formation is studied for a liquid filament subject to a sudden release of confinement. Characterizing the filament shape, the transition between two distinct breakup regimes is predicted by a simple geometric criterion. Additional breakup regimes are reported and described upon increasing the width of the filament. The internal flow field of elongated droplets in rectangular microchannels is demonstrated to qualitatively change with increasing droplet velocity, caused by deformation of the droplet's outer shape. Consequently, the velocity dependent accumulation of particles within droplets is explained by the interplay between the internal flow field and gravity driven sedimentation. Application of this field free particle accumulation to on-chip particle and cell enrichment is demonstrated. Additionally, a method to directly characterize the influence of defocused tracer particles on flow velocities measured by μPIV is proposed to facilitate design of experiments and interpretation of velocity fields measured in three dimensional flows.

Contents

1. Introduction

Miniaturization is one of the most vibrant and thriving trends in science and industry ever since the beginning of the microelectronic revolution in the 1960s. The miniaturization of electronic systems and the accompanying decrease of cost of computational power make communication and acquisition of information easier than ever, available everywhere at all times. These developments have changed the way of live in industrialized countries with a momentum and impact incomparable to any other technological achievement in the history of humanity.

To facilitate the production of microelectronic systems, a plethora of microfabrication techniques have been developed that are nowadays commonly used in semiconductor industry. However, researchers quickly realized that techniques like selective etching and deposition of functional material layers allow for much more than just purely electronic microsystems [1, 2]. Starting in the 1980s, increasing numbers of Micro Electro-Mechanical Systems (MEMS) were developed, combining electronics and miniaturized mechanical components. Today, MEMS are widely used in our everyday gadgets with applications ranging from microphones and position sensors in smartphones to acceleration sensors in cars.

Naturally, the next step was including the handling of tiny amounts of fluids on microchips to make MEMS valuable for (bio-)chemical detection and synthesis. However, it was not before the 1990s that the emerging new discipline in science and engineering called "microfluidics" gained in momentum. Initial microfluidic research mainly dealt with handling continuous streams of a single liquid phase or with inkjet-printing, where ink droplets are ejected from a micro-actuated nozzle [3–5]. Besides working on the development of fluid handling tools such as small valves, pumps and separation systems [6–9], researchers quickly began to specifically design microfluidic systems for chemical reactions or (bio-)chemical analysis, so called micro-Total Analysis Systems (μTAS) or Lab-on-a-Chip (LoC) devices [10, 11]. An early example of a commercialized LoC product are the widespread glucose-meter test strips used to monitor glucose levels of diabetes patients, that consume only minute amounts of blood.

Downscaling bulk methods to microfluidic systems offers significant advantages, i.e. minute sample and reagent consumption, possible portability of the analytic device, low-cost production of disposable chips and superior control over reaction conditions such as temperature and concentration gradients. However, several difficulties arise from the changing physics at small scales: Microfluidic flows are typically laminar as viscous dissipation quickly damps out any possible turbulence on small scales. While this is beneficial whenever precise control of the flow is needed, laminar flow prevents rapid mixing of fluids and reagents that can only proceed via diffusion. Additionally, the flow profile typically established due to viscous friction with channel walls causes plugs of sample liquids loaded into the channel to smear out due to Taylor-Aris dispersion. Thus, concentrations of analytes may be significantly reduced prior to analysis and channels are contaminated by the sample, preventing re-use of the same chip for subsequent analysis.

The disadvantages of continuous microfluidic systems can be overcome using multiphase flows in microfluidics. In "droplet based microfluidics", droplets surrounded by another immiscible liquid are manipulated. The presence of liquid/liquid interfaces induces recirculative swirling flow profiles within the droplet, that significantly reduce mixing timescales of reactants and thus effectively accelerate chemical reactions. Additionally, using droplets as discrete reaction vessels intrinsically reduces contamination of channel walls and dispersion [5,12]. Furthermore, the problem of channel clogging in the presence of particles or jellifying reactions can be significantly reduced using droplets to host the respective substances and to prevent contact to channel walls. Manipulating the content of each droplet, droplet based microfluidic systems offer the potential for massive parallelization and high-throughput screenings for (bio-)chemical or pharmaceutical application [13].

To exploit the full potential of droplet based systems, a profound understanding of the interfacial instabilities leading to the formation of monodisperse emulsions as well as the dynamics of droplets in microchannels is crucial, both studied within the framework of this thesis. The present work is comprised of six publications, which are presented in the Addendum of this thesis: Four scientific papers already published or accepted in peer-reviewed journals, accompanied by two conference proceedings. Although these publications are the offspring of different projects, they are strongly interconnected.

The results chapters are preluded by a short introduction to the physics of liquids on small scales in Chapter 2. Subsequently, device fabrication methods and quantitative measurement techniques employed in the framework of this thesis are elucidated in Chapter 3. These common fundamentals are essential to the three following result chapters. Each of these result chapters is comprised of a review summarizing the relevant literature and state of the art of the respective topic, followed by a short summary of the results presented in the journal articles and proceedings attached as addenda.

Chapter 4 deals with the breakup of a squeezed liquid filament co-flowing with an immiscible continuous phase in a shallow channel and subject to a sudden release of confinement at a topographic step. Droplet formation devices of this type, so called "Step-emulsification" geometries, typically feature two distinct breakup regimes. In the first regime the filament decays into monodisperse droplets right at the topographic step. The second regime features a jet of dispersed phase being ejected beyond the step, from which droplets detach primarily due to capillary instabilities. A quantitative model for the filament shape within the terrace channel is developed and verified experimentally in Addendum I, capable to accurately predict the transition between both droplet breakup regimes. Addendum II widens the parameter range studied in Addendum I, surprisingly finding a plethora of new droplet breakup regimes for very wide and shallow filaments. These new regimes, consisting of several coexisting droplet producing instabilities interacting on the same filament, are characterized experimentally and arguments for the transitions between individual regimes are proposed. Finally, Addendum III exemplifies practical application of two hydrodynamically coupled Step-emulsification geometries to on-chip production of solid particles via a sol-gel reaction scheme.

Chapter 5 and Addendum IV deal with particle accumulation and concentration within elongated droplets of several nanolitres in volume in rectangular microchannels. The ability to concentrate particles on-chip is a prerequisite for miniaturization of many biochemical assays using solid particles with functionalized surfaces or chemical reactions facilitated by the presence of a solid catalyst. Accumulation patterns depend on particle and dispersed phase properties as well as on the droplet traveling velocity, which is shown to be a consequence of a topologically changing flow field inside the droplets. The topological transition of the internal flow is shown to be caused by increasing deformation of the droplet interface at elevated droplet velocities.

The internal velocity field of droplets has been studied by μPIV, a non-invasive optical technique based on cross-correlation of images of small tracer particles which follow the internal flow. Tracer particles within a certain interval around the focal plane can significantly influence the measured in-plane velocities in the presence of out-of-plane velocity gradients. Knowing this distance is important when designing experiments and interpreting measurements on complex three-dimensional flows such as the internal recirculation within droplets in microfluidic channels. In Chapter 6 and Addenda V and VI, a novel method to determine the influence of out-of-focus particles on μPIV measurements from experimentally recorded particle images is introduced.

Finally, the presented findings and results are discussed in an overall summary and an outlook to possible future work is given in the concluding Chapter 7.

2. Theory and Background

Microfluidic systems have evolved to powerful tools in many different fields of application. The main reason for this success, besides the minute sample volumes that can be handled in typical microfluidic chips, is the changing physics of fluid flow upon decreasing the system size to the micro-scale. The phenomenon can be best illustrated by a simple scaling argument: surface forces typically scale with surface area, i.e. $\propto l^2$, while volume forces scale with $\propto l^3$. Consequently, the ratio of these two forces grows $\propto l^{-1}$. Thus, interfacial forces typically dominate over viscous forces and inertia on small scales, turbulence is suppressed by viscous dissipation and mixing is governed by diffusion. It is the purpose of this chapter to give a brief overview over the physics of fluid flow on small scales.

2.1. Flows on Small Scales - Fundamentals

2.1.1. General Equation of Motion

To describe the flow of liquids on any scale and without making any assumption on the nature of the fluid, the integral form of Newtons second law is a good starting point. Below, the general equation of motion is derived following the line of argumentation given in [14]. The sum of the forces acting on a small volume of fluid is related to its change of momentum:

$$\frac{d}{dt}\left[\iiint_V \rho\vec{u}\,d\tau\right] = \underbrace{\iiint_V \rho\vec{f}\,d\tau}_{\text{volume forces}} + \underbrace{\iint_S [\sigma]\vec{n}\,d\Sigma}_{\text{surface forces}}, \tag{2.1}$$

with $\frac{d}{dt}$ representing the Lagrangian derivative in the co-moving frame of reference, ρ the density of the fluid in the element $d\tau$, $\vec{u}$ the fluid velocity, V the volume, $\vec{f}$ body forces per unit mass acting on the fluid element $d\tau$ such as gravity and $[\sigma]$ the stress tensor including all surface forces caused by pressure and viscous forces acting on a surface element $d\Sigma$ with the normal vector $\vec{n}$. As any element of fluid in this frame of reference by definition contains the same number of molecules, $\rho d\tau$ is a constant and the left hand side of equation 2.1 reads as:

$$\frac{d}{dt}\left[\iiint\limits_V \rho\vec{u}\,d\tau\right] = \iiint\limits_V \rho\frac{d}{dt}\vec{u}\,d\tau \tag{2.2}$$

Using the Gauss theorem for each component i of the surface forces, the last term on the right hand side of 2.1 reads as:

$$\begin{aligned}\left[\iint\limits_S [\sigma]\vec{n}\,d\Sigma\right]_i &= \iint\limits_S \sigma_{ij}n_j\,d\Sigma \\ &\overset{\text{Gauss}}{=} \iiint\limits_V \frac{\partial\sigma_{ij}}{\partial x_j}\,d\tau\end{aligned} \tag{2.3}$$

with i, j indicating directional components of the vector $\vec{x} = (x,\ y,\ z)$ and Einstein implicit summation over the index j. Thus, for an infinitesimal volume element, the equation of motion is derived as:

$$\rho\frac{d\vec{u}}{dt} = \rho\vec{f} + \vec{\nabla}\cdot[\sigma] \tag{2.4}$$

Finally, decomposing the components of the stress tensor $[\sigma]$ into viscosity terms σ'_{ij} and pressure related terms $p\delta_{ij}$ [15]:

$$\begin{aligned}\sigma_{ij} &= \sigma'_{ij} - p\delta_{ij} \\ \text{with } \delta_{ij} &= \begin{cases}1 & i = j \\ 0 & i \neq j\end{cases} \\ \vec{\nabla}\cdot[\sigma] &= \vec{\nabla}\cdot[\sigma'] - \vec{\nabla}p\end{aligned} \tag{2.5}$$

and using the Lagrangian derivative of the fluid velocity $\vec{u}$:

$$\frac{d\vec{u}}{dt} = \frac{\partial\vec{u}}{\partial t} + (\vec{u}\cdot\vec{\nabla})\vec{u} \tag{2.6}$$

the general equation of motion for fluids is obtained:

$$\rho\frac{\partial\vec{u}}{\partial t} + \rho(\vec{u}\cdot\vec{\nabla})\vec{u} = \rho\vec{f} - \vec{\nabla}p + \vec{\nabla}\cdot[\sigma'] \tag{2.7}$$

with $[\sigma']$ being the viscous stress tensor.

2.1.2. Navier-Stokes Equation

Using 2.7, the equation of motion for Newtonian liquids, i.e. liquids with a constant viscosity, can be derived. The ith component of the gradient of $[\sigma']$ can be substituted by:

$$\begin{aligned} \{\vec{\nabla}\cdot[\sigma']\}_i &= \frac{\partial \sigma'_{ij}}{\partial x_j} \\ &= \mu\frac{\partial^2 u_i}{\partial x_j \partial x_j} + (\zeta + \frac{\mu}{3})\frac{\partial}{\partial x_i}\frac{\partial u_l}{\partial x_l} && (2.8) \\ \vec{\nabla}\cdot[\sigma'] &= \mu\vec{\nabla}^2\vec{u} + \underbrace{(\zeta + \frac{\mu}{3})\vec{\nabla}(\vec{\nabla}\cdot\vec{u})}_{\text{compressibility}} && (2.9) \end{aligned}$$

again with Einstein summation over the indices [15]. Here, spatial variations of both viscosity coefficients μ and ζ are implicitly neglected, which holds true for most liquids. However, spatial variations of these coefficients have to be considered when dealing with the flow of inhomogeneous media such as emulsions or suspensions. Limiting the analysis to incompressible liquids, which is typically valid for Newtonian liquids even on the microscale, reduces the equation of continuity to:

$$\frac{\partial u_l}{\partial x_l} = \vec{\nabla}\cdot\vec{u} = 0 \tag{2.10}$$

Thus causing the last term in eq. 2.9 to vanish. The Navier-Stokes equation is obtained substituting eq. 2.9 and 2.10 into eq. 2.7 [14,15]:

$$\rho\frac{\partial \vec{u}}{\partial t} + \rho(\vec{u}\cdot\vec{\nabla})\vec{u} = \rho\vec{f} - \vec{\nabla}p + \mu\vec{\nabla}^2\vec{u} \tag{2.11}$$

μ represents the dynamic viscosity. Equation 2.11 represents the balance of forces for an incompressible fluid element. The terms on the left represent inertial forces, while the terms on the right include viscous dissipation, pressure gradients and body forces such as gravity. This equation is often considered the basic equation of fluidics. Indeed, a lot of physical understanding of the flow of liquids, especially on small scales, can be derived from equation 2.11, provided the fluids can still be assumed to be a continuous medium. The latter assumption, however, remains valid in the course of the present work, as all channel dimensions typically remain well above molecular scales.

2.1.3. The Reynolds Number

Before turning back on the simplification of the Navier-Stokes equation specifically interesting to flows on the micro-scale, the Reynolds Number Re is introduced, that is frequently used to non-dimensionalize the Navier-Stokes equation [14].

$$Re = \frac{\rho U L}{\mu} \tag{2.12}$$

with U being a typical velocity and L a characteristic length, respectively. Re represents the ratio of convective flux of momentum to diffusive flux of momentum and determines the relative importance of fluid inertia compared to viscous forces: At low Re viscous forces dominate and thus the emergent flow field is determined by an equilibrium between viscous dissipation and external forcing, e.g. by an external pressure gradient. In this regime, the flow field is usually stationary with streamlines regularly spaced relative to each other. Additionally, the flow field is very stable, as any disturbance is quickly suppressed by viscous dissipation. This regime is called laminar flow. Equation 2.12 illustrates that the laminar regime can be maintained by either increasing the fluid viscosity μ or decreasing the typical dimension or velocity, keeping Re small. At elevated values of Re, however, the flow is mainly dominated by inertia. Thus, small disturbances are amplified and the flow field becomes increasingly chaotic and non-stationary upon increasing the average velocity. This regime is referred to as turbulent flow. For pipe flow, complete turbulence is typically reached for $Re \approx O(10^2 - 10^3)$. In the course of the present work and for typical microfluidic systems Re is typically $O(10^{-3} - 10^0)$, thus deep within the laminar regime. However, depending on the considered problem, fluid inertia might become relevant already in the laminar regime at $Re \approx O(10^0)$.

2.1.4. Stokes and Hele-Shaw Approximation

As described above, flows at small scales typically present low Reynolds numbers $Re <<$ 1. In this regime, the Navier Stokes equation 2.11 can be significantly simplified by neglecting all inertia terms, i.e.$\rho\frac{\partial\vec{u}}{\partial t} + \rho(\vec{u} \cdot \vec{\nabla})\vec{u} = 0$. The result is the Stokes equation, that describes the flow of viscous fluids at low Re:

$$\rho\vec{f} - \vec{\nabla}p + \mu\vec{\nabla}^2\vec{u} = 0 \tag{2.13}$$

Albeit being much easier to handle than the full Navier-Stokes equation, equation 2.13 is still only numerically solvable in many cases. One special case that can be solved analytically is the so called Hele-Shaw approximation. In this approximation, the liquid flow is confined by two flat plates of distance W at $y = 0$ and $y = W$, cf. Fig. 2.1. Thus

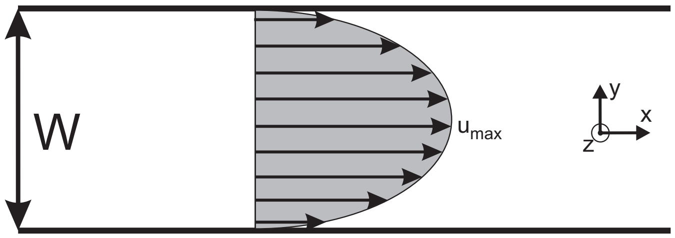

Figure 2.1.: Poiseuille flow established between two parallel plates.

the problem reduces to a two dimensional flow problem. The velocity components u_y and u_z are neglected. Employing the No-Slip boundary condition $u_x(y = 0, W) = 0$ at the walls, resulting from the friction with the walls and absence of additional body forces, the resulting flow profile is derived from equation 2.13 [14]:

$$\begin{aligned} u_x(y) &= \frac{-\partial_x p}{2\mu}(yW - y^2) \\ &= \underbrace{\frac{-\partial_x p}{8\mu} W^2}_{u_{max}} \cdot \left(\frac{4y}{W} - \frac{4y^2}{W^2}\right) \end{aligned} \tag{2.14}$$

with the plates being at $y = 0$ and $y = W$. Equation 2.14 shows a quadratic y-dependence of $u_x(y)$. Thus the velocity profile between two parallel plates takes a parabolic shape and is referred to as Poiseuille flow. This well known flow-profile also represents a good approximation for rectangular channels of high aspect ratio [4].

The presented Hele-Shaw approximation is the theoretical foundation for the volume-of-fluid simulations used to model the interface between two immiscible phases in Addendum I.

Averaging equation 2.14 results in:

$$\bar{u} = \frac{-\partial_x p W^2}{12\mu} \tag{2.15}$$

This relation is often referred to as Darcy's law. From equation 2.15 it can be easily seen, that:

$$\omega = rot_y \bar{u} = 0 \tag{2.16}$$

Here ω is the vorticity of the flow. Thus, the flow field in Hele-Shaw cells is free of vortices [4]. In multiphase flow, however, the situation is changed by the presence of liquid/liquid interfaces, e.g. the interface of droplets of one phase dispersed in another immiscible phase. These interfaces can introduce swirling flows and vortices within droplets that are caused by recirculation due to friction with the channel walls and volume conservation

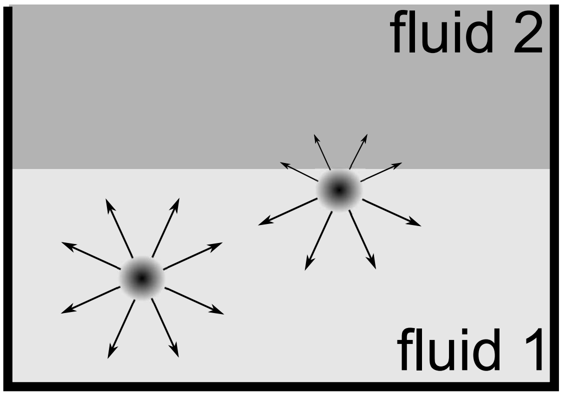

Figure 2.2.: Model explaining the interfacial tension by different forces on a molecule in the bulk of a fluid or at interfaces.

within the droplet.

2.2. Multiphase Flow and Emulsions

2.2.1. Interfacial Tension

The mathematical description of fluid flow derived in equation 2.7 is valid for any liquid flowing in any geometry. However, when dealing with mixtures of different immiscible liquids, such as emulsions consisting of droplets of a dispersed phase surrounded by a continuous phase, additional forces arise that have to be considered. The origin of these forces is the surface tension γ, also more precisely referred to as interfacial tension. The origin of the interfacial tension is depicted in Fig. 2.2. Molecules in liquids attract each other, e.g. via van der Waals forces (black arrows). Typically, these forces only range for a few nanometers and strongly depend on the molecules involved [4, 16]. For a molecule in the bulk of fluid 1, that is completely surrounded by molecules of the same family, these forces cancel out. For a molecule at an interface, however, a net force directed towards the bulk of fluid 1 arises due to the reduced attractive forces towards molecules of the second fluid. Thus, being at the interface is energetically unfavorable for molecules. However, volume conservation and the Pauli principle force some molecules towards the interface. As a consequence, immiscible liquids try to minimize their interfacial area, which explains the typically spherical shapes of small liquid droplets provided external forces and gravity are negligible. To create additional interfacial area A, more molecules have to be transported from the bulk of fluid 1 towards the second fluid, a process that consumes energy $E = \gamma A$. The interfacial tension counteracting the creation of new interfacial area physically represents a specific surface energy.

2.2.2. Laplace Pressure

A direct consequence of the interfacial tension and the resulting minimization of interfacial area is an additional pressure contribution within liquid volumes surrounded by another fluid. The pressure within a liquid volume surrounded by another liquid will be larger than the pressure in the surrounding medium to compensate for the surface-force generated by interfacial tension. For a liquid volume of arbitrary shape, comparing the work needed to increase the interfacial area with the corresponding work by the counteracting internal pressure $\Delta p = p_{in} - p_{out}$ leads to the Young-Laplace relation:

$$\Delta p = p_{in} - p_{out} = \gamma \left(\frac{1}{R} + \frac{1}{R'} \right) \tag{2.17}$$

with R and R' the principal radii of the considered liquid volume interface. Δp is commonly known as the Laplace pressure. If the liquid volume is not confined by walls or deformed by external forces, it will adopt a spherical shape with radius $R = R'$, which leads to an additional internal pressure of $\Delta p = 2\gamma/R$ [14].

2.2.3. Capillary and Weber Number

To characterize the relative importance of surface forces in multiphase systems two more non-dimensionalized numbers will be used in the remainder of this thesis.

The Capillary Number Ca is defined as the ratio of viscous friction and interfacial forces:

$$Ca = \frac{\mu U}{\gamma} \tag{2.18}$$

Note, that besides being a function of the liquid system properties, Ca may depend on the sample geometry via the definition U. Analogous to the definition of the Reynolds Number, U is a typical velocity for the considered problem and μ is a characteristic viscosity. While the average velocity over the entire sample may be low, local velocities might be significantly higher, e.g. in porous media flow, leading to viscous forces becoming relevant locally while the overall Ca remains small. This generality leads to a large variety of definitions for many non-dimensional numbers and specifically for Ca. In the course of this thesis Ca will be defined in different ways depending on the considered physical problem: μ is either chosen to be the viscosity of the dispersed phase within droplets or of the surrounding oily phase. U can represent either the average flow velocity of either phase at a given point or the average traveling velocity of a droplet in a channel, cf. chapters 4 and 5 and Addenda I, II and IV. However, typical values of Ca within this thesis range from $O(10^{-4} - 10^{-1})$. Thus interfacial forces typically dominate over viscous forces for all considered systems, irrespective of the different definitions of Ca.

The Weber Number We compares fluid inertia to surface forces and is thus defined by the ratio:

$$We = \frac{\rho U^2 L}{\gamma} \tag{2.19}$$

Again, We is typically < 1 in the present experiments, which shows that capillarity, i.e. forces by interfacial tension, dominates also over fluid inertia.

2.2.4. Wettability

The wettability of a solid surface by a liquid surrounded by another fluid is of massive relevance for many technical applications were a surface is coated by a liquid, e.g. in ink-jet printing, spray coating or photolithography. Whenever three different phases meet at a common contact line, interfacial energies will arrange the liquids to the energetically most favorable shapes at constant Laplace pressure, i.e. constant curvature of the free liquid interfaces [17].

To explain the interfacial tension driven organization of fluids on a substrate the example of a liquid droplet on a solid substrate, surrounded by a vapor phase will be considered. Nonetheless, the vapor phase can be replaced by a second liquid without any changes of the underlying processes. Depending on the combination of surface energies of the interfaces between solid/vapor γ_{sv}, solid/liquid γ_{sl} and liquid/vapor γ_{lv}, three different fundamental wetting situations can be distinguished, cf. Fig. 2.3. The liquid phase either wets the surface completely by spreading over the entire surface (Fig. 2.3a) or it forms a droplet shaped as a spherical cap (Fig. 2.3b). In the extreme case of non-wetting, the liquid will minimize the contact area with the solid surface by forming a spherical droplet sitting on the surface (Fig. 2.3c).

The macroscopic contact angle θ is used to quantify the wettability of a surface by a liquid surrounded by a given fluid. This contact angle can be calculated by the Young's construction, provided γ_{sv}, γ_{sl} and γ_{lv} are known, cf. (Fig. 2.3b). A droplet can only reach its equilibrium shapes once the forces acting on the three face contact line caused by the three interfacial tensions balance. To calculate the equilibrium contact angle θ, the variation of energy needed to displace the contact line by a distance δx is calculated:

$$\delta W = (\gamma_{sv} - \gamma_{sl})\delta x - \gamma_{lv}\cos(\theta)\delta x \tag{2.20}$$

In mechanical equilibrium $\delta W = 0$ and the Young's equation of the contact angle is

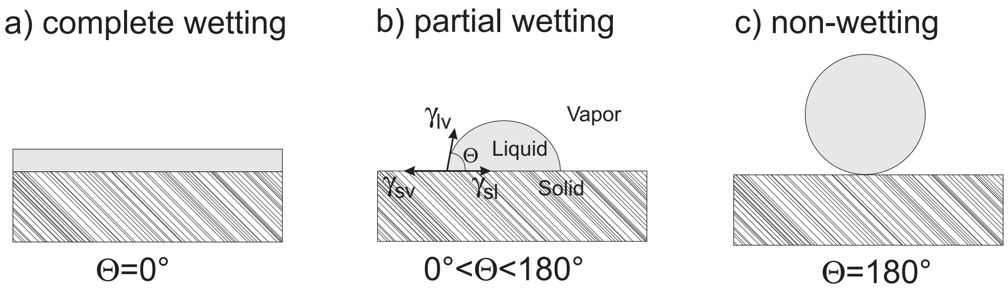

Figure 2.3.: Sketches of wetting regimes: a) Complete wetting resulting in a closed liquid film on the surface. b) Partial wetting: liquid droplets form spherical caps on the surface. c) Non-wetting: liquid minimizes the contact area to the surface by forming a spherical droplet.

obtained:

$$\gamma_{sv} - \gamma_{sl} = \gamma_{lv} \cos(\theta) \tag{2.21}$$

For $\theta = 0°$ the surface is completely wet by the liquid, cf. Fig. 2.3. For all intermediate values of θ, the surface is partially wet, while for $\theta = 180°$ the surface is non-wetting for the given liquid system.

The Young's equation works well on ideal surfaces. However, real surfaces usually present surface roughness or chemical inhomogeneities. Contact lines can become pinned at these surface inhomogeneities, leading to a large scatter in measured contact angles when simply placing a droplet on the surface. To quantify the wettability of real substrates the contact angles during advancing θ_{adv} and receding θ_{rec} of the three phase contact line have to be measured. This is typically done by inflating and deflating a droplet on the surface and measuring θ during the process. If the movement of the contact line is slow, i.e. $Ca << 1$ and $We << 1$, then the droplet is in quasi-equilibrium at all times and θ_{adv} and θ_{rec} are independent of the contact line velocity, with $\theta_{adv} > \theta_{rec}$. The hysteresis between θ_{adv} and θ_{rec} then presents a good measure for the surface quality. For faster moving contact lines, inertia and viscous forces are non-negligible and the dynamic contact angle depends on the contact line velocity.

2.2.5. Surfactants

Interfacial tensions between pure immiscible liquids are typically on the range of several tenth of mN/m. Such large interfacial tensions make it very difficult to control droplet producing instabilities on a micro-scale and to produce monodisperse droplets. Large surface forces destabilize the system and typically lead to random droplet breakup. Furthermore, as small droplets are energetically unfavorable due to their high surface to volume ratio, high interfacial tension prevents the production of stable emulsions. Small

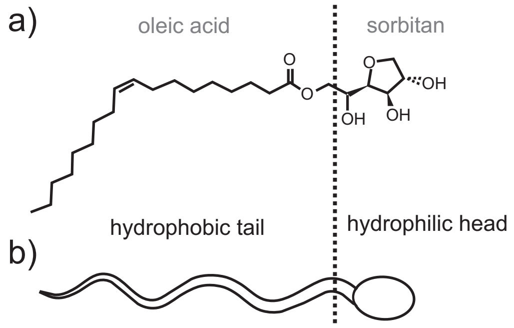

Figure 2.4.: a) Molecular structure of the surfactant sorbitane-monooleate (Span80), which is composed of a hydrophilic head (sorbitane) and a hydrophobic tail (oleic acid).
b) Simplified sketch of the amphiphilic structure of surfactant molecules.

droplets will rapidly disappear due to Ostwald ripening, which is caused by the higher Laplace pressure inside of small droplets. Dispersed phase from small droplets will preferentially dissolve in the continuous phase and diffuse into larger droplets with a smaller Laplace pressure. Additionally, coalescence occurs when two droplets approach each other by thinning and rupture of the liquid film separating the droplets. At high interfacial tension, coalescence can occur right at the droplet production site, thus disturbing the droplet production itself. These effects should be avoided when studying droplet generating liquid instabilities as in Chapter 4 and Addenda I and II.

To facilitate a stable droplet production and to stabilize the generated emulsion, a third component called surface active agent, or in short surfactant, is added to the liquids. Surfactants are amphiphilic molecules that are composed of a polar hydrophilic head and a non-polar hydrophobic tail. The tail typically consists of a hydrocarbon chain. Figure 2.4a shows the molecular structure of sorbitane-monooleate (Span80, ABCR), which is the non-ionic surfactant used in all experiments presented in this thesis. In the sketch in Fig. 2.4b the complex molecular structure is simplified reducing the molecule to its head and tail group.

The amphiphilic structure of surfactant molecules causes them to occupy the interface of emulsion droplets, forming a molecular film with the head groups pointing towards the aqueous phase and the tails pointing towards the oily phase, cf. Fig. 2.5a. By forming this film, surfactants effectively lower the interfacial tension with increasing surfactant concentration. Above a certain concentration, the Critical Micellar Concentration (CMC), the maximum solubility of surfactant monomers in the respective solvent is reached. Thus, the interface of emerging droplets is rapidly saturated with surfactant molecules and the interfacial tension plateaus at values of typically a few mN/m [4]. Surfactant molecules that cannot reach the interface will form micelles or inverse micelles as depicted in Fig. 2.5b for a surfactant in an oily solvent. This self assembly process is driven by an increase of the total entropy: surfactant molecules organize to geometrical structures

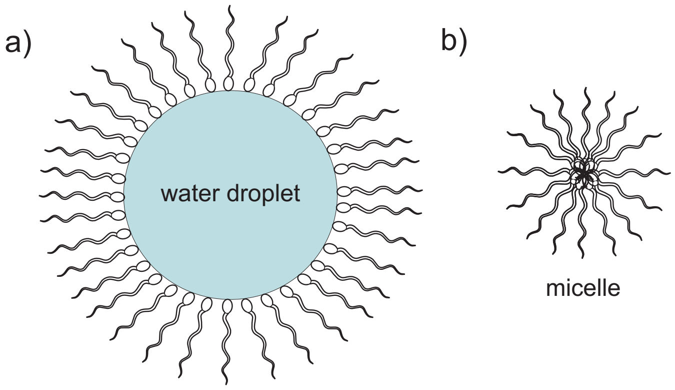

Figure 2.5.: a) Sketch of surfactant molecules covering a water droplet interface with the surrounding oily phase.
b) Sketch of surfactant molecules forming an inverse micelle in a surrounding oily phase.

that prevent the exposure of hydrophilic parts to the oily solvent. However, less solvent molecules need to organize to a cage-like structure surrounding micelles compared to cage-formation by solvent molecules surrounding each surfactant monomer. Thus the overall order of the system decreases. To ensure rapid maximum coverage of droplet interfaces with surfactants, all experiments were performed at a concentration of $2\,wt\%$ Span80, well above the CMC.

The presence of surfactants also has a dramatic effect on the contact angle of a droplet of dispersed phase surrounded by another liquid to a solid substrate. Already small concentrations of surfactants are typically sufficient to change the wettability of the substrate by the dispersed phase from partial wetting to non-wetting [4] and a small external flow will release the droplet from the surface. Thus, surfactants facilitate the formation of emulsions in microfluidic channels by preventing wetting of the channel walls by the dispersed phase, a precondition for the formation of emulsions. The strong effect of surfactants on the wetting characteristics can be understood by using equation 2.21 adapted to an aqueous droplet on a solid surrounded by an oily phase.

$$\cos(\theta) = \frac{\gamma_{so} - \gamma_{sw}}{\gamma_{wo}} \tag{2.22}$$

Here, γ_{so} denotes the interfacial energy at the solid/oil interface, γ_{sw} at the solid/water interface and γ_{wo} represents the interfacial tension of the water/oil interface. The surfactant lowers both γ_{so} and γ_{wo} significantly, while the effect on γ_{sw} is less pronounced, provided the surfactant is preferentially soluble in the oily phase. Thus, $\gamma_{so} - \gamma_{sw}$ becomes negative and the right term in equation 2.22 approaches its minimum, i.e. -1. Adding surfactant considerably increases θ, causing the water droplet to detach from the surface that is preferentially wet by the oil phase in the presence of surfactant. In the presented experiments, Span80 was chosen because it is preferentially soluble in hydrocarbon liquids, thus making it ideal to stabilize water in oil (W/O) emulsions.

3. Materials and Methods

In the course of this chapter the different device preparation methods are presented along with the experimental setups used within this thesis. While experimental methods are introduced by the underlying principles, experimental details and results will be given in the relevant chapters.

The selection of the device material is crucial for the design of droplet based microfluidic systems due to wettability constraints as described in chapter 2.2.5. Fortunately the large industrial and scientific progress made in the fields of microelectronics and MEMS gave rise to a large variety of microchannel production methods, allowing to select from a plethora of device materials. Softlithography and micromilling, the fabrication methods of choice within the present work, are introduced in Sections 3.1.1 and 3.1.2.

Optical methods were applied to characterize the liquid systems of interest and the flow properties within droplet based microfluidic systems. The Pendant Drop Method, employed to measure the interfacial tension between two liquids, is presented in Section 3.2.1. Optical microscopy is used to characterize the shape of liquid interfaces and the behavior of particles inside of droplets. Experimental setups and typical image analysis performed within this thesis are introduced in Section 3.2.2. Finally the optical setup used to characterize droplet shapes by fluorescence microscopy and flow fields inside of droplets by micro-Particle Image Velocimetry (μPIV) are presented in Section 3.2.3.

3.1. Device Preparation and Liquid Systems

3.1.1. Softlithography

Many microfluidic device preparation methods were originally developed to fabricate three dimensional MEMS-structures such as cavities for pressure or acceleration sensors. A comprehensive review on early micromechanical etching techniques along with early sensor structures and microfluidic applications was given by Petersen in 1982 [1]. In the early 1990's these mostly silicon based micro-fabrication techniques became widely used to produce microfluidic devices [3, 4]. However, the fabrication of microfluidic chips in silicon or glass is tedious, requires expensive cleanroom-technology and involves handling dangerous chemicals. Additionally, clogging of channels by particles or contamination of the channel regularly occur, making disposable and cheap devices desirable. In 1998 Duffy et al. introduced a technique named softlithography, which is a fast and low-cost replication technique producing microchannels in an elastomer substrate [18]. The most widespread polymer, used also in the framework of this thesis, is Polydimethylsiloxane (PDMS). PDMS is a silicon based polymer that is liquid in absence of a curing agent at room temperature, but readily solidifies to a transparent elastomer when mixed with the curing agent. PDMS is a good choice for many droplet microfluidic systems based on water in oil (W/O) emulsions as the PDMS-surface is naturally hydrophobic. Additionally, PDMS is highly transparent, which facilitates optical access to the device. Its flexibility allows for the fabrication of microchannels on curved surfaces. However, the high flexibility of the substrate has to be taken into account for high pressure applications, as channel deformation might occur. This was no issue within the experiments of this thesis. The major disadvantages of PDMS are the high diffusivity of many gases and liquids due to the porous molecular structure of the cured elastomer and swelling by a large variety of organic liquids. Both can lead to drainage of liquid from the channel and significant deformation of the channel cross-section, depending on the channel geometry. However, for the channel geometries and flow rates typically used within this thesis deformation of the channel structure and drainage of liquids did not pose significant problems.

The choice of the liquid system generally depends on the used device material and on the specific experiment. However, the main components of the liquid systems used within PDMS devices produced by softlithography were the same in all experiments. An aqueous phase was used as the dispersed phase and n-hexadecane (Alfa Aesar) as continuous phase. The viscosity of n-hexadecane is $\mu = 3.3\,\mathrm{mPas}$. $2\,wt.\%$ Span80 were added to the continuous phase to ensure wetting of the channel walls by the continuous phase and increase emulsion stability. Although n-hexadecane is known to significantly swell PDMS, no significant channel deformation was expected and observed within the used channel geometries on experimental timescales [19]. Depending on the aim of the experiment, various particle suspensions or dyes were added to the liquids. A specific description of the used emulsion systems are given in the context of the respective experiment.

Figure 3.1 illustrates the device fabrication process used in the present work. The device layout is created using AutoCAD software (Autodesk). Subsequently, the layout is printed on a transparency film mask with a maximum lateral resolution of $5\,\mu\mathrm{m}$ (Micro Lithography Services Ltd). Device fabrication starts by generating a master by standard photolithography. A silicon wafer (Silicon Materials) is spin-coated with negative photoresist of the SU-8 (MicroChem) family. The film thickness of the SU-8 layer, that determines the channel height of the final device, can be adjusted by changing the rotational velocity during the spin-coating process and the viscosity of the photoresist. As specified by the manufacturer, SU-8 100 is suitable for film thicknesses ranging from below $100\,\mu\mathrm{m}$ to about $250\,\mu\mathrm{m}$. SU-8 50 which is less viscous than SU-8 100 and allows for lower film thickness was used for devices with a channel height of about $50\,\mu\mathrm{m}$ utilized in Chapter 5 and Addendum IV. After spin-coating, the resist is soft-baked on a hotplate to improve adhesion to the silicon wafer and to remove remaining solvent (65°C for 10 to

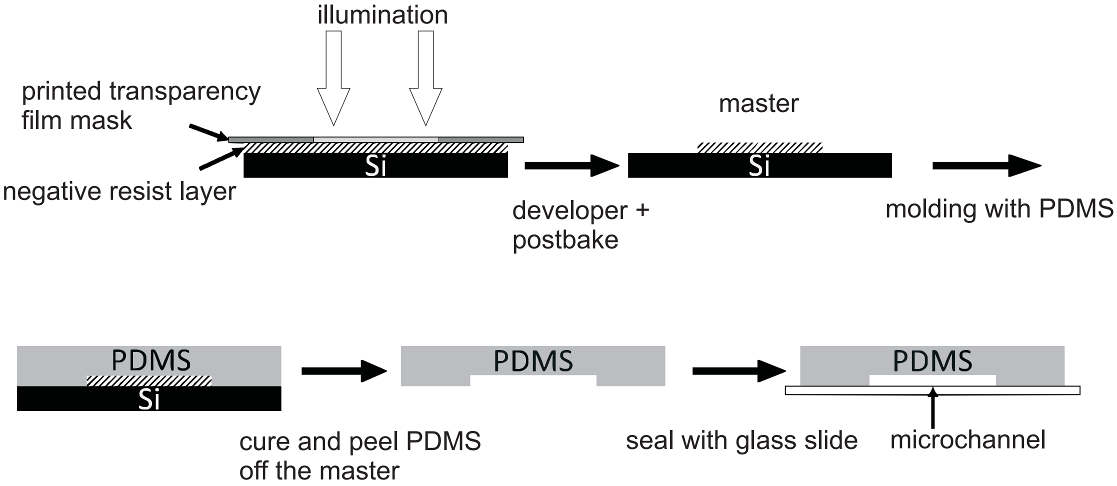

Figure 3.1.: Block-diagram of the softlithography process.

15 min and 95°C for 45 min). The resist polymers are cross-linked upon illumination with UV light, rendering it insoluble to the developer solution. UV-illumination is performed in contact with the printed mask using a Model 60DUV/MUV/Near UV exposure tool (ABM Inc.). To improve the cross-linking of the resist polymers, exposure is followed by a post-bake at 65°C for 1 min and 95°C for 10 min. Subsequently, the sample is bathed in a developer solution (MR-dev 600, MicroChem) to remove non-cross-linked regions of the resist film, thus obtaining the master used as a mold in the following steps. Figure 3.2a shows an example of such a master.

The fabrication of the actual microfluidic device starts by mixing PDMS base and curing agent (Sylgart184, DowCorning) at a ratio of 10:1 and degassing in a desiccator prior to pouring the PDMS onto the master. After degassing in a desiccator, the PDMS is cured on the master on a hotplate at 65°C for 2 to 3 h depending on the thickness of the PDMS layer. After the PDMS has solidified, the channel region is cut out with a scalpel and peeled off from the master. Holes are punched into the PDMS slap to create fluidic inlets and outlets. Subsequently, the PDMS slap and a clean glass slide are plasma treated (Femto, Diener electronic) to activate both the glass and the PDMS surface. An irreversible molecular bond forms upon placing the activated PDMS slap onto the activated glass slide. To ensure an hydrophobic surface, the sealed channel geometry is again placed on a hotplate at 150°C for at least 2 h to allow for hydrophobic recovery of the plasma treated PDMS surface. The elasticity of PDMS allows to directly insert Teflon tubing into the inlet and outlet ports punched into the PDMS to create a fluidic connection, cf. Fig. 3.2b. However, to further prevent leakage, inlets can be optionally sealed using PDMS or glue (Araldite rapid).

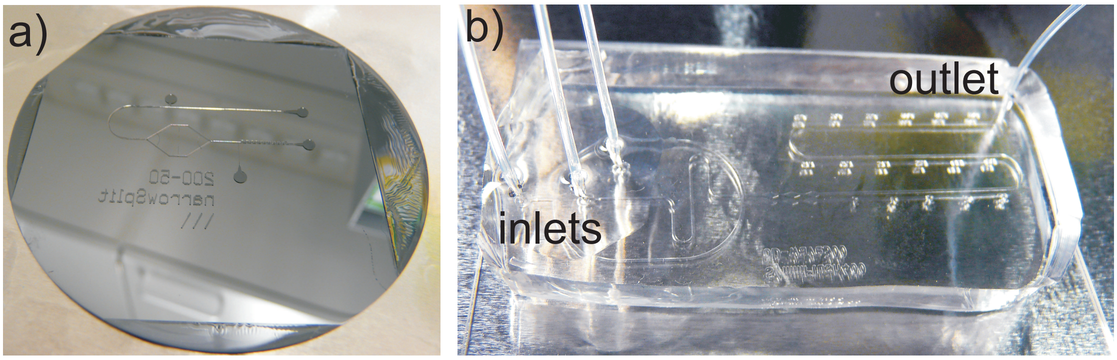

Figure 3.2.: a) Silicon mold with channel geometry composed of SU-8 photoresist.
b) PDMS chip sealed by a glass slide and connected with Teflon tubing.

3.1.2. Micromilling

Directly micromilling channel geometries into a solid substrate, e.g. a polymeric material, is a fast and simple option for device production whenever multiple channel depths are required on the same chip. The fabrication of such three dimensional structures by lithographic means is tedious as structuring of multiple layers of photoresist has to be performed. However, micromilling is only suitable for channel geometries with a width typically $> 150\,\mu$m and a height $> 10\,\mu$m. These constraints have to be considered when creating the channel layout. Polymethylmethacrylate (PMMA) was chosen as the material of microfluidic devices that feature a sudden increase in channel depth and height. PMMA is highly transparent, micromachinable and comparatively cheap. The PMMA blocks are micromachined in the workshop of the Physics Department at Saarland University using a Computerized Numerical Control (CNC) milling machine, that is also suitable for drilling and threading the fluidic connections. Teflon tubing is shaped at one end using a flanging tool and connected to the device by plastic fittings (Omnifit). Leakage is prevented by placing a rubber O-ring between the flanged end of the tubing and the fitting. The channels of the PMMA device are sealed by a PMMA sheet that is attached to the PMMA block by metal screws, cf. Fig. 3.3. One major advantage of PMMA compared to PDMS is that PMMA devices are reusable. They can be disassembled and cleaned by rinsing with ethanol, thus making them ideal whenever the same experiment has to be repeated many times using exactly the same channel geometry.

Devices made of PMMA were used with an emulsion system consisting of aqueous solution as dispersed phase and Isopar M (ExxonMobil Chemical) as continuous phase with a viscosity of $\mu = 2.1\,$mPas. Again, $2\,wt.\%$ Span80 were added to the continuous phase. The viscosity of the dispersed phase was adjusted by adding glycerol (Sigma Aldrich). A specific description of the used emulsions systems is given in the context of the respective experiment.

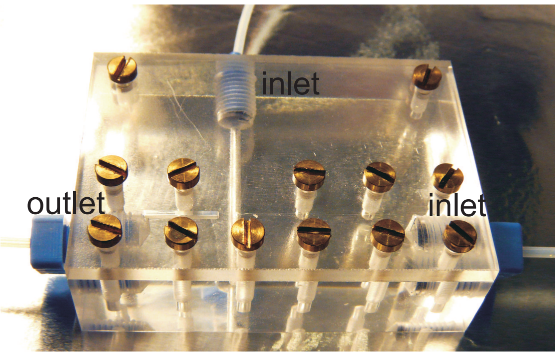

Figure 3.3.: Microfluidic device machined into a PMMA block and sealed by a PMMA sheet.

3.2. Quantitative Measurements

3.2.1. Pendant Drop Method

The interfacial tensions of the different liquid systems used in the present work were determined by the Pendant Drop Method. During the experiment a droplet is produced that is hanging from a needle and surrounded by another liquid of lower density. The droplet is inflated to the maximum volume that is achievable before the droplet detaches due to gravity. In this situation, the droplet shape is determined by gravity trying to elongate the droplet and interfacial tension γ counteracting the increase in interfacial area. Note, that the pendant drop method is a static method to determine γ as no liquid flow influences the measurement. A detailed description of the method is provided by Andreas et al. [20]. The only input parameter needed to determine the interfacial tension γ is the density difference between the surrounding fluid and the droplet phase. The measured droplet shape can then be related to the interfacial tension by comparison to either numerically calculated droplet shapes or experimental measurements taken with a liquid system of known γ [20].

In presence of surfactants, however, the interfacial tension becomes a function of time. Immediately after the droplet has been produced at the needle, the interface is only partially covered by surfactant molecules. Over time, more and more surfactant molecules diffuse to the interface reducing γ until the interface is fully decorated and a plateau-value of γ is reached. The pendant drop method allows to measure the time dependent interfacial tension, provided the droplet shape changes slowly and can be assumed to be in quasi-equilibrium at any instant of time. Figure 3.4 shows the example of the evolution of γ over time for a water droplet immersed in n-hexadecane (Alfa Aesar) with $2\,wt.\%$ Span80 added to the oil phase. In the remainder of the present thesis, the interfacial tension is always specified as the plateau value. This is justified as droplet interfaces in microfluidic channels have been shown to saturate much faster due to strong convection of surfactants to the interface caused by the flow of the surrounding oil phase

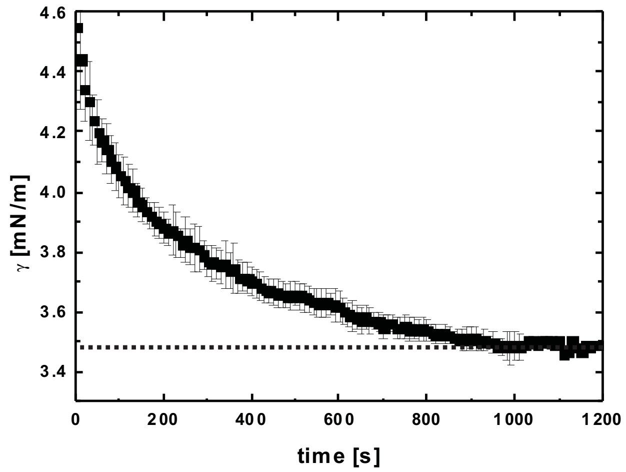

Figure 3.4.: Interfacial tension of water in n-hexadecane with 2 $wt.\%$ Span80 as a function of time measured by the pendant drop method at $T = 24 - 25°\text{C}$. Data are averaged over several measurements, error bars denote standard deviation.

[21].

All measurements in the present thesis were performed at lab temperature $T = 23 - 25°$ C by imaging droplets suspended in a glass cuvette in the respective continuous phase using an OCA 20 device (DataPhysics). The recorded images were directly analyzed by the corresponding software package SCA 20 (V3.6.02, DataPhysics).

3.2.2. Experimental Setup, Optical Microscopy and Image Analysis

A typical experimental setup for optical microscopy is illustrated in Figure 3.5. The central part is of course the microfluidic device, which is connected to gastight glass syringes (Hamilton) by Teflon tubing. The syringes are driven by custom-built, computer controlled syringe pumps that allow to precisely control the volume influx at each inlet. These pumps are controlled via a LabVIEW (National Instruments) interface. To observe and characterize droplet production and flow within a microfluidic device, it is placed either on an inverted microscope (AxioVert or AxioObserver Z1 (Zeiss) or MeF3 (Reichert and Jung)) or below a macroscope (Z16 (Leica)) equipped with a transmitted light source. Images are recorded in brightfield microscopy using a Charge Coupled Device (CCD) camera (1600 (PCO), Imager pro X (LaVision)) or Complementary Metal-Oxide Semiconductor (CMOS) cameras (1200 hs (PCO) and FastCam SA3 (Photron)), depending on the timescale of the considered experiment. Further image analysis was done using numerical image analysis software (Image J 1.49n (National Institue of Health USA) and Image-Pro Plus 6.3 (Media Cybernetics)). Lateral distances were directly measured from

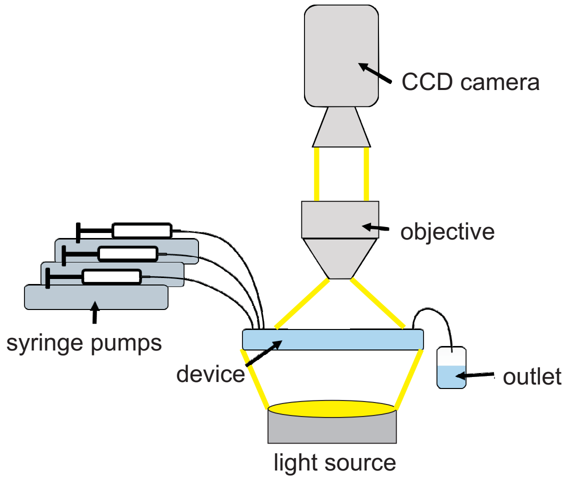

Figure 3.5.: Block-diagram of a typical experimental setup used for the characterization of droplet based microfluidic systems.

microscopy images. Droplet frequencies and velocities were calculated from the camera frame rate.

3.2.3. Fluorescence Microscopy and µPIV

Fluorescene Microscopy is an optical microscopy technique that uses selective staining with fluorescent dyes (fluorophores) to generate the contrast in a sample of interest. When a fluorophor molecule is illuminated with light of a certain wavelength λ, photons of the excitation wavelength increase the molecules energy by lifting an electron from a ground state to a higher state. However, these higher states are not stable and the molecule relaxes back to its ground state emitting another photon within typically a few nanoseconds. The loss of energy due to vibrational relaxation, that transfers the excited electron to lower states without emitting photons is called Stokes Shift. The Stokes Shift allows to separate scattered light from the excitation light source from the fluorescence signal of the sample. An in depth review about the underlying physical mechanisms as well as practical hints on optimizing fluorescence microscopy setups is given in [22]. Fluorescence microscopy meanwhile is a powerful tool to biologists and bio-physicists, e.g. allowing to selectively stain and observe certain cells in a tissue [23] or even study the self-organization of lipid membranes [24]. More advanced fluorescence based imaging techniques such as Stimulated Emission Depletion (STED) microscopy even permit to overcome the limitation of resolution of conventional optics as dictated by Abbé's law. STED enables researchers to study the organization of cells, their interior components and even transport processes on a molecular level. The impact of these imaging techniques on our understanding of the molecular processes within living organisms is expected to be so large, that the inventors of super-resolution fluorescence microscopy received the Nobel Price in Chemistry in 2014 [25].

In the course of this thesis, fluorescence microscopy was used to characterize the thickness of a fluorescently labeled oil layer surrounding an aqueous droplet flowing in a microchannel, cf. Chapter 5. The experimental setup used for these measurements is a standard epifluorescence setup illustrated in Figure 3.6. It consists of a computer controlled inverted microscope with a motorized focus system (AxioObserver Z1, Zeiss) equipped with filter cubes containing a dichroid mirror, a laser cut-off filter and an excitation filter (LaVision). The fluorescent sample can be excited through the same objective used for image recording by either a green laser ($\lambda = 532\,\mathrm{nm}$, pulsed DPSS, 2.72 W, LaVision) or a blue laser ($\lambda = 473\,\mathrm{nm}$, pulsed DPSS, 1.5 W, LaVision) coupled to the microscope by a multi-mode glass fiber. The fluorescence signal emitted by the sample is isolated from scattered laser light by the filter cube assembly and recorded by a CCD camera (ImagerPro X 2M, LaVision) coupled to the microscope by a 0.63 x camera adapter (Zeiss).

Micro-Particle Image Velocimetry (μPIV) is a non-invasive optical method to measure flow fields within microfluidic devices based on fluorescence microscopy. The flow is seeded with fluorescent tracer particles that are imaged using the optical setup depicted in Figure 3.6. These tracer particles are typically Polystyrene (PS) particles of a diameter ranging between 0.5 and $2\,\mu$m when measuring flow fields of an aqueous phase. Such particles have been shown to follow the flow of the liquid motion without lagging behind or significantly alternating the flow field by their presence [26].

In μPIV experiments, the CCD camera is operated in “double-frame” mode, which means that the CCD chip is subdivided in an active region and a storage area. This allows for rapid recording of two subsequent frames. The first frame is shifted from the active region to the storage area immediately after recording. Thus, the CCD is very quickly ready for a second exposure. The storage area is read out by the frame grabber while the second frame is recorded, prolonging the exposure time of the second frame, which can cause a significant increase of the image background. The big advantage of the double-frame recording mode is the option to record two images with an inter-frame time as low as 150 ns for the camera used, which facilitates tracking of fast objects moving in the sample. Images of these particles are recorded by illumination with two laser pulses synchronized to the end of the exposure of frame 1 and the beginning of frame 2. Thus the laser pulse width effectively determines the image exposure time. Subsequently, a two dimensional flow field is calculated from the known time interval between the laser pulses and the displacement of a group of particles, which is processed from the double-frames by a cross-correlation algorithm. An in depth description of μPIV is given in Chapter 6 and Addenda V and VI, where the influence of defocused particles and flow gradients on μPIV measurements is quantified. In the course of this thesis, μPIV is used to characterize the three dimensional flow pattern within elongated droplets moving in

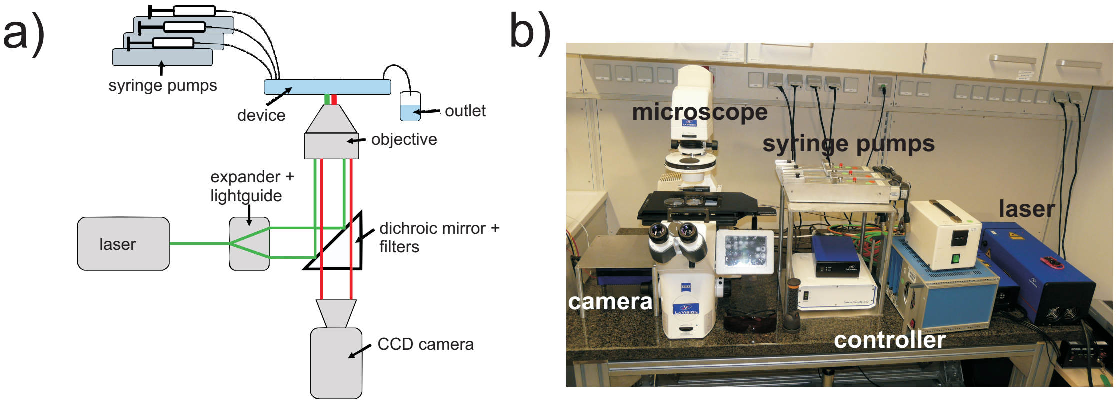

Figure 3.6.: a) Block-diagram of a typical optical setup used for fluorescence microscopy and μPIV. b) Foto of the actual custom built setup from LaVision, Göttingen, Germany.

rectangular microchannels.

4. Droplet Generation from Squeezed Filaments upon Release of Confinement

4.1. Emulsification - Overview

The production of droplets surrounded by a typically immiscible continuous phase is obviously the very first step in every emulsion system. Emulsions are typically formed either by water droplets in an oily phase or vice versa, often stabilized by surfactants, cf. Section 2.2.5. Emulsions are widely used, versatile materials with applications ranging from a simple vinaigrette on salad, elaborate food products to pharmaceutical products and cosmetics. Due to their compound structure and the presence of many liquid/liquid interfaces, the rheology of emulsions can be significantly altered without changing its liquid components by changing the volume fraction of the dispersed phase, the droplet size or the droplet size distribution. Additionally, monodisperse emulsions can be employed to compartmentalize (bio-)chemical reactions within the controlled volume of individual droplets, an approach offering the potential for massive parallelization of (bio-)chemical analysis [13, 27, 28]. Droplet sizes that can be reached by bulk emulsification methods can be as small as $0.1\,\mu$m. However, the production of droplets by classical bulk methods such as rapid stirring, colloid mills, high pressure valve homogenization or ultrasonic agitation has been shown to result in polydisperse emulsions [29]. This polydispersity is intrinsic to macrosystems exploiting shear induced instabilities for droplet breakup caused by e.g. the occurrence of turbulence and cavitation with spatially varying shear rates and the resistance to secondary breakup of mother droplets varying with droplet diameter, cf. Section 2.2.2.

Membrane emulsification has been developed for bulk production of emulsions with less polydispersity and uses spontaneous droplet formation that occurs when the dispersed phase is pushed into the continuous phase through pores of a membrane, cf. top left tile of Fig. 4.1. When the dispersed phase leaves the pore, it forms a round droplet in the continuous phase due to interfacial tension [29, 30]. The droplet is released from the pore by the decrease of Laplace pressure in the growing droplet which increases the flow rate of dispersed phase into the droplet. This leads to collapse of the fluid thread within the pore when the flow of liquid from the pore into the droplet exceeds the feed-ing volume flux [31]. Depending on the particular flow rates, shear exerted by the flow of continuous phase can aid the droplet release. The resulting droplet size distribution depends on the size distribution of the pores as well as on the flow rates applied. Using microfabrication techniques, membrane emulsification has been significantly improved by replacing the porous membrane by precisely manufactured parallel microchannels or perforated channel walls, thus allowing to produce emulsions with a coefficient of variation in droplet diameter $< 5\%$ [32].

4.2. Droplet Formation in Microfluidics

Many microfluidic techniques have been developed during the last two decades that exploit the superior control of the local laminar flow intrinsic to microfluidic systems to further improve the droplet monodispersity. Droplet sizes achievable with microfluidic systems vary from spherical droplets with diameters of typically several microns to elongated plugs of millimetric size, while polydispersities as low as a few percent can be reached [5]. However, the improved monodispersity comes on expense of low volume throughput with droplet production frequencies ranging from only a few to several thousands of droplets per second. In microfluidic devices, droplet breakup typically occurs sequentially, drop by drop, in one single droplet forming unit. Thus, microfluidic systems are less interesting for bulk applications of emulsions but rather offer new tools and applications for specialized material synthesis and (bio-)chemical analysis, i.e. droplet based Lab-on-a-Chip systems [5,13,33]. Addendum III presents one example of a droplet based microfluidic system exploiting excellent monodispersity and control of the droplet flow for production of mesoporous platinum doped silica particles by an optimized sol-gel synthesis route. The resulting particles feature superior surface area and catalytic activity compared to commercially available particles produced in bulk.

The high technological potential of droplet based microfluidic systems has lead to vast engineering and scientific research on microfluidic droplet formation devices. Recently, some active droplet formation units, that employ external fields or actuation by valves to destabilize liquid filaments or jets or to produce drops “on-demand”, have been proposed [34–36]. However, passive droplet formation units are usually much easier to incorporate on-chip and allow to produce continuous streams of monodisperse droplets with controlled spacing. These devices will be treated in the remainder of this sections as passive droplet formation units were employed in all experiments presented within this thesis. Newtonian liquids are used in all experiments and non-Newtonian liquids are consequently not considered in the following. However, viscoelastic effects and shear-thinning in polymer solutions have been recently examined and proven to significantly impact the droplet breakup process [37, 38].

Many different device geometries for passive microfluidic droplet production have been proposed and characterized, both experimentally as well as analytically and numerically.

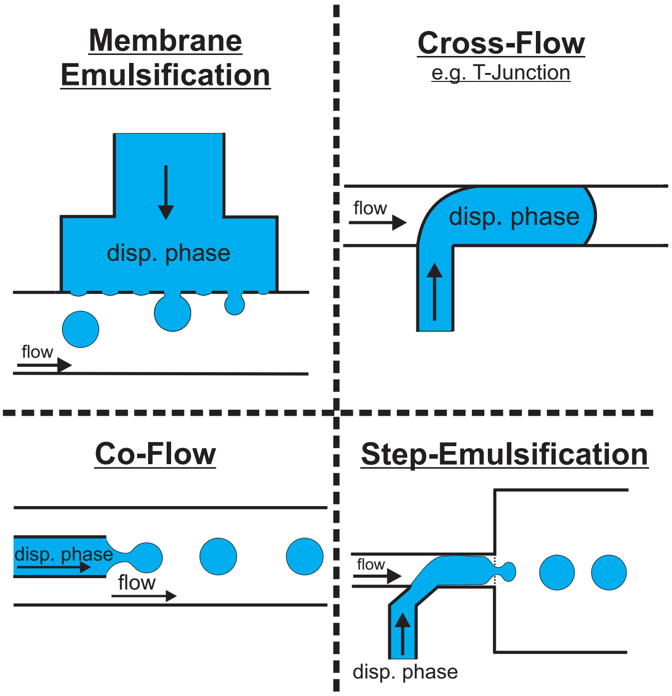

Figure 4.1.: Different droplet breakup systems used to produce emulsions in microfluidics.

Extensive reviews on droplet breakup in microfluidic junctions can be found in literature, cf. among others [5, 12, 39–41]. The vast majority of the proposed channel geometries can be grouped as 1) cross-flow, 2) co-flow and 3) step-emulsification droplet formation units, cf. Fig. 4.1. In all these junctions two or more immiscible liquids, driven either by controlling external pressures or volumetric flow rates, are guided into a common main channel where a liquid/liquid interface is formed. The dispersed phase protrudes into the main channel forming either a “finger”, a “jet” or a squeezed “filament”, depending on the particular channel geometries and flow rates. The interface subsequently is deformed by the local flow field or capillary effects, which amplifies free surface instabilities and finally causes the detachment of droplets. Generally, the entire process is characterized by a competition of forces that try to deform the liquid interface and interfacial tension fighting the creation of additional interfacial area. Depending on the relative flow rates of the dispersed and the continuous phase and on physical parameters such as interfacial tension and viscosities, different droplet breakup regimes have bee observed in each of the junction families. All presented channel junction geometries are readily characterized experimentally and can thus be easily calibrated for controlled droplet production. However, a more general understanding of the underlying droplet breakup mechanisms and especially a prediction criterion for the transitions between different droplet breakup regimes for each particular geometry is desirable. Similar droplet breakup mechanisms act in all presented systems, however, each of the above mentioned families of droplet forming junctions has to be studied separately due to geometrical differences changing the local flow fields and the influence of confinement effects. In the following, the three families of droplet forming junctions are presented in more detail.

4.2.1. Cross-Flow

Cross-flow geometries are typically comprised of two straight channels meeting at a junction at a certain angle. The most common and also the earliest example of a microfluidic cross-flow geometry is the “T-junction” introduced by Thorsen et al. [42], where the dispersed phase channel perpendicularly enters a main channel transporting the continuous phase, c.f also top right tile of Fig. 4.1. Breakup of the dispersed phase finger invading the main channel either occurs right at the inlet in the “dripping” and “squeezing” regime, or further downstream, when both phases initially form parallel flows in the “jetting” regime.

The dripping regime typically occurs for junctions with a dispersed phase inlet being much smaller than the continuous phase channel width or at low flow rate ratios of the dispersed to the continuous phase Q_1/Q_2. The finger of dispersed phase invading the main channel is sheared off by the flow of continuous phase before approaching the channel wall opposite of the dispersed phase inlet [5, 12]. Droplet sizes are controlled changing the flow rate of the continuous phase or the viscosity ratio of the liquids [37].

In the squeezing regime, typically occurring in T-junctions with both inlets having comparable dimensions or at low flow rates of the continuous phase, the dispersed phase protrudes far into the main channel and approaches the opposite channel wall. Thus, the flow of continuous phase is hindered which leads to a pressure built-up upstream of the junction. The higher pressure in the continuous phase aids to deform the interface which finally leads to pinch-off of large elongated droplets confined by the channel sidewalls [43,44]. In the squeezing regime, the droplet size can be primarily adjusted by changing the flow rate ratio Q_1/Q_2 and is largely independent of liquid viscosities and interfacial tension.

In the jetting regime, which occurs at high flow rates of both phases, the pressure at the dispersed phase inlet is large enough to resist deformation of the interface by shear exerted by the continuous phase and a liquid jet of dispersed phase is formed in the main channel. Droplets can be released downstream by growing capillary instabilities breaking the typically cylindrical jet. This breakup process reduces the overall interfacial area and thus the interfacial energy, similar to the classical Rayleigh-Plateau instability at a dripping faucet [45]. If interfacial tension causes the tip of the jet to bulge and grow to the same dimension as the surrounding channel, plugging of the main channel by the tip of the jet additionally promotes droplet breakup, similar to the squeezing regime [46].

Different angles of the channel junctions or altered junction geometries present similar droplet breakup behavior [46–48]. T-junctions have become widely used in microfluidics due to their relatively simple channel geometry and flexibility regarding droplet size and production frequency, as well as ease of fabrication and operation [5,49–53]. Accordingly, a T-junction has been used for the production of long, plug like droplets of millimetric length in the squeezing regime in Addendum IV, allowing to vary the droplet length by more than a factor of 10. However, both the monodispersity and production frequency of droplets can be significantly improved by more sophisticated channel geometries, as elucidated in the following.

4.2.2. Co-Flow

Another family of junction geometries frequently used for droplet generation are co-flow geometries, cf. lower left tile of Fig. 4.1. The dispersed phase and the continuous phase enter the common main channel as co-flowing streams through a set of concentric channels. Similar to T-junctions, co-flow geometries typically show two different droplet breakup regimes: 1) the "dripping" regime at low flow rates with droplet breakup close to the dispersed phase inlet and 2) the "jetting" regime at higher flow rates where droplet breakup occurs further downstream and a jet of dispersed phase is ejected into the main channel.

Dripping is caused by a competition between viscous drag pushing the droplet downstream and interfacial forces trying to hold it at the inlet of the dispersed phase. Thus, droplet sizes typically decrease with increasing flow rate of continuous phase Q_2.

Jetting, however, has been shown to either occur at increased Q_2, where the jet of dispersed phase thins as it moves downstream and decays into small droplets, or at increased flow rates of dispersed phase Q_1, where large droplets detach from a jet that grows in diameter along the main channel length [54, 55]. In both jetting cases, droplet breakup is driven by Rayleigh-Plateau type instabilities, but may be additionally aided by a squeezing mechanism when deformations of the jet approach the size of the channel cross-section [56], cf. section 4.2.1. Droplet size can be adjusted changing the flow rate ratio. Thinning jets emerge when the flow of the continuous phase exceeds a critical value where the resulting shear is sufficient to overcome the interfacial tension. Thus the dispersed phase is stretched as a thread into the main channel, where it decomposes into droplets. Widening jets, in contrast, are created by the momentum of the dispersed phase at high Q_1 which acts cooperatively with the viscous drag exerted by the continuous phase to drive the emerging droplet downstream in the main channel. The large velocity difference between both phases creates shear acting on the interface, that causes the jet to widen in diameter. Depending on Q_1, interfacial tension completely or partially pulls the jet back towards the dispersed phase inlet after droplet pinch-off and the droplet production cycle restarts.

Whether a jet of dispersed phase in a co-flowing system will decay into droplets or will remain stable in the entire microchannel largely depends on confinement [56, 57].

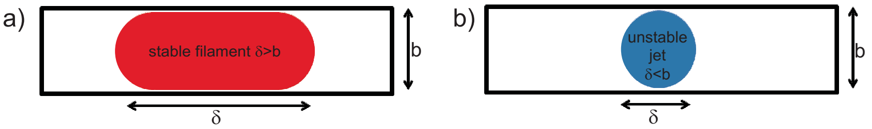

Figure 4.2.: Geometric stability criterion for confined liquid jets/filaments.

Rayleigh-Plateau like instabilities can only grow if an undulation of a free interface leads to a reduction in interfacial energy. If the jet is confined in any direction by channel walls, non-wetting conditions of the channel walls by the dispersed phase fix the radius of curvature of the interface in this direction to a constant value, cf. Fig. 4.2. Deformation in the remaining direction, however, corresponds to the creation of additional interfacial area and is energetically unfavorable. Thus, a jet with a diameter close to or larger than the minimal channel dimension will be stabilized by confinement and stable parallel flows are observed at high flow rates of the dispersed phase [57].

4.2.3. Step-Emulsification

The droplet formation unit discussed in the remainder of this chapter and characterized in more detail in Addenda I and II is the Step-emulsification geometry, cf. bottom right tile of Fig. 4.1. Devices of this family can be regarded as a combination of the previously mentioned families and droplet breakup mechanisms. Typically, the dispersed phase enters a high aspect ratio channel ("terrace'), where a filament of dispersed phase is stabilized by confinement by the channel walls and co-flows with the surrounding continuous phase. Further downstream, the channel width and/or depth suddenly increase at a topographic step to the "reservoir" channel. This sudden removal of confinement destabilizes the filament of dispersed phase, causing its decomposition into droplets. This geometry was first used by Chan et al. [58] and briefly after significantly simplified and experimentally characterized by Priest et al. [59]. Again several droplet breakup regimes have been identified, similar to cross- and co-flow systems [59, 60]. Priest et al. demonstrated, that droplet breakup in Step-emulsification is controlled by the filament aspect ratio, i.e. its width $w_{1\infty}$ remote from the step divided by the smaller dimension of the terrace channel b, and the dispersed phase Capillary Number $Ca = \mu_1 U_1/\gamma$ [59]. Here, U_1 is the dispersed phase average velocity calculated from the filament geometry and the dispersed phase flow rate. The width of the filament can be adjusted by changing the flow rate ratio Q_1/Q_2. At filament aspect ratios $w_{1\infty}/b \lesssim 1$ droplet breakup occurs right at the dispersed phase inlet when the dispersed phase finger does not touch the channel walls and accordingly is not stabilized by confinement. Thus, droplets are sheared off right at the inlet, similar to droplet breakup in a T-junction.

At higher filament aspect ratios $w_{1\infty}/b$ and low Ca, typically $O(10^{-2})$, spontaneous droplet breakup similar to droplet formation in membrane emulsification occurs in the

"Step" regime. Here, the filament decomposes into small droplets right at the topographic step. The filament adopts a tongue like shape in the terrace and retreats from the topographic step after droplet pinch off, restarting the droplet production cycle. Extremely monodisperse droplets are produced with a coefficient of variation in droplet diameter $< 1.5\%$, superior to all previous methods. Extremely high dispersed phase volume fractions up to $95\,\%$ are possible [59]. Strikingly, the droplet size only depends on the smaller dimension of the terrace channel b and on the flow rate ratio Q_1/Q_2 up to a critical Ca, allowing to vary the droplet frequency from a few to several hundred Hz independent of the droplet size [59–61]. Consequently, the "Step" regime is highly interesting for microfluidic applications whenever monodisperse droplets or dense emulsions are required. Two Step-emulsification junctions coupled to a single main channel allow to increase the droplet throughput but also enable strictly synchronized production of different droplet species [5, 62, 63]. Such a hydrodynamic coupling of two Step-emulsification units is employed in Addendum III to produce highly porous silica particles. Droplets containing the different reactants needed for particle synthesis are produced alternatingly by the coupled Step-emuslification units. Subsequently, droplets are fused to start the sol-gel reaction, thus avoiding contact of the jellifying liquids to channel walls and channel clogging.

Beyond the critical Ca, which is a function of the filament aspect ratio $w_{1\infty}/b$, another droplet breakup regime is observed, similar to jetting in co-flow geometries: In the "Jet" regime, the filament stops oscillating in the terrace channel and instead narrows down to a tip at the topographic step. This "capillary focusing" is a consequence of the Laplace pressure due to out-of-plane curvature of the liquid/liquid interface, increasing the pressure inside the filament. Upon reaching the topographic step and releasing the filament confinement, both phases have to balance their pressures. This causes the dispersed phase to flow faster within in the terrace while the continuous phase has to slow down. The filament narrows in downstream direction and forms a tip at the topographic step due to volume conservation [60]. A jet of dispersed phase is ejected from this tip into the reservoir and larger and typically more polydisperse droplets are released when the jet decays due to Rayleigh-Plateau like instabilities.

The Step to Jet transition can be understood by characterizing the shape of the dispersed phase filament in the terrace channel close to the topographic step. Malloggi et al. characterized the shape of the filament experimentally and analytically, using a simplified Hele-Shaw model based on volume conservation and introducing an unphysical decay length to make the resulting equations tractable [60]. The channel geometry used in this study is significantly smaller than in [59] and the authors do not distinguish the Step and the Jet regime. In agreement with experimental results, the width of the tip formed at the topographic step by capillary focusing is predicted to decrease with decreasing Ca. However, neglecting the dynamics of the interface, the presented analysis is only valid for large $Ca > O(10^{-1})$, i.e. small deformation of the filament close to the topographic step. Thus, the model cannot be used to predict the transition between the Jet and the Step regime. To overcome these limitations, Afkhami and Renardy demonstrated a Volume-of-Fluid numerical scheme capable to resolve the entire filament shape along with the pressure and velocity fields in the terrace region at small and medium $Ca = O(10^{-2})$, solving the full two-phase Hele-Shaw equations, cf. [64].

Afkhami's model is applied in Addendum I to predict the transition from the Jet to the Step regime and compared to the droplet breakup behavior and filament shapes found in experiments[1]. We demonstrate, that the filament shape in experiments fluctuates even in the Jet regime, contrasting the assumption of a static filament in previous studies and in theoretical models. The filament shape is influenced by the pressure at the topographic step, that in turn is altered due to the presence of the forming droplet in the reservoir. Additionally, the filament is disturbed by collisions of the forming droplet with other droplets crowded in the reservoir. The reservoir pressure commonly is assumed to be constant in quasi-static simulations and crowding effects are not included in the model. However, it is shown that the model accurately predicts filament shapes at the beginning of the droplet production cycle at medium to high Ca, remote from the Step to Jet transition. For smaller Ca, the strong capillary focusing causes the filament to thin to a tip of about the size of the smallest dimension b of the terrace channel, locally invalidating the Hele-Shaw approximation. Nonetheless, using a slight correction of the pressure outlet boundary condition of the filament, it is possible to precisely reproduce the Jet to Step transition within the experimental parameter space by applying a simple geometric criterion. The transition is assumed to occur at a critical Ca, when the tip diameter of the filament in the terrace channel becomes smaller than b, which was also confirmed experimentally, cf. Fig. 4.2. Thus, a cylindrical neck is formed at the topographic step that is prone to capillary instabilities. No jet can be ejected into the reservoir below this critical Ca. These results were later confirmed by Zi et al. [65], who developed a fully analytical model based based on quasi-2D Hele-Shaw hydrodynamics and solved the nonlinear differential equation for the quasi-static shape of the confined filament in the Jet regime, predicting the transition to the Step regime using the same geometric criterion.

Extending the range of studied filament aspect ratios to highly confined filaments with $w_{1\infty}/b \gtrsim 12$, Addendum II describes the emergence of additional droplet breakup regimes in Step-emulsification geometries. All of these breakup regimes are composed of the previously discussed Step and Jet instabilities, coexisting in various combinations on the same filament. A coexistence of several instabilities on the same liquid filament has not been reported before for co-flowing streams of immiscible liquids at low Reynolds Numbers. Surprisingly, even an asymmetric breakup regime is found that is comprised of Step and Jet instabilities operating in parallel on the same filament, despite the fully

---

[1] The theoretical model presented here was developed by S. Afkhami (NJIT, Newark, USA) and L. Kondic (NJIT, Newark, USA) with experimental input by M. Hein and R. Seemann. The numerical simulations were designed and analyzed by S. Afkhami.

symmetric boundary conditions. The different regimes are studied experimentally using two species of Step-geometries with a vertical or a horizontal orientation of the topographic step and different reservoir dimensions [2]. While the vertical step geometries offer a top view of the filament shape, the smaller reservoir dimensions of the horizontal step geometry reduce crowding and facilitate studies on the stability of liquid jets in the reservoir. Additionally, planar devices with horizontal steps are produced by standard softlithography and the use of two different device families proves the generality of the observed breakup behavior. Based on the experimental characterization of the various regimes, we propose key physical principles such as the minimization of interfacial energies, upper bounds for the volume throughput and inertia, which are responsible for the spontaneous symmetry breaking and the transitions between individual regimes. Additionally, the ability to produce distinct droplet families from a single filament is shown to allow for simultaneous on-chip concentration and encapsulation of particles into one droplet family, while excess bulk liquid is released into another family of droplets.

---

[2] Experiments in horizontal step geometries were designed by J.B. Fleury (Saarland University, Saarbrücken, Germany) and M. Hein, performed and analysed by J.B. Fleury

5. Employing Droplet Dynamics to Concentrate Particles

5.1. Introduction and State of the Art

Having dealt with controlled droplet generation in a microfluidic environment in Chapter 4, the following chapter describes a particle accumulation effect that occurs within elongated droplets flowing in rectangular microchannels. Accumulation, separation and concentration of small objects such as particles or cells are important steps in the process-flow of many (bio-)chemical assays. The functionalized surface of solid particles is regularly used for specific binding and extraction of target molecules [66–71]. Cells, on the other hand, regularly need to be removed from the sample either to analyze cell properties or because cellular components might interfere with subsequent analysis of the surrounding medium, e.g. blood plasma analysis [72]. For conventional assays, performed using bench-top instrumentation, the separation from surrounding continuous phase can be easily achieved by filtration or centrifugation. However, miniaturization to facilitate point-of care analysis, reduce reagent consumption and cost of analysis or to exploit the superior control of the local chemical environment on the micro-scale also demands for particle accumulation, concentration and separation on chip.

The following sections present an overview of already known particle accumulation methods in continuous single phase flow and in droplet based microfluidic systems along with current reports on flow fields within elongated droplets in rectangular channels in Section 5.1.1. Finally, Section 5.2 summarizes the experimental findings on particle accumulation within elongated droplets, which are presented in detail in Addendum IV.

5.1.1. Particle Accumulation in Microfluidics

A vast variety of particle and cell accumulation effects has been reported and applied in continuous single phase microfluidics. Only a few of these methods are introduced in the framework of this thesis for the sake of conciseness, but many excellent reviews on the topic can be found in literature, cf. among others [72–76].

In general, particle accumulation or separation methods are classified as either passive or active. Active methods rely on external fields for particle manipulation. Miniaturization is favorable for such systems as field strengths typically scale inversely proportional to the distance, e.g. to the magnet or between electrodes, allowing for large field strength and gradients in microfluidic devices. Many of the presented approaches are even capable to sort cells and particles according to intrinsic properties. One of the most obvious active methods described in literature combines (dia-)magnetic microbeads and external magnetic fields to achieve focusing of particles to a certain channel region [77–79] or to keep particles fixed at a distinct position [67, 80, 81]. Label-free particle manipulation can be achieved using external electric fields. In electrophoresis, charged objects or molecules are deflected by an external DC field, depending on their charge to size ratio [76, 82]. Particle deflection in electrophoretic systems, however, is slow due to the comparatively large size of particles and these systems are prone to electrolysis of the carrier liquid and clogging due to bubble formation caused by electrochemical reactions. Dielectrophoretic (DEP) methods overcome the latter problem by employing AC fields. In contrast to electrophoresis, no net charge of the particle is required. In DEP, polarizable dielectric particles experience a field-frequency dependent net force due to an inhomogeneous electric field. Changing the frequency of the electric field, the direction of particle motion can be adjusted [74], allowing to use DEP in a lot of applications like cell sorting [83, 84] or particle washing [85]. Optical and acoustic forces have also been applied for particle concentration and separation [86–89].

To perform active particle accumulation in microfluidic systems, additional components such as electrodes, magnets etc. have to be included into the chip design. These additional components increase both chip complexity and cost, making passive field free methods more desirable when it comes to Lab-on-a-Chip application. However, the typically simplified device layout comes on the expense of a limited achievable volume throughput and less flexibility regarding target particles.

The most obvious approach for particle or cell enrichment or separation by size and deformability in continuous microfluidics is filtration. However, classical head-on filtration methods based on geometric obstacles or membranes suffer from channel clogging or fouling [90], which can be overcome by extraction of buffer or smaller particles through sidechannels or perforated sidewalls [91, 92]. In contrast, purely hydrodynamic approaches exploit accumulation of particle species at a certain channel region due to interaction with the flow field of the surrounding liquid. In so called Pinched Flow Fractionation (PFF) a sample stream containing particles or cells of various sizes is forced to one side of a channel constriction by injection of a buffer stream [93]. Small objects are pressed closely to the sidewall, while the center of mass of larger objects leaves the original streamline due to their larger diameter. Thus, particles or cells follow different streamlines depending on their size upon a sudden increase of the channel width [93, 94]. Despite being typically several orders of magnitude lower than e.g. DEP or magnetic forces [76], also gravity can be exploited to concentrate or separate particles by a clever coupling to hydrodynamic flow fields, cf. [95]. While being very effective in concentrating or separating particles or cells, PFF and gravity driven concentration are limited to relatively low flow rates, posing a serious limitation regarding volume throughput. Inertial effects, that occur at large flow rates, can also cause particle accumulation at distinct positions within a (micro-)channel as first reported for centimeter sized systems in 1962 [96, 97]. The exact position of particle accumulation is determined by particle size and shape as well as channel geometry and flow velocity [98, 99]. A concise review on the vast literature on inertial particle focusing is given by Di Carlo [75]. However, these effects only become relevant at elevated $Re \gg 1$ and are thus neglected in the course of this thesis were particle flow is dominated by viscous drag.

Subsequent to particle accumulation in a certain region of the channel by any of the mechanisms described above, particles or cells can be concentrated or selectively enriched isolating the particle carrying stream from surrounding medium at a channel junction [93, 94, 100].

Despite the rich variety of particle separation and concentration approaches available in continuous microfluidics, relatively few reports on particle accumulation inside droplets moving in microchannels can be found in literature. Accumulation of particles within droplets is much more complex due to the swirling recirculative internal flow profile. These swirls prevent the use of most concentration or separation methods known from continuous flows, as particles are quickly redispersed over the entire droplet cross-section. However, some studies succeeded to concentrate particles encapsulated within droplets. Recently an active magnetic field based method pulling particles to one side of the droplet prior to splitting at a channel junction was presented [101, 102]. Kurup and Basu introduced the first passive particle accumulation effect inside elongated droplets flowing through round tubing [103]. Particles were observed to accumulate as a cloud located at the rear center of the drop. The length of the particle accumulation cloud was found to increase with increasing droplet velocity, until being limited by the droplet length. The same behavior was later reported for red blood cells dispersed in long liquid plugs moving through capillary tubing [104]. The accumulation of particles and cells was explained by a coupling of gravity driven sedimentation to the internal flow of the droplet, which can be predicted analytically for round channel geometries [105, 106]. Typically, the dispersed phase flows in droplet movement direction at the center of the channel and recirculates to the back side of the droplet along the channel walls. Sedimenting particles dispersed in the droplet phase will follow the internal flow, while simultaneously sinking to the bottom of the round channel, where they are advected to the rear. Thus, sedimenting particles are accumulated in a cloud at the rear of the droplet that scales in length with the droplet velocity. However, the practical relevance of this particle accumulation effect is limited. Most microfluidic systems nowadays are produced by softlithographic methods or dry etching techniques, which produce rectangular channel cross-sections. Thus, a field free particle accumulation effect inside droplets in rectangular microchannels is highly desirable for application and described in Addendum IV.

The internal flow field inside elongated droplets becomes more complex for rectangular

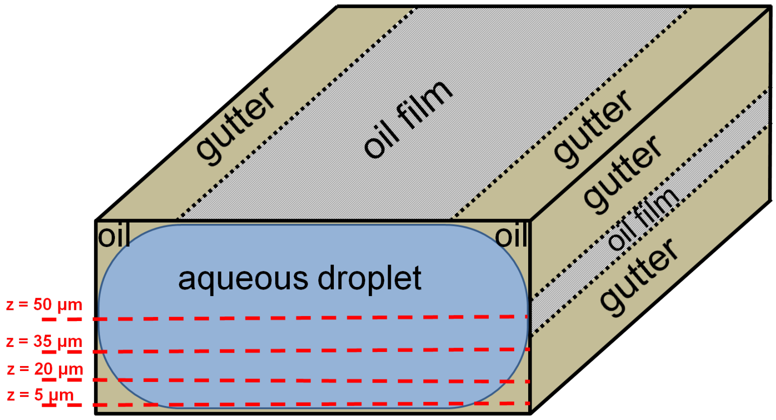

Figure 5.1.: Sketch of the droplet geometry in rectangular microchannels illustrating the gutter channels and positions of oil films. Red dashed lines denote the planes depicted in μPIV scans in Addendum IV.

channel cross-sections and accordingly a different particle accumulation behavior as in [103,104] is found. Contrary to round channels, droplets confined in a rectangular channel geometry cannot block the full channel cross-section, cf. Fig. 5.1. Surface tension tries to minimize the droplet interface, which prevents the droplet interface to fully invade the corners of the channel. Therefore, these corners act as gutter channels through which the continuous phase can bypass the droplet that is typically moving slightly slower than the average velocity of the surrounding continuous phase [107]. The gutter channels change the friction boundary condition of the droplet compared to round tubing: Wherever the droplet comes close to the channel walls, only separated by a thin film of continuous phase, the dispersed phase is expected to flow backwards in the reference frame of the droplet due to drag exerted on the droplet by the channel wall via the surrounding thin film. In the vicinity of the gutter channels, however, the dispersed phase is dragged towards the front by the bypassing continuous phase, creating a complex recirculating internal flow field. Furthermore dynamical effects change the outer shape of the droplet, i.e. the thickness of the surrounding oil films and the shape of the gutter channels [108] depending on the droplet velocity which in turn will influence the friction to the walls and thus the inner flow profile. Indeed, several experimental and numerical studies on flow profiles inside of elongated droplets in rectangular channels have been published recently revealing a variety of different flow patterns [109–115]. The large differences between the studied systems regarding parameters such as viscosity ratio of the dispersed and continuous phase, droplet velocity, droplet/droplet interactions, channel dimensions and surface tension hinder a qualitative comparison but stress the sensitivity of the internal flow profile to these parameters. Ma et al. systematically varied the viscosity ratio of the liquid system and observed qualitatively different flow patterns inside droplets of a given length and at similar Capillary Number Ca [115]. Jakiela et al. systematically varied

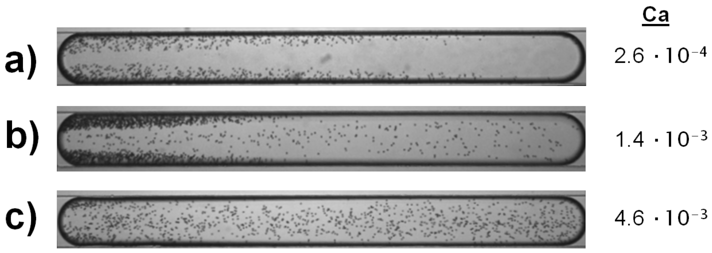

Figure 5.2.: Accumulation of PMMA-particles ($d_p = 8\,\mu$m) within water droplets of length $l_0 = 2.98 - 3.1$ mm surrounded by n-hexadecane at different droplet velocities. 2 wt.% Span80 were added to the continuous phase. Channel height is $100\,\mu$m, channel width $300\,\mu$m.

the viscosity ratio of the dispersed to the continuous phase and the velocity of elongated aqueous droplets surrounded by an oily phase in a channel of square cross-section [116]. For viscosity ratios similar to our experiments, they reported a significant change in the flow topology depending on the droplet velocity.

In the remainder of this chapter the accumulation of particles within droplets in rectangular channels is studied, which strongly depends on particle properties and droplet dynamics, specifically the internal flow field and droplet shape.

5.2. Particle Accumulation within Droplets in Rectangular Microchannels

Using an aqueous suspension of particles or cells as dispersed phase, field free particle accumulation can be readily observed depending on the droplet velocity v_0, respectively the droplet based Capillary Number $Ca = \mu_2 v_0/\gamma$. Three different particle accumulation patterns are typically found for $10^{-4} < Ca < 10^{-2}$, cf. Fig. 5.2. At low Ca, droplets typically accumulate in two distinct zones at the rear of the droplet. These zones are found close to the channel walls at the rim of the droplet. In this “accumulation” regime, recorded time series reveal that particles are advected towards the front of the droplet along the rim and recirculate towards the back whenever they come closer to the channel center. In the “intermediate” regime at higher Ca, particles start to redistribute over the entire droplet cross-section while both accumulation zones shorten in length. This peculiar behavior contradicts the trends observed in round tubing where particle clouds grow in length with increasing droplet velocities [103,104]. Further increasing Ca finally leads to complete redispersion over the entire droplet cross-section in the “mixing” regime. Particle accumulation patterns were systematically studied as a function of droplet length l_0 and Ca and particle properties, as demonstrated in Addendum IV. Particle accumulation was shown to occur for sedimenting particles. In contrast, no particle accumulation could be observed upon completely eliminating gravity driven sedimentation by matching the density of the dispersed phase and particles. Increasing the dispersed phase density beyond the density of the suspended particles results in the same particle accumulation patterns as observed for sedimenting particles, but within the upper half of the droplet, as expected due to the symmetry of the system. The observed dependence on particle settling velocity indicates that buoyancy or gravity driven sedimentation is one ingredient needed for successful particle accumulation. However, sedimentation alone is not sufficient to explain the emergence of the three observed particle accumulation regimes. The transitions between the different accumulation regimes are caused by the interaction of the internal flow field of the droplet with sedimenting particles. The internal flow field is shown in Addendum IV to topologically change with Ca due to increasing droplet deformation.

To understand the internal flow profile of droplets in rectangular channels, the outer shape of elongated droplets, which determines the drag on the droplet and thus dictates the internal flow field, was characterized by fluorescence microscopy. At small Ca, the gutter height h was found to remain about constant along the entire droplet length. Increasing Ca resulted in an increased intensity at the droplet rear that decreased towards the front of the droplet. Additionally, the evolution of the thin films of continuous phase between the droplet and the bottom of the channel could be characterized. The observed trends for both gutter height h and oil film thickness agree well with analytical predictions [107,108].

Micro-Particle Image Velocimetry measurements were performed in $x-y$ planes at several z positions to directly check for the evolution of the interior flow field inside of droplets in rectangular microchannels with increasing Ca, cf. Figure 5.1. The distance between these z positions was chosen according to the expected thickness of the measurement plane, the Depth of Correlation (DOC), determined by the method introduced in Chapter 6. Slow droplets at low Ca present a relatively simple internal flow field that consists of four long vortex rolls stretching along the droplet length. In contrast, faster droplets at $Ca > 2 \cdot 10^{-3}$ show a more complex internal flow profile. The most prominent change is that the velocity at the droplet rim becomes negative at the front part of the droplet within the gutter planes. Thus, the long vortices stretching along nearly the entire droplet length decrease to the rear part of the droplet while additional flow structures emerge at the front. A similar topological change of the internal flow field was reported for droplets in square microchannels by Jakiela et al. [116]. For a more detailed description of the measured internal flow profiles please confer Addendum IV.

Combining the information gained by fluorescence microscopy, μPIV and the observations of particle accumulation patterns, the particle accumulation behavior can be explained by gravity driven sedimentation and the Ca-dependent topology of the internal flow profile. At low Ca, particles follow the internal flow of the droplet, that is directed towards the front at the rim of the droplet, close to the gutters. Simultaneously, particles sediment towards the channel bottom, where a backwards flow is present that transports the particles towards the droplet rear. Thus, two discrete particle accumulation zones are formed at each side of the droplet. Within the “intermediate” regime at higher Ca , however, additional vortices appear within the droplet, that limit the length of the accumulation zones, while simultaneously more particles are dispersed over the entire droplet cross-section. At even higher Ca, the internal flow becomes too vigorous for accumulation to occur and the “mixing” regime is reached for short droplets, cf. Addendum IV for a more detailed description.

6. Determining the Weighting Function and Depth of Correlation in µPIV

6.1. PIV and µPIV- Basic Principles

The idea to use particles suspended in a fluid to visualize flow patterns is obvious to everybody with physical interest who ever stood on a bridge, watching floating debris and dust particles on a river surface. Particle Image Velocimetry (PIV) is a quantitative implementation of this simple principle. The term PIV refers to a whole family of optical, non-invasive methods capable of measuring and visualizing instantaneous velocity vector fields in fluid flow with high spatial and temporal resolution. These capabilities make PIV superior to previously popular punctual or scanning velocimetry approaches such as Hot Wire- or Laser Doppler-Annemometry (LDA). In PIV, the velocity field is obtained by imaging the displacement of small tracer particles suspended in a fluid, that accurately follow the fluid motion. The particle concentration can be relatively high, provided particle images remain distinguishable without too many overlapping particle images. The measurement plane and its thickness is typically defined by a thin laser lightsheet illuminating the particles. Two images of the tracer particle pattern are recorded quickly after each other and the velocity field is subsequently obtained by image interrogation: The recorded images are divided into subwindows typically containing several tracer particles. The particle patterns within the subwindows in both images are cross-correlated in both dimensions of the image plane, finding the most probable displacement in each subwindow by identification of the highest correlation peak, i.e. finding the displacement corresponding to the maximum overlap between subsequent images [117]. To prevent erroneous displacement vectors, the resultant vector can be excluded in a vector post-processing, e.g. removing vectors that differ too much from their closest neighbors or excluding vectors where the highest correlation peak cannot be clearly identified. The obtained pixel displacements are then easily translated into instantaneous velocity vectors, using the known time distance between subsequent particle images and spatial calibration of the optical setup.

In contrast to Particle Tracking, where the displacement of individual particles is measured, PIV tracks the movement of intensity patterns created by groups of tracer particles. Thus, PIV measurements offer a robustness, statistical accuracy and spatial resolution superior to typical particle tracking methods at lower tracer concentration

[26, 118]. Modern PIV systems use multiple cameras to observe the flow from multiple angles, even allowing to determine all three velocity components by cross-correlation of reconstructed three dimensional images [26, 118]. Since its introduction in 1984, PIV has become the dominant velocimetry tool to the fluid mechanics community with application ranging from fundamental studies on turbulence to optimization of aerodynamic drag in automotive and aviation industry [119–121]. An extensive review on current developments of the PIV technique along with examples of application to complex and turbulent flows has been presented by Westerweel et al. [122].

Micro-Particle Image Velocimetry (μPIV) represents the adaption of PIV to flow fields on a micro-scale, that was first introduced by Santiago et al. in 1998 [123]. In a μPIV experiment, the movement of small tracer particles dispersed in the fluid is imaged by a microscope and a camera. To facilitate the discrimination of tracer particles from impurities and image background, typically fluorescent particles are used. Optical access to microchannels is usually limited and implementation of a light sheet would be tedious, if possible at all. Thus, the fluorescent tracer particles in μPIV are excited by a laser through the same microscope objective used for imaging, illuminating the entire volume within the field of view. The emitted fluorescence signal is isolated from reflected laser light and background light using dichroidic mirrors and cut-off filters. An exemplary optical μPIV setup, that was also used in the framework of this thesis is depicted in Fig. 3.6. Analogous to standard PIV, the velocity field is subsequently obtained by cross-correlation of two recorded images.

Despite the relative simplicity of μPIV, several aspects have to be considered when designing an experimental setup for a specific application: The spatial resolution naturally depends on the choice of the microscope objective, which is in turn limited by the field of view required for the experiment. The chosen objective, however, limits the choice of the tracer particles and their concentration. If an insufficient number of particles is present in the focal plane, the quality of the correlation signal decreases [117]. Additionally, the combination of microscope objective, tracer particles and flow properties also determines the influence of defocused particles on the measured velocity and thus the thickness of the measurement plane. This thickness is specifically relevant for the characterization of three dimensional flow problems as considered in this thesis. However, we found contradicting experimental and theoretical values for this thickness in literature for high NA air objectives. To resolve the confusion about this important question in μPIV, we developed a novel method to directly determine the influence of out-of-plane particle images on the measured velocity and to directly measure the μPIV plane thickness depending on the optical setup, image processing parameters and flow velocity gradients. In the following, the present knowledge about the thickness of the measurement plane in μPIV is discussed and our novel approach to the problem is introduced.

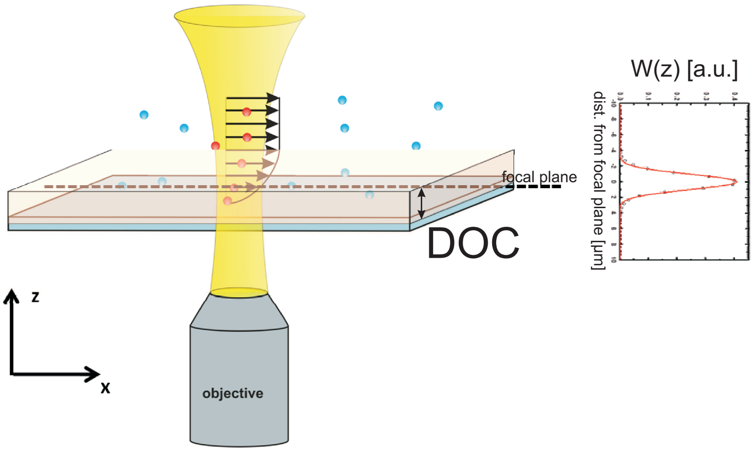

Figure 6.1.: Sketch illustrating the thickness of the measurement plane in μPIV due to the Depth of Correlation (*DOC*) and the weighting function $W(z)$.

6.2. Depth of Correlation and Weighting Function - Context and State of the Art

As introduced in the previous section, the particular feature discriminating μPIV from PIV is the use of volume illumination by simultaneous imaging and illumination through a single lens, cf. Fig 6.1. Hence, the thickness of the measurement plane is unknown as all particles within the fluid volume and the field of view are illuminated [124–126]. Cross-correlating recorded images tracks the movement of intensity patterns of all these particles. Even defocused particle images influence the measured velocity vector. However, the thickness of the measurement plane, named Depth of Correlation (*DOC*), can be pictured as twice the distance from the focal plane up to which particles can significantly influence the measured velocity [126–128]. A precise definition of the *DOC* is rather arbitrary. Meinhart et al. proposed to use a threshold of the peak intensity of particle images as a criterion for the PIV measurement depth [125], arguing that defocused particle images with a maximum intensity below 10 % of the maximum intensity of particles in the focal plane would not be able to significantly shift the correlation peak. Although this criterion produced reasonable results for most experimental setups, Olsen and Adrian published a more stringent analytical derivation of the *DOC* in the same year [126], assuming Gaussian optics and a single thin lens. They argued, that the displacement dx_{meas}, measured by finding the cross-correlation peak of two subsequent μPIV images, will be the weighted average of the true displacement function $dx(z)$ with a normed Weighting Function $W(z)$:

$$dx_{meas} = \frac{\int\limits_{-\infty}^{+\infty} dx(z) \cdot W(z) dz}{\underbrace{\int\limits_{-\infty}^{+\infty} W(z) dz}_{\int W(z) dz = 1}}, \tag{6.1}$$

with z being the distance from the focal plane. The DOC is determined by the nature of the Weighting Function $W(z)$ that depends on flow gradients and the optical system. Neglecting out-of-plane gradients of the velocity field, Olsen et al. derived an expression of $W(z)$ based on the optical particle image diameter and an analytical expression for the DOC based on a cut-off threshold $\epsilon = W(z)/W(0)$, typically chosen as $\epsilon = 0.01$. Even stronger defocused particles are assumed to be too blurry to significantly contribute to the measured signal. Note, however, that the choice of the exact value of ϵ is arbitrary. The expression for the DOC was later adapted to microscope objectives, including immersion in a medium of refractive index n_0 [128]:

$$DOC_{theory} = 2 \cdot \left\{ \frac{1 - \sqrt{\epsilon}}{\sqrt{\epsilon}} \left[\frac{n_0^2 d_p^2}{4NA^2} + \frac{5.95(M+1)^2 \lambda^2 n_0^4}{16M^2NA^4} \right] \right\}^{1/2} \tag{6.2}$$

Here M and NA denote the objectives Magnification and Numerical Aperture and d_p and λ are the fluorescent particles diameter and emission wavelength, respectively. When imaging into another medium with a refractive index n_w, equation 6.2 has to be corrected by multiplication with n_w/n_0 [129]. Equation 6.2 is regularly used in literature to estimate the DOC, e.g. [117, 130] and was experimentally verified for microscope objectives up to $NA \leq 0.4$ [127–129]. Bourdon et al. showed that $W(z)$ is proportional to the curvature at the maximum of auto-correlation functions of particle images at a known distance z from the focal plane. Thus, auto-correlation of images of fixed particles at various z positions was used to determine $W(z)$ and DOC. Nonetheless, equation 6.2 was found to significantly underestimate the DOC for high NA air objectives. While designing the μPIV setup used in the framework of this thesis, high NA objectives were used following the prediction of equation 6.2, that these objectives offer the lowest DOC. Testing the DOC with the method introduced by Meinhart et al., however, contradictory results were obtained [125]. The same underestimation of the DOC was reported by to Rossi et al., who found a significant underestimation of the DOC when calculated using the NA specified on the objective [129]. These deviations were attributed to the increased optical complexity of high NA air objectives invalidating the single thin lens model and Gaussian optics assumed when deriving equation 6.2.

Additional complexities arise from both in-plane and out-of-plane gradients of the measured flow field, that locally influence $W(z)$ and thus the DOC. Out-of-plane gradients typically reduce the DOC, while in-plane gradients typically lead to an increased DOC [131, 132]. While the latter can be reduced by adequate choice of correlation subwindow size and shape [133–135], out-of-plane gradients have to be considered when estimating the DOC in a three dimensional flow experiment. However, neither equation 6.2 nor the estimation of the DOC from Weighting functions $W(z)$ determined by auto-correlation of defocused particle images account for any flow gradients. Poelma et al. [136] introduced an artificial correlation function composed of the sum of auto-correlation peaks displaced by a parabolic velocity profile to test for the influence of out-plane gradients on velocity measurements in blood flow. Yet, to date none of the existing methods is capable to simultaneously quantify the influence of out-of-plane gradients, overlapping particle images, image pre-processing and filtering and variation of PIV-processing parameters on both DOC and $W(z)$.

6.3. Weighting Function and Depth of Correlation Determined from Experimental Particle Images

To overcome the ambiguity of the Depth of Correlation determination while planning and characterizing the experimental setup used in chapter 5 and Addendum IV, we developed a more direct approach to experimentally determine the influence of defocused particles on the measured velocity[3]: Averaged particle images were acquired from tracer particles fixed on a glass plate, that were systematically defocused. PIV-images were generated by superposing these particle images and applying a known displacement function $dx(z)$, cf. Fig. 6.2. The measured displacement dx_{meas} was subsequently computed for a given optical setup, particle size and out-of-plane gradients assigned by $dx(z)$ from these PIV-images. Comparing dx_{meas} to the known velocity profile $dx(z)$ allows to determine the DOC assuming a specific shape of the Weighting Function $W(z)$.

To clarify which shape of $W(z)$ could be assumed, a second method was developed to directly measure $W(z)$ from experimental particle images. In contrast to the previous method, images of particles at the considered z were omitted during PIV-image generation. The difference between the measured displacement to the displacement computed from a reference image containing particle images at all z positions presents a direct measure for $W(z)$. Subsequently, also the DOC can be determined from $W(z)$. It was shown that Weighting Functions for most particle/objective combinations are best represented by a simple Gaussian. Only for high NA air objectives the Weighting Function becomes significantly asymmetric and deviates from a Gaussian, which is in agreement to the findings of Rossi et al. [129]. Additionally, the precise knowledge of the Weighting

---

[3] Experiments presented in this chapter were performed by M. Hein. Data was analyzed by M. Hein and B. Wieneke. The theoretical backbone was developed by B. Wieneke and M. Hein.

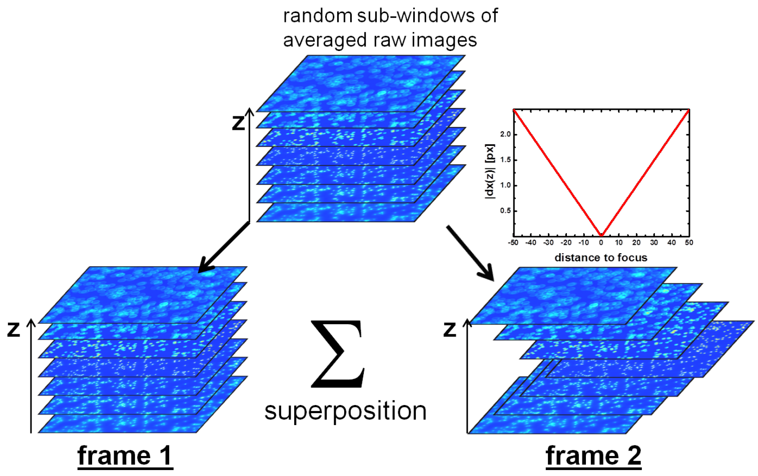

Figure 6.2.: Scheme of PIV-image generation by superposition of recorded particle images shifted according to an arbitrary displacement function $dx(z)$.

Function of a given experimental system can be employed to correct for measurement errors intrinsic to μPIV, cf. Addendum V.

Both, DOC-values computed assuming a Gaussian $W(z)$ and DOC-values calculated directly from the measured $W(z)$ agree well with each other and are relatively close to the theoretical prediction from equation 6.2 for immersion objectives and low NA air objectives. However, for high NA air objectives, major deviations from theoretical predictions have been found. For a detailed description of experimental procedures and the theoretical backbone of the DOC and $W(z)$ measurements as well as experimental results for several optical setups and particle diameters, please confer Addenda V and VI.

7. Summary and Outlook

The goal of the present thesis was to promote a deeper understanding of the interplay between interfacial forces and dynamic effects in flowing systems on the micro-scale.

Droplet formation was studied in “Step-emulsification” geometries, that feature a confined filament of dispersed phase co-flowing with an immiscible continuous phase in a shallow terrace channel. Upon a sudden release of confinement, the filament either decomposes into small and monodisperse droplets right at the step (Step regime) or forms a jet of dispersed phase that is ejected into the larger reservoir (Jet regime). The nature of the breakup behavior is determined by the filament geometry and the capillary number Ca, that set the degree of filament thinning close to the topographic step. We present and experimentally verify a Volume-of-Fluid numerical scheme, that accurately determines the filament shape in the terrace region by solving the full two-phase Hele-Shaw equations, without resorting to any undetermined parameters. Using a simple geometric criterion, the model is shown to accurately predict the transition to the Step regime at low Ca.

Significantly increasing the studied terrace aspect ratio, we report on the emergence of various new breakup regimes for very wide and shallow filaments. Depending on flow rates, these breakup regimes portray the coexistence of the two previously described types of droplet producing instabilities in various combinations on a single liquid filament. Transitions between the various regimes are explained by key physical arguments such as minimization of interfacial energy, upper bounds for the volume throughput of each instability and inertia. Specifically, the cross talk between coexisting instabilities is shown to cause a spontaneous breaking of system symmetry.

Adding sedimenting particles to the dispersed phase of elongated droplets in rectangular channels, three particle accumulation regimes could be identified: At low droplet velocities, particles typically accumulate in two clouds located at the rim and the rear side of the droplets. Increasing the droplet velocity, the length of these clouds decreases and progressively more particles become dispersed over the entire droplet cross-section. Further increasing the droplet velocity, no more particle accumulation was observed. The outer shape and the internal flow field of elongated droplets moving in rectangular microchannels were studied in order to explain this peculiar particle accumulation. Significant deformation of the droplet outer shape with increasing droplet velocity is observed, which changes the drag exerted on the droplet by the surrounding continuous phase and channel walls. Consequently, a topological transition of the internal flow field with increasing droplet velocity is found. These qualitative change of the flow topology is shown to explain the different particle accumulation patterns, that emerge at different droplet velocities.

To facilitate μPIV measurements within three dimensional flow fields, we introduce a new approach to determine the influence of defocused particles on the resulting velocity signal. The distance from the focal plane up to which defocused particles are relevant to the measured velocity, the Depth of Correlation (*DOC*), is shown to be nothing but a characteristic width of a system dependent Weighting Function $W(z)$. Both, the Depth of Correlation and the Weighting Function of any μPIV setup can be determined by cross-correlating PIV-images that are constructed from a set of experimental particle images. Cross-correlation of these PIV-images allows to determine $W(z)$ and the DOC as a function of out-of-plane gradients for a given optical setup. Experimental results reveal substantial deviations from theoretical predictions for high NA air-objectives. Moreover, knowing $W(z)$ is shown to allow for the correction of measured flow profiles for errors introduced by defocused particles.

In short, this thesis demonstrates that the presence of liquid/liquid interfaces creates interesting new physics in flows on the micro-scale: The interaction of interfacial tension with fluid inertia, that is not always negligible in microfluidic systems despite the small channel dimensions, can lead to complex breakup behavior of liquid filaments. Deformation of droplet interfaces at droplet velocities $O(10^{-3} - 10^{-2})$ m/s is shown to trigger a topological transition of the internal flow field. Both studied phenomena, besides being of fundamental scientific interest, allow for new technological application which could be further developed in more engineering oriented follow-up studies.

We demonstrate simultaneous particle accumulation and encapsulation exploiting the coexistence of two instabilities on the same filament. This potentially offers a useful tool to the Lab-on-a-Chip community. Thus, future studies should deal with a more elaborate characterization of the applicable parameter range and particle concentration efficiency. Similarly, the concentration of particles or cells accumulated within droplets in rectangular microchannels at a three channel junction provides large potential for “on-chip centrifugation”. Achievable particle concentrations in droplets could be further improved by cascading several of theses junctions, alternating droplet fusion of the two particle-laden daughter droplets, particle accumulation and droplet splitting. Yet, the splitting of droplets at three channel junctions was shown to be sensitive to the incoming droplet velocity and junction geometry in terms of the lengths of daughter droplets [137]. Future studies would have to consider these effects, aswell as the complex cross-talk between subsequent junctions due the changing hydrodynamic resistance in the presence of elongated droplets and Laplace pressure pulses related to splitting.

On the more fundamental side, the findings presented within the this thesis pose an interesting problem to the computational and analytical fluid dynamics community: We demonstrate that the Ca dependent change of the breakup behavior of liquid filaments at a topographic step is well described by the presented numerical model at low filament aspect ratios. In contrast, the situation is more challenging for wider filaments. The surprisingly large variety of breakup regimes and the respective transitions at high filament aspect ratios cannot be captured by the typically used Hele-Shaw models. Additionally, symmetry cannot be assumed a priori as pinpointed by asymmetric coexistence of two distinct droplet producing instabilities. To capture the peculiar breakup behavior, theoretical models have to be developed that include the cross-talk between individual instabilities aswell as inertia effects.

Finally, the presented approach to characterize the Weighting function $W(z)$ and therewith the DOC in μPIV allows to experimentally quantify the impact of image pre-processing and filtering, as well as different PIV-analysis schemes, regarding the influence of out-of-plane particles. So far, such factors are at best quantified using image auto-correlation, thus neglecting out-of-plane velocity gradients. Our method allows to overcome this limitation and to perform a detailed analysis of any image treatment or post-processing of the PIV result.

8. Addenda

Addendum I: Capillary focusing close to a topographic step: shape and instability of confined liquid filaments

Microfluidics and Nanofluidics **18**(5), 911-917 (2015) **DOI:** 10.1007/s10404-014-1481-0.

Authors: M. Hein[1], S. Afkhami[2], R. Seemann[1,3] and L. Kondic[2]

[1] Department of Experimental Physics, Saarland University, Saarbrücken, Germany
[2] Department of Mathematical Sciences, New Jersey Institute of Technology, Newark, NJ, USA
[3] Dynamics of Complex Fluids, MPI for Dynamics and Self-Organization, Göttingen, Germany

Author Contributions:

Experiments were performed, designed and analysed by M. Hein. The theoretical model was developed by S. Afkhami and L. Kondic with experimental input by M. Hein and R. Seemann. The numerical simulations were designed and analyzed by S. Afkhami. The article was written by M. Hein and S. Afkhami. Writing was supervised by L. Kondic and R. Seemann. Research was directed by S. Afkhami, R. Seemann and L. Kondic.

Abstract:

Step-emulsification is a microfluidic technique for droplet generation which relies on the abrupt decrease of confinement of a liquid filament surrounded by a continuous phase. A striking feature of this geometry is the transition between two distinct droplet breakup regimes, the 'step-regime' and 'jet-regime', at a critical capillary number. In the step-regime, small and monodisperse droplets break off from the filament directly at a topographic step, while in the jet-regime a jet protrudes into the larger channel region and large plug-like droplets are produced. We characterize the breakup behavior as a function of the filament geometry and the capillary number and present experimental results on the shape and evolution of the filament for a wide range of capillary numbers in the jet-regime. We compare the experimental results with numerical simulations. Assumptions based on the smallness of the depth of the microfluidic channel allow us to reduce the governing equations to the Hele-Shaw problem with surface tension. The full nonlinear equations are then solved numerically using a volume-of-fluid-based algorithm. The computational framework also captures the transition between both regimes, offering a deeper understanding of the underlying breakup mechanism.

Addendum I

Capillary focusing close to a topographic step: Shape and instability of confined liquid filaments

Received 17. June 2014 / Accepted 6. September 2014 / Published Online: 18.September 2014
Microfluid Nanofluid DOI: 10.1007/s10404-014-1481-0

Michael Hein · Shahriar Afkhami · Ralf Seemann · Lou Kondic

Abstract Step-emulsification is a microfluidic technique for droplet generation which relies on the abrupt decrease of confinement of a liquid filament surrounded by a continuous phase. A striking feature of this geometry is the transition between two distinct droplet breakup regimes, the “step-regime” and “jet-regime”, at a critical capillary number. In the step-regime, small and monodisperse droplets break off from the filament directly at a topographic step, while in the jet-regime a jet protrudes into the larger channel region and large plug-like droplets are produced. We characterize the breakup behavior as a function of the filament geometry and the capillary number and present experimental results on the shape and evolution of the filament for a wide range of capillary numbers in the jet-regime. We compare the experimental results with numerical simulations. Assumptions based on the smallness of the depth of the microfluidic channel allow to reduce the governing equations to the Hele-Shaw problem with surface tension. The full nonlinear equations are then solved numerically using a volume-of-fluid based algorithm. The computational framework also captures the transition between both regimes, offering a deeper understanding of the underlying breakup mechanism.

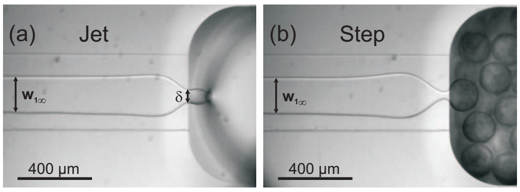

Fig. 1 Optical micrographs showing two regimes of droplet production. (a) “Jet-emulsification” for large Ca: Breakup occurs downstream, (b) “Step-emulsification” for low Ca: Breakup occurs at the step

Keywords Drops and Bubbles · Step-Emulsification · Capillary Focusing · Hele-Shaw Flow · Volume-of-Fluid

---

M. Hein
Saarland University
Experimental Physics, Saarland University, 66123 Saarbrücken, Germany
Tel.: +49-681-302 71704
Fax: +49-681-302 71700
E-mail: michael.hein@physik.uni-saarland.de

S. Afkhami
New Jersey Institute of Technology
Department of Mathematical Sciences, New Jersey Institute of Technology, Newark NJ 07102, USA
Tel.: +1-973-596-5719
Fax: +1-973-660-6467
E-mail: shahriar.afkhami@njit.edu

R. Seemann
Saarland University
Experimental Physics, Saarland University, 66123 Saarbrücken, Germany
Tel.: +49-681-302 71799
Fax: +49-681-302 71700
E-mail: r.seemann@physik.uni-saarland.de

L. Kondic
New Jersey Institute of Technology
Department of Mathematical Sciences, New Jersey Institute of Technology, Newark NJ 07102, USA
Tel.: +1-973-596-2996
Fax: +1-973-660-6467
E-mail: kondic@njit.edu

1 Introduction

Hydrodynamic instabilities leading to droplet formation by a decay of a liquid jet or filament have received considerable interest over the last two centuries (Rayleigh 1878), renewed especially since the emergence of two-phase microfluidic systems. Hydrodynamic instabilities are employed to generate droplets on the micro-scale, a technique that is promising for many lab-on-a-chip applications, where droplets could serve as discrete vials for chemical reactions or bio-analysis. Extensive reviews on experimental and theoretical studies of droplet production units and droplet handling in microfluidics have been written by Seemann et al. (2012) and Wörner (2012). Typically three different droplet production units are being used: In a T-Junction (Thorsen et al. 2001), in which the dispersed phase enters a channel filled with a continuous phase from a side channel, droplets are typically produced either by shearing or by a "Plug-and-Squeeze mechanism" (Garstecki et al. 2006). In co-flow or cross-flow geometries, which have received considerable interest from an experimental as well as from analytical perspective (Anna et al. 2003; Guillot et al. 2007, 2008), the dispersed phase flows parallel to the continuous phase and decays into droplets either directly at the inlet ("Dripping"), forms a jet that decays some distance downstream ("Jetting") or forms a liquid jet, which is absolutely stable ("Co-Flow"). All of these methods are widely used.

The instability of a liquid filament confined in a quasi two-dimensional geometry triggered by a sudden expansion of the channel has recently been described (Priest et al. 2006; Malloggi et al. 2010; Humphry et al. 2009; Shui et al. 2011; Dangla et al. 2013). The system consists of a shallow terrace and a larger microfluidic reservoir downstream, as shown in Fig. 1. In the terrace, the non-wetting dispersed liquid flows as a straight filament confined at the top and the bottom by the walls and surrounded by a continuous phase. The main control parameter is the capillary number, Ca, which represents the effect of viscous relative to capillary forces. Two distinct droplet breakup mechanisms can be observed for droplet generation. At high Ca, a mechanism called "jet-emulsification" occurs, in which the dispersed phase creates a stable tongue in the terrace. This tongue narrows to a neck close to the topographic step due to capillary focusing. From this neck, a jet protrudes, generating large and polydisperse droplets that fill the whole reservoir channel (see Fig. 1a). Below a critical Ca, the so called "step-emulsification" occurs (see Fig. 1b). In the latter case, the inner stream forms a droplet immediately after it reaches the topographic step, where the tip then becomes unstable, producing droplets at high throughput with a monodispersity superior to the previously mentioned droplet production methods (Priest et al. 2006; Dangla et al. 2013). Recent efforts to describe this emulsification process have resulted in models for predicting lower bounds for the generated droplet size in the step-regime (Dangla et al. 2013) and estimating the width of the tongue at the step in the jet-regime (Malloggi et al. 2010). However, rigorous study of the shape and instability of the confined tongue and comprehensive comparison of experimental results with theoretical models have not been carried out until now.

In this article, we study the capillary focusing phenomena in a step-emulsification microfluidic device. On one hand, the dynamic filament shape and stability in the jet-regime is experimentally analyzed for a wide parameter range. On the other hand, a computational framework is developed to solve the full Hele-Shaw (H-S) equations and to directly compute the shape of the liquid-liquid interface in the terrace, providing a better understanding of the observed experiments. By direct comparison of the numerical results with experiments, we show that the shape of the liquid filament in the jet-regime can be computed as a function of Ca and the flow rate ratio between the dispersed and continuous phase, without resorting to any undetermined parameter.

Here, a simple stability-criterion is used to show that the experimentally observed transition between the step- and jet-regime can also be predicted by the numerical simulations; the description of this transition based on the direct numerical solution of the two-phase H-S equations with surface tension has not been addressed before.

2 Experimental method

To characterize the droplet breakup regimes in a step-emulsification geometry and the filament shape in the jet-regime, experiments are performed using a device micromachined into a polymethylmethacrylate (PMMA)-block with a terrace of width $w = 400\,\mu$m and depth $b = 30\,\mu$m (i.e. with aspect ratio $w/b = 12.76$) and a downstream reservoir of cross-sectional area of about $1 \times 1\,\text{mm}^2$. The channel is sealed by a PMMA-sheet. An aqueous phase with 28 wt% glycerol is injected as a dispersed phase into an oily continuous phase, IsoparM (ExxonMobil Chemical). For the chosen liquid system, the viscosity of the dispersed phase, μ_1, is matched with the viscosity of the continuous phase, μ_2, and is approximately 2.1 mPas. 2 wt% of the surfactant Span 80 (Sigma Aldrich) are added to the continuous phase to increase the droplet stability and to ensure the wetting of the channel walls by the continuous phase. The interfacial tension coefficient, γ, determined using the pendant drop method, is 3.5 ± 0.1 mN/m. The evolution of the interface is imaged using a microscope (Zeiss AxioVert) and a high-speed CMOS camera (PCO 1200hs). The interface profiles as well as the tongue width, $w_{1\infty}$, far away from the neck, and the neck width, δ, directly at the step, are automatically measured using numerical image analysis (see Fig. 1a). Volumetric flow rates,

Q_1 and Q_2, of the dispersed and the continuous phase, respectively, are adjusted using computer controlled syringe pumps. The corresponding $\mathrm{Ca} = U_1\mu_1/\gamma$ is determined from the average flow velocity of the dispersed phase, U_1.

3 Computational framework

In addition to physical experiments, a computational framework is developed to provide a deeper insight into the effects governing the evolution of the liquid-liquid interface in the jet-regime and to predict the transition between the jet- and step-regime. The original governing equations are reduced to the time-dependent two-phase Hele-Shaw equations with surface tension. We stress that, even in this case, the full problem is nonlinear due to the curvature term in the surface tension and therefore the full problem has to be solved numerically. Furthermore, although not considered here, our numerical model allows to seamlessly vary the viscosity of both phases as well as the initial condition and the geometry of the Hele-Shaw problem. We use a volume-of-fluid (VOF) based method to directly solve the governing equations. Our numerical model, described in detail by Afkhami and Renardy (2013), has the distinctive feature of being capable of, accurately and robustly, modeling the surface tension force. In addition, the accurate interface reconstruction, the second-order curvature computation, and the use of adaptive mesh refinement allow for resolved description of the interface, enabling us to investigate the complex features of interface profiles extracted from experiments, which was not possible in prior studies. The order of accuracy and convergence properties of the numerical methods were previously studied by Afkhami and Renardy (2013).

The computational framework consists of the classical H-S model to simulate the shape of the interface between the dispersed and the continuous phase in the shallow channel. The depth-averaged velocity field in both phases is defined as

$$\mathbf{u}(x, y, t) = \frac{b^2}{12\mu}\left\{-\nabla p(x, y, t) + \mathbf{F}(x, y, t)\right\}, \tag{1}$$

where μ is the viscosity of the considered phase defined as

$$\mu(f) = \frac{\mu_1\mu_2}{(1-f)\mu_1 + f\mu_2}, \tag{2}$$

where μ_1 and μ_2 refer to the viscosity of fluid 1 and 2, respectively, b is the depth of the H-S cell, and $p(x, y, t)$ is the local pressure. The VOF function, $f(x, y, t)$, tracks the motion of the interface. In a VOF method, the discrete form of the function f represents the volume fraction of a cell filled with, in this case, fluid 1. Away from the interface, $f = 0$ (inside fluid 2) or $f = 1$ (inside fluid 1); "interface cells" correspond to $0 < f < 1$. The evolution of f satisfies the advection equation

$$\frac{\partial f}{\partial t} + \mathbf{u}(x, y, t) \cdot \nabla f = 0. \tag{3}$$

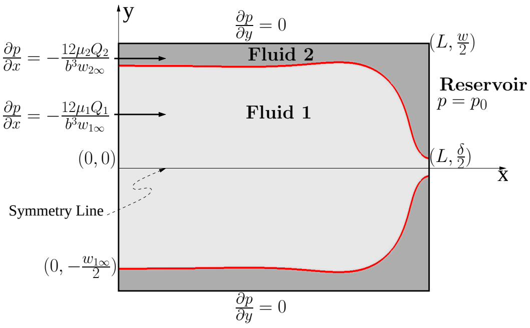

Fig. 2 Schematic of the flow domain for the Hele-Shaw model and the corresponding boundary conditions. The domain is bounded by walls at $|y| = w/2$. At $x = 0$, fluid 1 occupies $|y| \le w_{1\infty}/2$ and fluid 2 occupies $w_{1\infty}/2 < y \le w$ and $-w < y < -w_{1\infty}/2$; $w_{2\infty} = w - w_{1\infty}$

In this formulation, surface tension enters as a singular body force, $\mathbf{F}(x, y, t)$, centered at the interface between two fluids (Afkhami and Renardy 2013). Figure 2 is a schematic of the flow domain, $0 \le x \le L$, $|y| \le w/2$, representing the terrace. Due to symmetry, only half of the domain is simulated. We consider a constant pressure, p_0, in the reservoir and, as a first approximation for the outflow into a reservoir, an outflow pressure boundary condition at the exit, $x = L$, as

$$p(x, y, t) = \begin{cases} p_0 + 2A\gamma/b & 0 < f \le 1 \\ p_0 & f = 0 \end{cases} \tag{4}$$

where the out-of-plane curvature is given by $2/b$. Thus $2\gamma/b$ is the Laplace pressure inside the dispersed phase 1. Since the in-plane curvature at the step is typically much smaller than the out-of-plane curvature, it can be safely neglected. A pressure correction parameter, $A \le 1$, is included for modeling the flow configurations for which the H-S approximation is expected to be less accurate, as discussed further below. The boundary condition for f at the top and bottom walls is $f = 0$. At the outflow, the boundary condition for f is the interface being perpendicular to the topographic step: $\partial f/\partial x = 0$. This is justified experimentally in section 4.1. On the solid boundaries (side walls), $\partial p/\partial y = 0$. At the inlet, $x = 0$, the parallel flow solution holds, meaning that for both phases, the pressure gradient is prescribed as $\partial p(x, y, t)_i/\partial x = -(12\mu Q_i)/(b^3 w_{i\infty})$ where $i = (1, 2)$, $w_{i\infty}$ is the width occupied by the ith liquid at the inlet, and Q_i is the flow rate of the ith phase. As in the experiments, we chose $dp_1/dx|_{x=0} = dp_2/dx|_{x=0}$ and fix b and w. The initial condition at $t = 0$ is a flat interface defined by the initial distribution of f over the domain. We keep L large enough so the results are unaffected by its value.

4 Results and discussion

4.1 Filament shape: temporal evolution

In the jet-regime, i.e. at sufficiently high Ca (see Fig. 1a), a filament of a dispersed phase, sandwiched by the continuous phase, is stable over the terrace due to the geometric confinement of the flow. When pushed into the reservoir, in which the pressure is presumably constant, the two phases are forced to balance their pressure. The dispersed phase, however, experiences a higher pressure due to the Laplace pressure, generated by the out-of-plane curvature of the interface and the evolving meniscus. This induces a temporarily varying cross-stream pressure difference between the two fluids. Thus, to adjust to a constant pressure at the step, the dispersed phase has to increase its velocity, whereas the continuous phase moves more slowly over the terrace. Due to mass conservation, the interface between the two fluids must assume a tongue-like shape that narrows down to a thin neck along the mean flow, an effect known as "capillary focusing".

For droplet formation in an actual microfluidic device, the situation is more complex, since droplets are periodically formed in the reservoir, thus influencing the pressure at the step and consequently the tongue shape. Figure 3a-d shows a typical evolution of the tongue shape during droplet production in the jet-regime (see also the movie in the supplemental material). Figure 3e shows the tongue width (normalized by the filament width), $\delta/w_{1\infty}$, called the tongue shape factor, as a function of time. As shown, at the beginning of the droplet formation cycle (see Fig. 3a and regime 1 in Fig. 3e), when the droplet is initially pushed into the reservoir, $\delta/w_{1\infty}$ remains constant while the droplet inflates, maintaining a nearly spherical shape. During this inflation process, the liquid-liquid interface at the step is perpendicular to the topographic step (see the inset in Fig. 3a). The Laplace pressure that counteracts the inflation of the droplet rapidly decreases as the droplet radius increases and remains merely constant when the droplet reaches the reservoir dimension. Additional complexity may arise in the case of droplet collision in the reservoir channel. When the droplet touches the walls of the reservoir, $\delta/w_{1\infty}$ typically increases as the droplet starts to travel downstream, pulling the tongue towards the step (see Fig. 3b-c and regime 2 in Fig. 3e). Additionally, the droplet blocks the reservoir, except for small regions along the corners of the rectangular reservoir. Thus, an additional pressure contribution, that is expected to increase with the droplet length (Labrot et al. 2009), is needed to push the continuous phase at constant flow rate downstream in the reservoir. This pressure component is also expected to deform the interface in the shallow terrace. Thus $\delta/w_{1\infty}$ reaches a maximum during regime 2 in Fig. 3e and then decreases, showing the formation of a neck, that may evolve to a stable width in regime 3 in Fig. 3e. In regime 3, the neck elongates as the rear interface of the droplet travels downstream, until it bulges and finally ruptures (see Fig. 3d and regime 3 in Fig. 3e). After droplet breakup, the process repeats starting in regime 1. From the above description of the tongue evolution in the jet-regime at high Ca, it is obvious that only in regime 1 the pressure boundary condition at the topographic step is known a priori, resembling an open outlet with a constant pressure, p_0. Thus the experimental data taken in regime 1 is used for further comparison with computational results. In regime 2 and 3, however, the pressure

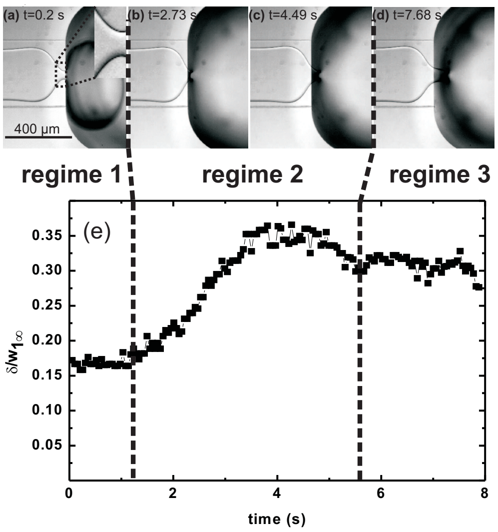

Fig. 3 Temporal evolution of the tongue in the jet-regime. (a)-(d) Micrographs with the inset showing the interface directly at the step and (e) the shape factor, $\delta/w_{1\infty}$, as a function of time; Ca $= 9.73 \times 10^{-3}$ and $Q_{1\infty}/Q_{2\infty} = 3$

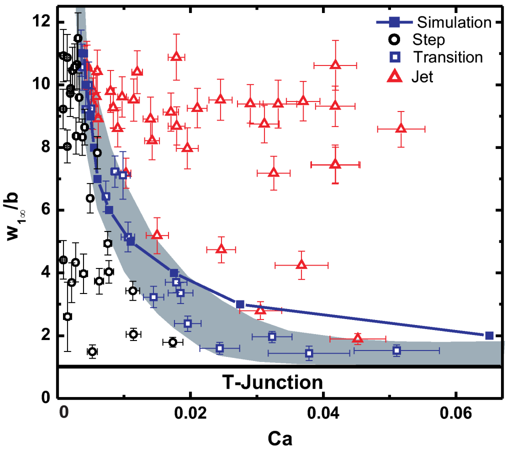

Fig. 4 Phase diagram demonstrating the transition of jet-regime (red triangles) to step-regime (black circles). Blue open squares denote the transition regime, where droplet production alternates between step- and jet-regime. Blue solid squares indicate the simulation results for $A = 0.4$, as discussed in the text. For $w_{1\infty}/b \leq 1$ no stable filament is formed

at the topographic step is significantly influenced by the evolving droplet in the reservoir. We note that regime 1 can be further expanded by increasing reservoir dimensions.

4.2 Transition from jet- to step-regime

A sudden transition to the step-regime occurs when reducing the Ca below a certain threshold, as shown in Fig. 4. The transition between jet- and step-regime can be qualitatively described as follows: At low Ca, when the width of the neck, δ, becomes comparable to the height of the terrace, b, the dispersed phase forms a nearly cylindrical neck, which is prone to a surface-tension-driven instability. As the neck is no longer stable, the filament breaks up rapidly and small droplets are continuously produced, accompanied by a periodic retraction of the tongue. We have confirmed this critical neck width experimentally by measuring δ in the metastable transition regime, where step- and jet-regime alternate (see shaded region in Fig. 4). Interestingly, despite the qualitative differences in tongue shape and stability between step- and jet-regime (cf. Fig. 1), we note that the tongue width far upstream from the step, $w_{1\infty}$, stays constant for a given $Q_{1\infty}/Q_{2\infty}$ when varying Ca. In particular, $w_{1\infty}$ is unaffected by the transition from the jet- to step-regime, which allows to characterize the transition as a function of the rescaled tongue width, $w_{1\infty}/b$, and Ca. Figure 4 shows the emulsification phase diagram in $(w_{1\infty}/b, \mathrm{Ca})$ space, with an increased data range compared to Priest et al. (2006), in which it is shown that the phase diagram is insensitive to the viscosity ratio of the dispersed phase to the continuous phase, μ_1/μ_2. We note that for $w_{1\infty}/b \leq 1$, droplet breakup occurs at the inlet of the dispersed phase. This regime is comparable to breakup in a T-junction and is not considered here.

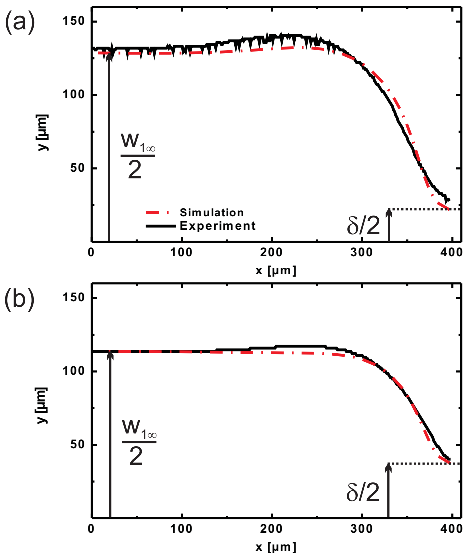

Fig. 5 Comparison of the tongue profiles in the terrace obtained from experiments (black solid line) and simulations with $A = 1$ (red dashed line). Both experimental profiles are obtained in the jet-regime. (a) $\mathrm{Ca} = 0.019$ and $w_{1\infty}/b = 7.97$ and (b) $\mathrm{Ca} = 0.042$ and $w_{1\infty}/b = 7.44$. For experiments, $Q_{1\infty}/Q_{2\infty} = 1.5$. For simulations, $Q_{1\infty}/Q_{2\infty} = 1.67$ in (a) and $Q_{1\infty}/Q_{2\infty} = 1.41$ in (b)

4.3 Comparison of experiments with numerical simulations

Figure 5 shows the direct comparison of the tongue profiles obtained from experiments with the corresponding simulations. As shown, the numerical simulations accurately reproduce the main features of the tongue shape, particularly the slight increase of the tongue width followed by the strong capillary focusing close to the topographic step. We also note that the agreement between the simulated results and experiments is best at higher Ca values, shown in Fig. 5b, remote from the transition to the step-regime, where the tongue width is larger and the validity of the H-S approximation (assumed in the

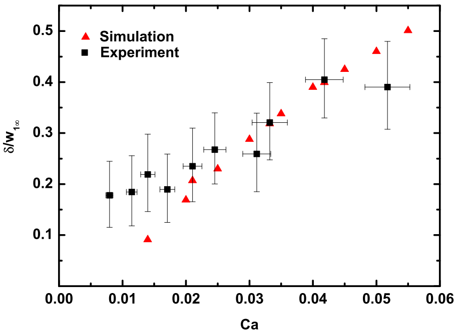

Fig. 6 Comparison of the experimentally determined shape factor, $\delta/w_{1\infty}$, for $Q_{1\infty}/Q_{2\infty} = 3$ (black squares) and the simulation results (red triangles) for $Q_{1\infty}/Q_{2\infty} = 2.81$ and $A = 1$

numerical scheme) is clearly fulfilled. To quantify the comparison between the numerical and experimental results, in Fig. 6, the shape factor, $\delta/w_{1\infty}$, measured from the obtained profiles, is plotted as a function of Ca. The error bars for the experimentally determined $\delta/w_{1\infty}$ are worst case estimates based on the width of the interface after image segmentation, and the error bars for Ca are Gaussian error estimates. The measured values for $\delta/w_{1\infty}$ agree within experimental accuracy with the results from the corresponding simulations, especially for medium to high Ca. Both the results from the experiment and the simulation show that the neck thickness increases with Ca, as also predicted analytically by Malloggi et al. (2010). However, for Ca $\lesssim 0.02$, close to the transition, simulation predicts a stronger focusing, i.e. a stronger decrease of $\delta/w_{1\infty}$ with Ca, when compared to the experimental data, as the neck becomes more and more cylindrical in this regime, making the H-S approximation less accurate. Thus the numerical model underestimates $\delta/w_{1\infty}$ for small Ca. This underestimation can be compensated by introducing a pressure correction, A, as described in Eq. 4, which increases δ by weakening the capillary focusing, at the cost of a reduced bulging prior to the hydrodynamic focusing. We apply this pressure correction and use the stability criterion, $\delta = b$, as described in section 4.2, and employ the numerical simulation to predict the transition from jet- to step-regime. Figure 4 shows the excellent agreement of the computationally predicted transition threshold when compared to experimental data for $A = 0.4$. As discussed previously, introducing A is needed when considering the regime where the H-S approximation is not strictly valid. A clear approach to improve the accuracy is to consider fully three-dimensional flow, as well as to consider possible influence of the viscosity contrast and capillary effects on the pressure correction factor. We leave these non-trivial extensions for future work.

5 Conclusion

In this article, the capillary focusing of a confined liquid filament at a topographic step is studied both experimentally and numerically. A novel computational framework, based on the Hele-Shaw approximation and the volume-of-fluid approach, is shown to predict experimental results quantitatively. We find that by modeling the reservoir with an applied pressure boundary condition, the computed shapes of the filament are in excellent agreement with experiments for moderate to high capillary numbers, without resorting to any undetermined parameters. Furthermore, we show that the numerical model can accurately predict the width of the tongue remote from the step. We also characterize the width of the tongue at the step as a function of Ca and show that the computational results are in very good agreement with the experimental findings in the jet-regime and close to the transition to the step-regime. Direct computations also provide an accurate estimate of the transition between two distinct droplet breakup mechanisms characterized experimentally. This work is expected to set ground for further numerical and analytical treatment of confined filament shapes in similar geometries. The presented computational framework solves the full Hele-Shaw equations without additional simplifications. Thus the model is not limited to predicting two-phase flow behavior in the specific geometry discussed in this paper and can easily be adapted to similar problems. Additionally, knowing the dependence of the breakup behaviour on filament geometry and capillary number will also facilitate application-specific designs of microfluidic droplet production units.

Acknowledgements Authors gratefully acknowledge Dr. Jean-Baptiste Fleury (Saarland University) for helpful discussions and the DFG-GRK1276 for financial support. This work was partially supported by the NSF Grant Nos. DMS-1320037 (S.A.) and CBET-1235710 (L.K.).

References

S. Afkhami and Y. Renardy. A volume-of-fluid formulation for the study of co-flowing fluids governed by the Hele-Shaw equations. *Phys. Fluids*, 25:082001, 2013.

S. Anna, N. Bontoux, and H. Stone. Formation of dispersions using "flow focusing" in microchannels. *Appl. Phys. Lett.*, 82:364–366, 2003.

R. Dangla, E. Fradet, Y. Lopez, and C. N. Baroud. The physical mechanisms of step emulsification. *J. Phys. D*, 46:114003, 2013.

P. Garstecki, M. J. Fuerstman, H. A. Stone, and G. M. Whitesides. Formation of droplets and bubbles in a microfluidic T-junction–scaling and mechanism of break-up. *Lab Chip*, 6:437–446, 2006.

P. Guillot, A. Colin, A. S. Utada, and A. Ajdari. Stability of a jet in confined pressure-driven biphasic flows at low Reynolds numbers. *Phys. Rev. Lett.*, 99:104502, 2007.

P. Guillot, A. Colin, and A. Ajdari. Stability of a jet in confined pressure-driven biphasic flows at low Reynolds number in various geometries. *Phys. Rev. E*, 78:016307, 2008.

K. J. Humphry, A. Ajdari, A. Fernández-Nieves, H. A. Stone, and D. A. Weitz. Suppression of instabilities in multiphase flow by geometric confinement. *Phys. Rev. E*, 79:056310, 2009.

V. Labrot, M. Schindler, P. Guillot, A. Colin, and M. Joanicot. Extracting the hydrodynamic resistance of droplets from their behavior in microchannel networks. *Biomicrofluidics*, 3:012804, 2009.

F. Malloggi, N. Pannacci, R. Attia, F. Monti, P. Mary, H. Willaime, and P. Tabeling. Monodisperse colloids synthesized with nanofluidic technology. *Langmuir*, 26:2369–2373, 2010.

C. Priest, S. Herminghaus, and R. Seemann. Generation of monodisperse gel emulsions in a microfluidic device. *Appl. Phys. Lett.*, 88:024106, 2006.

L. Rayleigh. On the instability of jets. *Proc. London Math. Soc.*, 10:4–13, 1878.

R. Seemann, M. Brinkmann, T. Pfohl, and S. Herminghaus. Droplet based microfluidics. *Rep. Prog. Phys.*, 75:016601, 2012.

L. Shui, A. van den Berg, and J. C. T. Eijkel. Scalable attoliter monodisperse droplet formation using multiphase nano-microfluidics. *Microfluid. Nanofluid.*, 11:87–92, 2011.

T. Thorsen, R. W. Roberts, F. H. Arnold, and S. R. Quake. Dynamic pattern formation in a vesicle-generating microfluidic device. *Phys. Rev. Lett.*, 86: 4163–4166, 2001.

M. Wörner. Numerical modeling of multiphase flows in microfluidics and micro process engineering: a review of methods and applications. *Microfluid. Nanofluid.*, 12:841–886, 2012.

Addendum II: Coexistence of different droplet generating instabilities: new breakup regimes of a liquid filament

accepted in Soft Matter (2015) **DOI:** 10.1039/C5SM00736D.

Authors: M. Hein[1], J.B. Fleury [1] and R. Seemann[1,2]

[1] Department of Experimental Physics, Saarland University, Saarbrücken, Germany
[2] Dynamics of Complex Fluids, MPI for Dynamics and Self-Organization, Göttingen, Germany

Author Contributions:

The emergence of multiple instabilities on a single filament under strong confined was discovered by M.Hein. Experiments in vertical step geometries were performed, designed and analyzed by M. Hein. Experiments in horizontal step geometries were designed by J.B. Fleury and M. Hein, performed and analyzed by J.B. Fleury. Particle concentration experiments were designed by J.B. Fleury, R. Seemann and M. Hein and performed by J.B. Fleury. The article was written by M. Hein and R. Seemann. Writing was supervised by J.B. Fleury and R. Seemann. Research was directed by R. Seemann and J.B. Fleury.

Abstract:

The coexistence of multiple droplet breakup instabilities in a Step-emulsification geometry is studied. A liquid filament, which is confined in one dimension by channel walls and surrounded by a co-flowing immiscible continuous phase, decays into droplets when subject to a sudden release of confinement. Depending on the filament aspect ratio and liquid flow rates, an unexpectedly rich variety of droplet breakup regimes is found. All of these breakup regimes are composed of two basic instabilities, i.e. a step- and a jet-instability, that coexist in various combinations on the same filament. Surprisingly, even an asymmetric breakup regime is found, producing droplet families of significantly different diameters, while the filament is subject to a fully symmetric flow field. We suggest key physical principles explaining the spontaneous symmetry breaking and the transitions between individual droplet breakup regimes. The particular ability to produce distinct droplet families from a single filament is demonstrated to allow for simultaneous concentration and encapsulation of particles into one droplet family while excess bulk liquid is released into another family of droplets.

Coexistence of different droplet generating instabilities: new breakup regimes of a liquid filament†

Michael Hein,[a] Jean-Baptiste Fleury,[a] and Ralf Seemann[a,b*]

Received 28th March 2015, Accepted 21st May 2015
First published on the web 22nd May 2015
Soft Matter DOI: 10.1039/C5SM00736D

The coexistence of multiple droplet breakup instabilities in a Step-emulsification geometry is studied. A liquid filament, which is confined in one dimension by channel walls and surrounded by a co-flowing immiscible continuous phase, decays into droplets when subject to a sudden release of confinement. Depending on the filament aspect ratio and liquid flow rates, an unexpectedly rich variety of droplet breakup regimes is found. All of these breakup regimes are composed of two basic instabilities, i.e. a step- and a jet-instability, that coexist in various combinations on the same filament. Surprisingly, even an asymmetric breakup regime is found, producing droplet families of significantly different diameters, while the filament is subject to a fully symmetric flow field. We suggest key physical principles explaining the spontaneous symmetry breaking and the transitions between individual droplet breakup regimes. The particular ability to produce distinct droplet families from a single filament is demonstrated to allow for simultaneous concentration and encapsulation of particles into one droplet family while excess bulk liquid is released into another family of droplets.

Hydrodynamic instabilities of liquid jets or filaments have been intensively studied over two centuries, starting with the early studies of Rayleigh and Plateau on the decay of a falling jet in the 19th century[1]. Droplet formation by these instabilities is of massive importance in nature and technical applications, ranging from the production of nanoparticles by decay of nanometric cylinders[2,3] or decay of submicrometric jets[4], food processing, bio-medical applications, and inkjet printing[5,6], to animal hunting strategies in nature[7]. With the emergence of multiphase microfluidics, offering the potential of miniaturizing chemical and biological synthesis and analysis[8], the interest in instabilities of liquid filaments and jets on the micro scale has peaked again[9–11].

Specifically, the instability of a confined liquid filament coflowing with a surrounding immiscible fluid over a quasi two-dimensional terrace into a large reservoir has recently been described[12–15]. So far, two possible instabilities were observed in this or similar geometries[12–19]. For small Capillary Numbers *Ca*, the filament is destabilized right at the step generating small droplets at high throughput. This 'Single-Step'-Emulsification offers superior monodispersity compared to alternative emulsification methods, which makes it interesting for a wide range of applications[11,20,21]. For large *Ca* the dispersed phase rather protrudes as a jet into the reservoir that decays into large and polydisperse droplets ('Single-Jet' emulsification). The transition between the 'Single-Step' regime at small *Ca* and the 'Single-Jet' regime at large *Ca* has recently been explained by a simple geometric stability criterion[13,15]. Other instabilities were not observed in such geometries.

In this article we show that additional breakup regimes emerge for strongly confined wide filaments in shallow terraces. These new breakup regimes feature two or more distinct instabilities, being fed by a single liquid filament. Surprisingly, even instabilities of different types can occur on the same filament, thus breaking the axisymmetric solutions of the system. The latter is not expected from the Navier-Stokes equation regarding the intrinsic symmetry of systems driven by a homogeneous forcing of the two immiscible phases. So far, asymmetric breakup of filaments and jets was only observed either at high Reynolds Numbers or when additional forcing, *i.e.* by electrical fields was applied[22,23]. In the following, these new droplet breakup regimes and their transitions as a function of *Ca* and filament geometry will be explored.

1 Experimental section

Two different geometries are used, one with a vertical step (Geometry A) and another with a horizontal step (Geometry B), see Fig. 1. All the various breakup regimes are identified in both geometries. However, each geometry offers specific advantages regarding the characterization of the liquid instabilities: In Geometry A, which offers a top-view of the ter-

---

[a] *Saarland University, Experimental Physics, Saarbrücken, Germany. Fax: +49 681 302 71700 ; Tel: +49 681 302 71777; E-mail: r.seemann@physik.uni-saarland.de*
[b] *Max Planck Institute for Dynamics and Self-Organization, Göttingen, Germany*

† Electronic Supplementary Information (ESI) available.

race channel, the shape of the filament and the coexistence of various droplet production mechanisms can be observed. To demonstrate the generality of the observed breakup behavior, Geometry B features a terrace that is tilted by 90°compared to Geometry A and centered to the reservoir to create a planar structure, typical for structures produced by lithographic techniques. In Geometry B, the generated liquid jets and droplets can be observed more clearly. Due to the particular channel geometry and smaller dimensions of the reservoir in Geometry B, crowding of droplets in the reservoir and buoyancy effects are reduced, as droplets are immediately advected downstream even at low volumetric flow rates. Thus, Geometry B is more suitable to study jet-instabilities, where liquid jets protrude into the reservoir that remain connected to the filament.

The Step-emulsification devices (Geometry A) were micromachined into Poly-Methylmethacrylate (PMMA) with a terrace of width $w = 400\,\mu$m and depth $b = 30\,\mu$m (i.e. $w/b = 12.8$) or $w = 385\,\mu$m and depth $b = 13\,\mu$m (i.e. $w/b = 30$), cf. Fig. 1a. The downstream reservoir has a cross-sectional area of about $1\times1\,\mathrm{mm}^2$ in both cases. The device is sealed by screwing a PMMA-sheet to it and connected to gastight glass syringes (Hamilton) by teflon tubing and threaded fittings (Omnifit). An aqueous phase with 28 wt% or 43 wt% glycerol is injected as a dispersed phase into an oily continuous phase, IsoparM (ExxonMobil Chemical), containing 2 wt% of the surfactant Span 80 (Sigma Aldrich). The liquid/liquid interfacial tension γ is determined to (3.5 ± 0.1) mN/m and (3.8 ± 0.1) mN/m for the 28 wt% and 43 wt% glycerol solution using the pendant drop method. The viscosity ratio of the dispersed to the continuous phase is $\mu_1/\mu_2 \approx 1$ for the 28 wt% glycerol solution and $\mu_1/\mu_2 \approx 2$ for the 43 wt% glycerol solution. To keep results comparable to previous publications, this liquid system is identical to the one used in[12,13].

Devices of Geometry B are fabricated in Sylgard 184 (Dow Corning) by standard one layer soft lithography[24] using SU8-100 photoresist. The device is sealed with a glass slide by plasma activation of the glass and PDMS surfaces (Femto Plasma-Cleaner, Diener Electronic GmbH) and connected with teflon tubing inserted into the Sylgard. Geometry B features a terrace of width $w \approx 210\,\mu$m, defined by the resist film height, and depth $b \approx 10\,\mu$m that is tilted by 90°compared to Geometry A and centered to the reservoir, see Fig. 1b. Thus the filament shape is not accessible experimentally. The reservoir height is $H \approx 210\,\mu$m and the reservoir width is $W = 200\,\mu$m. The liquids used in Geometry B were ultra-pure water (GenPure, TKA) as dispersed phase and n-hexadecane (AlfaAesar) as continuous phase. The viscosity ratio of the dispersed to the continuous phase is $\mu_1/\mu_2 \approx 0.3$. As for Geometry A, 2 wt% of the surfactant Span 80 (Sigma Aldrich) are added to the continuous phase. The liquid/liquid interfacial tension is determined to $\gamma = (3.5\pm0.1)$ mN/m. For particle concentration experiments PMMA particles of diameter $4\,\mu$m (Sigma Aldrich) were added to the dispersed phase.

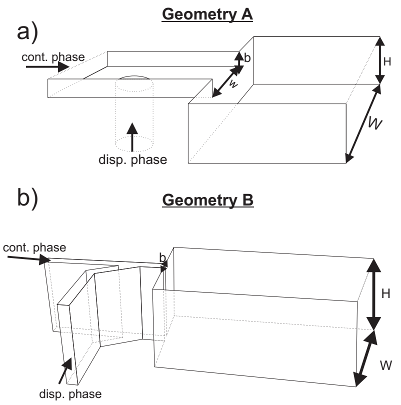

Fig. 1 Sketch of the two device geometries used: a) Geometry A milled into a PMMA-block featuring a vertical step b) Geometry B produced by soft lithography featuring a horizontal release of confinement.

For all experiments, volumetric flow rates, Q_1 and Q_2, of the dispersed and the continuous phase are adjusted using custom-built computer controlled precision syringe pumps. Droplet breakup behavior is observed using optical microscopy (Zeiss AxioVert, Leica Macroscope Z16 or Reichert-Jung MeF3) and high-speed CMOS cameras (PCO 1200hs or Photron Fastcam SA3). When characterizing the filament shape in the terrace using Geometry A, filament shapes and the filament width $w_{1\infty}$ are measured using automated numerical image analysis. Droplet production frequencies, droplet diameters, jet length, bulging wavelength λ, growth and retraction times were extracted from the recorded time series by direct measurements or by counting droplets.

2 Results and discussion

The continuous oily and the dispersed aqueous phases are injected into the microfluidic devices at constant volumetric flow rates, Q_1 and Q_2, respectively. Based on the chosen flow rates, a filament of dispersed phase surrounded by the continuous phase adjusts itself to a certain width $w_{1\infty}$ on the terrace remote from the step, cf. Fig. 2. When approaching the topographic step, the filament narrows to one or several coexisting necks from which droplets or jets are injected into the reservoir. The number of instabilities that might coexist on a single filament depends on its width $w_{1\infty}$. The observed breakup regimes are displayed in Fig. 2 for the two different device geometries used.

2.1 Overview of the various breakup regimes

The top row of Fig. 2 displays images from a vertical step geometry (Geometry A) in which the filament shape can be observed, whereas the bottom row presents images from a horizontal step geometry (Geometry B), where jets can be observed best. The appearance of the various breakup regimes upon varying the Capillary Number $Ca_{ch} = \frac{\mu_1 \cdot (Q_1+Q_2)}{\gamma \cdot w \cdot b}$ is independent of the exact device geometry and the liquid system used. The observed breakup regimes agree qualitatively among Geometry A and B. However, please note that even though the basic Geometries A and B are similar, they differ in details such as the reservoir in Geometry B widening in one dimension only and different continuous phases being used in Geometry A and B. Thus the observed droplet breakup regimes appear at different Ca_{ch} in Geometry A and B.

At low Ca_{ch} the breakup of small and monodisperse droplets occurs from a single step-instability right at the topographic step (left column of Fig. 2) for any filament geometry, i.e. the ratio of the filament width remote from the step to the terrace height $w_{1\infty}/b$. This situation corresponds to the known 'Single-Step' regime (I)[12]. When the confinement is suddenly removed, the liquid filament adjusts its shape to compensate for the large pressure difference between the filament and the reservoir[13,15]. The pressure within the filament is larger than in the continuous phase due to the Laplace pressure, that originates from the out-of-plane curvature of the filament. To equilibrate the pressure at the step, the filament narrows to a neck which is known as 'capillary focusing'[14]. An increasing Ca_{ch} at constant $w_{1\infty}/b$ leads to a growing width of the neck at the topographic step. In the limiting case, when Ca_{ch} is increased above a certain threshold, the width of the neck exceeds the terrace height b and the neck is stabilized by confinement up to the topographic step[16,25]. In this situation the dispersed phase protrudes as a jet into the reservoir from which large and polydisperse drops detach, see right column in Fig. 2. This situation corresponds to the known 'Single-Jet' (V) emulsification[12,13]. The step-instability and jet-instability are the only possible instabilities found for small filament aspect ratios $w_{1\infty}/b$, i.e. for small flow rate ratios Q_1/Q_2, featuring only a single instability on the filament. In contrast to the well understood droplet production for low $w_{1\infty}/b$, additional droplet breakup regimes emerge upon varying the absolute flow rate for sufficiently large filament aspect ratios $w_{1\infty}/b$, i.e. for sufficiently large flow rate ratios Q_1/Q_2.

These new breakup regimes feature at least two coexisting instabilities on the same filament. Starting at low Ca_{ch} in the regime I, the filament produces a second step-instability upon increasing the Capillary Number in regime II. The secondary step-instability emits monodisperse droplets of the same diameter as the initial step-instability, provided the height of the terrace is constant over the entire terrace width.

Upon further increasing Ca_{ch}, one of the two instabilities switches to jetting, entering regime III. Droplet volumes in this regime can easily span several orders of magnitude, ranging from picolitres for droplets produced by a step-instability to several tenth of nanolitres for droplets produced by a jet-instability.

Increasing Ca_{ch}, an additional step- or jet-instability can emerge within regime III for sufficiently wide filaments and a coexistence of up to three instabilities on one filament was observed. However, in particular for Geometry A having the larger reservoir, crowding of droplets is observed in the reservoir. Thus coexisting instabilities are temporarily fluctuating depending on collisions between forming droplets and already formed droplets in the reservoir.

For even larger Ca_{ch}, all the droplet generating instabilities switch to jetting (regime IV). In the tested geometries, up to four jets were found protruding from a single filament, depending on $w_{1\infty}/b$, Ca_{ch}, and crowding of droplets in the reservoir. However, the parameter range for the occurrence of more than two coexisting instabilities in both regimes is fairly small, limited to very large filament aspect ratios $w_{1\infty}/b$. For the sake of clarity, the discussion of those regimes with multiple coexisting instabilities is restricted to two instabilities, without loosing generality.

Further increasing Ca_{ch}, the multiple jets collapse to a single one, resulting in the known 'Single-Jet' (V) regime[12,13]. Movies showing examples of the different breakup-regimes equally found in both geometries are presented in SI 1.

The different droplet breakup regimes observed for different terrace aspect ratios w/b and viscosity ratios collapse onto the same parameter ranges for a given continuous phase when rescaling the filament width $w_{1\infty}$ with the terrace height b and using the Capillary Number of the dispersed phase based on the filament width $Ca = \frac{\mu_1 \cdot Q_1}{\gamma \cdot w_{1\infty} \cdot b}$, see Fig. 3. This rescaling obviously requires measuring the filament width $w_{1\infty}$, thus only the results from Geometry A are used in Fig. 3. The filament width is not accessible and a different continuous phase was used in Geometry B, cf. section 1 for details. Note, that a filament of dispersed phase cannot be stabilized by the confining channel walls for filament aspect ratio $w_{1\infty}/b \lesssim 1$ and droplet breakup occurs directly at the inlet of the dispersed phase into the terrace, similar to droplet breakup in a T-junction[12]. This situation is indicated by the gray horizontal box in Fig. 3. For larger filament aspect ratios $1 \lesssim w_{1\infty}/b \lesssim 12$, Fig. 3 clearly reveals the two known breakup regimes, namely the Single-Step' regime (I) at low Ca and the Single-Jet' regime (V) at high Ca, which agree quantitatively to[12,13]. However, upon increasing the rescaled filament width $w_{1\infty}/b$, which can be achieved using Geometry A with a wider and more shallow terrace, the above described additional breakup regimes emerge between the bracketing 'Single-Step' (I) and 'Single-Jet' (V) regimes. In the following, the additional breakup

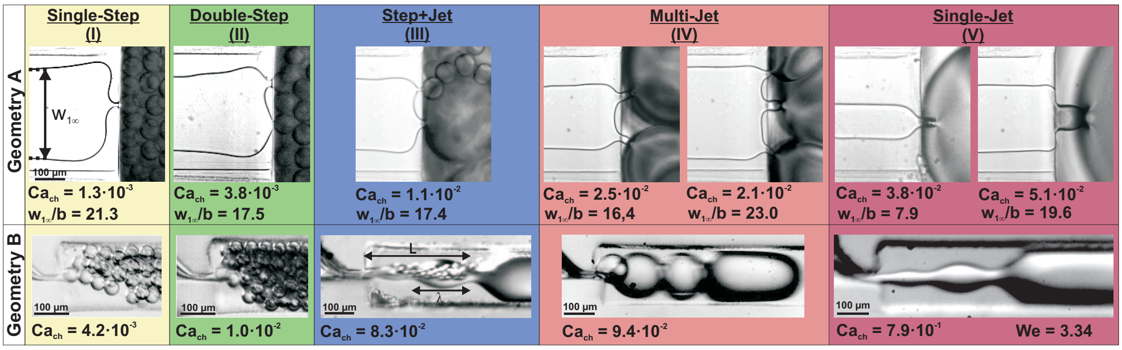

Fig. 2 Micrographs showing the different breakup-regimes for step geometries of vertical (Geometry A) and horizontal orientation (Geometry B) (cf. 'Experimental Section'). Top row: images taken from Geometry A ($w/b = 30$) Bottom row: images taken from Geometry B at a fixed $Q_1/Q_2 = 0.5$. The two micrographs from Geometry A in regime IV show the coexistence of two and three jet-instabilities on one filament at comparable Ca_{ch} and different $w_{1\infty}/b$. In regime V, micrographs from Geometry A show filament shapes with and without strong capillary focusing at low and high $w_{1\infty}/b$, respectively.

regimes occurring for $w_{1\infty}/b > 12$, i.e. regime II to IV and in particular their transitions will be explored in more detail.

2.2 Step-instabilities: transitions from regimes I to III

When reaching the topographic step, the initially straight filament interface is deformed locally due to capillary focusing (see first column Fig. 2). For a step-instability, a droplet starts to form when the filament front is pushed over the topographic step. After droplet pinch-off, the filament retracts shortly behind the step. For small Ca or sufficiently small $w_{1\infty}/b$, only a single step-instability is observed (regime I). For larger $w_{1\infty}/b$, the front of the filament is almost flat at the topographic step in agreement with the typical flow profile in Hele-Shaw cells. Such a wide and flat interface offers sufficient space for a second instability to occur in regime II, without imposing strong local curvatures and without a large penalty in interfacial energy. Using a similar device geometry with terrace aspect ratio >192, but without co-flow of continuous and dispersed phase, van Dijke et al.[26] reported spontaneous droplet breakup at multiple locations evenly spaced along a filament interface. They explain the regular distance between the breakup locations by steep local pressure gradients present at the droplet breakup sites, which was confirmed by CFD-simulations. Although no co-flow of the continuous phase is present in the work of van Dijke et al.[26], the same basic mechanisms are speculated to cause the emergence of regime II at low flow rates in our experiments, cf. also SI. However, van Dijke et al.[26] only observed one type of droplet producing instabilities.

Regime II is stable until Ca exceeds another threshold at

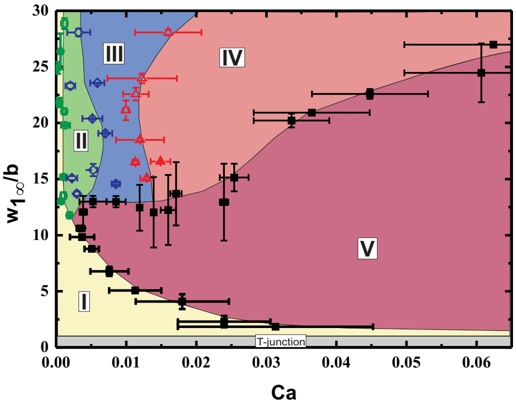

Fig. 3 'Phase-like' diagram of the different droplet breakup mechanisms. Symbols denote the transition between different breakup mechanisms which are derived from the average mean of the closest data points where the respective breakup mechanisms could be clearly identified. Error bars denote the difference between these points, i.e. the range where the breakup fluctuates between adjacent regimes. For $w_{1\infty}/b \leq 1$, droplet breakup occurs at the inlet by a mechanism comparable to a microfluidic T-junction. The different breakup regimes are shaded in the same color code and labeled with the same numbering as the respective column in Fig. 2.

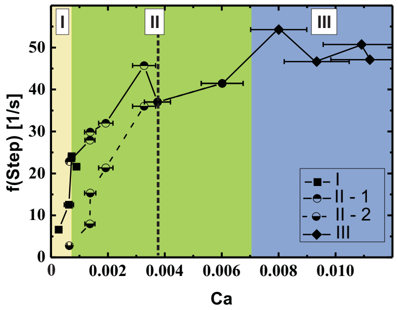

Fig. 4 Frequencies of step-instabilities in regimes I, II, and III. Error bars denote Gaussian error estimates. In regime III, only the maximum observed frequencies are displayed. Data measured at $Q_1/Q_2 = 1$, *i.e.* for a filament width of $w_{1\infty}/b = (19 \pm 2)$. The same qualitative behavior was observed for all tested flow rate ratios.

$Ca \approx 0.008$, where one of the step-instabilities switches to jetting. In regime III, step- and jet-instabilities coexist on a single filament producing two distinct droplet families of significantly different droplet size, cf. also SI. Such a phenomenon has not been reported before under symmetric boundary conditions. The frequency of the droplet production by step-instabilities is plotted as function of Ca for a fixed flow rate ratio, *i.e.* a fixed $w_{1\infty}/b$, in Fig. 4 to characterize the transition from regime II to III. In regime I, this frequency increases linearly with Ca, cf. also Priest et al.[12]. After the onset of a second step-instability, i.e. in regime II, the frequency of the existing step-instability grows slower with Ca as compared to regime I (top-filled circles in Fig. 4). However, the frequency of the second step-instability (bottom-filled circles in Fig. 4) grows significantly faster up to $Ca \approx 0.0037$ (cf. dashed vertical line in Fig. 4). At $Ca \gtrsim 0.0037$ both step-instabilities reach the same frequency and droplet production is strictly alternating between both sites. For further increasing Ca the droplet production frequency remains about constant, reaching an upper limit. Also, the diameter and polydispersity of droplets produced by step-instabilities were found to suddenly increase with growing Ca, close to the transition to regime III, cf. SI for further details. This contrasts the constant droplet diameters typically observed in step-emulsification for a given flow rate ratio. For further increasing flow rate, ultimately one of the step-instabilities switches to jetting, entering regime III. This transition occurs similarly to the transition from regime I to V at low $w_{1\infty}/b$[13,15] and an asymmetric droplet breakup behavior occurs at fully symmetric flow conditions, cf. Fig. 5. While large and polydisperse droplets are released by the jet-instability, the diameter and polydispersity of droplets emitted by the step-instability decrease again, indicating a relaxation of the step-instability, cf. SI for details.

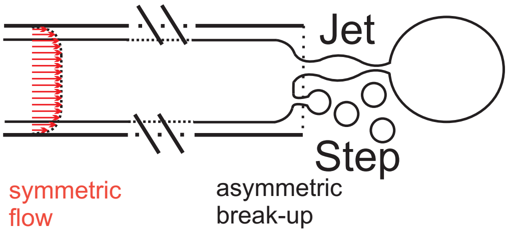

Fig. 5 Sketch illustrating the breaking of symmetry in regime III.

In regime III, the maximum frequency of the remaining step-instability remains about constant with increasing Ca. Here, the step- and jet-instability interfere with each other and the frequency of the occurring step-instabilities fluctuates depending on the position of the jet and crowding in the reservoir. Thus, only the maximum frequency of the step-instability in regime III is displayed in Fig.4, as we are interested in an upper bound only. However, the scatter of the maximum frequency was always found to be below 15 %.

For further increasing Ca also the remaining step-instability switches to jetting. This transitions to regime IV as well as the subsequent transition to regime V are determined by the properties of the jet-instabilities. Thus, the jet-instabilities will be characterized in the following.

2.3 Jet-instabilities: transitions from regimes III to V

For a jet-instability, a droplet is formed at the tip of the jet that grows until it is released downstream in the reservoir. During droplet formation, the liquid jet elongates while the droplet is traveling downstream in the reservoir. During this elongation, the jet starts to bulge and collapses after a certain length, releasing the droplet; subsequently the jet retracts and the entire droplet formation starts over again.

For the following discussion, the jets are observed in the horizontal step devices (Geometry B). As explained in the experimental section, crowding and buoyancy effects are reduced in Geometry B as droplets are immediately advected downstream, even at low volumetric flow rates. Thus, jets in the reservoir suffer less disturbance and are observed more clearly. However, the filament width cannot be seen in Geometry B as the terrace is rotated by 90° compared to Geometry A. Thus the following characterization is based on the Capillary Number Ca_{ch} calculated from the total volumetric flow determined externally by the syringe pumps and the terrace geometry. The analyzed jet length as function of Ca_{ch} shown in Fig. 6 is obtained for a constant flow rate ratio $Q_1/Q_2 = 1.5$. A constant flow rate ratio provides an approximately constant filament width and thus an approximately linearly scaling of Ca_{ch} with Ca. The displayed behavior in Fig. 6 is qualitatively also valid for other flow rate ratios. In regime III, the jet length L increases linearly with increasing Ca_{ch} and bulges with a wavelength λ. This wavelength λ plateaus at λ_{max} for $Ca_{ch} \gtrsim 0.066$ (dashed vertical line), see Fig. 6b. Measuring the maximum wavelength λ_{max} rescaled with the initial jet radius R_0 at the topographic step for several flow rate ratios ranging from 0.5 to 2, we find an average value of $\lambda_{max}/R_0 = 11 \pm 2$(SD). This value agrees well with the Rayleigh-Plateau wavelength of a cylindrical jet in a viscid surrounding for a similar viscosity ratio[27]. For jet length shorter than λ_{max}, the Rayleigh-Plateau instability is suppressed and droplets are most probably released due to viscous drag by the continuous phase and the increased pressure caused by the forming droplet blocking nearly the entire cross-section[28–30]. However, when the jet-length L exceeds λ_{max}, a second bulge develops and the jet is long enough to be destabilized by a Rayleigh-Plateau like instability. Thus, an upper limit of the volume throughput for the jet-instability is established. When further increasing the flow rate, the transition to regime IV occurs at $Ca_{ch} > 0.082$ shortly after λ has reached its plateau value λ_{max}. The coexisting step-instability, which already operates at maximum frequency, switches to jetting to release more volume over time. Measuring the growth and retraction times of jets additionally confirms this reasoning, confer Supplemental Information.

In the center of Fig. 6a the maximum length of both jets in regime IV is plotted as a function of Ca_{ch}. The length of the longer jet increases with Ca_{ch} while the second jet length remains constant at a length below the characteristic Rayleigh-Plateau wavelength. Note however, that superposing jets and droplets mask and strongly influence each other and are thus hard to be observed optically. Furthermore, the droplets forming at the tip of each jet span nearly the entire reservoir cross-section and deform the jet of the neighboring instability. Thus, both jet-instabilities interfere with each other, possibly breaking jets before the characteristic wavelength of the Rayleigh-Plateau instability is reached, cf. Fig. 2.

Increasing the Capillary Number above another threshold, the multiple jets collapse to a single jet. A single jet, i.e. regime V, is found irrespective of the filament aspect ratio $w_{1\infty}/b$, provided the Capillary Number Ca is sufficiently large (see Fig. 2 and 3). For $w_{1\infty}/b \lesssim 12$ a transition from regime I to V occurs and a strong capillary focusing is observed in the terrace channel, causing the filament to narrow down to a neck before the topographic step, as described previously[12–14]. For $w_{1\infty}/b \gtrsim 12$ a transition between regime IV and the 'Single-Jet' regime (V) occurs. This transition is shifted to larger Ca with increasing $w_{1\infty}/b$.

Within regime V, the filament shape at the step changes significantly with increasing $w_{1\infty}/b$, cf. Fig. 2: The capillary fo-

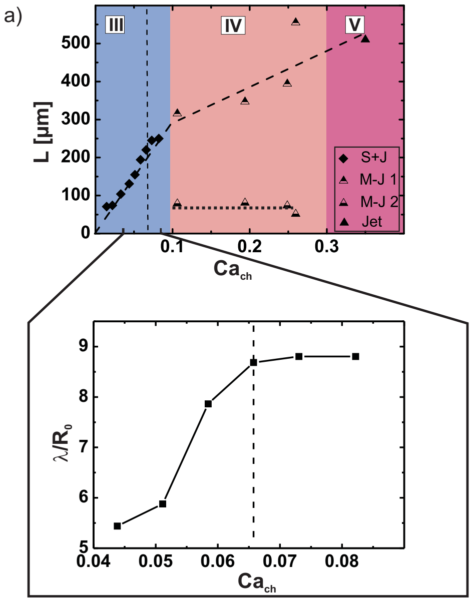

Fig. 6 a) Maximum length of jets before breakup measured in regimes III, IV, V. b) Wavelength λ (cf. Fig. 2) of a bulging jet in regime III rescaled in units of initial jet-radius R_0 at the topographic step. Vertical dashed lines denote $Ca_{ch} = 0.066$. All data are obtained for a fixed $Q_1/Q_2 = 1.5$. Error bars are below symbol size for jet length. Errors for λ/R_0 are on the order of 20% due to pixel resolution limiting the precision of measurement of initial jet radius.

cusing on the terrace is reduced for wider filaments and the filament is pushed over the step with almost its full width. A single jet of a much larger initial radius than the terrace channel height *b* is formed in the reservoir. The average radius of the bulging jet increases along the jet length. Droplet pinch-off can be followed by pinch-off of the largest bulge, forming a smaller satellite droplet, see SI 1. The transition from regime IV to V is speculated to be stimulated by inertia of the dispersed phase counteracting the capillary focusing on the terrace. The increase of jet radius along its length in regime V additionally hints towards an influence of inertia[31]. Indeed, within regime V, both the Reynolds Number $Re = \rho_1(Q_1 + Q_2)/(w\mu_1)$ and the Weber Number of the jet $We = 2\rho_1 Q_1^2/\gamma\pi^2 R_0^3$ exceed unity, indicating that inertia cannot be neglected despite the small system dimensions[31,32].

3 Conclusion and outlook

Compared to the already studied Step-emulsification device with small terrace width, a plethora of droplet generation instabilities can be found for wide terrace widths, respectively wide dispersed phase filaments. We identified and characterized the emerging droplet generation regimes on a liquid filament upon release of confinement. Most of these regimes present several coexisting droplet generation sites on the same filament. In particular, an asymmetric situation with different types of instabilities could be observed. Key physical principles based on minimization of interfacial energy, upper bounds for the volume throughput of each instability and inertia effects are suggested which are responsible for the transitions between the different regimes and which allow to control the emergence of a desired breakup regime. A quantitative theoretical modeling of the individual breakup regimes remains for future studies but seems quite challenging as internal symmetry, that is commonly used to model multiphase flows and droplet breakup in shallow channels, cannot be assumed a priory. Additionally, the cross-talk between the individual instabilities and inertia effects have to be considered.

Besides being of fundamental scientific interest, the found breakup regimes are also of technical relevance. By just varying flow parameters, different droplet species can be generated in parallel at several sites from a single filament. Volumes of the two droplet species in in regime III can easily differ by two to three orders of magnitude, ranging from tenth of nanolitres to picolitres, cf. Geometry B in SI 1. The found breakup regimes also allow to specifically encapsulate dispersed micro- or nano-particles or cells into one family of droplets. The latter is achievable by focusing the small objects to one side of a confined liquid filament using buoyancy effects, hydrodynamic forces or available active techniques using external fields. Figure 7 and movie SI 4 show simultaneous concentration and encapsulation of sedimenting PMMA particles for asymmetric droplet breakup in regime III and symmetric breakup behavior in regime IV. In both examples the particle concentration efficiency is on the order of 100%.

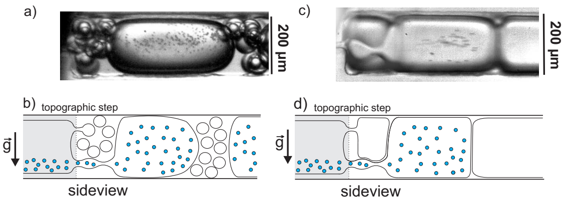

Fig. 7 Example of a selective one-step encapsulation of sedimenting PMMA (Ø4 μm) particles in Geometry B. a) Micrograph showing encapsulation of particles into large drops, while excess liquid is dispersed into small drops (topview) and b) sketch (sideview). c) Micrograph showing encapsulation of particles and excess liquid into droplets of similar volumes (topview) and c) sketch (sideview).

The generation of emulsions of two distinct droplet families of different size in regime III might be most interesting as small objects can be concentrated in either very small or very large droplets, which can be subsequently separated by passive techniques like an asymmetric y-junction. However, to specifically concentrate particles in smaller or larger droplets requires control of the position of the respective droplet production instability. The position of the particular instability can be possibly controlled by asymmetric terrace geometries with a tapered cross section, e.g. fabricated using the method presented by Dangla et. al.[19] or by taking advantage of the typical undercut of negative photo resist when generating the master for the microfluidic device.

4 Acknowledgments

Authors gratefully acknowledge the DFG-GRK1276 for financial support and Sabrina Haefner (Saarland University), Shahriar Afkhami (New Jersey Institute of Technology) and Kari Dalnoki-Veress (McMaster University) for inspiring discussions.

References

1 L. Rayleigh *Proc London Math Soc*, **1878**, *10*, 4.
2 L. Kondic, J. A. Diez, P. D. Rack, Y. Guan and J. D. Fowlkes, *Phys Rev E*, **2009**, *79*, 026302.
3 J. D. Fowlkes, N. A. Roberts, Y. Wu, J. A. Diez, A. G. González, C. Hartnett, K. Mahady, S. Afkhami, L. Kondic and P. D. Rack, *Nano Lett*, **2014**, *04*, 774-782.
4 A. M. Gañán-Calvo, R. Gonzáles-Prieto, P. Riesco-Chueca, M. A. Herrada and M. Flores-Mosquera, *Nature Phys*, **2007**, *3*, 737-742 .
5 B. De Heij, B. Van der Schoot, H. Bo, J. Hess and N. F. De Rooij, *Sensor Actuat A*, **2000**, *85*, 430-434.

6 L. Lin, W. He, *Proceedings of Digital Fabrication 2006, Denver*, **2006**, *2*, 98.

7 A. Vailati, L. Zinnato and R. Cerbino, *PLOS One*, **2012**, *7(10)*, e47867.

8 A. M. Nightingale, T. W. Phillips, J. H. Bannock and J. C. de Mello, *Nature Comm*, **2014**, *5*, 3777.

9 S. L. Anna, N. Bontoux and H. A. Stone, *Appl Phys Lett*, **2003**, *82*, 364.

10 G. F. Christopher and S. L. Anna, *J Phys D*, **2003**, *40*, R319-R336.

11 R. Seemann, M. Brinkmann, T. Pfohl, and S. Herminghaus, *Rep Prog Phys*, **2012**, *75*, 016601.

12 C. Priest, S. Herminghaus and R. Seemann, *Appl Phys Lett*, **2006**, *88*, 024106.

13 M. Hein, S. Afkhami, R. Seemann and L. Kondic, *Microfluid Nanofluid*, **2014**, DOI: 10.1007/s10404-014-1481-0.

14 F. Malloggi, N. Pannacci, R. Attia, F. Monti, P. Mary, H. Willaime, P. Tabeling, B. Cabane and P. Poncet *Langmuir*, **2010**, *26 (4)*, 2369-2373.

15 Z. Li, A. M. Leshansky, L.M. Pismen and P. Tabeling, *Lab Chip*, **2015**, *15*, 1023-1031 .

16 K. J. Humphry, A. Ajdari, A. Fernández-Nieves, H. A. Stone, and D. A. Weitz, *Phys Rev E*, **2009**, *79*, 056310.

17 L. Shui, A. van den Berg and J. C. T. Eijkel, *Microfluid Nanofluid*, **2011**, *11*, 87-92.

18 R. Dangla, E. Fradet, Y. Lopez, and C. N. Baroud, *J Phys D*, **2013**, *46*, 114003.

19 R. Dangla, S. Cagri Kayi and C. N. Baroud, *Proc Natl Acad Sci USA*, **2013**, *110 (3)*, 853-858.

20 V. Chokkalingam, R. Seemann, B. Weidenhof and W. F. Maier, in *Advances in Microfluidics*, ed. by R. Kelly, Intech, *77*, **2012**, ISBN 978-953-51-0106-2.

21 D. McClements, *Nanoparticle- and Microparticle-based Delivery Systems: Encapsulation, Protection and Release of Active Compounds*, **2014**, CRC Press, ISBN: 978-1482233155.

22 H. Q. Yang, *Phys Fluids A*, **1992**, *4(4)*, 681-689.

23 J. Guerrero, J. Rivero, V. R. Gundabala, M. Perez-Saborid and A. Fernández-Nieves, *Proc Natl Acad Sci USA*, **2014**, *111(38)*, 13763-13767.

24 D. C. Duffy, J. C. McDonald, O. J. A. Schueller and G. M. Whitesides, *Anal Chem*, **1998**, *70 (23)*, 4974-4984.

25 P. Guillot, A. Colin and A. Ajdari, *Phys Rev E*, **2008**, *78*, 016307.

26 K. van Dijke, R. de Ruiter, K. Schroen and R. Boom, *Soft Matter*, **2010**, *6*, 321-330.

27 S. Tomotika, *Proc R Soc Lond A*, **1935**, *150*, 322-337.

28 V. Labrot, M. Schindler, P. Guillot, A. Colin and M. Joanicot, *Biomicrofluidics*, **2009**, *3 (1)*, 012804.

29 P. A. Romero and A. R. Abate, *Lab Chip*, **2012**, *12*, 5130-5132.

30 P. Garstecki, M. J. Fuerstman, H. A. Stone and G. M. Whitesides, *Lab Chip*, **2006**, *6*, 437-446.

31 A. S. Utada, A. Fernández-Nieves, H. A. Stone and D. A. Weitz, *Phys Rev Lett*, **2007**, *99*, 094502.

32 W. Lee, H. Amini, H. A. Stone, and D. Di Carlo, *Proc Natl Acad Sci USA*, **2010**, *107, 52*, 22413-22418.

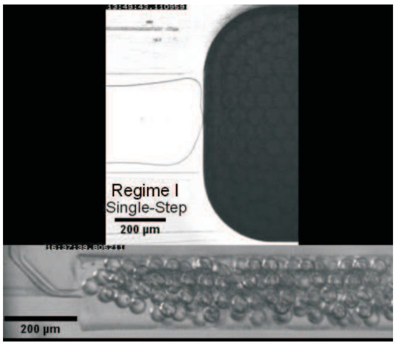

SI 1 Overview of the different breakup regimes by example movies taken in the two geometries used. Top row: Geometry A ($w/b = 30$) Bottom row: Geometry B. Movies recorded at different framerates, cf. timestamp.

SI 1: Overview

SI 2: A closer look to transitions

Regime I to II

Although only two step-instabilities were observed at a time in our experiments, it is assumed that additional step-emulsification sites can emerge on filaments with even larger aspect ratio. Using a similar device geometry with terrace aspect ratio >192 but without co-flow of continuous and dispersed phase van Dijke et al.[26] reported droplet breakup at multiple locations evenly spaced along a filament interface with an average spacing of $\approx 25 \cdot b$. The regular distance between the breakup locations is determined by steep local pressure gradients present at the droplet breakup sites and the terrace height b, as was confirmed by CFD-simulations. The typical distance between the two droplet formation sites in our experiments is in the range of $(7-16) \cdot b$. The different spacing of droplet formation sites observed in this study presumably originates from the enhanced horizontal filament confinement with filament width always below $30 \cdot b$.

Regime II to III

Average diameters of droplets produced in regimes I to III are displayed in Fig. SI 2 to additionally support the argument of a maximum volume throughput achievable by step-instabilities causing the transition to regime III. Droplet diameters were measured directly from the recorded time series. Typically 20-50 droplets produced by step-instabilities and 15-25 droplets produced by jet-instabilities were measured, depending on experimental conditions. The error bar denotes the standard deviation, indicating droplet polydispersity.

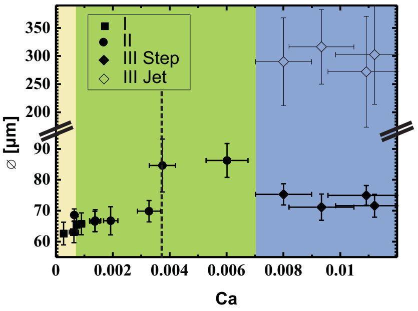

SI 2 Droplet diameter of step- and jet-instabilities. Data are mean ± SD indicating the droplet polydispersity. Data was measured at $Q_1/Q_2 = 1$, *i.e.* for a filament width of $w_{1\infty}/b = (19 \pm 2)$.

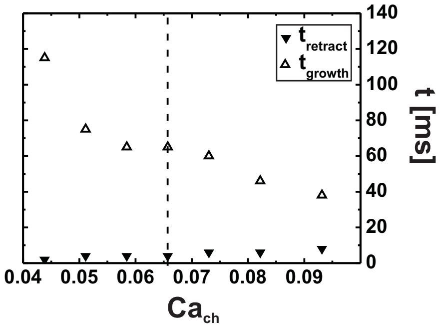

SI 3 Growth and retraction times of jets in regime III as a function of Ca_{ch}. Vertical dashed line denotes $Ca_{ch} = 0.066$. Data is obtained for a fixed $Q_1/Q_2 = 1.5$. Error bars are below symbol size.

Within regime I and II only step-instabilities occur. Up to $Ca \approx 0.0037$, droplet diameters remain constant within experimental uncertainty, irrespective of the transition to regime II, cf. filled symbols in Fig. SI 2. At $Ca \approx 0.0037$, the droplet production frequencies of the two step-instabilities in regime II synchronize (cf. dashed line in Fig. 4 and Fig. SI 2). Simultaneously, both droplet diameters and polydispersity suddenly increase while the droplet production frequency remains about constant with increasing Ca. This sudden change of behavior indicates destabilization of the step-instabilities that reach their upper threshold of the volume throughput, which ultimately causes the transition to the next regime.

After the transition to regime III has occurred, diameters of droplets generated by step-instabilities decrease again, cf. filled diamonds in Fig. SI 2, while the maximum observed frequency of droplet production by step-instabilities remains constant, cf. Fig. 4. This indicates, that more volume over time is released by the emerging jet-instability, allowing the remaining step-instability to relax while operating close to its maximum frequency.

Droplets produced by jet-instabilities are significantly larger and were found to be polydisperse, as characterized in Geometry A and displayed by hollow diamonds in Fig. SI 2. This polydispersity is caused by the irregular droplet detachment due to collisions and deformations of the growing droplet by crowding in the reservoir, see also SI 1.

Regime III to IV

To further characterize the transition between regime III and IV, the growth and the retraction time of a jet with in regime III is plotted as a function of Ca_{ch} in Fig. SI 3. The retraction time represents the time of the capillarity driven retraction of the jet after droplet pinch off, whereas the growth time determines the time the jet needs to elongate before a droplet is released. The growth time is significantly reduced with increasing Ca_{ch} while the retraction time only slightly increases. Both time scales approach each other upon reaching the transition to regime IV. Presumably, the strong reduction of the growth time originates from the increased flow rate and the onset of the Rayleigh-Plateau instability. The shortening of the lifetime of jets sets an upper limit of the volume throughput a jet-instability can perform. For further increased flow rates the coexisting step-instability, which already operates at maximum frequency, switches to jetting to release more volume over time. After this transition two jet-instabilities appear on the same liquid filament and regime IV is reached.

SI 3: Particle concentration

SI 4 Video exemplifying the simultaneous concentration and encapsulation of PMMA particles (Ø4 µm) by coexistence of step- and jet-instabilities on a single filament in Geometry B.

Addendum III: Template-Free Preparation of Platinum Doped Silica Catalyst Microspheres Through a Microfluidic Scheme

Proceedings of the 2nd European Conference on Microfluidics (Microfluidics 2010), Toulouse, France, μFLU10-168, (2010).

Authors: V. Chokkalingam[1], B. Weidenhof [2], M. Hein[1], W.F. Maier[2] and R. Seemann[1,3]

[1] Department of Experimental Physics, Saarland University, Saarbrücken, Germany
[2] Technical Chemistry, Saarland University, Saarbrücken, Germany
[3] Dynamics of Complex Fluids, MPI for Dynamics and Self-Organization, Göttingen, Germany

Author Contributions:

Experiments were performed by V. Chokkalingam and B. Weidenhof. Data was analyzed by V. Chokkalingam and B. Weidenhof. Article was written by V. Chokkalingam. Writing was supervised by B. Weidenhof, M. Hein, W. Maier, and R. Seemann. Research was directed by W. Maier, and R. Seemann. The presentation at the conference was prepared and given by M. Hein.

Abstract:

A novel droplet-based microfluidic scheme is developed to perform chemical reactions. The chemical reactants are dispensed with precise volume control into pairs of droplets produced via step-emulsification. The reaction is activated by merging the pairs of droplets by a geometrical constriction and fast mixing inside the merged droplets. Furthermore, the post-processing of the chemical products is also included within the microfluidic device. This microfluidic reaction scheme allows performing precisely volume controlled reactions with long and stable operation conditions without any clogging even if precipitates or sticky gels are formed during the reaction. We demonstrate the potential of our microfluidic scheme by producing mesoporous platinum doped silica particles from a rapid gelation optimized sol-gel synthesis route. The produced particles have a superior surface area of about $600 m^2/g$, a narrow pore radius distribution around $1.9\,nm$ and superior catalytic behavior than commercially available industrial catalysts.

Proceedings of the 2nd European Conference on Microfluidics - Microfluidics 2010 - Toulouse, December 8-10, 2010

µFLU10-168

TEMPLATE-FREE PREPARATION OF PLATINUM DOPED SILICA CATALYST MICROSPHERES THROUGH A MICROFLUIDIC SCHEME

Venkatachalam Chokkalingam[1], Boris Weidenhof[2], Michael Hein[1], Wilhelm F. Maier[2], and Ralf Seemann[1,3] *

[1] Experimental Physics, Saarland University, 66123 Saarbruecken, Germany
[3] Max Planck Institute for Dynamics and Self-Organization, 37073 Goettingen, Germany
venkat.chokkalingam@physik.uni-saarland.de, r.seemann@physik.uni-saarland.de

[2] Technical Chemistry, Saarland University, 66123 Saarbruecken, Germany.
b.weidenhof@mx.uni-saarland.de, w.f.maier@mx.uni-saarland.de

KEY WORDS

emulsions, microreactors, catalyst particles, surface area, microfluidics.

ABSTRACT

A novel droplet-based microfluidic scheme is developed to perform chemical reactions. The chemical reactants are dispensed with precise volume control into pairs of droplets produced via step-emulsification. The reaction is activated by merging the pairs of droplets by a geometrical constriction and fast mixing inside the merged droplets. Furthermore, the post-processing of the chemical products is also included within the microfluidic device. This microfluidic reaction scheme allows performing precisely volume controlled reactions with long and stable operation conditions without any clogging even if precipitates or sticky gels are formed during the reaction. We demonstrate the potential of our microfluidic scheme by producing mesoporous platinum doped silica particles from a rapid gelation optimized sol-gel synthesis route. The produced particles have a superior surface area of about 600 m^2g^{-1}*, a narrow pore radius distribution around 1.9 nm and superior catalytic behavior than commercially available industrial catalysts.*

1. INTRODUCTION

Flow in microfluidic channels typically occurs at low Reynolds numbers (*Re*), such that the flow is purely laminar. Due to this laminar flow, two or more streams flowing adjacent or side-by-side will mix only by diffusion. Such a mixing is very slow to perform chemical reactions within the length scales typically used in microfluidic systems. They require specially designed microfluidic channels (*e.g.* winding channels) to achieve mixing [1-3]. Thus, there has been considerable development towards the use of isolated dispersed phase droplets suspended in an immiscible continuous phase which allows to perform chemical reactions with minute amounts of reactants by fast mixing within the droplets [4-6].

In initial approaches using droplets as microreactors, the different reactants were commonly dispensed into droplets from a single inlet channel. In this method, the reagents are already in contact and reactive at the inlet channel even before being dispersed into droplets. The method of common dispensing will result in channel clogging and is not suitable for fast chemical reactions where a gel or precipitate is formed within

---

* Corresponding author

milliseconds of contact [7,8]. If long and stable operation conditions are not desired, this problem can be avoided by initiating the reaction by merging two droplets inside a microfluidic channel.

In the present paper, we explore a droplet-based microfluidic scheme to perform fast chemical reactions without channel clogging with precise volume and process control. This microfluidic scheme enables the device to function for long operation times with stable conditions. For that every microfluidic processing step is considered and adapted to meet the experimental requirements. We demonstrated this scheme explicitly for the production of platinum doped silica particles from a sol-gel synthesis route for heterogeneous catalytic purposes.

2. METHODS AND MATERIALS

2.1 Device Fabrication

Soft lithographic techniques [9,10] were used to fabricate micro channels with rectangular cross sections with typical channel dimensions of 120 µm in depth and 160 µm in width. The microfluidics device was molded against a SU-8 photo resist structure on a silicon wafer using a commercially available Poly (dimethylsiloxane) (PDMS) silicone elastomer (Sylgard 184, Dow Corning, USA). The surface of the Sylgard 184 devices was OH-terminated by a plasma treatment (Diener electronic GmbH, Germany) and sealed with a plasma treated glass microscopy cover slide. The surfaces of the devices were rendered hydrophobic by heating the devices to 60 °C for at least 6 hours. The liquids were dispensed from gastight syringes (Hamilton Bonaduz AG, Switzerland), which were connected to the microfluidic device by Teflon tubing (Novodirect GmbH, Germany). The syringes were driven by home built computer controlled syringe pumps for accurate adjustment of the flow rates. In all of our experiments we used constant volumetric flow rates. Microphotographs were acquired with a high speed CMOS camera (PCO 1200hs or Photron SA-3).

2.2 Sol-Gel Chemistry

By simultaneous hydrolysis and polycondensation of an organometallic precursor [7,8] an interlinked 3D network is formed. The liquid alkoxide precursor tetramethoxysilane (TMOS) is acid-catalyses hydrolyzed by mixing it with water and nitric acid. The hydrolysis reaction replaces alkoxide groups (OCH_3) with hydroxyl groups (OH). Subsequent condensation reactions involving the silanol groups produce siloxane bonds (Si-O-Si) plus the by-products water. Reactions of additional $Si(OH)_4$ with the formed intermediates occur as a poly-condensation reaction and thereby result in the formation of a 3D SiO_2 network (SiO_2-gel). In the presented experiments the reaction time was minimized such that the gel formation was completed within the residence time of the droplets within the microfluidic device.

To achieve this chemistry inside microfluidic channels, we dispensed the chemicals into two groups of droplets. Droplets A contain an acidified solution of 1.5 M TMOS (ABCR GmbH & Co. KG) in a mixture of methanol (Merck KGaA, Darmstadt, Germany) and water (Millipore^{TM} water) along with $Pt(NO_3)_2$. Droplets B contain ammonia (Merck KGaA, Darmstadt, Germany) in the same mixture of methanol and water. To produce silica particles it is required to produce stable drops from the dispersed phases consisting of methanol and water (droplets A and B). Consequently, for these experiments a continuous phase in which neither water nor methanol is soluble is used. We used a perfluorinated oil consisting of PFD (perfluorodecalin $C_{10}F_{18}$, ABCR GmbH & Co. KG) with 20 wt.% of perfluorinated surfactant (penta decafluoro-1-octanol, $C_8H_3F_{15}O$, ABCR GmbH & Co. KG).

2.3 Specific Surface Area and Catalytic Activity

In our experiments, the specific surface area (m^2/g) and pore volumes (cm^3/g) of the solid materials was measured by a Brunauer-Emmet-Teller (BET) multipoint technique [11] using an automated gas adsorption analyzer (Carlo Erba Sorptomatic 1990). The produced samples (at least 200 mg to reduce the signal to noise ratio) were loaded and degassed at 200 °C for 2 h in vacuum, followed by surface area analysis at the temperature of liquid nitrogen (77 K) with N_2 as the adsorbate gas.

The catalytic activity of the produced metal doped particles is determined by two techniques: emissivity corrected infrared thermography (ecIRT) [12-14] for fast screening and conventional fixed bed reactor [15] for quantitative analysis. The primary idea of the ecIRT measurement is to display temperature differences on a library which are considered to be proportional to catalytic activity. Prior to the measurement, the library was pretreated at 380 °C for 30 min in synthetic air (O_2 and N_2 only) at 50 ml/min to evaporate water and oxidize volatile organic combustion residues if present. After that, a six-point temperature calibration was carried out in a range of 10 K in the area of -4 to +6 K around each specific reaction temperature and images were taken. To examine the catalytic activity of the library samples (for e.g. propane oxidation), the reactor was held at a constant temperature while different reaction gas mixtures passed successively through the system with a constant flow rate of 50 ml/min.

To quantify the catalytic activity, the active samples were tested in a conventional fixed bed reactor. The premixed reaction gas and synthetic air enters the conventional gas flow reactor with a total feed flow rate of 50 ml/min where about 100 mg of sampled is stored. A suitable operating temperature range for the reaction is selected and the temperature of the catalyst is controlled by a thermo-element during the combustion (reaction). The product gas is analyzed using gas sensors.

3. MICROFLUIDIC SCHEME

3.1 DROPLET PRODUCTION

To perform chemical reactions by merging or coalescing droplets inside a microfluidic device or to synthesize particles it is not just enough to produce one kind of monodisperse droplets we rather have to produce two types of monodisperse droplets (with appropriate reagents) in a strictly alternating manner. To produce two types of monodisperse droplets (with appropriate reagents) in a strictly alternating manner, we employ the technique of step-emulsification (see Figure 1) [16,17]. This technique utilizes the destabilizing of a quasi 2D stream of dispersed phase at a topographic 'step' and allows producing emulsions with an with excellent monodispersity (variance in volume < 4 %). A double step-emulsification device essentially is a combination of two single devices connected to a common inlet and outlet channel. It thus allows for the production of two distinct droplet families with a fixed number ratio of e.g. 1:1 while the monodispersity of each droplet family is maintained. (see Figure 2). Several droplets with precise volume control and adjustable production frequency are produced. The synchronization mechanism is very robust and makes the step-emulsification devices ideal for complex chemical reactions.

A time series of the droplet formation process is shown in Figure 2: When a droplet forms in one production unit (e.g. bottom channel in Figure 2a), the Laplace pressure of the forming drop decreases as its radius increases. This results in a pressure drop redirecting the continuous phase flow towards this production unit (bottom channel in Figure 3b,c). Simultaneously, the pressure in the main channel increases due to the injected dispersed phase pushing the already formed stream of dispersed phase back into the other channel (top channel in Figure 2b,c). After the droplet pinched-off into the main channel, the Laplace pressure changes rapidly and the stream of the dispersed phase retracts into the bottom channel (Figure 2d). This, in turn, accelerates the dispersed phase in the top channel (Figure 2e). Next, a droplet will be formed at this channel outlet and the cycle is repeated. This pressure cross talk between the individual production units synchronizes the drop production and leads to strictly alternating pairs of droplets (see Figure 3a). This alternating droplet production is very robust even up to about 300 droplets per second and works up to a dispersed phase volume fraction (Φ) of about 96% (see Figure 3b).

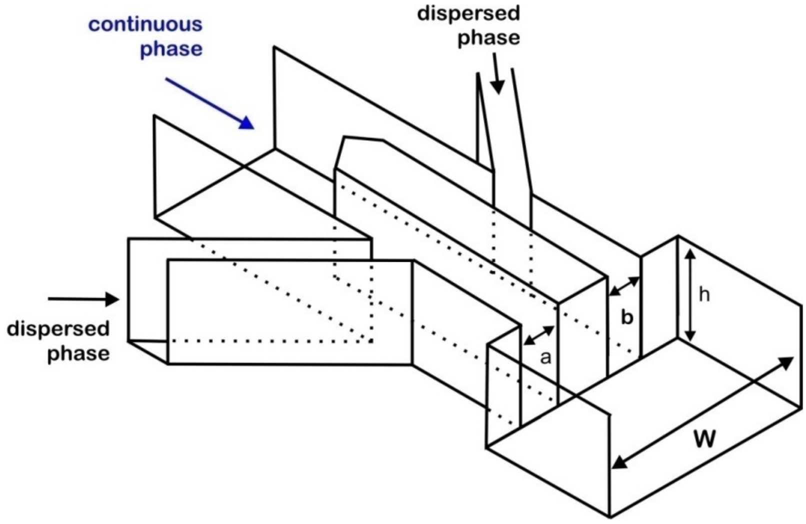

Figure 1. Schematic of the double step-emulsification device. The dimensions typically used in our experiments: a, b = 35 µm, h =120 µm and W = 160 - 420 µm.

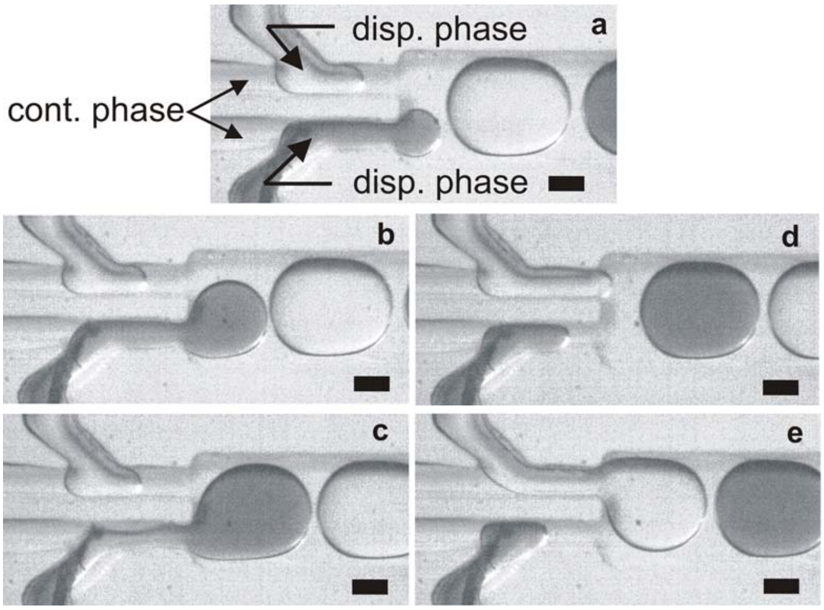

Figure 2. Time series of optical images displaying the droplet formation mechanism using a double step-emulsification device. For clarity, the aqueous phase entering the bottom production unit is dyed with nile blue. Scale bar: 50 µm.

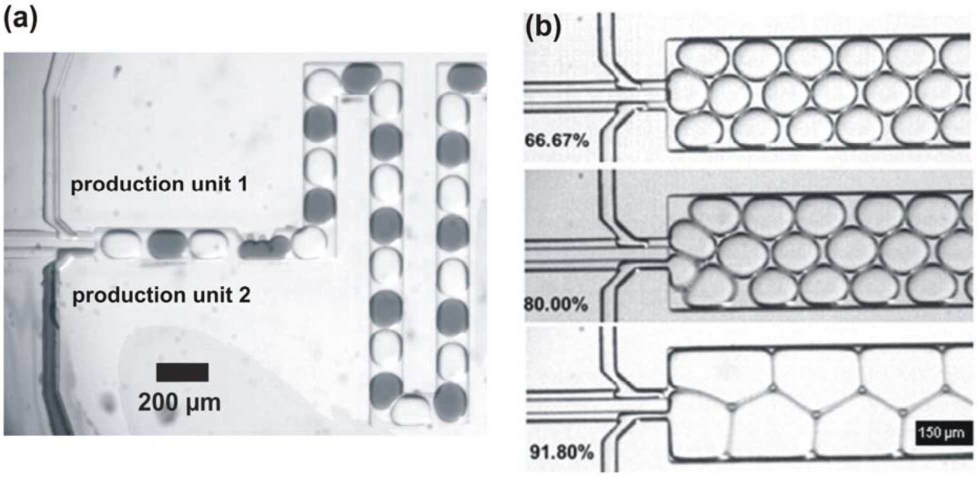

Figure 3. (a) Strictly alternating droplet generation with $d_1/d_2 = 1:1$; $v_1/v_2 = 1:1$ and $\Phi = 55$ %. (b) Droplet arrangement as a function of increasing dispersed phase volume fraction.

3.2 DROPLET MERGING

To account for the experimental needs, we developed a droplet merging technique where the aqueous droplet pairs can also be merged when they wanted to pass through a geometrical constriction. Such a merging technique works very effective for a system not stabilized with surfactants or with less effective surfactants i.e. surfactants that do not stabilize the emulsion very well. When the droplet pairs reach such a geometrical constriction, the merging of the two droplets is induced by slowing down the leading droplet at the constriction while the second droplet arrives and is pushed towards the first one. Depending on the exact paramerters the merging occurs either when the droplets are brought in contact or when the first droplet is flowing through the constriction during the re-separation of the two droplets. This technique has the lowest demands on the device fabrication and operation. Downstream mixing of the reagents proceeds very efficiently due to the twisty flow pattern inside the droplets generated by the flow induced friction of the surfactant lamellae with the channel walls.

Due to the particular concentration gradient present in case of merged droplets that are flowing behind each other, the mixing in the droplet is particularly fast as we will explain in the following. In case of a chemical gradient perpendicular to the flow direction mixing can be accelerated by repeatedly altering the symmetry of the flow pattern by back fold channel geometry. However, in the situation considered here, where two droplets are combined that are flowing behind each other, the resulting chemical gradient is along the flow direction and the symmetry of the concentration gradient does not need to be altered by a back fold or winding channel geometry. In this geometry the elongation of the merged droplet at the constriction and the followed expansion in the wider channel also promotes faster mixing.

In our experiments, two kinds of droplets were produced equally spaced but with different volumes; both droplets do not touch the sidewalls of the microfluidic channel (see Figure 4). Due to the parabolic flow profile, small droplets move to the center of the channel where they experience a larger mean flow velocity and travel faster than larger ones [18]. Accordingly, at a small distance downstream from the production unit, we find clearly separated droplet pairs where the larger droplet is leading and the smaller droplet is trailing behind. The coalescence occurs at the constriction as explained earlier.

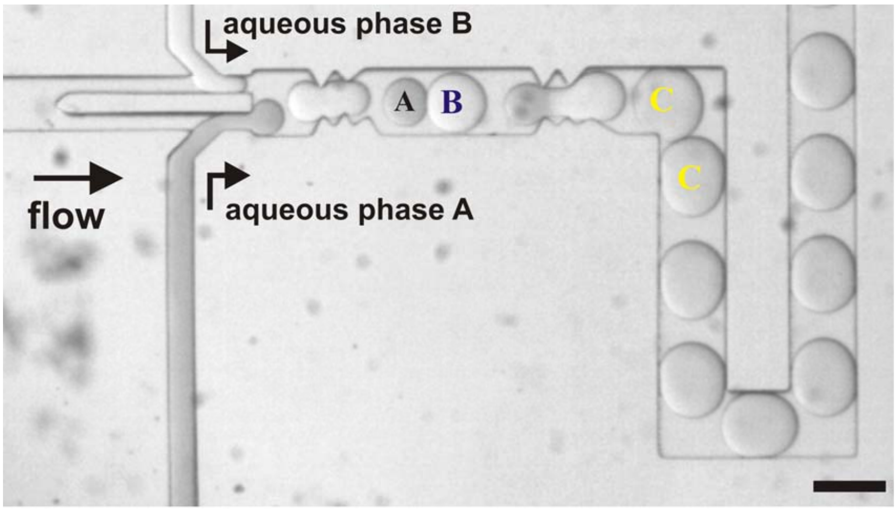

Figure 4. Optical micrograph showing the self-synchronized pair-wise production of different kinds of monodisperse droplets using a double step-emulsification device and the subsequent formation of separated droplet pairs and merging of two droplets at a geometrical constriction. The aqueous phase injected from the bottom channel is colored with nile blue for clarity. Scale bar: 200 µm.

4 PLATINUM DOPED SILICA CATALYSTS

We demonstrate the potential of our microfluidic scheme by producing mesoporous platinum doped silica particles from complex sol-gel precursor solutions with properties suitable for heterogeneous catalytic activities. The long and stable operation conditions of this reaction scheme allow producing sufficient quantities of the silica particles for quantitative analysis of their surface area and pore size. Furthermore, we characterize the microfluidically produced catalysts and compare them to commercially available products of identical chemical composition.

The two kinds of monodisperse droplets A and B were produced with different volumes (see Figure 5) for the sake of the subsequent droplet merging (droplet C) at the geometrical constriction as explained in the previous section. A rapid acid catalyzed hydrolysis of TMOS occurs in the aqueous solution A even before dispensing it into droplets A at pH 1-2. Because of the high molar ratio of Si:H_2O ($r > 10$) and the nearly nonexistent retarding effect of the methoxide group on the hydrolysis rate, a rapid and nearly quantitative hydrolysis of the precursor to silicic acid can be assumed within a few minutes [7]. The formation of the silica gel, however, is very slow at this pH range. To accelerate the condensation of silicic acid in our microfluidic synthesis route, we combined the TMOS containing droplets A with the ammonia containing droplets B to form droplets C and thereby adjust the pH to be between 6 and 7, above the iso-electric point of silica (pH > 3), where the gelation time is minimum [7,8] .

Mixing within the merged droplet C is performed within a travel distance of 500 µm, which corresponds to about twice the drop length, respectively within about 100 ms at a typical flow velocity of about 8 mm/s. To ensure that the pH of the droplets is not influenced by the large concentration of the fluoroalkyl groups of the surfactant [19], which might be also slightly soluble in the aqueous phase, we performed control experiments using the same microfluidic scheme, whereas a pH indicator was added to one of the droplets [Methyl red: red at pH below 4.4, yellow at pH over 6.2, and orange in between (see Figure 5a). Bromothymol blue: yellow at pH below 6, blue at pH over 7.6 and dark green in between (see Figure 5b)]. With these reactions we could confirm that the pH for our sol-gel reaction is in fact between 6.2 and 7.6 which is desired for faster gelation and can exclude a significant pH change by the large concentration of surfactant.

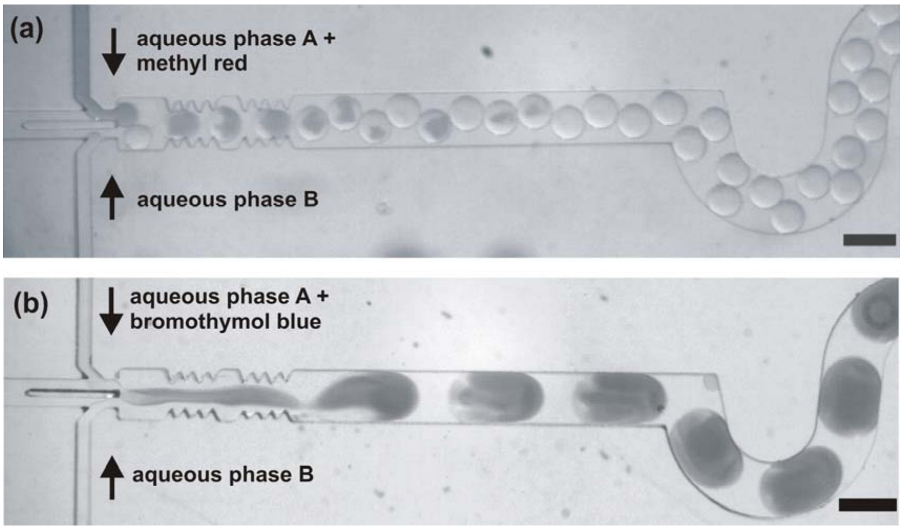

Figure 5. Control experiments to confirm that the pH of the droplets is in the desired range of pH 6 to 8 where the gel formation time is minimal and not influenced by the large concentration of the surfactant. Scale bar: 150 µm. (pH indicator: (a) methyl red (pH > 6.2), (b) bromothymol blue (pH < 7.6)).

The merged droplets C are subsequently given some time to develop the gel network in a delay line. In order to avoid the formation of clumps of silica gel at the rear side of the droplets [20] due to the motion induced twisty flow pattern inside the droplets, we reduce the flow velocity of the droplets in the delay line. Moreover, the emerging convective flow pattern in the merged droplet is further reduced since the droplets do not touch the side walls of the delay line. This is achieved by increasing the microfluidic channel width and guiding the gel particles into Teflon tubing with a cross sectional area which is more than ten times larger than that of the microfluidic channel. Also, to adapt our microfluidic scheme for this sol-gel synthesis and to ensure that the droplets do not undergo any unwanted coalescence events in the delay line or sticking to each other, the distance between the merged droplets C is increased by adding continuous oil phase after the back fold channels (see Figure 6), before entering the delay line.

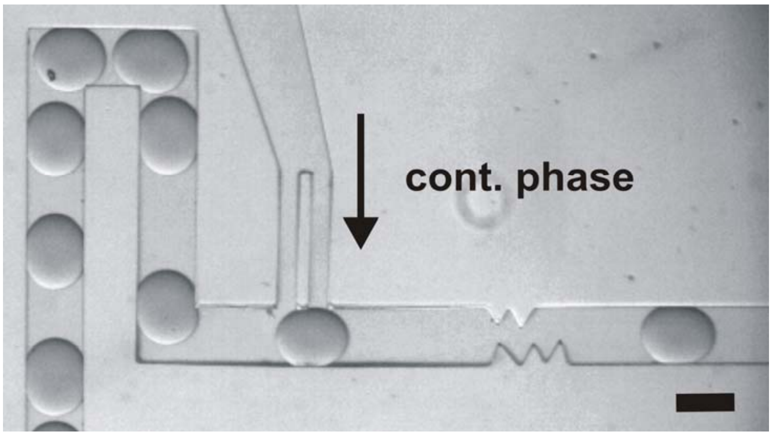

Figure 6. End of the back fold channel geometry with a side channel to inject continuous phase to increase the inter droplet distance. Scale bar: 150 µm.

The Teflon tubing is about 1 m in length and coiled up in a temperature controlled chamber at 65 °C, accelerating the gel formation and the removal of the solvent from the droplets. After a residence or flow time of about 20 min in the Teflon tubing, the monodisperse silica-gel particles are collected outside of this microfluidic device in a beaker containing the same perfluorinated continuous phase, which is also kept at the same temperature. In this beaker, the gel particles remain under continuous stirring for another 2 h, to ensure that the network formation has been completed and to gently evaporate remaining solvent. The collected gel particles are removed from the beaker and subsequently stored at room temperature for about 48 hours. To remove the remaining organics and surface absorbed species, the gel particles are calcined at an elevated temperature.

To determine the calcination temperature required for the synthesized silica gel particles a thermo-gravimetric analysis was performed using a TGA/DSC1 (Mettler-Toledo GmbH, Germany). It is important to determine an optimum temperature that is as high as needed to remove all organics but as low as possible not to densify the porous silica. The silica particles were filled into an alumina cup and heated at ramp rates of 10 °C/min from ambient temperature to 800 °C. The reference material was an empty alumina cup. A flow of synthetic air (O_2 and N_2 only) of 40 ml/min, was maintained during the experiment. Evolving gases were monitored online with a Balzers ThermoStar GSD 300 T quadrupole mass spectrometer. Figure 7 shows the recorded TGA curve. With mass spectrometer signals, the mass loss of the samples was mainly divided into two temperature regions: from ambient temperature to 120 °C water was evolved and between 120 to 550 °C perfluorodecalin (PFD) oil passed out at the lower temperatures (small peak between 120 °C to 250 °C in Figure 7) and combusted at higher temperatures leading to CO_2 desorption (small peak between 300 °C to 420 °C in Figure 7). As a result, a minimum temperature of about 500 °C is required for calcination to expel all volatile organic components completely from the silica gel particles. Accordingly, all the collected particles that were used for the analysis were calcined at a temperature of 550 °C. A close look at the surface morphology of these particles clearly shows a difference depending on the Pt concentration added. Scanning electron micrographs (Figure 8) of platinum doped silica particles revealed a cloudier surface morphology than silica particles without platinum doping.

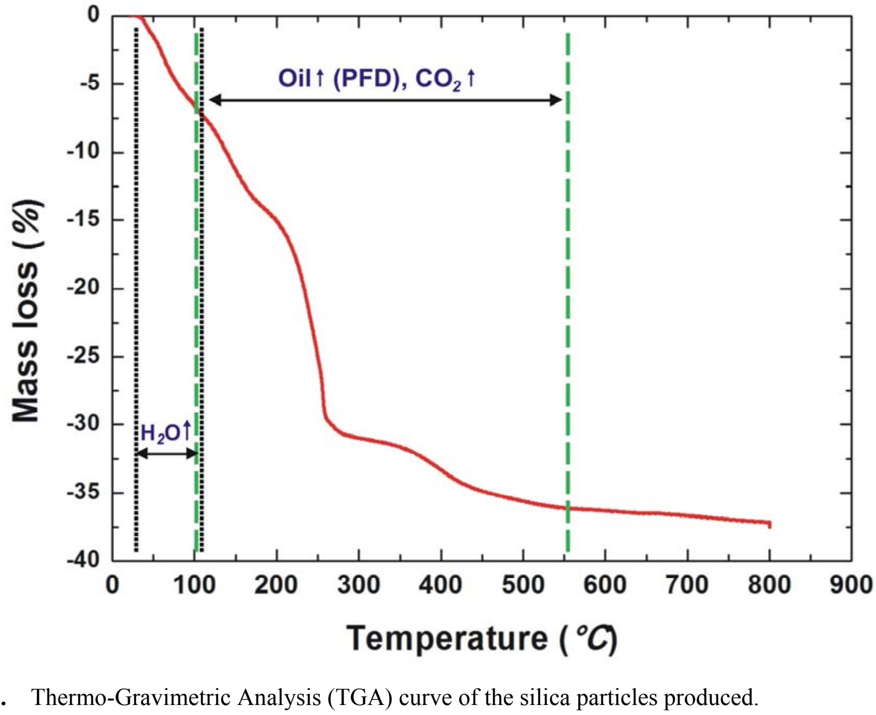

Figure 7. Thermo-Gravimetric Analysis (TGA) curve of the silica particles produced.

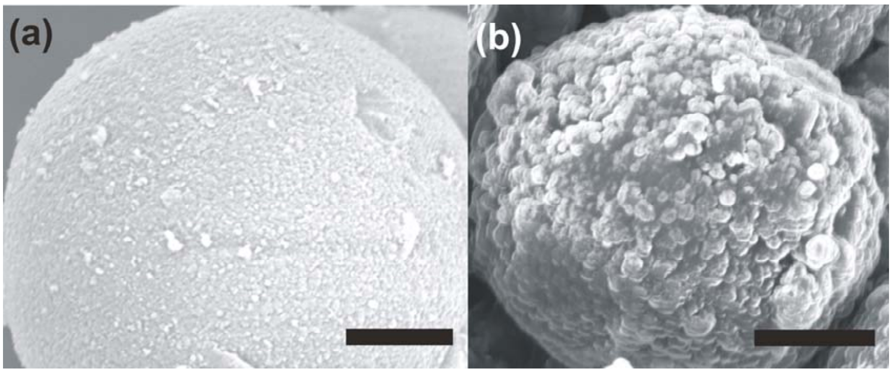

Figure 8. SEM images of Pt doped silica microspheres: (a) 3 mol. % (20 wt. %), (b) 7 mol. %. (46 wt. %). Scale bar: 1 µm.

In order to compare the composition and characteristics of the platinum doped silica particles produced via our microfluidic synthesis scheme with a commercially available platinum doped silica sample, we bought a commercial platinum doped silica catalyst (ABCR GmbH, Germany). This was used as a reference material for comparison. X-ray fluorescence (XRF) analysis of the samples was carried out to check the platinum content in the reference material. Results revealed about 30 wt. % of platinum in the reference material. To allow for the quantitative comparisons, the microfluidic synthesis recipe was adjusted accordingly to produce platinum doped silica particles with the same platinum content as the reference material (Table 1). Moreover, Transmission Electron Micrographs (TEM) indicated both the candidates for comparison had metallic platinum arranged in face centered cubic lattice (see Figure 9).

Material	**Specific Surface Area SSA (m^2/g)**	**Pore radius (nm)**	**Pt (mol. %)**	**Si (wt. %)**
Pt/SiO_2 – microfluidic synthesis scheme	590 (± 20 m^2/g)	1.994	4.91 mol. %	67.93
Pt/SiO_2 – ref. material (ABCR)	138 (± 20 m^2/g)	12.468	4.43 mol. %	70.46

Table 1. *Characterization results from the BET isotherms and XRF Analysis.*

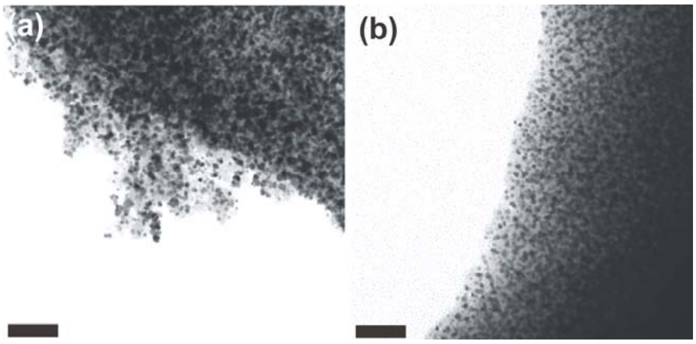

Figure 9. TEM micrographs for (a) bulk synthesized reference platinum on silica, (b) microfluidically synthesized platinum on silica. Scalebar: 100 nm.

To investigate if the microfluidically produced platinum doped silica particles are catalytically active, emissivity corrected InfraRed Thermography (ecIRT) [12-14] was used for initial screening of catalyst libraries. The test was done for the propane (C_3H_8) oxidation reaction with the feed gas consisting of $C_3H_8/O_2/N_2$ and with a composition of about 0.4/20/79.6 vol. % at a flow rate of 50 ml/min. ecIRT image of a library is shown in Figure 10. Commercially available industrial catalyst material Hopcolite (mixture of copper and manganese oxides) (Sigma Aldrich GmbH) was also used as a reference for this screening. It can be inferred from this screening that the microfluidic platinum doped silica particles were found catalytically active through the resulting differential temperature calculated by the software program. To understand the catalytic activity more precisely, conventional fixed bed catalyst testing was additionally performed.

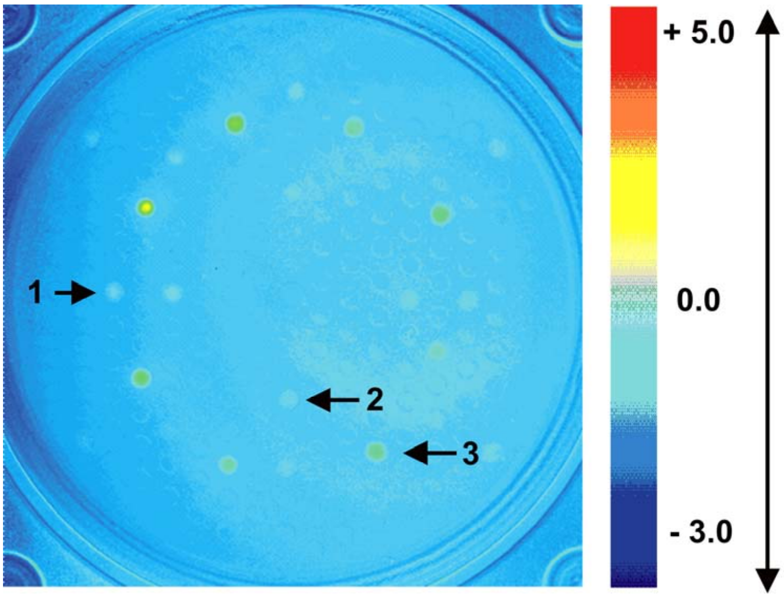

Figure 10. *Emissivity corrected infrared thermography (ecIRT) image for propane oxidation reactions. 1: 3 mol. % (20 wt. %) microfluidic Pt doped silica, 2: 7 mol. %. (46 wt. %) microfluidic Pt doped silica, 3: Hopcolite as reference.*

Conventional fixed bed tests [15] were done with platinum doped silica particles produced by our microfluidic synthesis scheme as well as with bulk produced reference material from ABCR for the propane oxidation reaction. Both the samples were tested in the fixed bed reactor [21] with a total feed flow rate of 50 ml/min with operating temperature between 150 up to 350°C and a feed gas concentration of $C_3H_8/O_2/N_2$ = 0.2/5/94.8 vol. %. The catalytic behavior of the particles was evaluated by measuring propane conversion versus temperature (see Figure 11). For best possible catalytic activity, it is very important for this conversion to take place at low temperatures [22]. Accordingly, the temperatures of 50 % conversion (T_{50}) were read out from the curves to compare the combustion activities of the catalysts. T_{50} for the reference ABCR sample (half filled circles in Figure 11) is about 425 °C and is significantly higher than that of catalysts produced via microfluidic synthesis scheme (295 °C) (half filled diamonds in Figure 11). For comparison, pure silica particles without platinum doping were also tested and were found with no catalytic behavior as expected (half filled pentagons in Figure 11). This shows that platinum doped on silica particles produced via microfluidic synthesis scheme is clearly favorable for propane oxidation reactions than those available commercially.

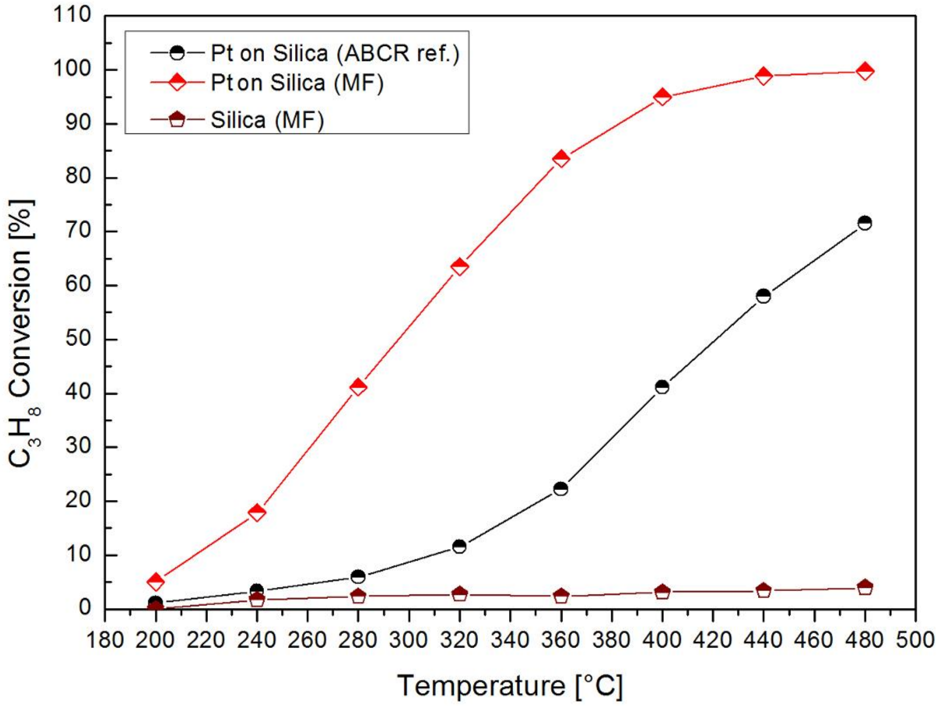

Figure 11. *Temperature dependence of the conversion of propane on Pt/SiO_2 in a gas phase flow reactor with reaction in increment order of temperatures from 200°C to 480°C. Dots: commercially catalyst, diamonds: microfluidically produced catalyst, pentagons: microfluidically produced silica particles with zero Pt concentration.*

To explain the superior catalytic behavior obtained for catalysts produced via our microfluidic synthesis scheme over the commercial catalysts, BET analysis was done to determine the respective porosity of the silica matrix using nitrogen as adsorbate. The specific surface area of the ABCR reference catalyst particles was determined to be around 138 m^2/g (± 20 m^2/g) with a pore size distribution maximum at 11.6 nm (± 0.2 nm) pore radius with a cumulative pore volume of 0.28 cm^3/g (± 0.02 cm^3/g). Similarly, the porosity and the pore volume of the microfluidically synthesized platinum doped silica particles are investigated in a similar manner by a BET analyzer. The specific surface area of the produced catalyst particles averaged over several production runs and for various measurements was determined to be around 590 m^2g^{-1} (± 20 m^2/g) with a pore size distribution maximum at 1.9 nm (± 0.1 nm) pore radius and a cumulative pore volume of 0.54 cm^3/g (± 0.02 cm^3/g). The corresponding BET isotherms and pore size distribution are shown in Figure 12. Platinum doped silica catalysts prepared via our microfluidic synthesis scheme are superior in surface area by more than 3 times compared to the commercial catalysts (reference material). Moreover, our microfluidically produced silica supported catalyst has much smaller pores than the commercial reference material. This might be a result of the fast mixing inside the droplets, the precise reaction control and due to the fast diffusions times of the solvent out of the silica network. From the obtained results it is clear that our novel droplet-based microfluidic sol-gel reaction scheme offers great possibilities to synthesize catalyst materials with superior properties than commercially available catalyst products.

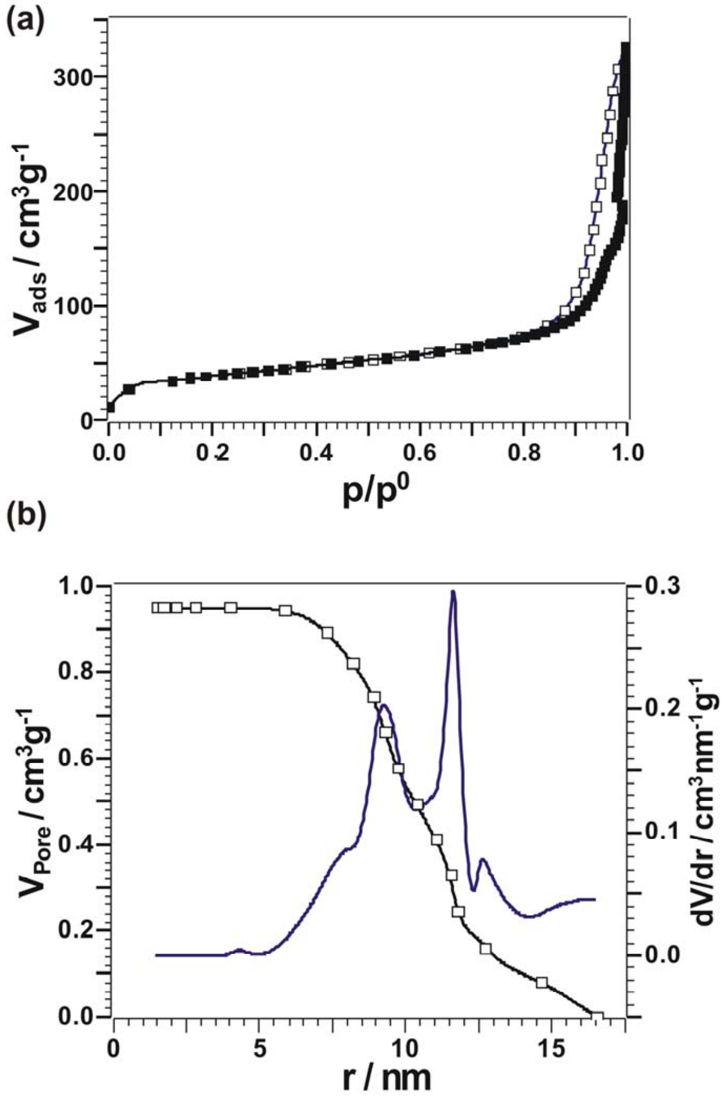

Figure 12. (a) BET Nitrogen adsorption-desorption isotherm of the reference platinum doped silica catalyst (ABCR GmbH), (b) Pore size distribution. V_{ads} = adsorbed volume, p/p_0 = reduced pressure, V_{pore} = pore volume, r = pore radius.

5 CONCLUSION

We have presented a novel droplet-based microfluidic reaction scheme to perform chemical reactions with precise volume and process control that allows for fast reactions even forming gels or precipitates. The important steps developed for this scheme are the synchronized production of droplet pairs containing different reactants, controlled merging of the droplet pairs and mixing of the reactants inside the merged droplets. We proved this microfluidic scheme by performing sol-gel reactions to produce silica particles and platinum doped silica particles with superior properties. From the obtained results we can conclude that the droplet-based microfluidic reaction scheme offers great possibilities to perform complex chemical reactions and to synthesize materials with superior properties that were not possible with any existing microfluidic approach. This type of droplet-based microfluidic scheme is thus expected to have a large potential not only for synthesizing reactions but also for drug screening purposes or even combinatorial approaches when being combined with techniques to manipulate, redistribute and split merged droplets.

ACKNOWLEDGEMENTS

We thank the group of Prof. U. Hartmann for help with SEM measurements. This work was partially funded by the DFG project Se 1118/4 and the GRK 1276/1.

REFERENCES

[1] H. Song et al., *Angew. Chem. Int. Ed.*, 2003, 115, 791.
[2] J. M. Ottino and S. Wiggins, *Phil. Trans. R. Soc. Lond. A*, 2004, 362, 923–935.
[3] M. R. Bringer, C. J. Gerdts, H. Song, J. D. Tice and R. F. Ismagilov, *Phil. Trans. R. Soc. Lond. A*, 2004, 362, 1087–1104.
[4] H. A. Stone, A. D. Stroock and A. Ajdari, *Annual Review of Fluid Mechanics*, 2004, 36, 381-411.
[5] B. Zheng, L. S Roach, and R F. Ismagilov, *J. Am. Chem. Soc.*, 2003, 125, 11170-11171.
[6] I. Shestopalov, J. D. Tice, R. F. Ismagilov, *Lab on a Chip*, 2004, 4, 316-321.
[7] Frenzer, G., Maier, W.F., 2006, “Amorphous Porous Mixed Oxides: Sol-Gel Ways to a Highly Versatile Class of Materials and Catalysts”, *Ann. Rev. Mater. Res.*, **36**, pp. 281-331.
[8] Larry L. Hench, and Jon K. West, 1990, “The Sol-Gel Process”, *Chem. Rev.*, 90, pp. 33-72.
[9] Y. Xia and G. M. Whitesides, *Annu. Rev. Mater. Sci.*, 1998, 28,153–84.
[10] Y. Xia and G. M. Whitesides, *Angew. Chem. Int. Edt.*, 1998, 37, 550.
[11] S. Brunauer, P. H. Emmett and E. Teller, *J. Am. Chem. Soc.*, 2002, 60, 309-319.
[12] A. Holzwarth, H. W. Schmidt, W.F. Maier, *Angew. Chem. Int. Edt.*, 1998, 37, 2644–2647.
[13] A. Holzwarth; W.F. Maier, *Platinum Met. Rev.*, 2000, 44, 16–21.
[14] G. Kirsten, W.F. Maier, High Throughput Screening in Chemical Catalysis; Hagemeyer, A., Strasser, V., Volpe, A. F., Eds.; Wiley-VCH: Weinheim, Germany, 2004. ISBN: 978-3-527-30814-9.
[15] C. Mirodatos, Y. Schurmann, C. Hayayud, A. Holzwarth, D. Farusseng, T. Richter, European Patent, 2003, 1293772.
[16] V. Chokkalingam, S. Herminghaus and R. Seemann, *Appl. Phys. Lett.*, 2008, 93, 254101-254103.
[17] C. Priest, S. Herminghaus and R. Seemann, *Appl. Phys. Lett.*, 2006, 88, 024106-024103.
[18] M. J. Fuerstman, A. Lai, M. E. Thurlow, S. S. Shevkoplyas, H. A. Stone and G. M. Whitesides, *Lab on a Chip*, 2007, 7, 1479-1489.
[19] V. Chokkalingam, B. Weidenhof, M. Krämer, W. F. Maier, S. Herminghaus and R. Seemann, *Lab on a Chip*, 2010, 10, 1700-1705.
[20] H. M. Evans, E. Surenjav, C. Priest, S. Herminghaus, R. Seemann and T. Pfohl, *Lab on a Chip*, 2009, 9, 1933-1941.
[21] C. Mirodatos, Y. Schurmann, C. Hayayud, A. Holzwarth, D. Farusseng, T. Richter, European Patent, 2003, 1293772.
[22] S. Storck, H. Bretinger and W. F. Maier, *Applied Catalysis A: General*, 1998, 174, 137-146.

Addendum IV: Flow field induced particle accumulation inside droplets in rectangular channels

accepted in Lab on a Chip (2015) **DOI:** 10.1039/C5LC00420A .

Authors: M. Hein[1], M. Moskopp[1] and R. Seemann[1,2]

[1] Department of Experimental Physics, Saarland University, Saarbrücken, Germany
[2] Dynamics of Complex Fluids, MPI for Dynamics and Self-Organization, Göttingen, Germany

Author Contributions:

Research was designed by M. Hein and R. Seemann. Experiments were performed by M. Moskopp and M. Hein. Data was analyzed by M. Moskopp and M. Hein. Experimental setups were designed by M. Hein. Article was written by M. Hein. Writing was supervised by R. Seemann and M. Moskopp . Research was directed by M. Hein and R. Seemann.

Abstract:

Particle concentration is a basic operation needed to perform washing steps or to improve subsequent analysis in many (bio)- chemical assays. In this article we present field free, hydrodynamic accumulation of particles and cells in droplets within rectangular microchannels. Depending on droplet velocity, particles either accumulate at the rear of the droplet or are dispersed over the entire droplet cross-section. We show that the observed particle accumulation behavior can be understood by a coupling of particle sedimentation to the internal flow field of the droplet. The changing accumulation patterns are explained by a qualitative change of the internal flow field. The topological change of the internal flow field, however, is explained by the evolution of the droplet shape with increasing droplet velocity altering the friction with the channel walls. In addition, we demonstrate that accumulated particles can be concentrated, removing excess dispersed phase by splitting the droplet at a simple channel junction.

Flow field induced particle accumulation inside droplets in rectangular channels†

Michael Hein,[a] Michael Moskopp,[a] and Ralf Seemann*[a,b]

Received 9th April 2015, Accepted 20th May 2015
First published on the web 20th May 2015
Lab on a Chip DOI: 10.1039/C5LC00420A

Particle concentration is a basic operation needed to perform washing steps or to improve subsequent analysis in many (bio)-chemical assays. In this article we present field free, hydrodynamic accumulation of particles and cells in droplets within rectangular micro-channels. Depending on droplet velocity, particles either accumulate at the rear of the droplet or are dispersed over the entire droplet cross-section. We show that the observed particle accumulation behavior can be understood by a coupling of particle sedimentation to the internal flow field of the droplet. The changing accumulation patterns are explained by a qualitative change of the internal flow field. The topological change of the internal flow field, however, is explained by the evolution of the droplet shape with increasing droplet velocity altering the friction with the channel walls. In addition, we demonstrate that accumulated particles can be concentrated, removing excess dispersed phase by splitting the droplet at a simple channel junction.

1 Introduction

Particle accumulation and concentration are integral components of many (bio-)chemical assays. Particles are regularly used as solid supports for catalysts or their functionalized surface is employed to detect or specifically harvest molecules after a reaction, e.g. in bead based PCR amplification of DNA [1] or in immunoassays [2]. Accumulation and concentration of particles is often desired for these applications. Similarly, the separation of cells from surrounding medium is often required to concentrate the cell suspension for further analysis or to remove cells which interfere with subsequent analysis of the medium, e.g. in blood plasma analysis [3,4].

A large variety of passive [5–9] and active [10–12] particle or cell concentration approaches have been developed for continuous flow microfluidics to satisfy the need of 'on-chip centrifugation', some approaches even capable of sorting different families of particles or cells [13,14]. In contrast, particle separation and concentration inside droplets, is much more complex due to the three dimensional recirculative flow profile emerging in confined droplets moving inside microfluidic channels. The strong swirls prevent the use of most continuous flow concentration or separation methods, as particles are quickly re-dispersed over the entire droplet cross-section. Nonetheless, some active methods succeed in particle concentration within droplets, e.g. by pulling magnetic particles to one side of a droplet while the droplet is split at a channel junction [15,16]. However, active methods require additional components like electrodes or magnets to be included into the chip design, increasing chip complexity and fabrication cost. Thus, passive methods are usually preferred.

Recently, the first passive method for particle [17] and blood cell [18] concentration inside elongated droplets flowing in round tubing has been reported. In both reports, particles or cells were found to concentrate within a single cloud at the rear center of the droplet. Particles were found to recirculate within this particle cloud and the length of the particle cloud was shown to increase linearly with droplet velocity until limited by the droplet length. The observed accumulation effect was shown to be primarily caused by a coupling of gravity driven sedimentation to the well known internal flow field of the droplet, which basically consist of a forward velocity of the dispersed phase in the droplet center, that recirculates close to the channel walls [19,20]. The center velocity is proportional to the traveling velocity of the droplet, in agreement to the observed growth of the particle accumulation cloud with droplet velocity. Additional vortices are present in the caps of elongated droplets and particles were found to accumulate in these caps, independent of the droplet velocity [17]. However, most microfluidic systems feature rectangular channel cross-sections in which droplets do not fully expand into the channel corners. Due to interfacial tension, the droplet interface assumes the shape of circular arcs in the channel corners. Thus, droplets do not block the entire rectangular cross-section and continuous phase can bypass the droplet through the remain-

---

† Electronic Supplementary Information (ESI) available: [Details on device fabrication, μPIV and fluorescence microscopy experiments along with additional 'phase-like' diagrams are given in the supplement].

[a] *Saarland University, Experimental Physics, Saarbrücken, Germany. Fax: +49 681 302 71700 ; Tel: +49 681 302 71777; E-mail: r.seemann@physik.uni-saarland.de*

[b] *Max Planck Institute for Dynamics and Self-Organization, Göttingen, Germany.*

ing gutters[21,22]. The locally varying drag exerted by the surrounding continuous phase within the gutters or the thin films in vicinity of the channel walls leads to a complex flow field inside of droplets. This complex flow field is influenced by a plethora of parameters such as viscosity ratio of the dispersed and continuous phase, droplet velocity, interactions between subsequent droplets, and interfacial tension[23–28].

In the present article we explore a passive accumulation effect of particles or cells inside droplets in rectangular microchannels.In contrast to the observed behaviour in round channels, particles and cells are found to accumulate in two distinct clouds close to the channel sidewalls at the rear of elongated droplets. An example of accumulation of yeast cells (bright objects) is shown in Fig. 1. The emergent accumulation behavior will be explained in terms of experimentally determined internal flow fields. The internal flow field, however, will be shown to evolve qualitatively with increasing droplet velocity, which in turn will be demonstrated to be induced by a changing outer droplet shape.

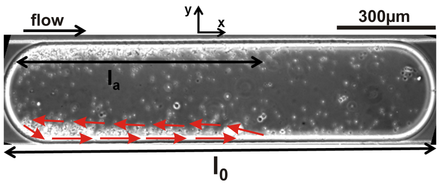

Fig. 1 Dark field micrograph showing the accumulation of yeast cells (W303) fixed by chloroform in a phosphate buffered saline (PBS) droplet surrounded by n-hexadecane with 2 wt.% Span 80. Channel height is 58 μm and $Ca \approx 2.3 \cdot 10^{-4}$. Arrows visualize the cell trajectories within the accumulation zones.

2 Experimental Section

The channel layout is shown in Fig. 2. Microfluidic devices with a constant channel height of 100 μm were produced in Polydimethylsiloxane (PDMS) by standard softlithography[29], cf. SI 1 for details. The observation, storage and inlet channels have identical channel width of 300 μm, allowing for controlled production of elongated droplets of variable length ranging from $0.4-3.5$ mm. The wavy structure after the junction between storage and flush channel allows to homogenize the shape of the droplet and to redisperse particles after droplet storage. Measurements were performed after the maximum length of the straight segments right before the curved parts.

The basic liquid system used in all experiments was comprised of ultra-pure water (GenPure, TKA) of viscosity $\mu_1 =$ 1 mPas as dispersed phase and n-hexadecane (Alfa Aesar) with 2 wt% of the surfactant Span 80 (ABCR) of viscosity $\mu_2 = 3.3$ mPas as continuous phase. The liquid/liquid interfacial tension was determined to $\gamma = (3.5 \pm 0.1)$ mN/m by the pendant drop method (OCA20, DataPhysics).

Volumetric flow rates were adjusted using custom built, computer-controlled precision syringe pumps. To reduce particle sedimentation within the syringe, the syringe pump of the dispersed particle suspensions was hung vertically and a magnetic stirrer was inserted into the syringe and externally driven by a rotating permanent magnet[30]. However, a certain variation in particle concentration could not be avoided due to sedimentation in the tubing and the inlets of the chip itself.

The used particles were selected by their sedimentation velocities $v_s = (\rho_p - \rho_1)gd_p^2/18\mu_1$, assuming force balance between buoyancy, gravity and Stokes friction. Here, ρ_p and ρ_1 are the densities of the particles and the dispersed phase, respectively, g is the gravitational acceleration and d_p is the particle diameter. Three different types of particles were used providing different sedimentation velocities v_s, without significantly altering the interfacial tension or dispersed phase viscosity. Aqueous suspensions of Poly-Methylmethacrylate (PMMA) particles ($d_p = 8\,\mu$m, Sigma Aldrich) and Polystyrene (PS) particles ($d_p = 10\,\mu$m, Sigma Aldrich) and a dry powder of Silica spheres ($d_p = 5\,\mu$m, Whitehouse Scientific) were added to pure water at particle concentrations of $6.3 \cdot 10^7\,\mathrm{ml}^{-1}$, $2.3 \cdot 10^7\,\mathrm{ml}^{-1}$ and $6.6 \cdot 10^7\,\mathrm{ml}^{-1}$, respectively. The selected particle diameters are in the range typically used within microfluidic bioanalytic systems. To entirely eliminate gravity driven sedimentation by density matching, the PS particles were added to a dispersed phase consisting of a mixture of heavy water and pure water at a particle concentration of $2.8 \cdot 10^7\,\mathrm{ml}^{-1}$, again without significantly changing μ_1 and γ. An overview of the four tested particle/liquid systems is presented in Table 1.

Table 1 Particle/liquid systems

Particles (d_p)	Dispersed -Phase	$\rho_p - \rho_1$ [g/cm^3]	v_s [μm/s]
Silica (5 μm)	H_2O	0.9 - 1.3	15.7 ± 3.8
PMMA (8 μm)	H_2O	0.19	6.7 ± 0.3
PS (10 μm)	H_2O	0.05	2.7 ± 0.2
PS (10 μm)	$H_2O + D_2O$	0	0

Particle accumulation patterns were recorded using optical microscopy (Leica Macroscope Z16) and a CCD (PCO1600) or a highspeed CMOS camera (PCO 1200hs). Only images of droplets containing sufficient particles to clearly show the accumulation patterns were used for further analysis. The droplet length l_0, the length of accumulation zone l_a (cf. Fig. 1) and the droplet velocity v_0 were directly determined from the recorded time series.

The flow fields inside of droplets were determined by μPIV in $x-y$ planes of the device, cross-correlating fluorescence

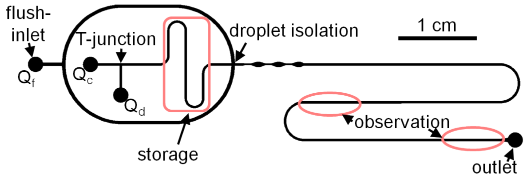

Fig. 2 Sketch of the channel layout.

microscopy images of suspended Polystyrene tracer particles ($d_p = 1\,\mu$m FluoroMax Red, Thermo Scientific). The same optical setup used for μPIV was also employed to characterize the thickness of the oil layer surrounding the droplet. For these experiments, the continuous phase was fluorescently labeled adding Fluorescein27 (Radiant Dyes), without significantly changing the interfacial tension and viscosity. The local oil thickness could then be characterized by measuring the local fluorescence intensity. For both, fluorescence microscopy and μPIV, the droplet length was kept constant at an average value of (1.2 ± 0.1) mm due to the limited field of view of the microscope objective, cf. SI 2 for details.

3 Results and discussion

Aqueous droplets were continuously produced in a surrounding oily phase using the T-junction until the storage channel of the device was filled with droplets of the desired length, cf. Fig. 2. Subsequently, continuous phase was inserted symmetrically through the ring-channel connected to the flush inlet, removing all droplets from the long observation channel. To start an experiment, one isolated droplet was injected from the storage channel into the observation channel. Subsequently, the droplet was accelerated by injecting continuous phase through the flush inlet. This approach allows to characterize particle accumulation, droplet shapes and flow fields inside of isolated elongated droplets at various length and droplet velocities. Additional complexities by interactions between subsequent droplets are avoided.

3.1 Particle accumulation patterns

Three different particle types of different size and density and thus different sedimentation velocity v_s were used to test for the influence of gravity driven sedimentation in droplets: Silica particles ($d_p = 5\,\mu$m, $v_s \approx 16\,\mu$m/s), PMMA particles ($d_p = 8\,\mu$m, $v_s \approx 7\,\mu$m/s) and PS particles ($d_p = 10\,\mu$m, $v_s \approx 3\,\mu$m/s). Additionally, a density matched system consisting of PS particles ($d_p = 10\,\mu$m) in a $H_2O + D_2O$ mixture was used with a sedimentation velocity of $v_s \approx 0$. For sedimenting particles, three different particle accumulation patterns were observed as function of $Ca = \mu_2 v_0/\gamma$ for different droplet length l_0. Here, μ_2, v_0, γ denote the viscosity of the continuous phase, the droplet traveling velocity, and the interfacial tension, respectively. Examples of the three accumulation regimes are shown in Fig. 3a for the PMMA particles having medium sedimentation velocity and are mapped in a 'phase-like' diagram in Fig. 3b.

For low Ca, typically $O(10^{-4})$, all particles accumulate in two distinct zones at the rim of the droplet ('accumulation regime'), cf. left box in Fig. 3a and left region in Fig. 3b. Within these zones, particles have been observed to move in closed loops, cf. indicated trajectories in Fig. 1. At the droplet rim, close to the channel walls, particles are transported to the droplet front at comparatively high velocity. During this transport, particles also move towards the droplet center and decelerate until finally being transported back to the rear of the drop. Typically, the accumulation zones decrease in width along the droplet length l_0, as more and more particles are transported backwards. Depending on l_0, the accumulation zones can either span the entire length of the droplet or, for longer droplets, have an accumulation length $l_a < l_0$. Increasing Ca leads to a reduction of l_a, see square symbols in Fig. 3c and a transition to the 'intermediate' regime at $Ca \gtrsim 10^{-3}$ is found for all tested l_0, cf. middle box of Fig. 3a and center region of Fig. 3b. This peculiar particle accumulation behavior contrasts previous findings in round tubing[17]. Within the 'intermediate' regime the two accumulation zones are maintained but their length further decreases with Ca and an increasing amount of particles becomes dispersed across the droplet cross section. The accumulation zones finally disappear and particles are dispersed across the entire droplet, c.f right box in Fig. 3a, in agreement to previous observations at high droplet velocities in round channels[17]. This 'mixing regime' was found at large Ca for sufficiently short droplets $l_0 < 1$ mm, cf. Fig. 3b.

Increasing the particle sedimentation velocity v_s by a factor of 2.4 compared to the PMMA particles by using the silica particles, the same qualitative particle accumulation behavior was observed, cf. Fig. SI 1a. The transitions between the three accumulation regimes were only slightly shifted to higher Ca compared to the PMMA particles, whereas the relative length l_a/l_0 of the accumulation zones remains constant, cf. circles in Fig. 3c. In contrast, reducing v_s by a factor of 2.5 compared to the PMMA particles by using the PS particles, results in a significant change in particle accumulation behavior, cf. Fig. SI 1b. The 'accumulation' regime disappears in the tested parameter range and could only be found for very long droplets $l_0 \geq 4$ mm at very small $Ca \sim O(10^{-4})$. For such small sedimentation velocity v_s, the 'intermediate' regime was predominantly found at low Ca while complete mixing was observed for all tested droplet length at $Ca > 1.5 \cdot 10^{-3}$. Upon completely eliminating sedimentation using the density matched system, no particle accumulation could be observed for the explored droplet length $0.5\,\mathrm{mm} \leq l_0 \leq 5\,\mathrm{mm}$ and $1 \cdot 10^{-4} \leq Ca \leq 6 \cdot 10^{-3}$. Obviously, particles accumulate in certain patterns for sufficiently large v_s but will follow the internal flow when the sedimentation velocity v_s is too small.

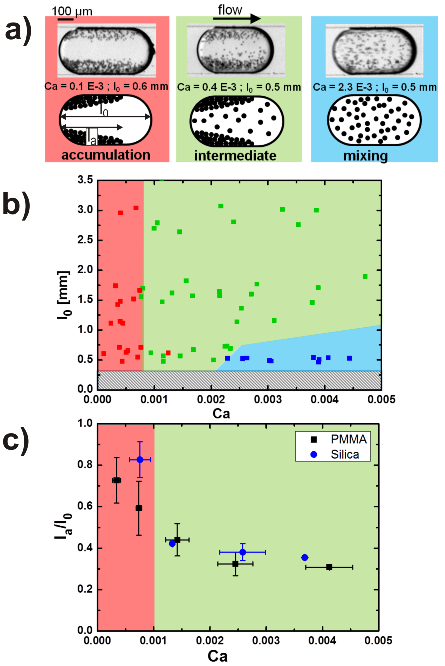

Fig. 3 Classification of the observed particle patterns as observed for the $d_p = 8\,\mu$m PMMA particles. a) Upper row: Micrographs of the shortest tested droplet family; lower row: sketches. Particle accumulation in two distinct zones (left, red), 'intermediate' regime (middle, green), complete 'mixing' regime (right, blue). b) 'phase-like' diagram showing the accumulation behavior as a function of l_0 and Ca. c) Normalized accumulation length l_a/l_0 as a function of Ca for $d_p = 8\mu$m PMMA (squares) and $d_p = 5\mu$m silica (dots) particles. To be able to span a large range of Ca, the probed droplet length was limited to $1-2\,$mm.

The different particle accumulation behavior in round and rectangular channels results from the different flow pattern as will be clarified in this article. To explain the observed particle accumulation regimes, the variation of the droplet shape is explored as a function of Ca in sec. 3.2. The varying outer droplet shape is used in sec. 3.3 to explain the emerging flow fields in droplets. Finally, the particle accumulation regimes are explained by the internal flow fields in sec. 3.4.

3.2 Outer shape of droplets

To determine the shape of the droplet interface, the continuous phase was dyed fluorescently. Focusing on the bottom of the channel, the fluorescence intensity was observed to be proportional to the local layer thickness of the continuous phase, cf. SI 2 for details. Figure 4a shows a contour plot of the oil film thickness at three different Ca. The apparent contact area of the droplets with the channel bottom is dotted for better visualization. Three different regions are labeled in the contour plots. At low $Ca = 0.8 \cdot 10^{-3}$, the droplet is in close contact to the channel bottom along the entire droplet length close to the sidewalls (region 1), as well as in the front half of the droplet. The front interface of the droplet (region 2) has a circular shape. Only in the rear half of the droplet the film rearranges, growing in height towards the rear starting from the droplet center-line (region 3). Increasing Ca to $2.8 \cdot 10^{-3}$, the contour plot reveals changes both in the profile of the oil film and in the outer shape of the droplet. The front cap of the droplet (region 2) becomes more pointed, which indicates an earlier lift-off of the droplet interface from the channel bottom. At the rear of the droplet, a lift-off from the sidewalls is observed. Close to the channel sidewalls (region 1) the droplet maintains apparent contact with the channel bottom, while the thickness of the surrounding oil film increases in the middle of the droplet. Further increasing Ca to $6.2 \cdot 10^{-3}$ finally amplifies all of these trends: The apparent contact to the channel bottom is further reduced to elongated areas close to the sidewalls (region 1) while the thickness of the oil film is further increased in the middle of the droplet, forming a tongue of continuous phase that extends along the entire droplet length (region 3). It is also visible that the droplet width at the rear side is reduced with growing Ca, indicating an increased gutter width at the rear of the droplet.

The observed evolution of the thin film profile is in good qualitative agreement to the analytical predictions of Wong[21], who calculated the evolution of thin films of continuous phase surrounding incompressible, inviscid bubbles with a surfactant free interface. However, for the described Ca range, the absolute variation of the continuous phase film thickness is small and the drag at the top and the bottom of the rectangular channel will remain about constant. Changes of the gutter geometry are expected to be more relevant, as variations of the drag exerted on the dispersed phase by the continuous phase bypassing the droplet through the gutters will cause changes in the internal flow field.

The left tile of Fig. 4b presents fluorescence intensity profiles measured within the gutter region along the entire droplet length close to the channel sidewalls. The fluorescence intensity determining the gutter height was measured about $9\,\mu$m from the estimated position of the channel sidewalls and averaged over both sides of the droplet, indicated by the dashed lines in the lower tile of Fig. 4a, cf. SI 2 for further details. For very small $Ca = 0.2 \cdot 10^{-3}$ the droplet is nearly at its equilibrium shape with an approximately constant gutter height, as can be seen by the constant fluorescence intensity along the droplet length. The constant gutter height is sketched by the dashed line in the right tile of Fig. 4b. Increasing Ca to $3.3 \cdot 10^{-3}$, however, the gutter height increases at the droplet rear while it decreases towards the droplet front. This agrees with the growing oil layer thickness between the rear of the drop and the sidewalls, as observed in the contour plots of Fig. 4a. Increasing Ca to $7.9 \cdot 10^{-3}$ results in a further increase of the gutter height at the rear of the droplet. Obviously, the droplet changes its shape with increasing Ca and the contact of the droplet with the channel sidewall is significantly reduced at the rear and slightly increased at the front, cf. solid (red) line in the right tile of Fig. 4b. This changed droplet shape at high Ca leads to a higher drag with the sidewalls at the front of the droplet whereas the flow in the rear part of the droplet is expected to be primarily influenced by the bypassing continuous phase through the increased gutters. As the drag between the dispersed phase and the thin films of continuous phase close to channel walls, respectively to the continuous phase in the gutters determines the internal flow pattern in the droplet, a topographical change of the internal flow pattern with increasing Ca is expected.

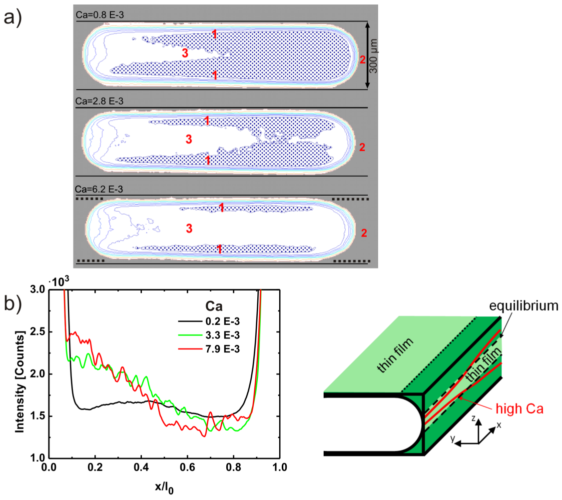

Fig. 4 a) Contour plot of the oil film thickness close to the channel bottom at $z \approx 0$. The area of apparent contact with the channel bottom is dotted for better visualization. Lines correspond to equal film height. b) *Left*: fluorescence intensity in the gutters close to the channel wall (cf. dotted lines in a)) as a function of x/l_0 for various Ca. Data is averaged over several droplet images and smoothed by a sliding average. *Right*: sketch illustrating the change of the apparent contact line of the droplet with the sidewalls with Ca.

3.3 Flow field inside elongated droplets

Using μPIV, the 2D velocity components in $x-y$ planes within the droplet were measured at three different distances from the bottom of the channel $z = 20, 35, 50\,\mu$m and for different velocities. Figure 5 shows the resulting stack of measured flow fields in the co-moving reference frame of the droplets with an average length $l_0 = (1.2 \pm 0.1)\,$mm. The droplet interface is illustrated as guide to the eye. Velocity vectors measured by μPIV are displayed as small arrows. For a better visualization, the main features of the flow are highlighted by larger grey (green) arrows.

The internal flow is directed backwards at areas where droplets are in almost contact with the channels walls at $y = \pm 150\,\mu$m due to the large drag with the nearly stagnant surrounding film of continuous phase between droplet and channel wall. Accordingly, the flow in planes close to the channel bottom was always found to be directed backwards and is just sketched for $z \approx 5\,\mu$m for a better visualization. Similarly, the flow inside the droplet is mostly directed forward at the interfaces to the gutters where the continuous oil phase is bypassing the droplets which are typically slower than the average velocity of the continuous phase for the considered viscosity ratio[24,27,31]. The contact areas of droplets with the channel walls and the size of the gutters change with increasing Ca due to droplet deformation. Consequently the internal flow field is altered.

In Fig. 5a the measured flow field inside a droplet moving at $Ca = 0.7 \cdot 10^{-3}$ is shown. For such low Ca, a relatively simple three dimensional flow profile is found. In the center plane of the channel at $z = 50\,\mu$m, the main flow direction is towards the front of the droplet, except close to the sidewalls. Small vortices can be found in the front and back caps of the droplet, that are present in all measured planes. In the planes at $z = 35\,\mu$m and $z = 20\,\mu$m, the flow at the droplet/oil interface is directed to the front along the entire droplet length, caused by the continuous phase bypassing the droplet through the gutters. The flow in the middle of these planes is directed backwards, as the dispersed phase has to recirculate within the droplet. Additionally, dispersed phase is transported backwards close to the channel bottom. Thus, at low Ca, the main feature of the three dimensional flow within elongated droplets are four long vortex roles stretching along nearly the entire droplet length, reflecting the symmetry of the rectangular channel cross-section. For similar Ca, consistent flow fields inside elongated droplets in rectangular channels have been observed in references [24,27].

At intermediate Ca, the characteristics of the flow field start to change as a result of the varying droplet shape, as exemplified in Fig. 5b for $Ca = 2.6 \cdot 10^{-3}$. The backwards flow found close to the sidewalls at $z = 50\,\mu$m begins to expand into lower layers at the droplet front as the contact area of the droplet with the channel side walls increases towards the front, cf. the $z = 35\,\mu$m plane. The topological change of the overall flow profile indicates the emergence of new vortices and a flow reversal at the droplet front and continues for increasing Ca, as shown in Fig. 5c. At $Ca = 5.5 \cdot 10^{-3}$, droplet deformation leads to an even larger gutter height at the rear that rapidly decreases towards the droplet front, cf. Fig. 4b. Consequently, the apparent contact area of the droplet with the channel walls decreases at the droplet rear and increases at the front. This causes the backwards directed flow to expand further towards the channel bottom, even reaching the layer at $z = 20\,\mu$m.

To stress the topological transition of the recirculative flow, the x-component of the internal flow velocity close to the rim, v_{rim}, determined at $z = 35\,\mu$m planes along the droplet length is plotted in Fig. 6 for several Ca. v_{rim} is always positive for $Ca < 2 \cdot 10^{-3}$. Thus, at low Ca, the flow at the droplet rim is always directed towards the front. However, with increasing Ca, v_{rim} is found to significantly decrease at the front of the droplet, as the contact of the droplet with the channel walls increases. Above $Ca \approx 2 \cdot 10^{-3}$ the decrease of v_{rim} at the droplet front even results in a flow reversal at the droplet front. This flow reversal, i.e. $v_{rim} < 0$, clearly indicates the topological change from a simple flow with four main vortices to a more complex recirculative flow field. The flow reversal was found to occur at larger x-values, i.e. closer to the droplet front, in planes closer to the channel bottom.

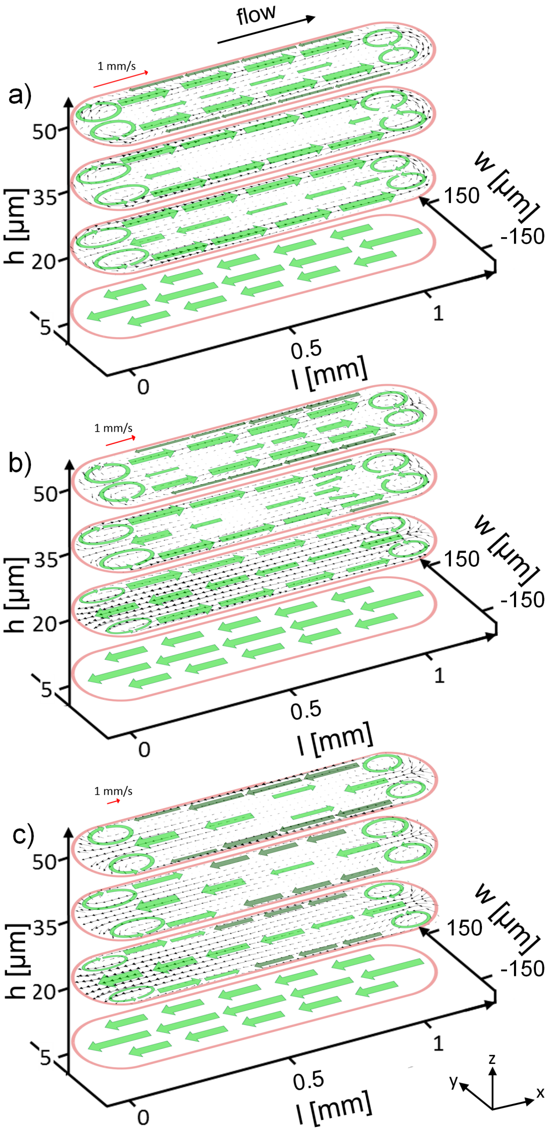

Fig. 5 a) Averaged flow fields in three $x-y$ planes for $z = 20,\ 35,\ 50\,\mu$m in the co-moving frame of the droplets. Sketched vectors close to the channel bottom and droplet interface are guides to the eye. a) $Ca = 0.7 \cdot 10^{-3}$, b) $Ca = 2.6 \cdot 10^{-3}$, c) $Ca = 5.5 \cdot 10^{-3}$.

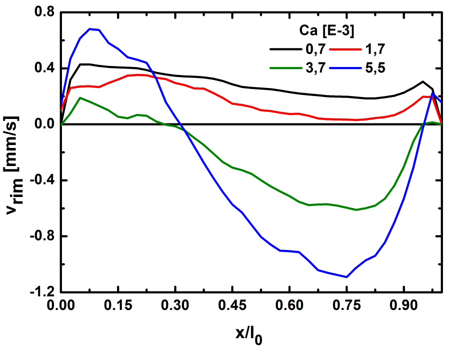

Fig. 6 x-component of the measured velocity in the co-moving reference frame along the droplet rim at $z = 35\,\mu$m. Data is averaged within $30\,\mu$m from the droplet interface over both sides of the droplet. Positive velocities indicate flow direction of droplet motion.

A similar topological transition of the flow field was reported for droplets in square micro-channels by Jakiela et al.[27], with a sharp transition at $Ca \approx 1 \cdot 10^{-3}$. However, in the flow fields determined here, a rather continuous transition of the internal flow fields with increasing Ca was found, which is in agreement with the continuously changing droplets shape.

3.4 Explanation of particle accumulation

Knowing the Ca dependent internal flow fields resulting from a changed droplet shape, we come back to the observed particle accumulation: Figure 7 compares micrographs illustrating the particle accumulation pattern for high, medium and low Ca to the corresponding internal flow fields determined in the $z = 35\,\mu$m plane. Trajectories of particles trapped within the accumulation zones are indicated by (red) arrows. Blurry particles outside of these zones in the 'intermediate' regime in Fig. 7 b and c recirculate all over the droplet cross-section. Please note that the particle accumulation in Fig. 7a corresponds to the 'accumulation' regime whereas Fig. 7b,c correspond to different Ca within the 'intermediate' regime.

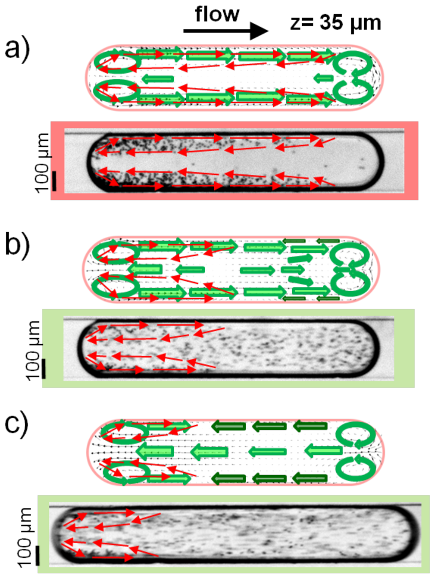

Fig. 7 Comparison of flow fields at $z = 35\,\mu$m and micrographs showing particle accumulation at corresponding Ca for the PMMA particles in pure water droplets: a) $Ca = 0.7 \cdot 10^{-3}$, $l_0 = 1.5\,$mm, $l_a/l_0 = 0.83$, b) $Ca = 2.6 \cdot 10^{-3}$, $l_0 = 1.5\,$mm, $l_a/l_0 = 0.83$ and c) $Ca = 5.5 \cdot 10^{-3}$, $l_0 = 1.9\,$mm, $l_a/l_0 = 0.31$. Closed particle trajectories within the accumulation zones visualized by arrows.

At low Ca, i.e. in the 'accumulation' regime, the gutters have a nearly constant height along the droplet. The continuous phase bypasses the droplet through these gutters, thus creating a three dimensional flow field inside the droplet that consists of four long vortex rolls spanning the entire droplet length. Following this flow field, particles suspended in the dispersed phase are transported to the droplet front along the rim of the droplet. If the sedimentation velocity of the particles is sufficiently large, i.e. here for the PMMA and the silica beads, particles sink to the droplet bottom while being transported forward. During this process, particles slide down the curved droplet interface which transports them towards the middle of the channel. In layers close to the channel bottom, the flow is directed backwards, transporting the sedimented particles to the rear. When the particles reach the rear cap of the droplet, the curved interface lifts them into higher layers, where particles again get caught by the strong forward flow in the gutter region, restarting the entire circle. The observed closed trajectories of the particles are visualized by arrows showing a good agreement between the particle accumulation zones and the vortices at the rim of the droplet, cf. Fig. 7a.

For sufficiently large Ca, droplets deform as discussed in section 3.2, which changes both the friction with the channel walls and with the continuous phase bypassing the droplets through the gutters. The changed friction induces a topological transition of the flow field. The four main vortices found at low Ca are replaced by a more complex pattern: In the droplet rear, the internal flow close to the rim is directed forwards whereas a backwards flow emerges in the droplet front in planes closer to the top and bottom of the channel. The backwards flow, however, limits the length of the particle accumulation zones in the 'intermediate' regime as illustrated in Fig. 7b and c. Thus, the extension of backwards flow regions explains the decaying length of the accumulation zones l_a/l_0 for increasing Ca, cf. Fig. 3c. Further increasing Ca, the internal flow inside the droplet becomes so vigorous that v_s is too slow for particles to sediment while being transported to the droplet front. Thus, complete mixing is observed particularly for short droplets at high Ca, cf. Fig. 3b.

In case of the PS particles with a 2.5 x lower sedimentation velocity compared to the PMMA particles, the particles do not sediment fast enough for the studied droplet length. Thus, even at low Ca, many particles reach the front cap of the droplet, where the flow transports them towards the droplet center. As a result the two accumulation zones at the droplets sides are found in coexistence with circulating particles in the droplet center ('intermediate' regime). For the slower sedimenting PS particles the 'accumulation' regime was found only for very long droplets $l_0 \geq 4\,\mathrm{mm}$. If sedimentation is entirely eliminated by density matching, particles simply follow the internal flow field and no accumulation was observed.

Obviously, the precondition for particle accumulation is sedimentation. As the density of biological cells is typically larger than the density of water or PBS buffer ,e.g. ρ(Yeast W303)$\approx 1.10\,\mathrm{g/cm^3}$ [32], ρ(E. Coli)$\approx 1.16\,\mathrm{g/cm^3}$ and ρ(Red Blood Cells)$\approx 1.14\,\mathrm{g/cm^3}$ [33], depending on cell cycle progression, environmental conditions and cell treatment, the present accumulation effect can be applied to concentrate cells on chip. Figure 1 presents one example of fixed yeast cells (bright particles) which accumulate in two clouds at the rear of a PBS droplet. Yeast represents a good model system due to its spherical shape and relatively large cell diameter, typically $4-6\,\mu\mathrm{m}$, resulting in a sedimentation velocity comparable to the used PS-particles in water. Accumulation of smaller and non-spherical species such as Escherichia Coli or red blood cells might deviate from the behavior of spherical particles. In general, the relatively small density differences between cells and surrounding buffer, in particular for small cell diameters, demands for long droplets and $Ca \approx O(10^{-4})$ for successful accumulation. Using shallower channels might facilitate cell accumulation by reducing the sedimentation height and thus lowering the threshold sedimentation velocity.

4 Conclusion and outlook

In the present paper a field-free particle accumulation effect is presented and characterized, acting on particles suspended in the dispersed phase of droplets flowing in rectangular channels, which are typically used in microfluidics. Three different particle accumulation regimes are observed: accumulation of all particles in two distinct zones at the rear side of the droplets for small Ca, an intermediate regime with coexisting accumulation zones and particles dispersed in the entire droplet for intermediate Ca and complete mixing for large Ca. The emergence of these patterns was explained by a coupling of gravity driven particle sedimentation to the internal flow field of the droplets. The internal flow field in droplets presents a topological transition upon increasing Ca, which has been shown to be caused by a shape change altering the drag of the droplet with surrounding continuous phase.

The present effect provides an efficient way to passively concentrate particles as well as biological cells in droplet microfluidics, allowing to perform washing steps. By simply adjusting the droplet velocity or altering the channel dimensions, particles can be easily accumulated or accumulated particles can be resuspended. To exploit accumulation of small particles and cells, most applications additionally require a step to finally increase the particle concentration within droplets. Using the particular symmetry of the accumulation zones, the channel geometry presented in Fig. 8 demonstrates one possible method to concentrate particles within different droplets. The droplet enters a triple-junction, where the main channel is split into three smaller channels. While passing the triple-junction, the droplet is split into three sub-droplets and excess dispersed phase is effectively removed by cutting out the depleted center region of the droplet. Particles are trapped in the two side droplets. Optimizing the channel dimensions and potentially cascading several droplet splitting steps alternating with merging steps of particle laden droplets, the particle concentration in the resulting droplets could be further increased. Combining the presented particle accumulation with such a concentration step potentially allows to include washing steps on-chip, e.g. for chemical binding of reactants to the particle surface and subsequent analysis.

The presented particle accumulation effect has been shown to be robust with respect to particle properties. Increasing particle density and diameter both increase the sedimentation velocity v_s and thus facilitate particle accumulation. However, once a sufficient sedimentation velocity is reached, particle accumulation did not significantly change within the examined parameter range upon varying particle properties to further increase v_s. Particle accumulation is most effective in long and wide droplets. In this situation, particle accumulation clouds are not limited by droplet length leading to a wider parameter range of the accumulation regime. Additionally, accumulation zones were found to merge for small droplet width, making concentration by splitting at triple junctions less effective. The achievable throughput for particle concentration at triple junctions is typically limited to few droplets by second due to droplet length and the velocity range suitable for particle accumulation, but could potentially be increased significantly by parallelization of splitting junctions. Also, using shallower channels might increase the achievable throughput by reducing the required sedimentation height. However, changing the channel aspect ratio might also impact the internal flow field.

Thus, it will be interesting for future studies to explore particle accumulation inside of droplets by systematically changing the aspect ratio of rectangular channels.

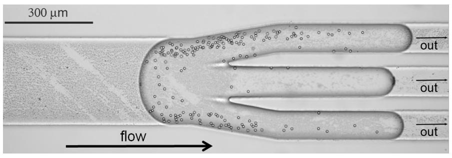

Fig. 8 Concentration of $d_p = 8\,\mu$m PMMA-particles by splitting a droplet showing particle accumulation. Channel height is $\approx 50\,\mu$m and $Ca \approx 6.1 \cdot 10^{-4}$.

5 Acknowledgements

Authors gratefully acknowledge the DFG-GRK1276 for financial support, Philipp Jung (Saarland University) for supplying the yeast cells used in Fig. 1, Dr. Jean-Baptiste Fleury (Saarland University) for vivid discussions and Dr. Hendrik Hähl (Saarland University) for advice in Matlab programming.

References

1 M. Schmitt, I. G. Bravo, P. J. F. Snijders, M. Pawlita, T. Waterboer and L. Gissmann, *J. Clin. Microbiol.*, 2006, **44**, 504512.
2 J.-W. Choi, K. W. Oh, J. H. Thomas, W. R. Heineman, H. B. Halsall, J. H. Nevin, A. J. Helmicki, H. T. Henderson and C. H. Ahn, *Lab Chip*, 2002, **2**, 27–30.
3 M. Toner and D. Irimia, *Annu. Rev. Biomed. Eng.*, 2005, **7**, 77–103.
4 K. Aran, A. Fok, L. A. Sasso, N. Kamdar, Y. Guan, Q. Sun, A. Ündar and J. D. Zahn, *Lab Chip*, 2011, **11**, 2858.
5 M. Yamada and M. Seki, *Lab Chip*, 2005, **5**, 12331239.
6 D. Di Carlo, D. Irimia, R. G. Tompkins and M. Toner, *Proc. Natl. Acad. Sci. USA*, 2007, **104**, 18892–18897.
7 D. Huh, J. H. Bahng, Y. Ling, H.-H. Wei, O. D. Kripfgans, J. B. Fowlkes, J. B. Grotberg and S. Takayama, *Anal. Chem.*, 2007, **79**, 13691376.
8 A. A. S. Bhagat, S. S. Kuntaegowdanahalli and I. Papautsky, *Microfluid. Nanofluid.*, 2009, **7**, 217226.
9 D. Di Carlo, *Lab Chip*, 2009, **9**, 30383046.
10 S. Patel, D. Showers, P. Vedantam, T.-R. Tzeng, S. Qian and X. Xuan, *Biomicrofluidics*, 2012, **6**, 034102.
11 C. Grenvall, C. Antfolk, C. Z. Bisgaard and T. Laurell, *Lab Chip*, 2014, **14**, 4629.
12 C. Derec, C. Wilhelm, J. Servais and B. Jean-Claude, *Microfluid. Nanofluid.*, 2010, **8**, 123130.
13 N. Pamme, *Lab Chip*, 2007, **7**, 16441659.
14 P. Sajeesh and A. K. Sen, *Microfluid. Nanofluid.*, 2014, **17**, 1–52.
15 D. Lombardi and P. S. Dittrich, *Anal. Bioanal. Chem.*, 2011, **399**, 347352.
16 E. Brouzes, T. Kruse, R. Kimmerling and H. H. Strey, *Lab Chip*, 2015, **15**, 908–919.
17 G. Kurup and A. S. Basu, *Biomicrofluidics*, 2012, **6**, 022008.
18 M. Sun, Z. S. Khan and S. A. Vanapalli, *Lab Chip*, 2012, **12**, 5225–5230.
19 F. P. Bretherton, *J. Fluid Mech.*, 1962, **10**, 166188.
20 S. Hodges, O. Jensen and J. Rallison, *J. Fluid Mech.*, 2004, **501**, 279–301.
21 H. Wong, C. Radke and S. Morris, *J . Fluid Mech.*, 1995, **292**, 71–94.
22 H. Wong, C. Radke and S. Morris, *J. Fluid Mech.*, 1995, **292**, 95–110.
23 F. Sarrazin, K. Loubière, L. Prat and C. Gourdon, *AIChE Journal*, 2006, **52**, 4061–4070.
24 H. Kinoshita, S. Kaneda, T. Fujii and M. Oshima, *Lab Chip*, 2007, **7**, 338–346.
25 D. Malsch, M. Kielpinski, R. Merthan, J. Albert, G. Mayera, J. Köhler, H. Süße, M. Stahl and T. Henkel, *Chem. Eng. J.*, 2008, **135S**, S166S172.
26 M. Oishi, H. Kinoshita, T. Fujii and M. Oshima, *Meas. Sci. Technol.*, 2011, **22**, 105401.
27 S. Jakiela, P. M. Korczyk, S. Makulska, O. Cybulski and P. Garstecki, *Phys. Rev. Lett.*, 2012, **108**, 134501.
28 S. Ma, J. M. Sherwood, W. T. S. Huck and S. Balabani, *Lab Chip*, 2014, **14**, 3611–3620.
29 D. C. Duffy, J. C. McDonald, O. J. A. Schueller and G. M. Whitesides, *Anal. Chem.*, 1998, **70**, 4974–4984.
30 J.-C. Baret, *Lab Chip: Chips and Tips*, 2009.
31 S. Jakiela, S. Makulska, P. M. Korczyk and P. Garstecki, *Lab Chip*, 2011, **11**, 3603.
32 A. K. Bryan, A. Goranov, A. Amon and S. R. Manalis, *Proc. Natl. Acad. Sci. USA*, 2010, **107**, 999–1004.
33 M. Godin, A. K. Bryan, T. P. Burg, K. Babcock and S. R. Manalis, *Appl. Phys. Lett.*, 2007, **91**, 123121.

Flow field induced particle accumulation inside droplets in rectangular channels - Supplemental Information

Michael Hein,[a] **Michael Moskopp,**[a] **and Ralf Seemann***[a,b]

Received 9th April 2015, Accepted 20th May 2015
First published on the web 20th May 2015
Lab on a Chip DOI: 10.1039/C5LC00420A

1 Device Fabrication

Experiments were performed in microfluidic chips produced by standard soft-lithography[1]. In a first step, a negative photo resists (Su-8-100, MichroChem) was spin-coated on a silicon wafer, resulting in a resist film of $(100 \pm 5)\,\mu$m thickness that determines the channel height of the final device. SU-8 50, which is less viscous than SU-8 100, allows for lower film thickness and was used for devices with a smaller channel height, as used in Fig. 1 and Fig. 8. After transferring the channel geometry by UV-exposure and developing the resist, the resulting structure was used as a mold for device production. Liquid PDMS (Sylgard 184, DowCorning) was mixed at a ratio of base to curing agent of 10:1, poured onto the mold, cured and subsequently peeled off. The resulting PDMS slap containing the channel geometry was plasma bonded (Femto Plasma-Cleaner, Diener Electronic GmbH) to a glass slide to seal the channel after punching holes for inlets and outlets. Teflon tubing was inserted into these holes and inlets were connected to gas-tight glass syringes (Hamilton).

2 μPIV and fluorescence microscopy

Micro-Particle Image Velocimetry (μPIV) is a non-invasive, optical method to measure 2D flow fields on a micro-scale, first introduced by Santiago et al.[2]. In a μPIV experiment, the movement of small fluorescent tracer particles dispersed in the fluid and illuminated by two following laser pulses is imaged by a microscope and a camera. Subsequently, the two dimensional flow field in the image plane is calculated by cross-correlation of the recorded particle patterns. The optical setup consisted of an inverted microscope (Axio Observer Z1, Zeiss) with a motorized focal positioning system (motorized z-axis) and equipped with a 10x0.45 air objective (Apochromat, Zeiss). Images were recorded at different z-positions with a CCD camera (ImagerProX 2M, LaVision) coupled to the microscope by a 0.63 x camera adapter (Zeiss). Sample illumination was performed using a 532 nm DPSS-laser (LaVision, 2.72W) with pulse lengths ranging from 0.5 ms to 2 ms. The setup was computer controlled and PIV processing of the recorded images was performed using the DaVis 8.1.2 software package (LaVision). In μPIV experiments, fluorescent particles made of PS with a diameter of $1\,\mu$m (FluoroMax Red, Thermo Scientific) were mixed with the dispersed phase at a concentration of about $3.1 \cdot 10^9\,\mathrm{ml}^{-1}$.

One particular feature of μPIV is the use of volume illumination, which results in a typically unknown thickness of the measurement plane, known as Depth of Correlation (DOC), that depends on flow gradients, the tracer particles and the specific optical system. Estimating the DOC is crucial when planning experiments on complex 3D flows as present in droplets in rectangular channels, as the final measured velocity vector is a weighted average of all particle signals within the DOC. Recently, Hein et al.[3] published a method to precisely determine the DOC, considering out-of-plane gradients. Using this method and estimating the out-of-plane gradients from experimental data, the DOC in the present experiments was determined to vary between $11.2\,\mu$m and $15.3\,\mu$m. The vertical distance between measured planes was chosen accordingly.

The optical setup used to measure the flow field inside of elongated droplets by μPIV was also used to characterize the thickness of the surrounding oil films and the depth of the oil filled gutters in the corners of the channels. For these measurements, the continuous phase was dyed with Fluorescein27 at a concentration of 2 g/l. Focusing on the bottom of the channel, the fluorescence intensity then is a function of oil layer thickness. Calibration measurements performed on oil-filled channels of heights ranging from $11\,\mu$m to $68\,\mu$m indicate a linear increase of fluorescence intensity with oil layer thickness. However, the presence of the curved droplet interface, the channel walls and the second oil-filled gutter are expected to influence the measured intensities, especially when determining the gutter height next to the channel walls, cf. Fig. 4b. Thus, we refrain from converting the measured fluorescence intensities into absolute height values, although converted gut-

---

[a] *Saarland University, Experimental Physics, Saarbrücken, Germany. Fax: +49 681 302 71700 ; Tel: +49 681 302 71777; E-mail: r.seemann@physik.uni-saarland.de*
[b] *Max Planck Institute for Dynamics and Self-Organization, Göttingen, Germany.*

ter heights and oil film thickness surrounding the droplet quantitatively agree with theoretical predictions[4]. Instead, the data in Fig. 4 is given in intensity counts and solely used to indicate changes of the droplet shape with increasing *Ca*.

The droplet motion through the field of view poses additional complexities when measuring both the flow fields as well as the fluorescence intensity of the oil phase that determines the height of the surrounding oil films. To reduce the effect of outliers in the instantaneous flow fields calculated by DaVis, a custom matlab script was used to perform averaging over several measured droplets. First the droplet velocity was subtracted from the measured flow fields to transform to the co-moving frame of reference of the droplet. To account for experimental fluctuations of droplet length, each vector field was superposed by a grid of (45x11) boxes. All vectors inside the same box were averaged, thus creating velocity fields of a given size and a typical spacial resolution of (30x30) μm. In a next step these velocity fields of uniform size were averaged for each measured droplet velocity and each measurement plane. Thus for each measured plane the x and y components of the flow velocity were determined, whereas the out-of-plane component is not accessible with the available μPIV-system. The same averaging procedure with a grid of (446x163) boxes was used for statistical analysis of the fluorescence intensity distribution of the surrounding oil layers. Profiles in Fig. 4 and Fig. 6 were subsequently extracted from the averaged data. $v_{rim}(x)$ was averaged over the boxes at the droplet interface on both sides. The fluorescence intensity determining the gutter height was averaged over three boxes on each side of the droplet about 9 μm from the estimated position of the channel sidewalls. Subsequently, a smoothing over the next 10 neighbors was used to reduce noise in the fluorescence signals.

References

1 D. C. Duffy, J. C. McDonald, O. J. A. Schueller and G. M. Whitesides, *Anal. Chem.*, 1998, **70**, 4974–4984.

2 J. G. Santiago, S. T. Wereley, C. D. Meinhart, D. J. Beebe and R. J. Adrian, *Exp. Fluids*, 1998, **25**, 316–319.

3 M. Hein, B. Wieneke and R. Seemann, *Meas. Sci. Technol.*, 2014, **25**, 084008.

4 H. Wong, C. Radke and S. Morris, *J . Fluid Mech.*, 1995, **292**, 71–94.

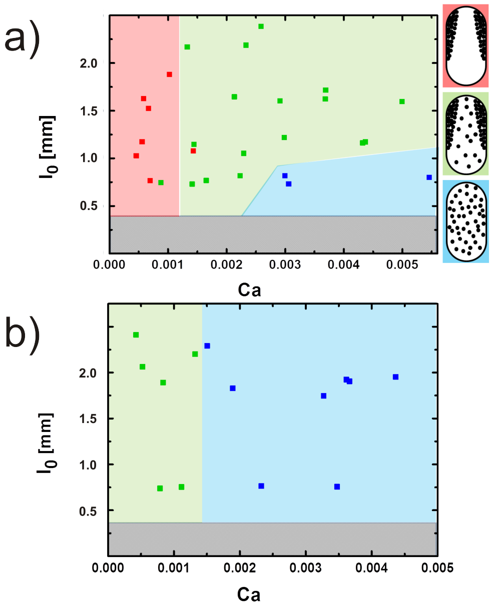

SI 1 'Phase-like' diagrams of particle accumulation for a) silica particles (Ø5 μm) and b) PS particles(Ø10 μm) within water droplets surrounded by n-hexadecane. 2 wt.% Span80 were added to the continuous phase. Sketches on the right depict the 'accumulation', 'intermediate' and 'mixing' regime and are shaded in the color of the corresponding phase.

Addendum V: Calculation of the weighting function and determination of the depth of correlation in micro-PIV from experimental particle images

Meas. Sci. Technol. **25** (8) 084008 (2014) **DOI:** 10.1088/0957-0233/25/8/084008.

Authors: M. Hein[1], B. Wieneke[2] and R. Seemann[1,3]

[1] Department of Experimental Physics, Saarland University, Saarbrücken, Germany
[2] LaVision GmbH, Göttingen, Germany
[3] Dynamics of Complex Fluids, MPI for Dynamics and Self-Organization, Göttingen, Germany

With kind permission of IOP Publishing.

This is an author-created, un-copyedited version of an article accepted for publication in Measurement Science and Technology. IOP Publishing Ltd is not responsible for any errors or omissions in this version of the manuscript or any version derived from it. The Version of Record is available online at DOI: 10.1088/0957-0233/25/8/084008.

Author Contributions:

Research was designed by M. Hein and B. Wieneke. Experiments were performed by M. Hein. Data was analyzed by M. Hein and B. Wieneke. The theoretical backbone was developed by B. Wieneke and M. Hein. Article was written by M. Hein. Writing was supervised by B. Wieneke, and R. Seemann. Research was directed by B. Wieneke and R. Seemann.

Abstract:

Micro-particle image velocimetry (μPIV) uses volume-illumination and imaging of particles through a single microscope objective. Displacement fields are obtained by image correlation and depend on all imaged particles, including defocused particles. The measured in-plane displacement is a weighted spatial average of the true displacement, with a weighting function $W(z)$ that depends on the optical system and flow-gradients. The characteristic width of the weighting function $W(z)$ is also referred to as depth of correlation (DOC) and is a measure up to which distance from the focal plane particles influence the measurement, which is crucial for the interpretation of measured flow fields. We present procedures to determine the $W(z)$ from which the DOC can be derived and to directly determine the *DOC* from PIV double images, generated from experimentally recorded particle images. Both procedures provide comparable *DOC* results. Our approach allows determination of the *DOC* and $W(z)$ as a function of out of plane gradients, optical setup parameters and PIV-analysis parameters. Experimental results for different objectives and particle sizes are discussed, revealing substantial deviations from theoretical predictions for high NA air-objectives. Moreover, using the determined weighting function $W(z)$, the correction of measured flow profiles for errors introduced by the spatial averaging is demonstrated.

Calculation of the weighting function and determination of the depth of correlation in μPIV from experimental particle images

M Hein[1,3], B Wieneke[2] and R Seemann[1,3]

[1] Department of Experimental Physics,
Saarland University, Saarbrücken, Germany
[2] LaVision GmbH, Göttingen, Germany
[3] MPI for Dynamics and Self-Organization,
Göttingen, Germany

E-mail: michael.hein@physik.uni-saarland.de

Meas. Sci.Technol. 25 (8) 084008 (2014) DOI: 10.1088/0957-0233/25/8/084008
Special Issue PIV'13 "Current developments in Particle Image Velocimetry"
Received 30 November 2013, Accepted 3 June 2014, Published 14 July 2014

Abstract. Microscopic Particle Image Velocimetry (μPIV) uses volume-illumination and imaging of particles through a single microscope objective. Displacement fields are obtained by image correlation and depend on all imaged particles, including defocused particles. The measured in-plane displacement is a weighted spatial average of the true displacement with a weighting function *W(z)*, that depends on the optical system and flow-gradients. The characteristic width of the weighting function *W(z)* is also referred to as Depth of Correlation (*DOC*) and is a measure up to which distance from the focal plane particles influence the measurement, which is crucial for the interpretation of measured flow fields. We present procedures to determine the *W(z)* from which the *DOC* can be derived and to directly determine the *DOC* from PIV double-images generated from experimentally recorded particle images. Both procedures provide comparable *DOC*-results. Our approach allows to determine the *DOC* and *W(z)* as a function of out of plane gradients, optical setup parameters and PIV-analysis parameters. Experimental results for different objectives and particle sizes are discussed, revealing substantial deviations from theoretical predictions for high *NA* air-objectives. Moreover, using the determined weighting function *W(z)*, the correction of measured flow profiles for errors introduced by the spatial averaging is demonstrated.

Keywords: microscopic particle image velocimetry, PIV, depth of correlation, weighting function, microfluidics
PACS: 47.80.Jk, 47.80.-v, 47.85.Np, 47.85.-g

1. Introduction

Due to its simplicity, reliability and its non-invasive measurement technique Particle Image Velocimetry (Adrian 1991) is one of the most frequently used methods to measure flow profiles on a macro-scale. In standard PIV experiments tracer particles suspended in the fluid are imaged using a camera and a laser light sheet illumination. If the focal length of the imaging setup is large, all tracer-particles in the light-sheet are in focus. Thus the spatial extent of the measurement plane is precisely known by the light-sheet dimensions and the camera field of view. Typically two images with a short time delay are recorded. By cross-correlating these two images a displacement pattern is obtained, which can be transferred into a velocity field.

To measure flows on the micro-scale Santiago et al. (1998) introduced Micro-Particle Image Velocimetry (µPIV) which is employed in many fields ranging from fluids-engineering to biological systems (Meinhart and Zhang 2000, Vennemann et al. 2006) both in fundamental research and industrial application. In a µPIV experiment tracer particles suspended in the fluid are imaged using a microscope and a camera. Typically, fluorescent particles are used to reduce background noise and their emission signal is isolated from reflected laser or background light by cut-off filters. µPIV illuminates and records the particles through a single microscope objective. Because all tracer particles in the whole volume are illuminated and even defocused particles contribute to the measured displacement, it is difficult to determine the thickness of the measurement plane (Depth of Correlation, *DOC*). To be able to interpret the measured velocity profiles, especially in the case of complex three dimensional flows, a precise knowledge of the *DOC* is essential.

In order to predict the influence of defocused particles on µPIV measurements several approaches to determine the *DOC* have been presented. Olsen and Adrian (2000) analytically examined the influence of out-of-focus particles on the measured displacement dx_{meas}, assuming that the defocusing of particles can be described using Gauss-optics, a single thin lens model and neglecting the influence of any velocity gradients. For a better understanding of the reasoning in this article, the most important steps in deriving a theoretical prediction of the DOC which was first introduced by Olsen and Adrian (2000) are briefly summarized. In their original work it was stated that the measured velocity in an ideal µPIV-experiment is given by a weighted average of the true displacement function $dx(z)$, provided the out-of-plane gradients are not too large:

$$dx_{meas} = \frac{\int_{-\infty}^{+\infty} dx(z) \cdot W(z) dz}{\int_{-\infty}^{+\infty} W(z) dz}, \qquad (1)$$

where in the following the weighting function $W(z)$ is normalized with $\int W(z) dz = 1$. For the focal distance of an objective being much larger than the distance of the particle from the focal plane the weighting function has been expressed as:

$$W_{part}(z) = \frac{const.}{d_e^4(z)} \tag{2}$$

Using $d_e(z) = (a + bz^2)^{1/2}$ which is a simplified expression for the particle image diameter the weighting function has the functional form of $W(z) = c/(a + bz^2)^2$. With $\int W(z)dz = 1$ and using the standard deviation σ, defined by $\sigma^2 = \int z^2 W(z)dz$, this can be rewritten as:

$$W_{part}(z) = \frac{2}{\pi\sigma_{part}} \cdot \frac{1}{\left(1 + \left(\frac{z}{\sigma_{part}}\right)^2\right)^2}, \tag{3}$$

where σ_{part} is a function of particle diameter, f-Number and magnification of the optical setup. Olsen and Adrian (2000) defined a *DOC* by twice the distance *z* from the focal plane where *W(z)* drops to certain drop-off threshold, $\varepsilon W(z=0)$. Inserting (3) into this definition of the DOC leads to:

$$DOC_{theory} = 2 \cdot \left(\frac{(1-\sqrt{\varepsilon})}{\sqrt{\varepsilon}}\right)^{\frac{1}{2}} \sigma_{part}. \tag{4}$$

Bourdon et al. (2006) adapted the DOC derived by Olsen and Adrian (2000) by including immersion optics and using the numerical aperture *NA* which is more common for microscope objectives than the f-Number :

$$DOC_{theory} = 2 \cdot \left(\frac{(1-\sqrt{\varepsilon})}{\sqrt{\varepsilon}}\left[\frac{n_0^2 d_p^2}{4NA^2} + \frac{5.95(M+1)^2 \lambda^2 n_0^4}{16M^2 NA^4}\right]\right)^{\frac{1}{2}}. \tag{5}$$

Here, n_0 is the refractive index of the immersion medium of the objective, *M* is the magnification of the objective, λ specifies the wavelength of the detected fluorescence light and d_p is the particle diameter. Equation (5) is, with minor changes, frequently used to estimate the *DOC* (Vennemann et al. 2006, Lindken et al. 2009). However, (5) does not account for optical refraction when imaging in a medium having different refractive index, n_w, than the immersion medium. In such a situation, (5) has to be corrected using the paraxial approximation, i.e. multiplying (5) with $\frac{n_w}{n_0}$ as proposed by Rossi et al. (2012).

The theoretically derived equations for the DOC (4), (5) depend on the rather arbitrary choice of the drop-off threshold ε. In the past, often a value of $\varepsilon = 0.01$ has been chosen which relates to a *DOC* of 6σ. However, filter kernel sizes are usually defined by e.g. the full width half maximum FWHM, $\pm\sigma$, or at most $\pm 2\sigma$. Since one commonly associates a *DOC* with the range of depth where the measured velocity is roughly the average of the true velocities, a choice of 6σ is rather misleading; for comparison, a simple top-hat filter has a length L of $2\sqrt{3}\sigma = 3.46\sigma$. Therefore, *DOC* = 4σ, corresponding to a drop-off value of $\varepsilon = 0.04$, is chosen in the following. The thus defined DOC_{theory} (5) will be used for later comparison to experimental results.

While any such definition of the *DOC* is arbitrary, it is the underlying weighting function *W(z)* – and not only the curve width but also the shape - which determines the measured displacement. Moreover, a known weighting function *W(z)* can be used to correct measured velocity fields by solving (1) for *dx(z)* as shown later in the present work.

To determine *W(z)* and thus the *DOC*, several groups analyzed the shape of autocorrelation peaks of particle images. Thus, similar to the derivation of (5) they neglected any velocity gradients, that are expected to influence the *DOC* and the shape of *W(z)*. Out-of-plane gradients lead to a reduction of the *DOC* (Olsen 2010) whereas in-plane gradients should increase the *DOC* (Olsen 2009). While the influence of in-plane gradients can be compensated by decreasing the size of the interrogation windows or by window-deformation techniques, the influence of out-of-plane shear cannot easily be accounted for (Westerweel et al. 2004, Nogueira et al 2001,Nogueira et al 1999). Additionally, by analyzing the shape of autocorrelation peaks, effects of overlapping particle images at different distances to the focal plane are not taken into account. Both the influence of out-of-plane gradients and overlapping particle images are included in our approach to determine *W(z)* and the *DOC*. Bourdon, Olsen and Gorby (2006 and 2004b) observed good agreement between Olsen and Adrian's (2000) model and experimental results for *NA* ≤ 0.4 air and immersion objectives. Recently, Rossi et al. (2012) showed significant asymmetries in the measured *W(z)* not predicted by existing theory for high *NA* air objectives or more complex optical setups, such as multi-lens systems or specialized microscopes. In these cases, where the simplifications used by Olsen and Adrian (2000) do not hold anymore, (5) significantly underestimates the *DOC* (see also Kloosterman et al. 2011).

To include the influence of out-of-plane gradients, Poelma et al. (2012) recently presented an attempt to model the *DOC*-related underestimation of blood-flow velocities by µPIV as a function of the optical setup, tracer size and blood vessel size. They used autocorrelations of experimental particle images to create a correlation peak function by summing up the radial components of autocorrelation peaks of particle images at varying distances from the focal plane shifted by an assumed parabolic flow profile. From these correlation maps, the position of the correlation peak and thus the measured velocity was determined and compared to the average velocity imposed when generating the final correlation map. Thus their method also neglects any effects of overlapping particle images and is limited to determination of the *DOC* only.

In this paper two approaches to determine the weighting function *W(z)* and the *DOC* from experimental images are presented. The first method determines the shape of *W(z)* from which the *DOC* can be derived while the second method uses an approximation for *W(z)* to determine the *DOC*.

This second approach is faster and easier and is thus especially useful when planning experiments and in any situation where knowledge of the measurement volume is sufficient to interpret measurement results. Both approaches account for out-of-plane shear expected to reduce the *DOC* (Olsen 2010) and allow varying parameters such as particle size and PIV analysis parameters. Thus it is possible to explicitly determine both the exact shape of *W(z)* and the *DOC* for any expected experimental situation, using the same experimental setup and analysis parameters as for actual experiments.

The presented methods are based on correlating generated PIV double-images that have been constructed from experimentally recorded particle images, imposing any specific displacement field as a function of depth. Both the *DOC* and the weighting functions *W(z)* can be determined from the displacement fields obtained by using any typical PIV-algorithm. The results of the determined *W(z)* and *DOCs* are discussed for several objectives typically used for µPIV with numerical apertures ranging from 0.5 to 1.4 using different tracer particle diameters and a range of out-of-plane gradients spanning two orders of magnitude. Finally, the knowledge of *W(z)* for a given experimental situation is used to correct an actual PIV-measurement of an out-of-plane parabolic flow profile.

2. Methods

The methods presented here to determine the weighting function *W(z)* and the *DOC* are based on the analysis of PIV-double images generated from experimental particle images. In the following subsections the general strategy for generating synthetic PIV double-images and how the weighting function *W(z)* and the *DOC* can be derived is described.

2.1. Particle image recording and double-image generation

Experimental particle images were obtained by imaging polystyrene micro-particles (Thermo Scientific, Fluoro-Max, Green fluorescent, 0.5, 1 and 2 µm diameter) fixed on a microscopy slide. The particles were fixed on a cleaned microscopy slide by blow-drying a drop of the particle suspension. To avoid the formation of particle agglomerates the particle suspensions were diluted with ethanol prior to the deposition. Using this procedure, patches with randomly distributed particles were obtained with only very few particle clusters, that might influence the *DOC* determination.

The imaging system consists of an inverted microscope (Zeiss Axio Observer Z1) equipped with a motorized focal positioning system (motorized *z*-axis), a CCD camera (Imager ProX, LaVision) coupled to the microscope by a 0.63x camera adapter (Zeiss), a laser for fluorophor excitation (473 nm, 1.5 W, LaVision), and a filter cube that isolates the fluorescence signal from scattered laser- and background-light. The whole setup was computer-controlled using the DaVis 8.1.2 package of LaVision.

Several objectives, including air, water and oil immersion objectives, were tested with magnifications ranging from 20x to 50x having numerical apertures from 0.5 to 1.4. To account for the typical differences in intensity and background noise of the two frames constituting a PIV double-image, which are caused by the different camera exposure times, double-images were recorded as in real measurements. To capture not only the raw-images of the particles in focus but also the raw images which 'simulate' the unfocused particles in the subsequently generated PIV double-images, double-images were recorded in 0.5 µm steps along the *z*-axis below and above the particle plane. At every focal position typically 30-100 double-images were captured and averaged to reduce camera and laser noise. The resulting averaged double image for every *z*-position was used for all subsequent data treatment.

In the following it is explained how the PIV double-images used to determine *W(z)* and the *DOC* are generated from the experimental particle images. In a first step sub-windows at the same random position in both frames of the averaged particle images are selected for each *z*-position. To achieve a desired seeding density, multiple of those random sub-windows were summed up to one double-image of the same size as the sub-windows. In the experiments typically 30 sub-windows were used. A sliding minimum subtraction was performed to remove background glow that is increased by the summation of sub-windows. This image generation guarantees a sufficiently large particle density in the sub-windows and avoids large particle clusters which would appear when imaging samples with larger prepared particle densities and which could influence the subsequent analysis.

The first frame of the final 'PIV-double images' were generated by summing up the thus constructed sub-windows of the first frames for all recorded z-positions. Similarly, the particle-images for each *z*-position in the second frame were also summed up but were additionally shifted laterally according to a given displacement function *dx(z)* before summation, as illustrated in figure 1. By specifying the displacement function *dx(z)* used to construct the PIV double-images, any flow field can be mimicked. For the latter analysis of the *DOC* and *W(z)* different displacements functions *dx(z)* and different strategies for the image summation are used as specified in detail in the following sections. To determine dx_{meas} the thus generated PIV double-images can be cross-correlated using any PIV algorithm. By comparing dx_{meas} to the applied displacement function *dx(z), W(z)* and the *DOC* can be derived as will be explained in the remainder.

For the results presented here, the standard multi-pass PIV-algorithm implemented in DaVis 8.1.2 with square interrogation windows of (128x128) px^2 and 4 iterations was used. The double-images were post processed using standard multi-pass post processing (1x median filter to remove and replace outliers based on an rms-threshold, comparing the vector to its neighbors and replacing it with the next highest correlation peak if this better fits the threshold). However, as the applied displacement function is uniform over the whole image, outliers are not expected and multi-pass post processing is not expected to have any relevant influence on the measured displacement.

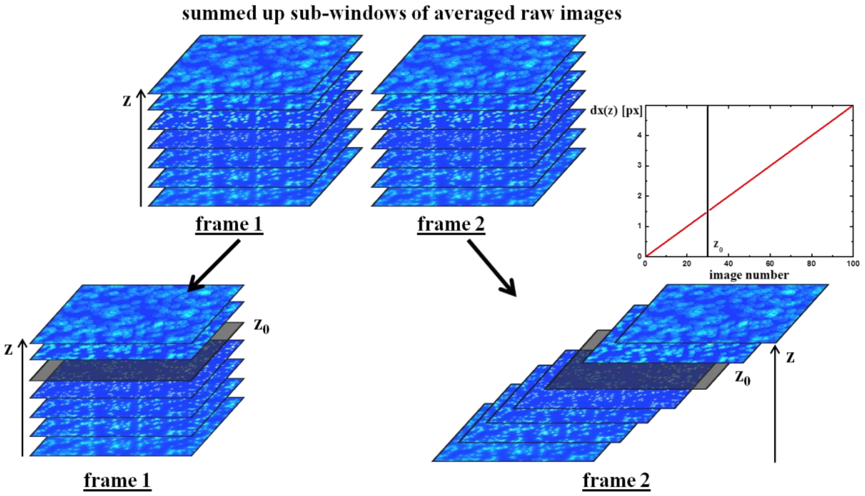

Figure 1 Schematic of the PIV double-image generation: Top row: *z*-stacks of averaged (and summed up) sub-windows for the first and second frame of a double image. Bottom row: Both frames of the generated PIV double-images. To determine the weighting function *W(z)*, particle images at one particular *z*-position were left out (dark planes at z_0).

2.2. Determination of the weighting function W(z) and DOC

In this section, it is explained how the weighting function *W(z)* can be extracted from synthetic particle images and how the *DOC* can be determined from *W(z)*. Calculations or measurements in correlation space are not needed. To generate the synthetic images a linear displacement $dx(z) = zg_z$ is applied (see figure 2) where g_z is the gradient of the velocity in *z*-direction.

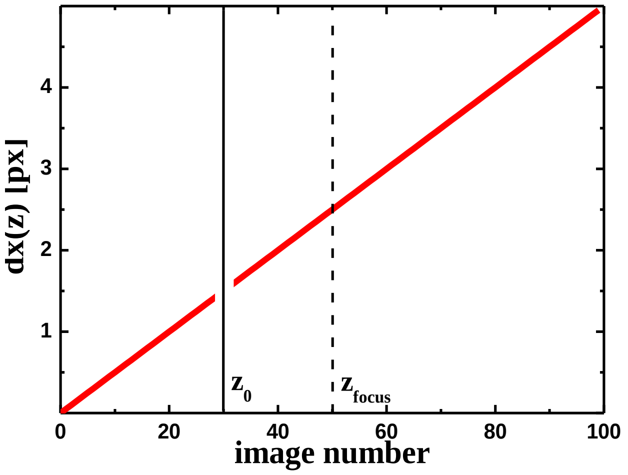

Figure 2 Linear displacement function *dx(z)* for generating PIV double-images used to derive *W(z).*

First, a single PIV double-image is computed by shifting the sub-windows of the averaged raw-images at all z positions in the second frame. The measured displacement dx_{meas} from this double-image will later serve as a reference. Furthermore, the position of the focal plane z_{focus} can be directly determined by $z_{focus} = dx_{meas} / g_z$ according to (1). For the example given in figure 2, the focal plane is at about 50 µm. This is used later for deriving $W(z)$. In experiments, the focal positions determined this way varied less than 1 µm from the visually determined position. Secondly, PIV double-images are computed applying the same displacement function but omitting particle images at one particular z-position z_0, as indicated in figure 2 by a break in the red (bold) line and by the darker planes in figure 1. By systematically varying the position of the omitted particle image the influence of particles at every z_0-position can be explored by a standard PIV-analysis. For every such generated double-image a measured displacement $dx_{meas}(z_0)$ is obtained. dx_{meas} is about 1 – 40 pixel, depending on the applied gradient g_z with an uncertainty of typically about 0.01 - 0.1 pixel.

Subtracting $dx_{meas}(z_0)$ from the displacement dx_{meas} of the reference double-image using (1) leads to:

$$\Delta dx(z_0) = \sum_{z'} W(z'-z_{focus}) \cdot g_z \cdot z' - \frac{\sum_{z' \neq z_0} W(z'-z_{focus}) \cdot g_z \cdot z'}{\sum_{z' \neq z_0} W(z'-z_{focus})}, \qquad (6)$$

where W is now the dimensionless discrete weighting function satisfying $\sum W(z) = 1$ due to the discrete nature of the experimental data. An example of the thus determined displacement differences $\Delta dx(z_0)$ is shown in figure 3a. The displacement differences $\Delta dx(z_0)$ are about zero remote from the focus point, indicating that the particle images remote from the focus point do not significantly contribute to the measured displacement. The focus point z_{focus} is exactly at the zero-crossing of $\Delta dx(z_0)$. For a symmetric weighting function $W(z)$ the shape of $\Delta dx(z_0)$ is point symmetric as seen in the given example.

According to (1) the first term on the right-hand side of (6) is $g_z z_{focus}$ and the nominator of the second term therefore $g_z z_{focus} - W(z_0 - z_{focus}) g_z z_0$. Replacing the denominator of the second term by $1 - W\left(z_0 - z_{focus}\right)$ leads to:

$$\Delta dx(z_0) = g_z \cdot z_{focus} - \frac{g_z \cdot z_{focus} - W(z_0 - z_{focus}) \cdot g_z z_0}{1 - W(z_0 - z_{focus})} . \qquad (7)$$

Replacing $z_0 - z_{focus}$ by z and solving for $W(z)$, an expression for the weighting function is derived that solely depends on known or measurable parameters (see figure 3b):

$$W(z) = \frac{\Delta dx(z)}{g_z \cdot z + \Delta dx(z)}. \tag{8}$$

Close to the focus position $z = 0$ both the denominator and the numerator are about zero, (8) becomes unstable and large error in the measured weighting function are expected. To reduce the error caused by noise the measured *W(z)*-profiles are smoothed by a 3-point Gaussian weighting for each data point.

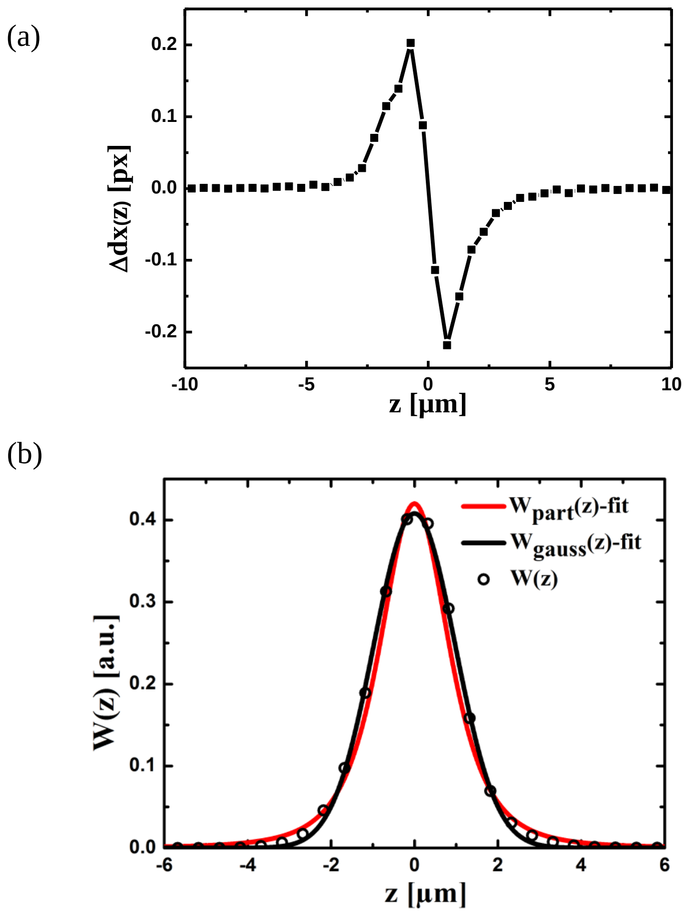

Figure 3 Displacement difference *Δdx(z)* (a) and weighting function *W(z)* (b) for a 40x1.4 Plan Apochromat oil immersion objective (Zeiss) using 1 µm particles and an out-of-plane gradient of $g_z = 0.7$ px/µm. The focal plane is at $z = 0$.

Having determined the weighting function *W(z)*, the *DOC* is readily obtained: The *DOC* is a measure for the distance to the focal plane to which particles influence the measured displacement and is defined here as proportional to the curve width of the weighting function *W(z)*. As discussed earlier, the definition of *DOC* = $k\sigma$ with k = 4 is applied:

$$DOC_{W(z)} = 4 \cdot \sigma_{W(z)} = 4 \cdot \sqrt{\sum_z W(z) \cdot z^2} \, . \tag{9}$$

As the measured *W(z)* always presents noise, only the center region of the measured *W(z)* between the first points where *W(z) = 0* is considered to calculate the *DOC*-values. The results of measured weighting functions and the derived $DOC_{w(z)}$ values are discussed for several objectives, out-of-plane gradients g_z and particle sizes in section 3. Furthermore, in section 4 it is presented that µPIV inherent errors in measured flow profiles close to channel walls or regions of large out-of-plane curvatures of the flow profile can be successfully corrected with a known weighting function.

2.3. Quantification of the DOC using approximations for W(z)

In the previous section a method was presented to derive the weighting function *W(z)* from a series of generated PIV double-images and how the *DOC* can be obtained from the curve width of *W(z).* In this section a method is presented to determine the *DOC* from a single PIV double-image for different out-of-plane gradients approximating the weighting function e.g. by a Gaussian shape.

Following the protocol described in section 2.1 a single synthetic double-image is generated for all *z*-positions applying the displacement function $dx(z) = g_z|z|$ that increases symmetrically with distance from the focal plane at z = 0 (see figure 4, red (grey) line). The displacement dx_{meas} measured from such a synthetic double-image (circle) is non-zero at the focal plane z = 0 due to the influence of the positive velocities at both sides of the focal plane. This displacement dx_{meas} is directly related to the width of the weighting function (black line) which determines the *DOC*-value. The random error of dx_{meas} is typically within 0.001 - 0.05 pixel, which is very accurate compared to the corresponding displacement dx_{meas} of 0.03 - 3 pixel, depending on the gradient g_z. With dx_{meas} the *DOC* can be calculated using (1) assuming a specific functional type for the weighting function *W(z).* Using a Gaussian to approximate *W(z)*, (1) yields

$$dx_{meas} = \int_{-\infty}^{+\infty} g_z|z| \cdot \frac{1}{\sqrt{2\pi} \cdot \sigma} e^{\frac{-z^2}{2\sigma_{gauss}^2}} dz = g_z \cdot \sigma_{gauss} \cdot \sqrt{\frac{2}{\pi}} \, , \tag{10}$$

where σ_{gauss} is the standard deviation. Following the same arguments as used to derive (9), i.e. that the *DOC* can be expressed in terms of the standard deviation, yields:

$$DOC_{gauss} = 4 \cdot \sigma_{gauss} = 4 \cdot \sqrt{\frac{\pi}{2}} \frac{dx_{meas}}{g_z} \, . \tag{11}$$

Using this formula the *DOC* can be determined from a single PIV double-image for the out-of-plane gradient as specified by g_z and for the fluorescent particles and objective used to capture the raw data. Note, that the chosen value $k = 4$ in (11) would compare to a drop-off threshold ε of 0.13 in (4).

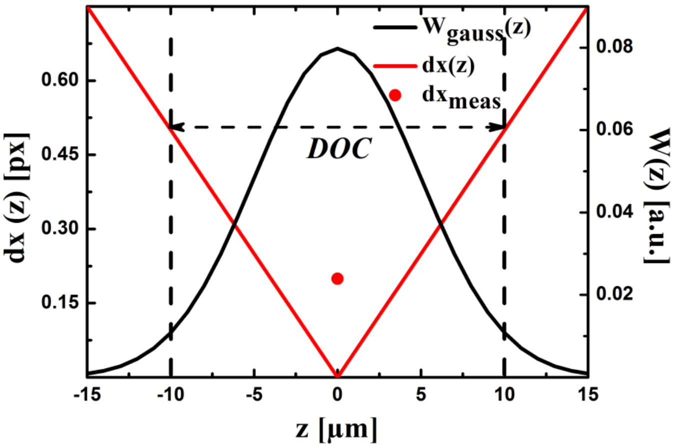

Figure 4 Schematic of the dependence of dx_{meas} on both the displacement function *dx(z)* used to generate the PIV double-images and the width of the weighting function *W(z)*.

Alternatively to the Gaussian weighting function the *DOC* can be also calculated using the classical particle weighting function $W_{part}(z)$ according to (2) and (3) that is based on the analysis of the diameter d_e of a particle image assuming Gaussian optics. The integral $\int g_z|z|\,W_{part}(z)dz$ can be readily solved leading to $dx_{meas}(z=0) = \frac{2}{\pi} g_z \sigma_{part}$, thus:

$$DOC_{part} = 4 \cdot \sigma_{part} = 2 \cdot \pi \cdot \frac{dx_{meas}}{g_z}, \tag{12}$$

which agrees within a factor of $\sqrt{\pi/2} \approx 1.25$ with DOC_{gauss}.

In the derived expressions for the *DOC* (11) and (12) all parameters are either directly measured or can be estimated from the experiments. Thus, the *DOC* can be determined using the same setup and set of parameters as for actual experiments together with the influence of out-of-plane gradients. The *DOC*-values obtained by (11) and (12) as a function of particle size and gradient g_z are discussed in section 3 together with the results of section 2.2.

3. Results and discussion I: W(z) and DOC for several objectives

In this section, the results for both the measured weighting function *W(z)* and the determined *DOCs* (c.f. sections 2.2 & 2.3) are presented and discussed. To cover a wide range of parameters relevant to µPIV measurements this is done for several objectives, different particles sizes and out-of plane gradients g_z. In the subsequent section 4, such a measured weighting function is used to correct a parabolic flow profile measured along the depth of a microchannel.

First it is analyzed which of the two approximations for *W(z)* used in (11) and (12) fits best the measured weighting functions and compares best to existing theory for the *DOC*:

Both assumed functional shapes of the weighting function describe the measured *W(z)*. However, for the vast majority of tested objectives, particle sizes and out-of-plane gradients the Gaussian weighting function fits the shape of the directly calculated *W(z)* better than the particle weighting function (3) (see figure 3b). This can be additionally quantified by comparing the respective standard deviations σ where σ_{gauss} compares better to $\sigma_{W(z)}$ than σ_{part}. As the *DOC* is defined as $k\sigma$, thus the Gaussian approximation will also give better *DOC*-results than the particle weighting function (3).

Furthermore, figure 5 presents an example of measured *DOCs* from (9), (11) and (12) as function of out-of-plane gradient g_z together with theoretical predictions DOC_{theory} from (5) (Bourdon et al. 2006). Comparing the various results it becomes obvious that the choice of $k = 4$ is reasonable. All determined *DOC*-values decrease with increasing out-of-plane gradients as predicted by Olsen (2010) and agree reasonably well with the theoretical predictions (5) for most low *NA* air or immersion objectives. The DOC_{part}-values are 25% larger than DOC_{gauss}-values and typically overestimate both the theoretical and the measured $DOC_{W(z)}$-values. In the following discussion we will thus concentrate on the *DOC*-results calculated from the measured weighting function *W(z)* (9) and the Gaussian approximation of the weighting function (11).

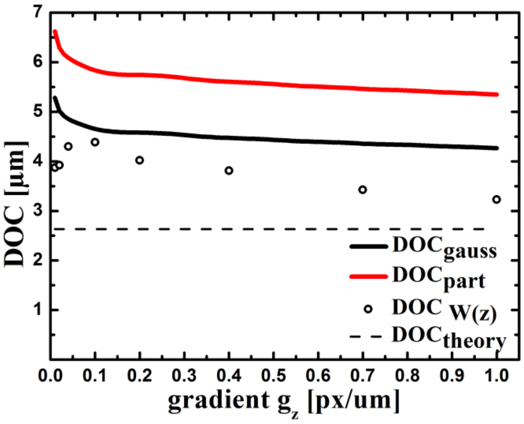

Figure 5 *DOC*-values as function of out-of-plane gradient g_z for a 40x1.4 Plan Apochromat oil immersion objective (Zeiss) using 1 µm particles in comparison with theory (see (5)).

The results for the weighting function *W(z)* and the depth of correlation *DOC* obtained as described in the methods section are grouped in figure 6 as air (a), water immersion (b), and oil immersion objectives (c). The right tiles in figure 6 present the measured weighting function *W(z)* for 1 µm particles and different out-of-plane gradients g_z. The data for a gradient of $g_z = 0.2$ px/µm are additionally connected with solid lines for easier visual inspection. As the shape, specifically the width (*DOC*), of *W(z)* depends on out-of-plane gradients (Olsen 2010), for an easier comparison the *W(z)* are rescaled in height by the maximum of their Gauss-fit and in width by 4 times the standard deviation $\sigma_{W(z)}$, thus the depth of correlation $DOC_{W(z)}$ (see (9)). This rescaling employs the self similarity of the Gaussian approximation of *W(z)*, as self similar Gaussian curves will collapse onto one single curve in these coordinates. Indeed, the weighting functions for different gradients nicely collapse onto a single curve for most tested objectives supporting the assumption of a Gaussian like weighting function. Slight deviations of the weighting function from a Gaussian function around the focal point, $z = 0$, are partly caused by noise in $\Delta dx(z \approx 0)$ as explained in the methods section. Significant deviations from a Gaussian weighting function are observed for high *NA* air objectives figure 6a, middle and bottom. For these two high *NA* air objectives, the measured *W(z)* show a strong asymmetry, and the deviation from a Gaussian function is visible by the varying curve heights and curve width. Similar asymmetries of weighting functions *W(z)*, derived from the curvature of auto-correlation peaks of particle images have also been found by Rossi et al. (2012) explicitly neglecting any out-of-plane gradients. Considering the asymmetric weighting function measured for high-*NA* air objectives which deviate from the symmetric *W(z)* (3) used by Bourdon et al. (2006) to predict the *DOC* (5), it is expected that also the measured *DOC* values will deviate from the predicted values.

The *DOC* values calculated from the measured weighting function $DOC_{W(z)}$ (symbols) and the Gaussian weighting function DOC_{gauss} (solid lines) are plotted in the left tiles of figure 6 as function of the out-of-plane gradient g_z. Data are shown for several particle sizes of 0.5 µm (green (light grey)), 1 µm (black) and 2 µm (blue(grey)) together with the theoretical prediction from Bourdon, Olsen and Gorby (5) (dashed horizontal lines). For the tested particle diameters, both DOC_{gauss} and $DOC_{W(z)}$ are in good agreement with each other. For all tested objectives and particle sizes a decrease of the *DOC* with increasing out-of-plane gradient g_z is found (up to a factor of ~2.5) and the determined *DOC* always increases with increasing particle size. Both of these findings are in qualitative agreement with the theoretical predictions by Olsen (2010) and Bourdon et al. (2006) (c.f. (5)). However, for gradients smaller than about $g_z \approx 0.1$ px/µm, the shift of particle images in between the two frames is too small to be properly resolved and noise influences the *DOC*-results for both presented methods. For larger particles and large magnification objectives it is observed that the boundary for reliable $DOC_{W(z)}$ data is shifted to larger gradients g_z (c.f. figure 6c bottom), which is probably caused by a significantly smaller number of particles in the interrogation windows.

For air objectives with small numerical aperture *NA* and all immersion objectives the obtained *DOC* values are also in reasonable agreement with the values predicted by (5) using a simple one-lens model and as experimentally observed by Bourdon et al. (2006, 2004b). The measured *DOC*-values are usually larger than those calculated using (5) but the maximum deviation is typically smaller than a factor of 2. In contrast, the measured *DOC*-values for the high-*NA* air objectives clearly deviate from these theoretical predictions, c.f. figure 6a (middle and bottom), as already expected from the measured weighting functions. For these high-*NA* air objectives the *DOC* values determined by both presented approaches lie significantly above the predicted values for all tested particle diameters and gradients. The latter finding is in qualitative agreement with the results obtained by Rossi et al. (2012). A reason for the deviation between the measured and calculated *DOC* values observed for high *NA* air objectives is, that the assumptions of a symmetric weighting function (2) does not hold for these objectives. Most likely this originates from assumptions of purely Gaussian particle images and a simple one lens system as used by Olsen and Adrian (2000) which are not valid for high-*NA* air objectives.

(a)

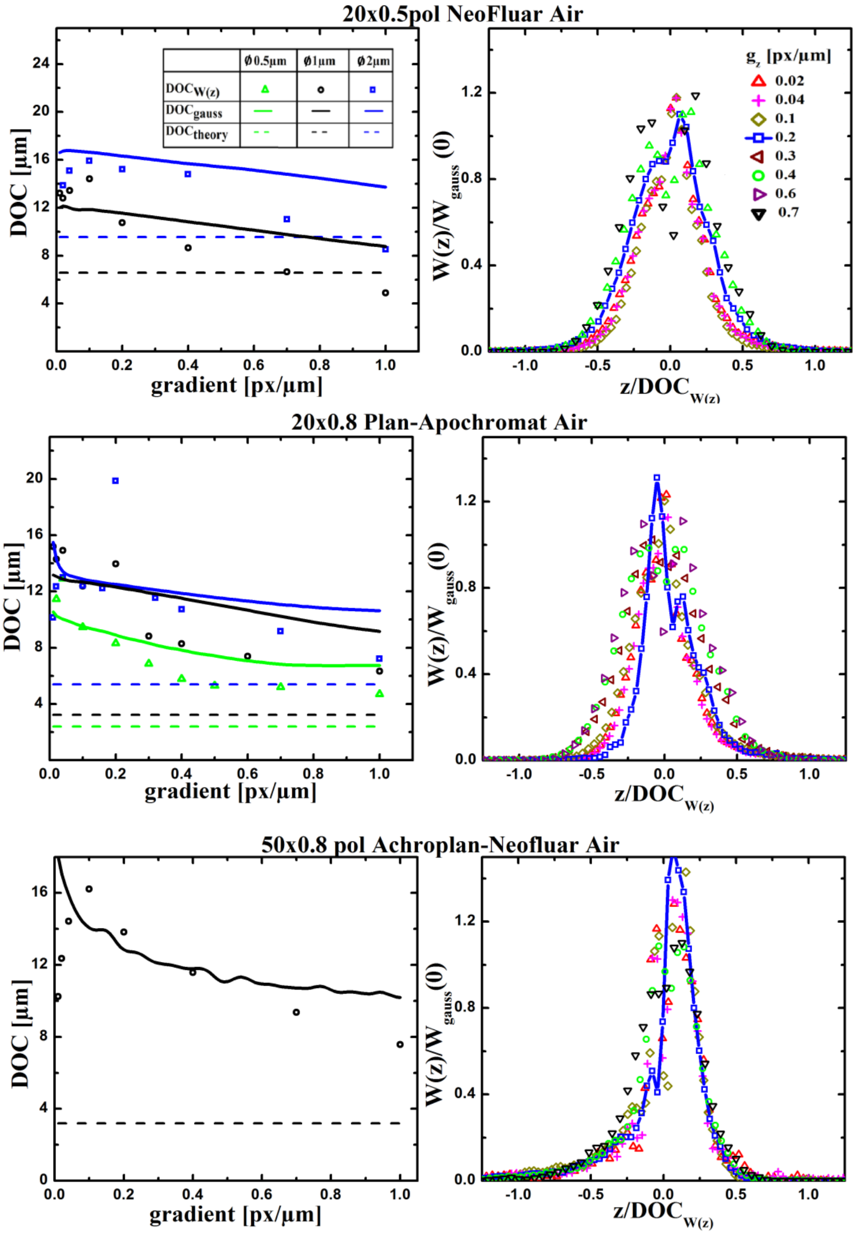
20x0.5pol NeoFluar Air
20x0.8 Plan-Apochromat Air
50x0.8 pol Achroplan-Neofluar Air
DOC [µm]
gradient [px/µm]
W(z)/W$_{gauss}$(0)
z/DOC$_{W(z)}$
Ø0.5µm
Ø1µm
Ø2µm
DOC$_{W(z)}$
DOC$_{gauss}$
DOC$_{theory}$
g$_z$ [px/µm]
0.02
0.04
0.1
0.2
0.3
0.4
0.6
0.7

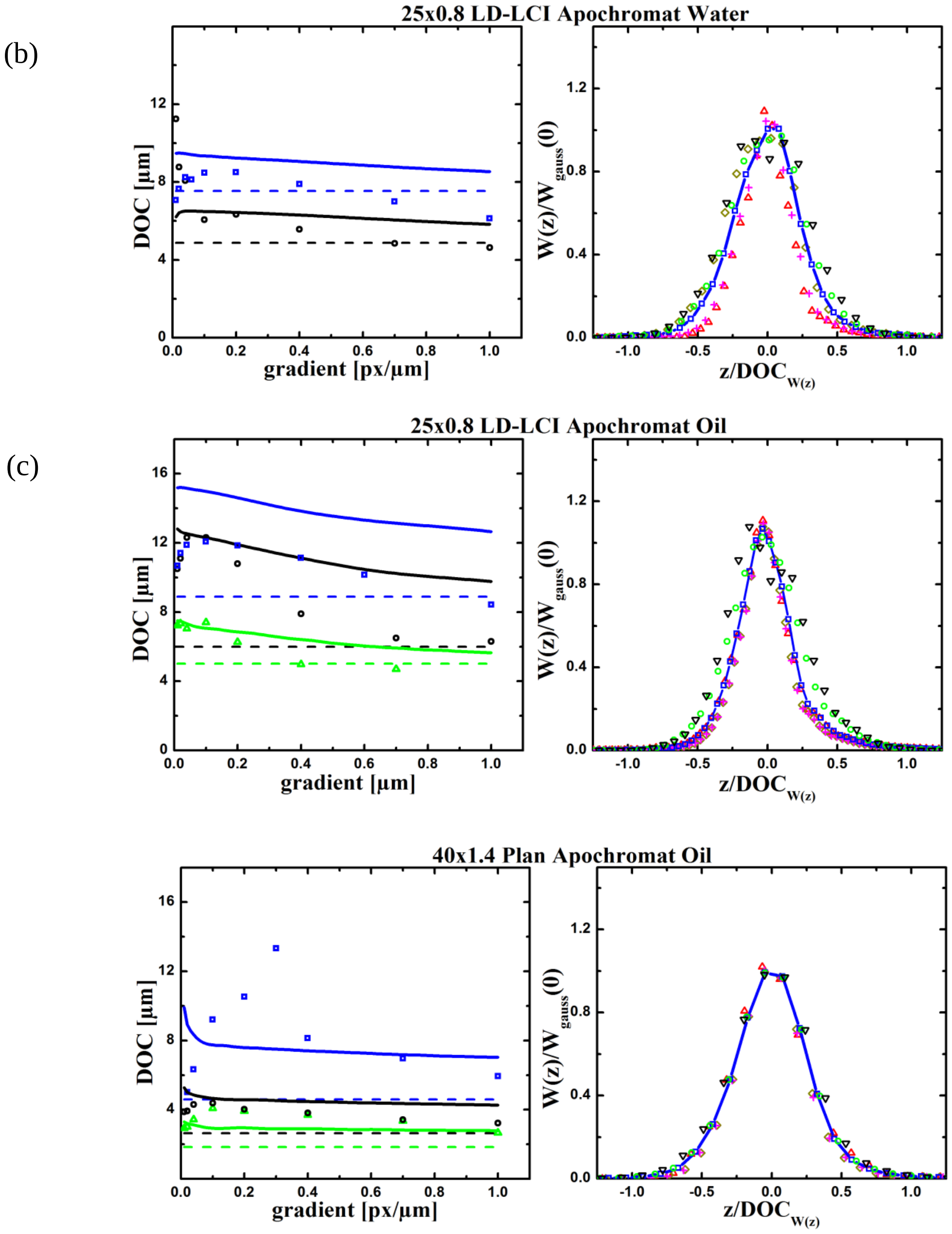

Figure 6 measured *DOC*-values compared to theory (5) (left) and rescaled *W(z)* for 1 µm particles and various out-of-plane gradients (right) for several tested objectives of 20x-40x magnification with air (a), water (b) and oil immersion (c). Legends apply to all shown graphs.

4. Results and discussion II: Deconvolution of flow profiles

Knowing the weighting function for a given objective and the expected out-of-plane gradients, the systematic errors in experimentally measured flow profiles in regions with large out-of-plane curvatures of the flow profile and close to channel boundaries can be corrected. These systematic errors originate from the finite curve width of the weighting function defining the spatial averaging (1) which is intrinsic to all volume illuminated PIV measurements. The possibility to correct the flow profile using the example of a well known static parabolic flow profile in a rectangular channel is demonstrated in figure 7. The flow-profile was measured in a rectangular channel (width 300 µm, height 90 µm) molded in Sylgard 184 (Dow Corning) and plasma bonded to a glass cover slip. Ultrapure water seeded with 1 µm particles was driven through the channel by hydrostatic pressure. 10 double-images were recorded at each *z*-position using the optical setup described in section 2 and a 20x0.5pol NeoFluar (Zeiss) objective. The *z*-axis was scanned in steps of 0.75 µm corresponding to a displacement of the focal plane of 1 µm imaging with an air immersion objective in water (see Rossi et al. (2012)). As before, a sliding minimum was subtracted to reduce the image background. The same PIV-parameters as explained in section 2 were used to calculate the flow-profile for each recorded double-image. All ten recorded velocity fields for each *z*-position were time averaged. The velocities displayed in figure 7 were measured in the center region of the channel to avoid the influence of the side-walls.

Close to the channel boundaries the flow velocity plateaus at finite velocities resulting from the weighted spatial averaging as discussed above (close up in figure 7b). As a first correction, the non-existing finite flow velocities in the channel wall can be ignored. When measuring the flow profile along the channel height, the focal position and thus the weighting function $W(z)$ was shifted along the spatially fixed flow profile $dx(z)$. In this case the measured displacement dx_{meas} in (1) becomes a function of channel height z. This is especially relevant in regions of large curvature of the flow profile and close to the limits of the microfluidic channel. When focusing on the channel wall, only a part of the channel lies within the relevant width of $W(z)$ and thus contributes to the measured velocity. If the focal plane moves further away from the channel wall, the velocities from regions within the channel contribute stronger to the measured velocity due to the flattening of $W(z)$ far from the focal plane. Thus an increase of the measured displacement as seen from the raw data in figure 7 (red triangles) is expected, which was also shown by Rossi et al. (2012).

To correct the measured flow profile, (1) has to be modified to the experimental situation:
To account for the broken norm of $W(z)$ due to the lack of signal outside of the channel boundaries, a rectangular function $\Theta(z)$ of height 1 and a width equal to the height of the channel is introduced. Outside of the channel $\Theta(z)$ is 0. Thus the measured displacement is represented by a convolution of the actual flow profile and the weighting function $W(z)$ divided by a convolution of $W(z)$ with $\Theta(z)$ that eliminates the increase of the measured displacement $dx_{meas}(z)$ close to the channel boundaries.

$$dx_{meas}(z) = \frac{\sum_{z'} W(z-z')\cdot dx(z')}{\sum_{z'} W(z-z')\cdot \Theta(z')} = \frac{W(z)\otimes dx(z)}{W(z)\otimes \Theta(z)}\,. \tag{13}$$

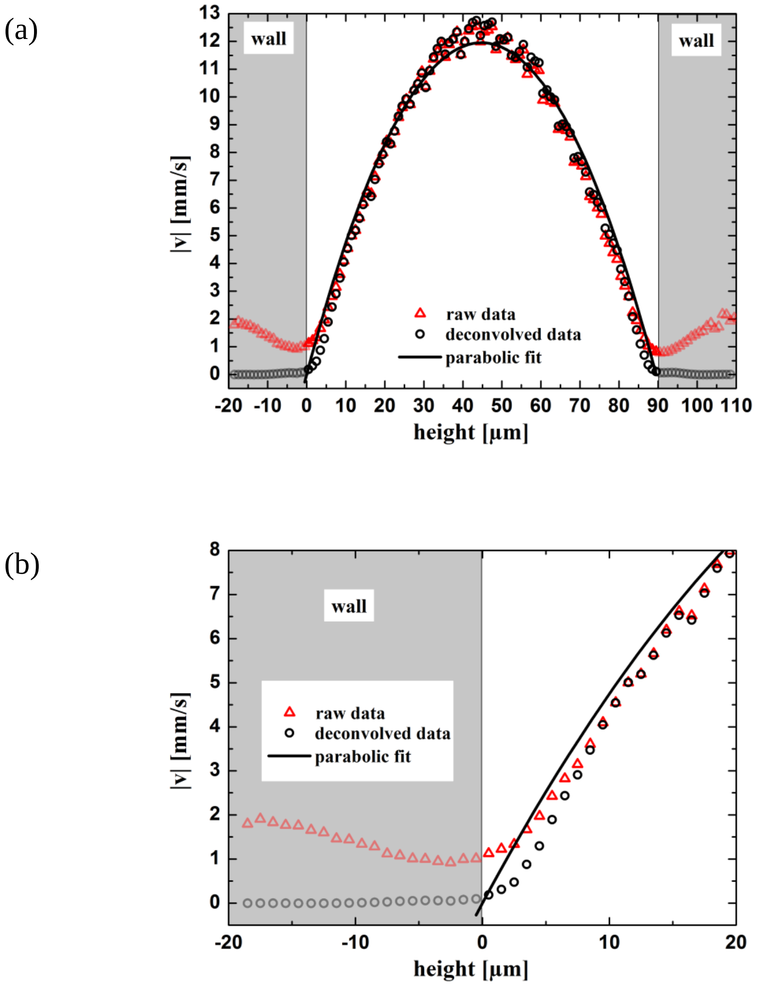

Figure 7 Flow profile measured along the height of a rectangular channel of about 300 µm x 90 µm using a 20x0.5pol NeoFluar (Zeiss). Data measured at positions outside of the channel are shown as faint symbols in the shaded wall region. The raw data and the deconvolved data are compared to a parabolic fit of the deconvolved data: a) complete flow profile b) close up of the region next to the channel bottom.

All parameters that enter (13) are known: $dx_{meas}(z)$ is the outcome of the PIV measurement, $W(z)$ can be measured using generated PIV double-images for a given gradient and $\Theta(z)$ represents the height of the channel where the flow profile was measured. Thus (13) can be solved for $dx(z)$:

$$W(z) \otimes dx(z) = dx_{meas}(z) \cdot W(z) \otimes \Theta(z) = G(z) \, . \tag{14}$$

For convenience, $G(z)$ is defined as the product of $dx_{meas}(z)$ and the convolution of $W(z)$ and $\Theta(z)$. Thus the true displacement function $dx(z)$ is the deconvolution of the completely known function $G(z)$ with $W(z)$.

To deconvolve the measured flow profile with the experimentally determined weighting function, five iterations of a van-Cittert algorithm (van Cittert 1931) have been conducted. The iterative van-Cittert method allows to suppress the amplification of measurement noise by subtracting n times the difference between the nth and (n+1)st iteration, which represents the amplified noise assuming convergence of the method for the nth iteration. Typically n is chosen to be 10 or less.

The weighting function $W(z)$ used for the deconvolution shown in figure 7 was computed for a gradient estimated by linearly fitting the raw data close to the channel walls. The weighting function $W(z)$ was measured as described above by imaging particles prepared on a glass slide. As in the PIV-experiment itself, the objective was shifted in z-intervalls of 0.75 µm which results in a 1 µm displacement of the focal plane in water. This simple correction by the paraxial approximation was shown to be sufficient to include the influence of refraction on the weighting function (Bourdon et al. 2004b). The measured weighting function for the used 20x0.5 air-objective presents some spikiness close to the focal plane (comparable to Fig 6a). Thus the weighting function was fitted by a Gaussian as justified in section 3 and the Gaussian fit was used to deconvolve the data. The deconvolution slightly increases the velocity values particularly close to the center of the channel, as the volume averaging that leads to an underestimation of the velocity in this region is reduced. Note, that the actual weighting function depends on the velocity gradient g_z which is different in the center region than close to the channel walls. Thus a different $W(z)$ would have to be used here, to precisely capture the velocities in the center of the channel.

However, the deconvolution significantly reduces the overestimation of the velocities close to the channel walls, which is always present in µPIV data. Thus the presented approach successfully corrects the measured velocities close to walls or in regions of a strongly curved flow profile. For comparison the deconvolved data has been fitted by a parabolic curve assuming no-slip at the channel wall, representing the expected Poisseuille-flow profile (black curve). The position of the channel walls used for this fit have been precisely determined by finding the maximum of the convolution of $\Theta(z)$ with the measured $dx(z)$, thus finding the best overlap.

5. Conclusion

An approach has been presented to determine the weighting function *W(z)* from a series of generated PIV double-images accounting for all relevant parameters including out-of-plane gradients, shape of the flow profile, particle size and optical setup. The knowledge of the weighting function for a particular experimental situation, in particular the out-of-plane gradient, allows correcting for measurement errors intrinsic to volume illuminated PIV. This correction has been explicitly demonstrated for a stationary flow field in a rectangular channel.

From the determined weighting function *W(z)* the depth of correlation (*DOC)*, which is equivalent to the thickness of the measurement plane, is derived from the curve width of *W(z)*. It was found that the determined weighting function *W(z)* can be best approximated with a Gaussian. Assuming a Gaussian approximation the *DOC* can be determined from a single PIV double-image generated with a V-shaped velocity profile for a given out-of-plane gradient. Both *DOC* values – from the width of *W(z)* as well as from the single V-shaped image - agree well with each other for different out-of-plane gradients and particle sizes. For most objectives the determined *DOC*-values also show acceptable agreement with the frequently used theoretical prediction (Bourdon et al. 2006). However, significant disagreement between theoretically predicted and determined *DOC*-values has been observed for high numerical aperture air objectives.

Both methods allow testing for the influence of image-processing such as power filters or histogram filters (Rossi et al 2012, Bourdon et al 2004a) and various PIV-analysis parameters. The methods can be easily implemented and automated to determine the system dependent weighting function and *DOC*. This allows optimization of experiments, increasing the precision of PIV measurements without the necessity of sophisticated and expensive setups such as confocal microscopy and interpretation of measured flow profiles having large out-of-plane gradients.

Acknowledgement

The authors gratefully acknowledge Carl Zeiss Microscopy GmbH for supplying some of the tested objectives, Dr. Frank Müller (Saarland University) for helpful discussions and for supplying the van-Cittert deconvolution software and the DFG-GRK1276 for financial support.

References

Adrian R J 1991 Particle-imaging techniques for experimental fluid mechanics *Annu. Rev. Fluid Mech.* **23** 261–304

Bourdon C J, Olsen M G and Gorby A D 2004a Power-filter technique for modifying depth of correlation in micro-PIV experiments *Exp. Fluids* **37** 263–71

Bourdon C J, Olsen M G and Gorby A D 2004b Validation of an analytical solution for depth of correlation in microscopic particle image velocimetry *Meas. Sci. Technol.* **15** 318–27

Bourdon C J, Olsen M G and Gorby A D 2006 The depth of correlation in micro-PIV for high numerical aperture and immersion objectives *J. Fluids Eng.* **128** 883–6

Kloosterman A, Poelma C and Westerweel J 2011 Flow rate estimation in large depth-of-field micro-PIV *Exp Fluids* **50** 1587–99

Lindken R, Rossi M, Große S and Westerweel J 2009 Micro-Particle Image Velocimetry (μPIV): Recent developments, applications, and guidelines *Lab Chip* **9** 2551–2567

Meinhart C D and Zhang H 2000 The flow structure inside a microfabricated inkjet printhead *J Microelectromech. Syst.* **9 (1)** 67–75

Nogueira J, Lecuona A and Rodriguez P A 1999 Local field correction PIV: on the increase of accuracy for digital PIV systems *Exp Fluids* **27** 107–16

Nogueira J, Lecuona A and Rodriguez P A 2001 Local field correction PIV, implemented by means of simple algorithms, and multigrid versions *Meas. Sci. Technol.* **12** 1911–21

Olsen M G 2009 Directional dependence of depth of correlation due to in-plane fluid shear in microscopic particle image velocimetry *Meas. Sci. Technol.* **20** 015402

Olsen M G 2010 Depth of correlation reduction due to out-of-plane shear in microscopic particle image velocimetry *Meas. Sci. Technol.* **21** 105406

Olsen M G and Adrian R J 2000 Out-of-focus effects on particle image visibility and correlation in microscopic particle image velocimetry *ExpFluids* **29** S1, S166–74

Poelma C, Kloosterman A, Hierck B P and Westerweel J 2012 Accurate blood flow measurements: Are artificial tracers necessary? *PLOS One* **7 (9)** e45247

Rossi M, Segura R, Cierpka C and Kähler C J 2012 On the effect of particle image intensity and image preprocessing on the depth of correlation in micro-PIV *Exp Fluids* **52** 1063–75

Santiago J G, Wereley S T, Meinhart C D, Beebe D J and Adrian R J 1998 A particle image velocimetry system for microfluidics. *Exp Fluids* **25** 316–19

van Cittert P 1931 Zum Einfluss der Spaltbreite auf die Intensitaetsverteilung in Spektrallinien *Z.Phys.* **69** 298-308

Vennemann P, Kiger K T, Lindken R, Groenendijk B C, de Vosd S S, ten Hagen T L, Ursem N T, Poelmann R E, Westerweel J, and Hierck B P 2006 In vivo micro particle image velocimetry measurements of blood-plasma in the embryonic avian heart *J. Biomech.* **39** 1191–200

Westerweel J, Geelhoed P F and Lindken R 2004 Single-pixel resolution ensemble correlation for micro-PIV applications *Exp. Fluids* **37** 375–84

Addendum VI: Direct calculation of depth of correlation and weighting function in µPIV from experimental particle images

10th International Symposium on Particle Image Velocimetry (PIV13), Delft, The Netherlands(2013).
available (open access) at: `http://repository.tudelft.nl` uuid: 0e75dbdf-81ae-4b92-bab7-b9d47bcff6b6

Authors: M. Hein[1], B. Wieneke[2] and R. Seemann[1,3]
[1] Department of Experimental Physics, Saarland University, Saarbrücken, Germany
[2] LaVision GmbH, Göttingen, Germany
[3] Dynamics of Complex Fluids, MPI for Dynamics and Self-Organization, Göttingen, Germany

With kind permission of Delft Repository (Technical University Delft, The Netherlands).

Author Contributions:

Research was designed by M. Hein and B. Wieneke. Experiments were performed by M. Hein. Data was analyzed by M. Hein and B. Wieneke. The theoretical backbone was developed by B. Wieneke and M. Hein. Article was written by M. Hein. Writing was supervised by B. Wieneke, and R. Seemann. Research was directed by B. Wieneke and R. Seemann.

Abstract:

Micro-PIV (μPIV) uses volume-illumination and imaging of fluorescent tracer particles through a single microscope objective. Displacement fields measured by image correlation depend on all imaged particles, including defocused particles. The measured in-plane displacement is a weighted average of the true displacement with a weighting function $W(z)$, that depends on the optical system and gradients of the measured flow profile. The width of the weighting function $W(z)$ is a measure for the distance to the focal plane up to which particles can influence the measured displacement (Depth of Correlation - *DOC*). We present two procedures to determine the *DOC* by comparing a measured displacement to a given displacement function and by directly measuring $W(z)$ using PIV double-images generated from experimentally recorded particle-images. This allows to measure the *DOC* in dependence of out-of-plane gradients and to include image preprocessing or different PIV-algorithms. Experimental results for different objectives and particle sizes are discussed, revealing deviations from theoretical predictions for high NA air-objectives.

10TH INTERNATIONAL SYMPOSIUM ON PARTICLE IMAGE VELOCIMETRY – PIV13

Delft, The Netherlands, July 2-4, 2013

Direct calculation of depth of correlation and weighting function in µPIV from experimental particle images

Michael Hein[1,3], Bernhard Wieneke[2] and Ralf Seemann[1,3]

[1] Department of Experimental Physics, Saarland University, Saarbrücken, Germany
michael.hein@physik.uni-saarland.de

[2] LaVision GmbH, Göttingen, Germany
[3] MPI for Dynamics and Self-Organization, Göttingen, Germany

Micro-PIV (µPIV) uses volume-illumination and imaging of fluorescent tracer particles through a single microscope objective. Displacement fields measured by image correlation depend on all imaged particles, including defocused particles. The measured in-plane displacement is a weighted average of the true displacement with a weighting function *W(z)*, that depends on the optical system and gradients of the measured flow profile. The width of the weighting function *W(z)* is a measure for the distance to the focal plane up to which particles can influence the measured displacement (Depth of Correlation - *DOC*). We present two procedures to determine the *DOC* by comparing a measured displacement to a given displacement function and by directly measuring *W(z)* using PIV double-images generated from experimentally recorded particle-images. This allows to measure the *DOC* in dependence of out-of-plane gradients [4] and to include image preprocessing or different PIV-algorithms [5, 17]. Experimental results for different objectives and particle sizes are discussed, revealing deviations from theoretical predictions [1,2,3] for high *NA* air-objectives.

Introduction

Due to its simplicity and reliability Micro-Particle Image Velocimetry (µPIV) [6] is one of the most frequently used techniques to measure flow-profiles on a micro-scale. It is employed in many different fields ranging from fluids-engineering to biological systems [7, 8] both in research and industrial application. In a µPIV experiment tracer particles suspended in the fluid are imaged using a microscope and a CCD-camera. To reduce background noise, usually fluorescent particles are used and their emission signal is isolated from reflected laser or background light by cut-off filters. Typically two images with a short time delay are recorded. By correlating these two images a displacement pattern is obtained, which can be transferred into a velocity field with the known time delay between the two images.

The main difference of µPIV to standard PIV [9] is the illumination used. Standard PIV uses a laser light-sheet to illuminate the particles. If the focal length of the camera is chosen to be large, all tracer-particles in the light-sheet are in focus. Thus the spacial dimensions of the measurement region are well known by the extension of the light sheet. In contrast, µPIV illuminates and records the particles through a single microscope objective, as it is very difficult to create a light-sheet in microfluidic devices due to small channel-dimensions and limited optical access.

This represents one of the major drawbacks of µPIV: As all tracer particles in the whole volume are illuminated, even defocused particles can contribute to the measured displacement, making it difficult to determine the thickness of the measurement plane (Depth of Correlation, *DOC*). To be able to interpret the measured velocity profiles, especially in the case of complex three dimensional flows, a precise knowledge of the *DOC* is essential, as the measured velocities will be a weighted average of all particle velocities along the line-of-sight, with the weighting function *W(z)* depending on particle distance from the focal plane [1, 10].

Olsen [1] derived an analytical model for the weighting function and the *DOC* part of which we use as a starting point for our work. Bourdon, Olsen and Gorby [3,11] slightly adapted these analyses to microscope objectives and showed one method to measure both *W(z)* and *DOC* by analyzing the shape of autocorrelation peaks from both experimental and synthetic particle images. They observed good agreement between Olsen's model and experimental results for low *NA* air and immersion objectives. Using a similar approach to characterize *W(z)*, Rossi [5] showed that the existing theory significantly underestimates the *DOC* for high *NA* air objectives or more complex optical setups.

We present a new and more straightforward approach to determine both the *DOC* and *W(z)* from experimental images. In contrast to the present literature our method also allows to account for out-of-plane shear that is expected to reduce the *DOC* [4]. The method presented here is based on correlating PIV double-images that have been constructed from experimentally recorded particle images summed up synthetically, imposing a specific displacement field as a function of depth. The *DOC* and *W(z)* is determined from the calculated displacement fields using any typical PIV-algorithm. It is also possible to check for the influence of image processing or vector post-processing, using the same experimental setup and analysis parameters as for actual experiments.

We discuss the weighting function *W(z)* and the *DOC* for objectives with numerical apertures ranging from 0.5 to 1.4 using different tracer particle diameters, a range of out-of-plane gradients spanning two orders of magnitude and compare our results to the existing theory.

Experimental Setup

Particle images used to determine both the *DOC* and the weighting function *W(z)* were taken by imaging micro-particles of Polystyrene (Thermo Scientific, Fluoro-Max, Green fluorescent), that were fixed on a 130 µm thick glass plate. The particle suspensions were diluted with ethanol. Subsequently a drop of the suspensions was placed on the glass plate and blow-dried with clean nitrogen. Using this method we were able to produce patches with randomly located particles on the glass plate with only very few clusters of particles, that might increase the measured *DOC*. Three different particle diameters of 0.5, 1 and 2 µm were tested.

The imaging system consists of a Zeiss AxioObserver Z1 microscope equipped with a motorized focal positioning system (motorized z-axis), a CCD Camera (Imager ProX, LaVision) coupled to the microscope by a 0.63x camera adapter (Zeiss), a laser for fluorophor excitation (473 nm (1.5 W), LaVision) and a filter cube that isolates fluorescence signal from scattered laser- and background-light. The whole setup was computer-controlled using the DaVis 8.1.2 package of LaVision.

Several Zeiss objectives were tested with magnifications ranging from 20x to 40x and *NA*s from 0.5 to 1.4 with air, water and oil immersion and the measured weighting functions and *DOC*-values compared to literature.

To account for differences in intensity and background noise of the two frames caused by the different camera exposure times of both frames in double-frame mode, we recorded double-images as would be done in real measurements. The *z*-axis was scanned in 0.5 µm steps using the positioning system of the microscope and 100 double-images were taken at every focal-position below and above the object plane. Each set of 100 images was averaged to suppress intensity fluctuations due to camera and laser noise. To increase the seeding density, typically 30 sub-windows at the same random position in both frames within the averaged images were summed up in one double-image of the same size as the random sub-windows. A sliding minimum subtraction was performed to remove background glow that is increased by this summation.

Finally, the generated PIV double-images were created by overlaying the frames for all *z*-positions into a single double-image, while the particle-images in the second frame were shifted according to the displacement function *dx(z)*.

The final double-images were then evaluated using the standard PIV-algorithm implemented in DaVis 8.1.2 with square interrogation windows of 128x128 px (Multipass 4x, high accuracy mode). The only post-processing performed was a 1x median filter to remove and replace outliers.

Theoretical framework

Determining the *DOC* and the weighting function *W(z)*, that determines the relative contribution of particles at each *z*-position to the measured displacement dx_{meas}, is possible by comparing the measured displacement to the displacement function *dx(z)* applied when generating the double-images as described above. Olsen and Adrian [1] analytically examined the influence of out-of-focus particles on the measured displacement dx_{meas}, assuming that the defocusing of particles can be described using Gauss-optics and a single thin lens model. They stated that the measured velocity in an ideal PIV-experiment, where out-of-plane gradients are not too large, is given by a weighted average

$$dx_{meas} = \frac{\int_{-\infty}^{+\infty} dx(z)\cdot W(z)dz}{\int_{-\infty}^{+\infty} W(z)dz} \quad (1)$$

When scanning the focal plane along the height of a channel where a static flow-profile is established, the focal position and thus the weighting function *W(z)* is shifted along the spatially fixed flow-profile *dx(z)*. In this cases dx_{meas} in equation (1) becomes a function of *z* and is represented by a convolution of the actual flow-profile and the weighting function *W(z)*.

The weighting function *W(z)* is comparable to a probability density function and we assume from now on that

$$\int_{-\infty}^{+\infty} W(z)dz = 1 \quad (2)$$

The maximum of *W(z)* is in the focal plane at $z = 0$ and *W(z)* is decreasing with increasing distance to the focal plane.

Olsen and Adrian [1] derived an expression for *W(z)* as a function of f-Number $f^{\#}$ and magnification assuming a one lens system. The *DOC* is defined by twice the distance *z* where *W(z)* drops to $\varepsilon\cdot W(z=0)$ with ε typically chosen to be $\varepsilon=0.01$. While any such definition of *DOC* is rather arbitrary, it is the underlying *W(z)*-function which determines the measured displacement in the end. Bourdon, Olsen and Gorby adapted this formula to the for microscope objectives more frequently specified numerical aperture *NA* and validated and tested it for microscope air objectives with $NA \leq 0.4$ and immersion optics [3,11]:

$$DOC = 2 \cdot \left(\frac{(1-\sqrt{\varepsilon})}{\sqrt{\varepsilon}} \left[\frac{n_0^2 d_p^2}{4NA^2} + \frac{5.95(M+1)^2 \lambda^2 n_0^4}{16 M^2 NA^4} \right] \right)^{\frac{1}{2}} \quad (3)$$

Here n_0 is the refractive index of the immersion medium of the objective, M is the magnification, λ specifies the wavelength of the detected fluorescence light and d_p is the particle diameter. Equation 3 is, with minor changes, frequently used to estimate the *DOC* [8].

For more complex systems, where the simplifications used by Olsen [1] do not hold anymore, such as high *NA* air-objectives, multi-lens systems or specialized microscopes, significant deviations from the results given by equation 3 have been found [5,12]. Furthermore, the *DOC*-formula above does not account for any velocity gradients of the flow-field. Out-of-plane gradients lead to a reduction of the *DOC* [4] whereas in-plane gradients should increase the *DOC* [13]. While the influence of in-plane gradients can be compensated for by decreasing the size of the interrogation windows or by window-deformation techniques, the influence of out-of-plane shear cannot easily be accounted for [14, 15, 16].

We present two new approaches to determine the *DOC* and the weighting function *W(z)* from experimentally recorded particle images and thus a protocol to determine the *DOC* particularly for the used system, the measured flow-profile and the analysis parameters used.

Direct determination of the *DOC* from particle images

To measure the Depth of Correlation we first generate a double-image as explained above. The first frame contains particle images from all *z*-positions. The second frame contains the same particle images, but shifted according to a given displacement function *dx(z)*. Thus a set of frames is gained with a known velocity profile with out-of-plane shear. By preprocessing and correlating these frames with the same filters, algorithm and parameters as used for actual PIV-measurements, the measured displacement dx_{meas} can be determined. The *DOC* can be directly extracted from dx_{meas}, which will be explained in the following section.

Applying a linear increase of the velocity with distance from the focal plane at $z = 0$

$$dx(z) = g_z \cdot |z| \quad (4)$$

where g_z is the gradient of the velocity, the *DOC* can be determined from dx_{meas} using equation 1 and employing an analytical approximation for the weighting function *W(z)*. We assume *W(z)* to be approximately a Gaussian distribution

$$W_{Gauss}(z) = \frac{1}{\sqrt{2\pi} \cdot \sigma_{Gauss}} e^{\frac{-z^2}{2\sigma_{Gauss}^2}} \quad (5)$$

where σ_{Gauss} is the standard deviation of $W_{Gauss}(z)$.

Now the *DOC* of the system can directly be calculated from dx_{meas} by putting $W_{Gauss}(z)$ (eqn. 5) and the given displacement profile (eqn. 4) into equation 1:

$$dx_{meas} = \int_{-\infty}^{+\infty} g_z |z| \cdot \frac{1}{\sqrt{2\pi} \cdot \sigma} e^{\frac{-z^2}{2\sigma_{Gauss}^2}} dz = g_z \cdot \sigma_{Gauss} \cdot \sqrt{\frac{2}{\pi}} \quad (6)$$

The *DOC* can be defined as a curve-width $k \cdot \sigma_{Gauss}$ of the weighting function *W(z)*. A common choice is the range $\pm 2\sigma_{Gauss}$ with k=4:

$$DOC_{Gauss} = 4 \cdot \sigma_{Gauss} = 4 \cdot \sqrt{\frac{\pi}{2}} \frac{dx_{meas}}{g_z} \quad (7)$$

In equation 7 all parameters are either directly measured or can be estimated from the experiments. Thus our procedure allows to determine the *DOC* directly from generated double-images applying a certain gradient and using the same setup and set of parameters as for actual experiments. Calculations or measurements in correlation space do not have to be performed.

We discuss the *DOC*-values obtained by this method for several objectives as a function of particle size and gradient g_z in the results section of this paper. Before discussing the results, we introduce a second method, using the same experimental particle images. This method is not only capable of determining the *DOC* but directly measures the weighting function *W(z)*. This allows to check the assumption of a Gaussian shape of *W(z)* used to determine the *DOC* from equation 7, as well as to determine the *DOC* from the curve width of *W(z)*.

Determination of the weighting function *W(z)* from particle images

A similar approach as introduced before can be used to determine the weighting function *W(z)*. As displacement function *dx(z)* we choose a linear displacement (see figure 1) proportional to the absolute position (and thus to the image number) of the microscope objective where the experimental particle images were taken.

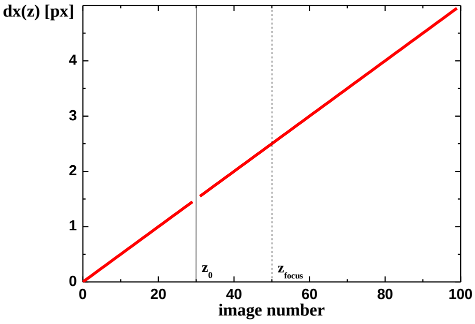

Figure 1 Example of the linear displacement function *dx(z)* leaving out one image at z_0 used to measure *W(z)* from experimental particle images.

Applying this linear *dx(z)*, we create a stack of double-images as explained in the experimental section. Each of these double-images contains recorded particle images from all *z*-positions, leaving out only the images of one position z_0, which is shifted with the image-number in the stack as indicated in figure 1. Thus we can systematically check for the influence of particles at every *z*-position.

Again every generated double-image is evaluated using standard PIV-analysis and a measured displacement $dx_{meas}(z_0)$ is obtained for every z_0-position. Subtracting $dx_{meas}(z_0)$ from the displacement measured from an image containing particle images from all *z*-positions and applying equation 1 and 2 we get:

$$\Delta dx(z_0) = \sum_{z'} W(z'-z_{focus}) \cdot g_z \cdot z' - \frac{\sum_{z' \neq z_0} W(z'-z_{focus}) \cdot g_z \cdot z'}{1 - W(z_0 - z_{focus})} \quad (8)$$

Setting the focal plane at $z_{focus} = 0$, replacing z_0 by the distance from the focal plane *z* and solving equation 8 for *W(z)* an equation for the weighting function is derived that solely depends on known or measurable parameters:

$$W(z) = \frac{\Delta dx(z)}{g_z \cdot z + \Delta dx(z)} \quad (9)$$

Figure 2 shows examples of $\Delta dx(z_0)$ and *W(z)* for a 20x0.5 air-objective determined from experimental images of 1 µm particles.

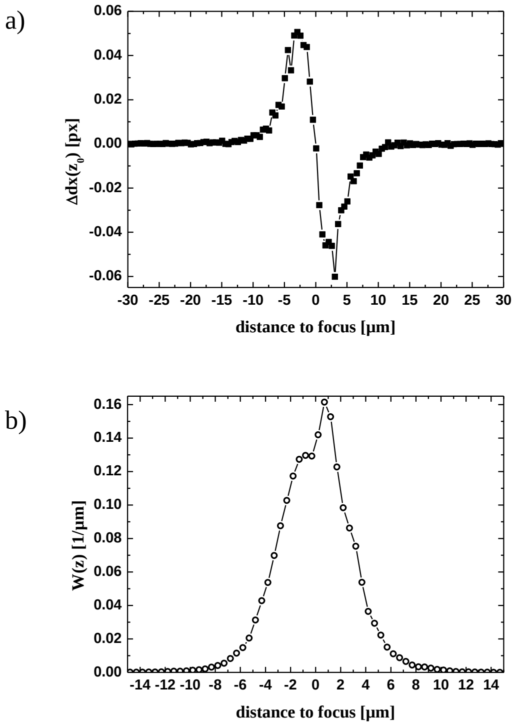

Figure 2 Example of a) $\Delta dx(z_0)$ and b) $W(z)$ (see equation 8 and 9) for a 20x0.5 air objective using 1µm particles and g_z = 0.2 px/µm.

At the same time equation 8 allows to determine the exact position z_{focus}, where the particles are in focus. Assuming that $W(z)$ has its mean value at z_{focus}, the linearity of the displacement function $dx(z)$ demands the second and the first term of the right hand side of equation 8 to be equal to the velocity in the focal plane. Thus, at $z_0 = z_{focus}$, $\Delta dx(z_0)$ becomes 0 and we can calculate the exact position where the particles are in focus. This also has some impact on the determination of $W(z)$ from equation 9. At z = 0, exactly at the focus position, equation 9 becomes unstable. The largest errors in the measured weighting function will be found around this position. To reduce the errors caused by noise in the measurement we apply a one-time smoothing by weighted averaging over the closest neighbors to the measured $W(z)$-profile.

The Depth of Correlation can then easily be calculated from the measured weighting function, by again using the definition of the standard deviation and calculating the curve-width $4\sigma_{W(z)}$ of $W(z)$:

$$DOC_{W(z)} = 4 \cdot \sigma_{W(z)} = 4 \cdot \sqrt{\sum_z W(z) \cdot z^2} \qquad (10)$$

As the measured $W(z)$ will always present some noise, especially in the flat tail region, that will influence the calculated DOC-values, only the region of the measured $W(z)$ between the first points where $W(z)=0$ on both sides of the focal plane of the particles was used.

Results

Following the procedures described in the previous sections, particle images were taken and processed to PIV double-images. These images were used to determine both the weighting function $W(z)$ and the DOC as a function of the gradient g_z and of the particle diameter (see figure 3).

20x0.5pol NeoFluar Air

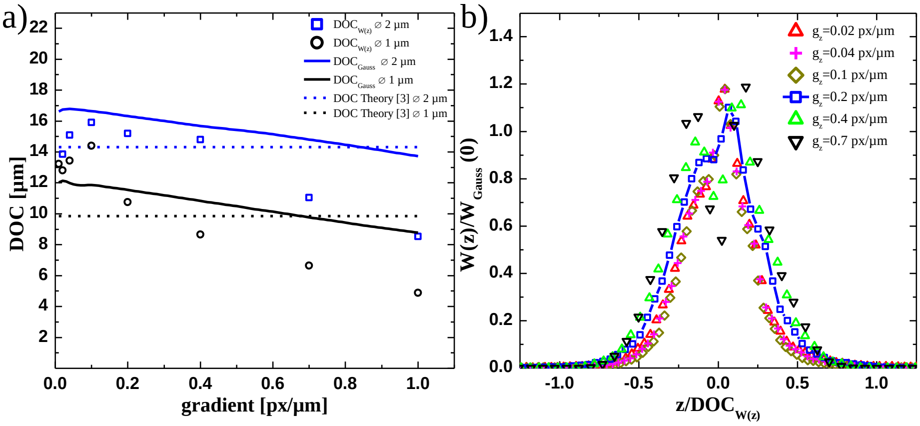

20x0.8 Plan-Apochromat Air

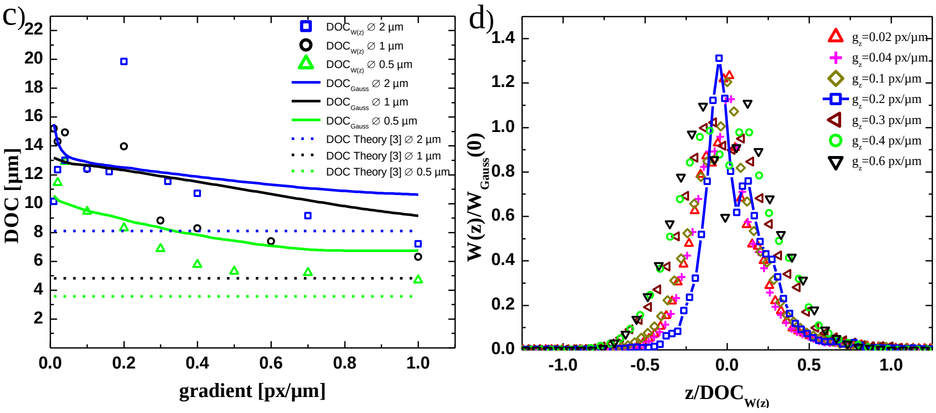

Figure 3 (a,c) measured *DOC* and theory values from [3] using different particle diameters for two tested objectives of 20x magnification (b,d) measured weighting function *W(z)* for 1 µm particles, data-points for g_z=0.2 px/µm connected by blue line as a guide to the eye.

For the 20x0.5 air objective, figure 3a) presents the *DOC* values measured either directly from a measured displacement assuming a Gaussian *W(z)* (solid lines, see equation 7) or by determining the weighting function and calculating the *DOC* from its curve width according to equation 10 (symbols). We measured the *DOC* following both procedures for several particle sizes and a range of velocity gradients g_z and compared the results with the *DOC* calculated using the formula of Bourdon and Olsen [3] in equation 3 (dashed lines). Both DOC_{Gauss} and $DOC_{W(z)}$ are in good agreement with each other as well as with the values predicted using equation 3 for the tested particle diameters. As expected, all measured *DOC* values for 1 µm particles lie below those for the 2 µm particles.

For gradients smaller than g_z = 0.1 px/µm the shift of particle images between the two frames seems to be too small to be properly resolved and noise can influence the *DOC*-results for both presented methods. For larger gradients, the measured DOC_{Gauss} and $DOC_{W(z)}$ both show the expected decrease of the *DOC* with increasing gradient g_z as predicted by Olsen [4].

Figure 3c) presents the measured *DOC* values for the 20x 0.8 air objective in the same way as figure 3a). In contrast to the lower *NA* air objective, the *DOC* values determined by both equation 7 and 10 lie significantly above the value calculated using Bourdon's and Olsen's formula (equation 3) for all tested particle diameters and gradients, though again both methods reproduce the expected decrease of the *DOC* for increasing gradients.

Table 1 shows the measured *DOC* values for the tested objectives, a fixed gradient of 0.2 px/µm and 1 µm particles compared to the DOC calculated from equation 3. Again, the 20x0.8 air objective is the only objective where strong deviations are observed. Equation 3 underestimates the Depth of Correlation as compared to our results by a factor of up to 2.9, while the results obtained by equation 3 still give a good estimate of the *DOC* for high-*NA* immersion objectives. This is in qualitative agreement with the results obtained by [3,5]. The good agreement between $DOC_{W(z)}$ and DOC_{Gauss} is a clear hint, that the assumption of a Gaussian weighting function does not introduce significant error when deriving DOC_{Gauss}.

objective / immersion	$DOC_{W(z)}$ [µm]	DOC_{Gauss} [µm]	*DOC* from eq. (3) [µm]
20x0.5 air	10.74	11.55	9.85
20x0.8 air	13.96	12.32	4.83
25x0.8 water	6.35	6.44	7.31
25x0.8 oil	10.8	11.89	8.99
40x1.4 oil	4.02	4.58	3.95

Table 1 Measured *DOC* values for a fixed gradient of 0.2 px/µm and 1 µm particles compared to the *DOC* calculated from equation 3 [3].

To further characterize the differences between both 20x air objectives we rescale the determined weighting function by the maximum value of its Gauss-fit and plot it as a function of the distance from focus *z* normalized by the measured $DOC_{W(z)}$ for 1 µm particles and several gradients g_z. Figure 3b) shows the resulting curves for the 20x0.5 air objective. Data-points for $g_z = 0.2$ px/µm have been connected by blue lines as a guide to the eye. If the assumption of Gaussian like weighting functions holds, all the measured *W(z)* should be self similar and collapse onto a single curve. The 20x0.5 air immersion objectives indeed shows a good agreement to the assumption of a Gaussian shaped weighting function and a narrow distribution of the rescaled weighting functions with slight deviations around $z = 0$ (figure 3b) due to a noisy $\Delta dx(z)$ as explained in the theory section.

In the case of the 20x0.8 air objective (figure 3d), the measured *W(z)* presents a strong asymmetry, and the distribution of the rescaled weighting functions is wider for different gradients g_z of the tested displacement function *dx(z)*. Additionally, the maximum deviation of the measured *W(z)* compared to the maximum of its Gauss-fit, is also larger than in the case of a lower *NA* objective.

One reason for the deviations from the expected shape of the *W(z)* and the big difference between the measured *DOC* values and the *DOC* calculated from equation 3 for the high *NA* air objective might be, that the assumptions of purely Gaussian particle images and a simple one lens system used by Olsen [1] to derive the shape of the *W(z)* and finally the *DOC* in equation 3 do not hold for high *NA* air objectives due to their more airy-like point-spread function. Similar asymmetries and deviations of measured *W(z)*, based on measuring the curvature of the auto-correlation peak of particle images around its maximum, have been found by Rossi, who also observed non-Gaussian images of defocused particles for comparable objectives [5].

Conclusion

Two methods have been presented to determine the *DOC* based on experimental images of fixed tracer particles taken at several distances from the focal plane. One method determines both the weighting function *W(z)* and its curve-width, the *DOC*, by testing for the influence of particles at a known distance from the in-focus plane on the measured displacement. The second method uses the same particle images. Assuming *W(z)* to be Gaussian the displacement for PIV double-images with a known displacement function was measured. From this measured displacement the *DOC* can be calculated, while the displacement function can be chosen to be similar to the flow field in real PIV measurements.

Good agreement to the existing *DOC* formula [1, 3, 11] for both of our methods has been found for a low *NA* air and for immersion objectives. For a large *NA* air objective we found that theory based on the *NA* specified on the objective significantly underestimates the *DOC*. This is in qualitative agreement with the results found by Rossi [5].

Analyzing the shape of the measured weighting function, again, the high *NA* air objective behaved different from the low *NA* air objective. While the later shows symmetric self similar *W(z)* for different gradients, this is not true for the high *NA* air objective, again indicating that the assumptions made in literature when deriving equations for the *DOC* do not hold for these objectives.

Both of our methods are capable of testing the influence of image-processing such as power filters or histogram filters [5, 17] or changed PIV-analysis parameters and are easy to implement. The same optical setup and particles as for actual measurements can be employed, resulting in a good estimate of the *DOC* for a given experimental situation.

The main advantage of our approach to measure the *DOC* and *W(z)* is that it allows to include the influence of out-of plane gradients to mimic real experimental flow-profiles. Our results show the expected decrease of the *DOC* for larger gradients as predicted by Olsen [4].

Especially calculating the *DOC* assuming a Gaussian shape of *W(z)* can be used to design experiments as it allows to scan a large range of out-of-plane gradients by an automated procedure without having to deal with the actual shape of the weighting function. As the resulting *DOC*s are usually larger than those calculated from measured weighting functions, this can be used to reasonably choose experimental parameters such as optical components to be used or inter-frame times (and thus the out-of-plane gradients present in the PIV double-images).

We believe that the knowledge of the *DOC* will allow for a more precise interpretation, especially for complex three dimensional flows. Furthermore, the computed weighting function of a system in dependence of gradients in the velocity profile could be used to correct for the influence of out-of-focus particles on measured velocity profiles by appropriate deconvolution with *W(z).*

References

[1] Olsen MG and Adrian RJ “Out-of-focus effects on particle image visibility and correlation in microscopic particle image velocimetry” Exp Fluids 29 7 (2000) S166–S174

[2] Wereley ST, Meinhart CD and Gray MHB (1999) Depth effects in volume illuminated particle image velocimetry. Third International Workshop on Particle Image Velocimetry Santa Barbara, CA, USA.

[3] Bourdon CJ, Olsen MG and Gorby AD “The Depth of Correlation in Micro-PIV for High Numerical Aperture and Immersion Objectives” J Fluids Eng 128 (2006) pp. 883–886

[4] Olsen MG “Depth of correlation reduction due to out-of-plane shear in microscopic particle image velocimetry” Meas:Sci.Tech. 21 (2010) 105406

[5] Rossi M, Segura R, Cierpka C, Kähler CJ “On the effect of particle image intensity and image preprocessing on the depth of correlation in micro-PIV” Exp Fluids 52 (2012) pp. 1063–1075

[6] Santiago JG, Wereley ST, Meinhart CD, Beebe DJ and Adrian RJ “A particle image velocimetry system for microfluidics” Exp Fluids 25(4) (1998) pp. 316–319

[7] Meinhart CD and Zhang H “The flow structure inside a micro-fabricated inkjet printhead” J Microelectromech Syst 9 (2000) pp. 67–75

[8] Vennemann P, Kiger KT, Lindken R, Groenendijk BCW, Stekelenburg-de Vos S, ten Hagen TLM, Ursem NTC, Poelmann RE Westerweel J and Hierck BP “In vivo micro particle image velocimetry measurements of blood-plasma in the embryonic avian heart”, Journal of Biomechanics 39 (2006) pp. 1191–1200

[9] Adrian RJ “Particle-imaging techniques for experimental fluid mechanics” Annu Rev Fluid Mech 23 (1991) pp. 261–304

[10] Meinhart CD, Wereley ST and Gray MHB “Volume illumination for two-dimensional particle image velocimetry” Meas. Sci. Technol. 11 (2000) pp. 809–814

[11] Bourdon CJ, Olsen MG and Gorby AD “Validation of an analytical solution for depth of correlation in microscopicparticle image velocimetry” Meas. Sci. Technol. 15 (2004) pp.318–327

[12] Kloosterman A, Poelma C, Westerweel J “Flow rate estimation in large depth-of-field micro-PIV” Exp Fluids 50 (2011) pp.1587–1599

[13] Olsen MG “Directional dependence of depth of correlation due to in-plane fluid shear in microscopic particle image velocimetry” Meas. Sci. Technol. 20 (2009) 015402

[14] Westerweel J, Geelhoed PF and Lindken R “Single-pixel resolution ensemble correlation for micro-PIV applications” Exp. Fluids 37(2004) pp. 375–384

[15] Nogueira J, Lecuona A and Rodriguez PA “Local field correction PIV, implemented by means of simple flow algorithms and multigrid versions” Meas. Sci. Technol.12 (2001) pp. 1911–1921

[16] Nogueira J, Lecuona A and Rodriguez PA “Local field correction PIV: on the increase of accuracy for digital PIV systems” Exp.Fluids 27 (1999) pp. 107-116

[17] Bourdon CJ, Olsen MG and Gorby AD “Power-filter technique for modifying depth of correlation in microPIV experiments”. Exp Fluids 37(2) (2004) pp. 263–271

List of Figures

Bibliography

[1] K. E. Petersen, *Silicon as a mechanical material*, Proc. of the IEEE **70** (1982) 420–457.

[2] H. Seidel and L. Csepregi, *Three-dimensional structuring of silicon for sensor applications*, Sensor. Actuator. **4** (1983) 455–463.

[3] P. Gravesen, J. Branebjerg, and O. S. Jensen, *Microfluidics-a review*, J. Mioromech. Microeng. **3** (1993) 168–182.

[4] P. Tabeling, *Introduction to Microfluidics* (S. Chen, ed.), Oxford University Press, 2005.

[5] R. Seemann, M. Brinkmann, T. Pfohl, and S. Herminghaus, *Droplet based microfluidics*, Rep. Prog. Phys. **75** (2012) 016601.

[6] R. L. Smith, R. W. Bower, and S. D. Collins, *The design and fabrication of a magnetically actuated micromachined flow valve*, Sens. Actuat. A: Physical **24** (1990) 47–53.

[7] H. T. G. van Lintel, F. C. M. van de Pol, and S. Bouwstra, *A piezoelectric micropump based on micromachining of silicon*, Sens. Actuat. **15** (1988) 153–167.

[8] R. Zengerle, A. Richter, and H. Sandmaier, *A micro membrane pump with electrostatic actuation* (W. Benecke and H. C. Petzold, ed.), 1992.

[9] A. Manz, D. J. Harrison, E. M. J. Verpoorte, J. C. Fettinger, A. Paulus, H. Ludi, and H.Widmer, *Planar chips technology for miniaturization and integration of separation techniques into monitoring systems: Capillary electrophoresis on a chip*, J. Chromat. A **593** (1992) 253–258.

[10] A. Manz, N. Graber, and H. M. Widmer, *Miniaturized total chemical analysis systems: a novel concept for chemical sensing*, Sens. Actuat. B **1** (1990) 244–248.

[11] M. A. Burns, B. N. Johnson, S. N. Brahmasandra, K. Handique, J. R. Webster, M. Krishnan, T. S. Sammarco, P. M. Man, D. Jones, D. Heldsinger, C. H. Mastrangelo, and D. T. Burke, *An integrated nanoliter DNA analysis device*, Science **282** (1998) 484–487.

[12] G. F. Christopher and S. L. Anna, *Microfluidic methods for generating continuous droplet streams*, J. Phys. D: Appl. Phys. **40** (2007) R319–R336.

[13] A. B. Theberge, F. Courtois, Y. Schaerli, M. Fischlechner, C. Abell, F. Hallfelder, and W. T. S. Huck, *Microdroplets in microfluidics: An evolving platform for discoveries in chemistry and biology*, Angew. Chem. Int. Ed. **49** (2010) 2–25.

[14] E. Guyon, J.-P. Hulin, L. Petit, and C. D. Mitescu, *Physical Hydrodynamics*, Oxford University Press, 2001.

[15] L. D. Landau and E. M. Lifschitz, *Lehrbuch der theroretischen Physik IV: Hydrodynamik* (G. Heber, ed.), Akademie Verlag Berlin, 1966.

[16] D. Meschede, *Gerthsen Physik*, Springer, 2004.

[17] S. Bommer, F. Cartellier, S. Jachalski, DirkPeschka, R. Seemann, and B. Wagner, *Droplets on liquids and their journey into equilibrium*, Euro. Phys. J. E: Soft Matter **36** (2013) 87.

[18] D. C. Duffy, J. C. McDonald, O. J. A. Schueller, and G. M. Whitesides, *Rapid prototyping of microfluidic systems in Poly(DiMethylSiloxane)*, Anal. Chem. **70** (1998) 4974–4984.

[19] R. Dangla, F. Gallaire, and C. N. Baroud, *Microchannel deformations due to solvent-induced PDMS swelling*, Lab Chip **10** (2010) 2972–2978.

[20] J. M. Andreas, E. A. Hauser, and W. B. Tucker, *Boundary tension by pendant drops*, J. Phys. Chem. **42** (1938) 1001–1019.

[21] Q. Brosseau, J. Vrignon, and J.-C. Baret, *Microfluidic dynamic interfacial tensiometry*, Soft Mat. **10** (2014) 3066–3076.

[22] J. W. Lichtman and J.-A. Conchello, *Fluorescence microscopy*, Nat. Methods **2** (2005) 910–919.

[23] D. Coling and B. Kachar, *Principles and application of fluorescence microscopy*, Current Protocols in Molecular Biology **44** (1998) 14.10.1–14.10.11.

[24] S. L. Veatch and S. L. Keller, *Separation of liquid phases in giant vesicles of ternary mixtures of phospholipides and cholesterol*, Biophys. J. **85** (2003) 3074–3083.

[25] M. Ehrenberg, *Scientific background on the Nobel Prize in chemistry 2014: Super-resolved fluorescence microscopy*, Royal Swedish Academy of Science, 2014.

[26] R. J. Adrian and J. Westerweel, *Particle Image Velocimetry*, Cambridge University Press, 2011.

[27] R. Williams, S. G. Peisajovich, O. J. Miller, S. Magdassi, D. S. Tawfik, and A. D. Griffiths, *Amplification of complex gene libraries by emulsion PCR*, Nat. Methods **3** (2006) 545–550.

[28] O. J. Miller, A. E. Harrak, T. Mangeat, J.-C. Baret, L. Frenz, B. E. Debs, E. Mayot, M. L. Samuels, E. K. Rooney, P. Dieu, M. Galvan, D. R. Link, and A. D. Griffiths, *High-resolution dose-response screening using droplet-based microfluidics*, Proc Nat. Acad. Sci. USA **109** (2012) 378–383.

[29] D. J. McClements, *Food Emulsions: Principles, Practices, and Techniques*, 2nd Edition (F. M. Clydesdale, ed.), CRC Series in Contemporary Food Science, CRC Press, 2005.

[30] T. Nakashima, M. Shimizu, and M. Kukizaki, *Membrane emulsification by micro-porous glass*, Key Eng. Mater. **61-62** (1992) 513–516.

[31] K. C. van Dijke, K. C. P. G. H. Schroën, and R. M. Boom, *Microchannel emulsification: From computational fluid dynamics to predictive analytical model*, Langmuir **24** (2008) 10107–10115.

[32] G. T. Vladisavljević, I. Kobayashi, and M. Nakajima, *Production of uniform droplets using membrane, microchannel and microfluidic emulsification devices*, Microfluid. Nanofluid. **13** (2012) 151–178.

[33] S.-Y. Teh, R. Lin, L.-H. Hung, and A. P. Lee, *Droplet microfluidics*, Lab Chip **8** (2008) 198–220. Review.

[34] C. D. Meinhart and H. Zhang, *The flow structure inside a microfabricated inkjet printhead*, J. Microelectromech. Syst. **9 (1)** (2000) 67–75.

[35] K. Churski, J. Michalski, and P. Garstecki, *Droplet on demand system utilizing a computer controlled microvalve integrated into a stiff polymeric microfluidic device*, Lab Chip **10** (2010) 512–518.

[36] S. H. Tan, B. Semin, and J.-C. Baret, *Microfluidic flow-focusing in AC electric fields*, Lab Chip **14** (2014) 1099–1106.

[37] J. Husny and J. J. Cooper-White, *The effect of elasticity on drop creation in T-shaped microchannels*, J. Non-Newtonian Fluid Mech. **137** (2006) 121–136.

[38] Y. Ren, Z. Liu, and H. C. Shum, *Breakup dynamics and dripping-to-jetting transition in a newtonian/shear-thinning multiphase microsystem*, Lab Chip **15** (2015) 121–134.

[39] C. N. Baroud, F. Gallaire, and R. Dangla, *Dynamics of microfluidic droplets*, Lab Chip **10** (2010) 2032–2045.

[40] H. Gu, M. H. G. Duits, and F. Mugele, *Droplets formation and merging in two-phase flow microfluidics*, Int. J. Mol. Sci. **12** (2011) 2572–2597.

[41] M. Wörner, *Numerical modeling of multiphase flows in microfluidics and micro process engineering: A review of methods and applications*, Microfluid. Nanofluid. **12** (2012) 841–886.

[42] T. Thorsen, R. W. Roberts, F. H. Arnold, and S. R. Quake, *Dynamic pattern formation in a vesicle-generating microfluidic device*, Phys. Rev. Lett. **86** (2001) 4163–4166.

[43] P. Garstecki, M. J. Fuerstman, H. A. Stone, and G. M. Whitesides, *Formation of droplets and bubbles in a microfluidic T-junction - scaling and mechanism of break-up*, Lab Chip **6** (2006) 437–446.

[44] A. R. Abate, P. Mary, V. van Steijn, and D. A. Weitz, *Experimental validation of plugging during drop formation in a T-junction*, Lab Chip **12** (2012) 1516–1521.

[45] L. Rayleigh, *On the instability of jets*, Proc. London Math. Soc. **s1-10** (1878) 4–13.

[46] P. Guillot and A. Colin, *Stability of parallel flows in a microchannel after a T-junction*, Phys. Rev. E **72** (2005) 066301.

[47] L. Shui, F. Mugele, A. van den Berg, and J. C. T. Eijkel, *Geometry-controlled droplet generation in head-on microfluidic devices*, Appl. Phys. Lett. **93** (2008) 153113.

[48] M. L. J. Steegmans, K. C. P. G. H. Schroën, and R. M. Boom, *Characterization of emulsification at flat microchannel Y-junctions*, Langmuir **25** (2009) 3396–3401.

[49] J. D. Tice, H. Song, A. D. Lyon, and R. F. Ismagilov, *Formation of droplets and mixing in multiphase microfluidics at low values of the reynolds and the capillary numbers*, Langmuir **19** (2003) 9127–9133.

[50] L. S. Roach, H. Song, and R. F. Ismagilov, *Controlling nonspecific protein adsorption in a plug-based microfluidic system by controlling interfacial chemistry using fluorous-phase surfactants*, Anal. Chem. **77** (2005) 785–796.

[51] H. Song, H.-W. Li, M. S. Munson, T. G. V. Ha, and R. F. Ismagilov, *On-chip titration of an anticoagulant argatroban and determination of the clotting time within whole blood or plasma using a plug-based microfluidic system*, Anal. Chem. **2006** (2006) 4839–4849.

[52] S. Makulska, S. Jakiela, and P. Garstecki, *A micro-rheological method for determination of blood type*, Lab Chip **13** (2013) 2796–2801.

[53] H. Song, D. L. Chen, and R. F. Ismagilov, *Reactions in droplets in microfluidic channels*, Angew. Chem. Int. Ed. **45** (2006Nov) 7336–7356.

[54] P. Guillot, A. Colin, A. S. Utada, and A. Ajdari, *Stability of a jet in confined pressure-driven biphasic flows at low Reynolds numbers*, Phys. Rev. Lett. **99** (2007) 104502.

[55] A. S. Utada, A. Fernández-Nieves, H. A. Stone, and D. A. Weitz, *Dripping to jetting transitions in coflowing liquid streams*, Phys. Rev. Lett. **99** (2007) 094502.

[56] P. Guillot, A. Colin, and A. Ajdari, *Stability of a jet in confined pressure-driven biphasic flows at low Reynolds number in various geometries*, Phys. Rev. E **78** (2008) 016307.

[57] K. J. Humphry, A. Ajdari, A. Fernández-Nieves, H. A. Stone, and D. A. Weitz, *Suppression of instabilities in multiphase flow by geometric confinement*, Phys. Rev. E **79** (2009) 056310.

[58] E. M. Chan, A. P. Alivisatos, and R. A. Mathies, *High-temperature microfluidic synthesis of CdSe nanocrystals in nanoliter droplets*, J. Am. Chem. Soc. **127** (2005) 13854–13861.

[59] C. Priest, S. Herminghaus, and R. Seemann, *Generation of monodisperse gel emulsions in a microfluidic device*, Appl. Phys. Lett. **88** (2006) 024106.

[60] F. Malloggi, N. Pannacci, R. Attia, F. Monti, P. Mary, H. Willaime, P. Tabeling, B. Cabane, and P. Poncet, *Monodisperse colloids synthesized with nanofluidic technology*, Langmuir **26(4)** (2010) 2369–2373.

[61] R. Dangla, E. Fradet, Y. Lopez, and C. N. Baroud, *The physical mechanisms of step emulsification*, J. Phys. D: Appl.Phys. **46** (2013) 114003.

[62] V. Chokkalingam, S. Herminghaus, and R. Seemann, *Self-synchronizing pairwise production of monodisperse droplets by microfluidic step emulsification*, Appl. Phys. Lett. **93** (2008) 254101.

[63] V. Chokkalingam, B. Weidenhof, M. Krämer, S. Herminghaus, R. Seemann, and W. F. Maier, *Template-free preparation of mesoporous silica spheres through optimized microfluidics*, Chem. Phys. Chem. **11** (2010) 2091–2095.

[64] S. Afkhami and Y. Renardy, *A volume-of-fluid formulation for the study of co-flowing fluids governed by the Hele-Shaw equations*, Phys. Fluids. **25** (2013) 082001.

[65] Z. Li, A. M. Leshansky, L. M. Pismen, and P. Tabeling, *Step-emulsification in a microfluidic device*, Lab Chip **15** (2015) 1023–1031.

[66] C. A. Wijayawardhana, H. B. Halsall, and W. R. Heineman, *Micro volume rotating disk electrode (RDE) amperometric detection for a bead-based immunoassay*, Anal. Chim. Acta **399** (1999) 3–11.

[67] J.-W. Choi, K. W. Oh, J. H. Thomas, W. R. Heineman, H. B. Halsall, J. H. Nevin, A. J. Helmicki, H. T. Henderson, and C. H.Ahn, *An integrated microfluidic biochemical detection system for protein analysis with magnetic bead-based sampling capabilities*, Lab Chip **2** (2002) 27–30.

[68] K. L. Kellar and M. A. Iannone, *Multiplexed microsphere-based flow cytometric assays*, Exp. Hematol. **30** (2002) 1227–1237.

[69] A.-J. Cheng, L.-C. Chen, K.-Y. Chien, Y.-J. Chen, J. T.-C. Chang, H.-M. Wang, C.-T. Liao, and I.-H. Chen, *Oral cancer plasma tumor marker identified with bead-based affinity-fractionated proteomic technology*, Clin. Chem. **51:12** (2005) 2236–2244.

[70] M. Schmitt, I. G. Bravo, P. J. F. Snijders, L. Gissmann, M. Pawlita, and T. Waterboer, *Bead-based multiplex genotyping of human papillomaviruses*, J. Clin. Microbiol. **44** (2006) 2.

[71] D. Holmes, J. K. She, P. L. Roach, and H. Morgan, *Bead-based immunoassays using a micro-chip flow cytometer*, Lab Chip **7** (2007) 1048–1056.

[72] M. Toner and D. Irimia, *Blood-on-a-chip*, Annu. Rev. Biomed. Eng. **7** (2005) 77–103.

[73] A. Lenshof and T. Laurell, *Continuous separation of cells and particles in microfluidic systems*, Chem. Soc. Rev. **39** (2010) 1203–1217.

[74] P. Sajeesh and A. K. Sen, *Particle separation and sorting in microfluidic devices: a review*, Microfluid. Nanofluid. (2013).

[75] D. DiCarlo, *Inertial microfluidics*, Lab Chip **9** (2009) 3038–3046.

[76] N. Pamme, *Continuous flow separations in microfluidic devices*, Lab Chip **7** (2007) 1644–1659.

[77] N. Chronis, W. Lam, and L. Lee, *Micro total analysis systems 2001* (J. M. Ramsey and A. van den Berg, ed.), Kluwer Academic Publishers, 2001.

[78] N. Pamme and A. Manz, *On-chip free-flow magnetophoresis: Continuous flow separation of magnetic particles and agglomerates*, Anal. Chem. **76** (2004) 7250–7256.

[79] Y. Zhou, Y. Wang, and Q. Lin, *A microfluidic device for continuous-flow magnetically controlled capture and isolation of microparticles*, J. Microelectromech. Syst. **19** (2010) 743–751.

[80] Q. Ramadan and M. A. M. Gijs, *Simultaneous magnetic particles washing and concentration in a microfluidic channel*, Proc. Chem. **1** (2009) 1499–1502.

[81] D. Gao, H.-F. Li, G.-S. Guo, and J.-M. Lin, *Magnetic bead based immunoassay for enumeration of CD4+ T lymphocytes on a microfluidic device*, Talanta **82** (2010) 528–533.

[82] C. R. Cabrera and P. Yager, *Continuous concentration of bacteria in a microfluidic flow cell using electrokinetic techniques*, Electrophoresis **22** (2001) 355–362.

[83] U. Kim, J. R. Qian, S. A. Kenrick, P. S. Daugherty, and H. T. Soh, *Multitarget dielectrophoresis activated cell sorter*, Anal. Chem. **80** (2008) 8656–8661.

[84] S. Patel, D. Showers, P. Vedantam, T.-R. Tzeng, S. Qian, and X. Xuan, *Microfluidic separation of live and dead yeast cells using reservoir-based dielectrophoresis*, Biomicrofluidics **6** (2012) 034102.

[85] R. L. Tornay, T. Braschler, N. Demierre, B. Steitz, A. Finka, H. Hofmann, J. A. Hubbell, and P. Renaud, *Dielectrophoresis-based particle exchanger for the manipulation and surface functionalization of particles.*, Lab Chip **8** (2008) 267–273.

[86] M. P. MacDonald, G. C. Spalding, and K. Dholakia, *Microfluidic sorting in an optical lattice*, Nature **426** (2003) 421–424.

[87] P. Augustsson, J. Persson, S. Ekström, M. Ohlin, and T. Laurell, *Decomplexing biofluids using microchip based acoustophoresis*, Lab Chip **9** (2009) 810–818.

[88] R. V. Raghavan, J. R. Friend, and L. Y. Yeo, *Particle concentration via acoustically driven microcentrifugation: microPIV flow visualization and numerical modelling studies*, Microfluid. Nanofluid. **8** (2010) 73–84.

[89] C. Grenvall, C. Antfolk, C. Z. Bisgaard, and T. Laurell, *Two-dimensional acoustic particle focusing enables sheathless chip coulter counter with planar electrode configuration*, Lab Chip **14** (2014) 4629.

[90] H. Mohamed, L. D. McCurdy, D. H. Szarowski, S. Duva, J. N. Turner, and M. Caggana, *Development of a rare cell fractionation device: Application for cancer detection*, IEEE Trans. Nanobiosci. **3** (2004) 251–256.

[91] M. Yamada and M. Seki, *Hydrodynamic filtration for on-chip particle concentration and classification utilizing microfluidics*, Lab Chip **5** (2005) 1233–1239.

[92] X. Chen, D. F. Cui, C. C. Liu, and H. Li, *Microfluidic chip for blood cell separation and collection based on crossflow filtration*, Sens. Actuators B **130** (2008) 216–221.

[93] M. Yamada, M. Nakashima, and M. Seki, *Pinched flow fractionation: Continuous size separation of particles utilizing a laminar flow profile in a pinched microchannel*, Anal. Chem. **76** (2004) 5465–5471.

[94] J. Takagi, M. Yamada, M. Yasudaa, and M. Seki, *Continuous particle separation in a microchannel having asymmetrically arranged multiple branches*, Lab Chip **5** (2005) 778–784.

[95] D. Huh, J. H. Bahng, Y. Ling, H.-H. Wei, O. D. Kripfgans, J. B. Fowlkes, J. B. Grotberg, and S. Takayama, *Gravity-driven microfluidic particle sorting device with hydrodynamic separation amplification*, Anal. Chem. **79** (2007) 1369–1376.

[96] G. Segré and A. Silberberg, *Behaviour of macroscopic rigid spheres in poiseuille flow - Part 1: Determination of local concentration by statistical analysis of particle passages through crossed light beams*, J. Fluid Mech. **14** (1962) 115–135.

[97] G. Segré and A. Silberberg, *Behaviour of macroscopic rigid spheres in poiseuille flow - Part 2: Experimental results and interpretation*, J. Fluid Mech. **14** (1962) 136–157.

[98] D. DiCarlo, D. Irimia, R. G. Tompkins, and M. Toner, *Continuous inertial focusing, ordering and separation of particles in microchannels*, Proc. Nat. Acad. Sci. USA **104** (2007) 18892–18897.

[99] A. A. S. Bhagat, S. S. Kuntaegowdanahalli, and I. Papautsky, *Inertial microfluidics for continuous particle filtration and extraction*, Microfluid. Nanofluid. **7** (2009) 217–226.

[100] J. C. Giddings, *A system based on split-flow lateral-transport thin (SPLITT) separation cells for rapid and continuous particle fractionation*, Sep. Sci. Technol. **20** (1985) 749–768.

[101] D. Lombardi and P. S. Dittrich, *Droplet microfluidics with magnetic beads: A new tool to investigate drug-protein interactions*, Anal. Bioanal. Chem. **399** (2011) 347–352.

[102] E. Brouzes, T. Kruse, R. Kimmerling, and H. H. Strey, *Rapid and continuous magnetic separation in droplet microfluidic devices*, Lab Chip **15** (2015) 908–919.

[103] G. K. Kurup and A. S. Basu, *Field-free particle focusing in microfluidic plugs*, Biomicrofluidics **6** (2012) 022008.

[104] M. Sun, Z. S. Khan, and S. A. Vanapalli, *Blood plasma separation in a long two-phase plug flowing through disposable tubing*, Lab Chip **12** (2012) 5225–5230.

[105] F. P. Bretherton, *The motion of long bubbles in tubes*, J. Fluid Mech. **10** (1962) 166–188.

[106] S. R. A. Hodges, O. E. Jensen, and J. M. Rallison, *The motion of a viscous drop through a cylindrical tube*, J. Fluid Mech. **501** (2004) 279–301.

[107] H. Wong, C. J. Radke, and S. Morris, *The motion of long bubbles in polygonal capillaries Part 2: Drag, fluid pressure and fluid flow*, J. Fluid Mech. **292** (1995) 95–110.

[108] H. Wong, C. J. Radke, and S. Morris, *The motion of long bubbles in polygonal capillaries. Part 1: Thin films*, J . Fluid Mech. **292** (1995) 71–94.

[109] F. Sarrazin, K. Loubiere, L. Prat, C. Gourdon, T. Bonometti, and J. Magnaudet, *Experimental and numerical study of droplets hydrodynamics in microchannels*, AIChE Journal **52** (2006) 4061.

[110] F. Sarrazin, T. Bonometti, L. Prat, C. Gourdon, and J. Magnaudet, *Hydrodynamic structures of droplets engineered in rectangular micro-channels*, Microfluid. Nanofluid. (2007).

[111] H. Kinoshita, S. Kaneda, T. Fujii, and M. Oshima, *Three-dimensional measurement and visualization of internal flow of a moving droplet using confocal micro-PIV*, Lab Chip **7** (2007) 338–346.

[112] U. Miessner, R. Lindken, and J. Westerweel, *3D - velocity measurements in microscopic two-phase flows by means of micro PIV*, Band 14, 2008.

[113] D. Malsch, M. Kielpinski, R. Merthan, J. Albert, G. Mayera, J. M. Köhler, H. Süße, M. Stahl, and T. Henkel, *Micro-PIV analysis of taylor flow in micro channels*, Chem. Eng. J. **135S** (2008) s166–s172.

[114] M. Oishi, H. Kinoshita, T. Fujii, and M. Oshima, *Simultaneous measurement of internal and surrounding flows of a moving droplet using multicolour confocal micro-particle image velocimetry (micro-PIV)*, Meas. Sci. Technol. **22** (2011) 105401.

[115] S. Ma, J. M. Sherwood, W. T. S. Huck, and S. Balabani, *On the flow topology inside droplets moving in rectangular microchannels*, Lab Chip **14** (2014) 3611–3620.

[116] S. Jakiela, P. M. Korczyk, S. Makulska, O. Cybulski, and P. Garstecki, *Discontinuous transition in a laminar fluid flow: A change of flow topology inside a droplet moving in a micron-size channel*, Phys. Rev. Lett. **108** (2012) 134501.

[117] R. Lindken, M. Rossi, S. Große, and J. Westerweel, *Micro-particle image velocimetry (µPIV): Recent developments, applications, and guidelines*, Lab Chip **9** (2009) 2551–2567.

[118] G. Elsinga, F. Scarano, B. Wieneke, and B. van Oudheusen, *Tomographic particle image velocimetry*, Exp. Fluids **41** (2006) 933–947.

[119] R. J. Adrian, *Scattering particle characteristics and their effect on pulsed laser measurements of fluid flow: speckle velocimetry vs particle image velocimetry.*, Appl. Opt. **23** (1984) 1690–1691.

[120] R. J. Adrian, *Particle-imaging techniques for experimental fluid mechanics*, Annu. Rev. Fluid Mech. **23** (1991) 261–304.

[121] R. J. Adrian, *Twenty years of particle image velocimetry*, Exp. Fluids **39** (2005) 159–169.

[122] J. Westerweel, G. E. Elsinga, and R. J. Adrian, *Particle image velocimetry for complex and turbulent flows*, Annu. Rev. Fluid. Mech. **45** (2013) 409–436.

[123] J. G. Santiago, S. T. Wereley, C. D. Meinhart, D. J. Beebe, and R. J. Adrian, *A particle image velocimetry system for microfluidics*, Exp. Fluids **25** (1998) 316–319.

[124] S. T. Wereley, C. D. Meinhart, and M. H. B. Gray, *Depth effects in volume illuminated particle image velocimetry*, Third International Workshop on Particle Image Velocimetry Santa Barbara, CA, USA. (1999).

[125] C. D. Meinhart, S. T. Wereley, and M. H. B. Gray, *Volume illumination for two-dimensional particle image velocimetry*, Meas. Sci. Technol. **11** (2000) 809–814.

[126] M. G. Olsen and R. J. Adrian, *Out-of-focus effects on particle image visibility and correlation in microscopic particle image velocimetry*, Exp. Fluids **29 S1** (2000) S166–174.

[127] C. J. Bourdon, M. G. Olsen, and A. D. Gorby, *Validation of an analytical solution for depth of correlation in microscopic particle image velocimetry*, Meas. Sci. Technol. **15** (2004) 318–327.

[128] C. J. Bourdon, M. G. Olsen, and A. D. Gorby, *The depth of correlation in microPIV for high numerical aperture and immersion objectives*, J. Fluids Eng. **128** (2006) 883–886.

[129] M. Rossi, R. Segura, C. Cierpka, and C. J. Kähler, *On the effect of particle image intensity and image preprocessing on the depth of correlation in micro-PIV*, Exp. Fluids **52** (2012) 1063–1075.

[130] P. Vennemann, K. T. Kiger, R. Lindken, B. C. W. Groenendijk, S. S. de Vosd, T. L. M. ten Hagen, N. T. C. Ursem, R. E. Poelmann, J. Westerweel, and B. P. Hierck, *In vivo micro particle image velocimetry measurements of blood-plasma in the embryonic avian heart*, J. Biomech. **39** (2006) 1191–1200.

[131] M. G. Olsen, *Depth of correlation reduction due to out-of-plane shear in microscopic particle image velocimetry*, Meas. Sci. Technol. **21** (2010) 105406.

[132] M. G. Olsen, *Directional dependence of depth of correlation due to in-plane fluid shear in microscopic particle image velocimetry*, Meas. Sci. Technol. **20** (2009) 015402.

[133] J. Westerweel, P. F. Geelhoed, and R. Lindken, *Single-pixel resolution ensemble correlation for micro-PIV applications*, Exp. Fluids **37** (2004) 375–384.

[134] J. Nogueira, A. Lecuona, and P. A. Rodriguez, *Local field correction PIV: on the increase of accuracy for digital PIV systems*, Exp. Fluids **27** (1999) 107–116.

[135] J. Nogueira, A. Lecuona, and P. A. Rodriguez, *Local field correction PIV, implemented by means of simple algorithms and multigrid versions*, Meas. Sci. Technol. **12** (2001) 1911–1921.

[136] C. Poelma, A. Kloosterman, B. P. Hierck, and J. Westerweel, *Accurate blood flow measurements: Are artificial tracers necessary?*, PLOS One **7 (9)** (2012) e45247.

[137] M. Moskopp, *Charakterisierung einer neuartigen Methode zur Tropfenteilung in der Mikrofluidik*, Bachelorarbeit (2012).

A. Publications and Conference Contributions

Articles

- 'Calculation of the weighting function and determination of the depth of correlation in μPIV from experimental particle images', Michael Hein, Bernhard Wieneke and Ralf Seemann,
  Meas. Sci. Technol. 25 (8) 084008 (11pp). DOI: 10.1088/0957-0233/25/8/084008, 2014
  Special Issue "Characterization of PIV Systems", invited peer-reviewed article

- 'Capillary focusing close to a topographic step: shape and instability of confined liquid filaments', Michael Hein, Shahriar Afkhami, Ralf Seemann, Lou Kondic, Microfluid. Nanofluid. 18 (5), 911-917 DOI: 10.1007/s10404-014-1481-0, 2015.

- 'Coexistence of different droplet generating instabilities: new breakup regimes of a liquid filament', Michael Hein, Jean-Baptiste Fleury and Ralf Seemann,
  accepted in Soft Matter, DOI: 10.1039/C5SM00736D, 2015

- 'Flow field induced particle accumulation inside droplets in rectangular channels', Michael Hein, Michael Moskopp and Ralf Seemann,
  accepted in Lab on a Chip, DOI: 10.1039/C5LC00420A , 2015

Conference Proceedings

- 'Template-Free Preparation of Platinum Doped Silica Catalyst Microspheres Through a Microfluidic Scheme', Venkatachalam Chokkalingam, Boris Weidenhof, Michael Hein, Wilhelm Maier and Ralf Seemann, Proceedings of the 2nd European Conference on Microfluidics (MicroFlu'10), Toulouse, France, 2010.

- 'Direct calculation of depth of correlation and weighting function in μPIV from experimental particle images', Michael Hein, Bernhard Wieneke and Ralf Seemann, 10th International Symposium on Particle Image Velocimetry - PIV13 Delft, The Netherlands, July 2-4, 2013

Scientific Talks (selected)

- ’Microfluidic Sol-Gel Synthesis Scheme for Complex Chemical Reactions’, 2nd European Conference on Microfluidics, Toulouse (F), 2010
- ’Microparticle Separation in Droplet Based Microfluidics’, Feldberg Winter School, Saarbrücken (D), 2010
- ’Field Free On-Chip Particle Concentration in Droplet Based Microfluidics’, Feldberg Winter School, Feldberg (D), 2012
- ’Direct Calculation of Depth of Correlation and Weighting Function in μPIV from Experimental Particle Images’, PIV2013, Delft (NL), 2013
- ’Droplet Based Microfluidics: Interface and Dynamics’, NJIT Fluid Dynamics Seminar, New Jersey Institute of Technology, Newark (NJ, USA), 2013
- ’Breakup of Liquid Filaments: Step-Emulsification’, Feldberg Winter School, Feldberg (D), 2013
- ’Direct Calculation of the Weighting Function and Depth of Correlation in Micro-Particle Image Velocimetry (Micro-PIV) from Particle Images’, APS Division of Fluid Dynamics Fall meeeting, Pittsburgh (PA, USA), 2013
- ’Capillary focusing: New Breakup Regimes in Step-Emulsification’, DPG March meeting, Dresden (D), 2014
- ’Controllable Coexistence of Multiple Instabilities on a Single Liquid Filament’, APS March meeting, San Antonio (TX, USA), 2015

Selected Poster Contributions

- ’Microparticle Separation in Droplet Based Microfluidics’, Michael Hein, Jean-Baptiste Fleury and Ralf Seemann, DPG March meeting, Dresden (D), 2011
- ’Microparticle Separation in Droplet Based Microfluidics’, Michael Hein, Jean-Baptiste Fleury and Ralf Seemann, DPG March meeting, Berlin (D), 2012
- ’A New Approach to Measure the Depth of Correlation in Micro-PIV’, Michael Hein, Bernhard Wieneke and Ralf Seemann, DPG March meeting, Regensburg (D), 2013
- ’Characterisation of a Novel Splitting Geometry for Microdroplets’, Michael Moskopp, Michael Hein and Ralf Seemann, DPG March meeting, Dresden (D), 2014

B. Acknowledgements

First of all, I'd like to thank Prof. Ralf Seemann for giving me the opportunity to do research in his group. I really appreciate the scientific freedom you grant to PhD-students, allowing me to pursue my own projects and follow my curiosity. Thanks a lot for all the support, including late discussions and paper-writing sessions in your office. (Sorry Karin!)

I can not sufficiently thank Dr. Jean-Baptiste Fleury. I really enjoyed our long discussions about, but not limited to, our projects. I learned a lot about conducting research and physics from you, all spiced up with your special charm. Thanks for all the good advice and fun and all the best!

Cheers to the colleagues of the Seemann Group, especially Dr. Michael Jung, Marc Schaber, Dr. Stefan Bommer, Hagen Scholl, Anna-Lena Hippler and Carsten Herrmann for suggestions and input or just for goofing off in our offices. The good atmosphere in this peer-group made work enjoyable on a daily basis! Same holds for the colleagues of the Jacobs group, specifically but not limited to Dr. Matthias Lessel, Dr. Hendrik Hähl, Dr. Frank Müller, Sabrina Haefner and Dr. Joshua McGraw. Special thanks goes to Michael Moskopp, whom I was allowed to tutor as a student research assistant, bachelor- and master-student. I appreciated working with you and am very grateful for your contribution to this thesis. Michael Schmidt and the team of the physics machine shop were a great help, too. Last but not least, the two good spirits of the Jacobs/Seemann group: Judith Rech and Monika Schuck. Thanks for giving orientation in the jungle of administration and support in lab maintenance.

I also acknowledge all my collaborators for their efforts and the great experience of the different projects: Thanks to Shahriar Afkhami and Lou Kondic for approaching us to restart working on Step-emulsification. Thanks to Bernhard Wieneke from LaVision GmbH for his open mind and for teaching me a lot about PIV while being with LaVision in Göttingen and to Philipp Jung from the "Institut für Medizinische Mikrobiologie und Hygiene" in Homburg for discussions about possible bio-applications of our systems and supplying yeast cells.

In my private life, I would like to thank my parents, who always and unconditionally support me. And, of course, my fiancé Susanne Blum. Thank you thousandfold for sharing joy and frustration as PhD-students, bearing my unbearable moods and for calming me with your comforting smile or a prick of your ready wit when needed. You make life meaningful in the best sense!

C. Eidesstattliche Versicherung

Hiermit versichere ich an Eides statt, dass ich die vorliegende Arbeit selbstständig und ohne Benutzung anderer als der angegebenen Hilfsmittel angefertigt habe. Die aus anderen Quellen oder indirekt übernommenen Daten und Konzepte sind unter Angabe der Quelle gekennzeichnet. Die Arbeit wurde bisher weder im In- noch im Ausland in gleicher oder ähnlicher Form in einem Verfahren zur Erlangung eines akademischen Grades vorgelegt.

Saarbrücken, den 21. August 2015

Michael Hein